University of Naples 'Federico II'

Department of Structures for Engineering and Architecture

Mariana Zimbru

BOLTED CONNECTIONS FOR EASILY REPAIRABLE SEISMIC RESISTANT STEEL STRUCTURES

PhD Thesis

Structural Engineering, Geotechnics and Seismic Risk

XXXI Cycle

PhD Coordinator: Prof Dr. Luciano Rosati

*Tutor:*Prof Dr. Raffaele Landolfo

Co-tutor: Assoc. Prof. Dr. Mario D'Aniello

Naples, Italy - January 2019

Acknowledgements

Although it's difficult to summarize in a few paragraphs the gratitude that I feel I must send in so many directions, I'll try to address the task in a systematic way.

I cannot but start with the immense gratitude I owe to my suppervisors Prof. Dr. Raffaele Landolfo and Assoc. Prof. Dr. Mario D'Aniello who not only welcomed me into their research group and offered me guidance and support as much as one could possibly ask, but also allowed me to grow as an independent young researcher.

My thoughts and thanks go towards the colleagues that offered me friendship and opportunities to discuss the obstacles in research and otherwise. Honorable mentions go to the one who has been both my daily moral support and/or pain, Dr. Roberto Tartaglia – the office part of the research life would have been so boring without you. For my fellow PhD colleagues Sofia and Akiko, I have special thanks, since the course would have been so much lonelier. I'm happy we've grown closer throughout the years, and thank you for your patience, support and understanding.

I thank my parents who were patiently waiting for me to call and and understanding the late hours. I thank them for listening to me and compassionate understanding as well as for the heart-warming attempts to make me go home more often.To my sisters, Ana-Ramona and Ioana, I'm so grateful for becoming the older sisters when I was not able to stand the role anymore, as well as to my brother Adrian, who has encouraged me always on my path.

My best friends and comrades in good and bad times: Alexandru, Cristina, Gabriel and Slobodanka – thank you for being a call away and in all this time, encouraging me to become better than I am.

The research leading to these results has partially received funding from the European Union's Research Fund for Coal and Steel (RFCS) research programme under grant agreement No. 709434 INNOSEIS (2016-2018) and RFSR-CT-2015-00022 (FREEDAM "Free from Damage friction connection").

Abstract

Recent years have brought significant advances in the design capabilities and construction practices of steel structures. These were partially caused by technological development and a direct effect of the research community efforts towards the mitigation of the earthquake induced damage. Making the traditional structural systems more resilient is one of the directions taken but, more and more, solutions with reduced post-earthquake repair costs are preferred. Steel structures are particularly malleable in the modern spirit of integrating devices which render the structure as “low-damage” or “easily repairable”. The recent earthquakes of Japan and New Zealand have demonstrated the feasibility and the advantages of such structural typologies.

The current work presents an investigation on two steel structural solutions, including thus both moment resisting and braced frames, which have the potential of being easily used in practice, with minimal alteration of the design and erection procedures and improved post-earthquake economic benefits. The thesis focuses on (i) bolted connections of detachable short links for eccentrically braced frame and on (ii) bolted friction connections for moment resisting frames. The main objective is to facilitate the application of these structural solutions in practice by enhancing the knowledge of their relevant bolted connection design and behavior.

Table of Contents

List of figures

List of Tables

List of Symbols and Abbreviations

Abbreviations:

AFC	Asymmetric friction connection
B31	a 2-node linear beam in space
BC	Boundary conditions
BRB	Buckling restrained braces
C3D8I	8-Node linear brick incompatible mode element
C3D8R	8-Node linear brick reduced integration
CBF	Concentrically braced frames
CP	Collapse prevention performance level
D-EBF	Dual eccentrically braced frame
DL	Damage limitation performance level
DR	Deformable restraints boundary conditions
DS	Disc spring washers
DOF	Degree of freedom
EBF	Eccentrically braced frame
EC8	Eurocode 8 compliant set of frames
EC8-MRF	Moment resisting frame designed with traditional joints (Eurocode compliant)
EEP	extended end-plate connection
FD	FREEDAM friction device
FD-A	Set of frames designed according to the FD-A design procedure
FD-B	Set of frames designed according to the FD-A design procedure
FD-MRF	Moment resisting frames designed with friction dampers
FE	Finite element
FEA	finite element analysis
FEM	finite element model
FEP	Flush end-plate connection
FO	Fully operational test
FR	Fully restrained boundary conditions
FREEDAM	Free from damage connections
GM	Ground motion
IDA	Incremental dynamic analysis
HH	high seismic hazard

HR	British-French style preloadable bolts *'High Resistance'*
HV	German style preloadable bolts *'Hochfeste Bolzen mit Vorspannung'*
MH	Damage limitation limit state
MR	Moment resisting
MRF	moment resisting frame
NA	Neutral axis
NC	Near collapse limit state
PEEQ	equivalent plastic strain
PGA	peak ground acceleration
PO	Pushover test
PRID	Peak residual interstorey drift
PTID	Peak transient interstorey drift
RBS	reduced beam sections
RC	Reinforced concrete
RF	Reaction force
RID	Residual interstorey drift
SD	Significant damage performance level
SF	Scaling factor
SFC	Symmetric friction connection
SLS	Serviceability limit state
TID	Transient interstorey drift
U	Displacement in Abaqus
UR	Rotation in Abaqus
ULS	Ultimate limit state
VHH	very high hazard

Symbols:

A	Aria of cross section
A_b:	Nominal area of the bolt shank
A_{be}:	Effective area of the threads
$A_{effective}$:	Area of the threaded region
A_{fl}	Flange area
A_{gross}:	Gross cross section of the shank
A_s	Bolt tensile area
A_{vz}	Web area of hot-rolled cross section according to EC3
A_w	Web area
E	Nominal modulus of elasticity of steel
F	Force
$F_{c,fb,Rd}$	Flange and web of beam or column in compression component
$F_{C,Rd}$	Compression resultant of the joint
F_i	Force of component *i*
$F_{p,C}$	Recommended bolt preloading force according to EN1993 1-8
F_{Rd}	Resistance of component
$F_{slip,eff}$	Effective slip force
$F_{slip,req}$	Required slip force
$F_{t,Rd}$	Resistance of a bolt in tension
$F_{t,i,Rd}$	Tensile resistance of component *i*

$F_{T,Rd}$	Resistance of T stub
$F_{T,1,Rd}$	Resistance of T stub at Failure Mode 1
$F_{T,2,Rd}$	Resistance of T stub at Failure Mode 2
$F_{T,3,Rd}$	Resistance of T stub at Failure Mode 3
$F_{t,i,Rd}$	Resistance of component *i* in tension
$F_{t,wb,Rd}$	Beam web in tension component
$F_{v,Rd}$	Shear resistance of one bolt
$G_{k,i}$	Characteristic value of the permanent load *i*
$H_{i,d}$	Equivalent horizontal forces accounting for frame imperfections
K	Axial stiffness of joint component
K_{axial}	Axial stiffness of the EBF
$K_{ax,link}$	Link axial stiffness
$K_{fl,link}$	Link flexural stiffness
$K_{j,ax}$	Joint axial stiffness
$K_{rotational}$	Rotational stiffness of the EBF
L	Distance from the column axis to the point of application of the displacement histories
L_1	Deformation of spring 1 (measurement of link distortion)
L_2	Deformation of spring 2 (measurement of link distortion)
L_b	The bolt elongation taken equal to the grip length (total thickness of material and washers), plus half the sum of the height of the bolt head and the height of the nut
L_b*	Limit tifhtening length for the development of the prying forces
L_s	Shank length of the bolt
L_{tg}	the length of the threaded portion included in the bolt's grip
M	Bending moment
M_{Rd}	Bending resistance
$M_{b,Rd}$	is the design moment resistance of the beam cross-section, reduced if necessary, to allow for shear
M_{CD}	Design bending moment for non-dissipative elements in moment resisting frames equipped with friction connections
M_{CD}^*	Initial value of design bending moment for non-dissipative elements
M_{Ed}	Design bending moment from the seismic combination
$M_{Ed,E}$	Contribution of the exceptional loads to the design bending moment
$M_{Ed,G}$	Contribution of the gravitational loads to the design bending moment
M_{FD}	Design bending moment for the friction damper (dissipative element for moment resisting frames equipped with friction connections)
M_j	Bending moment in joint
$M_{j,Ed}$	Joint design bending moment
$M_{j,Rd}$:	Design bending resistance of the joint
$M_{j,Sd}$	Bending moment in the joint at a given moment
$M_{pl,b,Rd}$	Beam plastic bending resistance
$M_{pl,link}$	Plastic bending moment of the link evaluated according to EC8
M_{Rb}	Moment of resistance of the beams framing the node
M_{Rc}	Moment of resistance of the columns framing the node
N	Axial force
N_b	Design pre-loading force in the bolts
N_{Ed}	Design axial force
$N_{Ed,E}$	Design axial force – contribution of exceptional loads
$N_{Ed,G}$	Design axial force – contribution of gravitational loads

$N_{fl,link}$	Plastic axial strength of the flanges ($N_{pl,fl}$)
$N_{j,Ed}$	Joint design axial force
$N_{j,Rd}$	Joint axial resistance
$N_{pl,Rd}$	Plastic axial strength
$N_{pl,fl}$	Plastic axial strength of the flanges ($N_{fl,link}$)
P_{tot}	Total gravity load at and above the storey considered in the seismic design situation (for P-Δ effects)
R	Position of the M-N curve
R^*	Deviation of the design pair from the M-N curve
Q	Prying forces
$Q_{k,i}$	Characteristic value of the variable load i
S_j	Joint stiffness
$S_{j,ini}$	Joint initial flexural stiffness
V	Shear force
V_1	Base shear at the occurrence of the first nonlinear event
V_d	Design base shear evaluated according to EC8
V_{Ed}	Design shear force
$V_{Ed,E}$	Design shear force – contribution of exceptional loads
V_{Ed}	Design shear force– contribution of gravitational loads
$V_{j,Ed}$	Joint design shear force
$V_{j,Rd}$	Joint shear resistance
$V_{pl,link}$	Plastic shear strength of the link evaluated based on the EC8 recommendations
V_{tot}	Total seismic storey shear (for P-Δ effects)
V_y	Maximum base shear (occurrence of collapse)
Z	Lever arm
a	Length of the friction device (from tip to column face)
a_g	Gravitational acceleration
b	Width of the profile
b_{fl}	Width of profile flange
b_p	Width of end-plate
$b_{eff,t,wb}$	Effective width of the beam web in tension
d	Depth of cross section
d	Bolt diameter
d_b	Nominal diameter of the bolt
d_t	Design interstorey drift (for P-Δ effects)
e, e_x	Distance from the bolt to the plate edge (Design of bolted connections according to EC3 1-8)
e	Link length
e_{link}	Link lenght
e_{min}	Minimum between e and e_x
e_s	Shear (short) link length limit
f	Stiffness correlation factor assumed equal to 0.55
$f_{effective}$	Effective stress
f_{actual}	Actual stress
f_y	Yield strength
$f_{y,k}$	Characteristic yield strength
$f_{y,fl}$	Yield strength of the flange
$f_{y,wb}$	Yield strength of the web of the beam
f_{ub}	Ultimate bolt strength
g	Gravitational acceleration

h	Depth of section
h_i	Lever arm of component i
h_r	Lever arm of bolt row r
h_{storey}	Storey height
k_5	Stiffness coefficient of end-plate in bending
k_{10}	Stiffness coefficient of bolts in tension
k_a	Assembly stiffness
k_b	Bolt stiffness
k_e	Elastic stiffness
$k_{eff,r}$	Equivalent stiffness coefficient
k_{eq}	Equivalent stiffness coefficient accounting for multiple bolt rows in tension
k_i	Stiffness of component i
$k_{i,r}$	Stiffness of component i of bolt row r
$k_{j,ax}$	Ratio between axial stiffness of connection and link axial stiffness ($K_{\text{j,ax}}/K_{\text{ax,link}}$)
$k_{j,fl}$	Ratio between connection initial stiffness and link flexural stiffness ($S_{\text{j,ini}}/K_{\text{fl,link}}$)
l_{eff}	Effective length of the T-stub in tension
$l_{eff,cp}$	Effective length considering circular patterns of the yield lines
$l_{eff,ncp}$	Effective length considering non-circular patterns of the yield lines
m_i	Mass of floor i
m_j	Connection bending utilization factor ($M_{\text{j,Ed}}/M_{\text{j,Rd}}$)
m, m_x	Geometrical distance of connection defined in Figure 6.11 in EN1993 1-8. m_x is the value of m for bolt rows outside the tension flange
m	Utilization factor for beams of the FD-MRFs ($M_{Ed}/M_{pl,b,Rd}$)
n	Minimum between $1.25m$ and $e_{\min}$
n_b	Number of bolts
n_c	Number of bolts in compression
n_{fl}	Normalized axial force in link with respect to the axial capacity of the flanges
$n_{fl,T,max}$	The axial force at $0.08rad$ link rotation, for the link alone assuming fully restrained boundary conditions
n_t	Number of bolts in tension
n_s	Number of friction surfaces
p	Vertical distance between bolt rows
p_d	Total design vertical loads for evaluation of frame imperfections
q	Behavior factor
s_h	Distance from the tip of the haunch/rib plate to the column face
t_{EP}	Thickness of end-plate
t_f	Thickness of T-stub flange
t_{fl}	Thickness of flange
t_{fb}	Thickness of beam flange
t_p	Thickness of the plate
t_w	Thickness of web
t_{wb}	Thickness of beam web
u_{gap}	End-plate gap opening
v	Normalized shear (with respect to $V_{\text{pl,link}}$)
$v_{0.08}$	Shear overstrength of the link in a link-connection assembly, assuming fully restrained boundary conditions, at $0.08rad$ link rotation
$v_{0.08,FR}$	Shear overstrength of the link considered alone, assuming fully restrained boundary conditions, at $0.08rad$ link rotation

v_j	Connection shear utilization factor ($M_{j,Ed}/M_{j,Rd}$)
w	Horizontal distance between the bolts
z	Connection lever arm
z_{eq}	Equivalent lever arm of bolt rows in tension
Δ	Deformation/Displacement
$\Delta_{res,top}$	Residual top drift
α	Coefficient for the evaluation of effective length of the T-stub (EC3 1-8)
α_h	Reduction factor for the height h
α_m	Reduction factor for the number of columns in a row m
$\gamma_{connection}$	Link connection rotation
γ_{link}	Link rotation
γ_{M0}	Partial safety factor
γ_{max}	Maximum link rotation
γ_{ov}	Coefficient accounting for the material yield strength variability
γ_{rez}	Maximum residual link rotation
δ	Horizontal damper displacement
δ_{adm}	Admissible interstorey drift
δ_i	Deformation of component i
δ_r	Design interstorey drift
δ_{Rd}	Ultimate deformation of component
$\delta_{res,storey}$	Maximum residual interstorey drift
ε_0^{pl}	Fracture plastic strain
ε_n^{pl}	Necking plastic strain
ε_{eng}	Engineering strain
ε_{true}	True strain
θ	Chord rotation
θ	Interstorey drift sensitivity coefficient (for P-Δ effects)
$\theta_{connection}$	Connection rotation evaluated based on the damper horizontal displacement
ν	Poisson coefficient
ν	Reduction factor accounting for lower return period of earthquakes associated with DL requirements
μ	Friction coefficient
$\mu_{dyn\ 5\%}$	5% fractile of the dynamic friction coefficient
$\mu_{dyn\ 95\%}$	95% fractile of the dynamic friction coefficient
μ_{avg}	Average value of the dynamic friction coefficient
φ	Rotation
ϕ	Global initial frame deformation
ϕ_0	Basic value for the initial frame deformation
σ_{eng}	Engineering stress
σ_{true}	True stress
$\psi_{2,i}$	Factor for the quasi-permanent value of the variable action

1 INTRODUCTION

The capacity-based design methodology applied for traditional steel structures like moment resisting frames or braced frames has been successful for many years now, yielding solutions capable to withstand severe earthquakes with diminishing casualties and economic losses. Proper design rules implemented at all levels (from global to the material) combined with advances in the design and analysis tools and the construction technologies available, led to structures with safe, predictable response under catastrophic events.

However, the last couple decades have seen severe earthquakes like the ones in Northridge (US, 1994), Kobe (Japan, 1995) or Christchurch (New Zealand, 2011) during which not only old, but also relatively new structures collapsed. Consequently, large research ventures took the direction of addressing the critical aspects related to the traditional systems (the SAC project - for the qualification of steel joints for moment frames in the US) while other research groups focused on proposing innovative solutions for seismic resistant structures. Many of the surfaced solutions, like the base isolation, the buckling restrained braces, viscous dampers and the friction connections (to name some), are being codified and implemented in practice in seismic areas around the world and have shown good performance in recent earthquakes (Bruneau & McRae, 2017).

Emerging innovative seismic devices enhance the seismic safety of buildings, represent sustainable alternatives by lowering the life-cycle costs and thus rendering steel structures more appealing compared with other materials. The new structural typologies also contribute to the number of code-compliant steel solutions, making the material more competitive.

The advantages are numerous for all the solutions which are already gaining popularity and most likely they will continue to be used, especially as they get tested in real-life in active seismic areas like New Zealand, Japan, California or central Italy. Nevertheless, some of the proposed devices are expensive and/or represent special patented devices, needing qualified workers and working by modifying the structural components or introducing significant changes in the design process.

Solutions that modify minimally the conventional structural systems (MRFs, EBFs, CBFs) are better understood and accepted by the environment of construction industry. The ideal solutions would therefore be based on existing structural configurations, would minimally modify the structure and its design and most importantly would render the building easily-repairable in the earthquake aftermath.

From the point of view of structural configuration suitability, there is no universally accepted superior solution – different types of structures adequate differently to different seismic zones. For example, braces naturally buckle at low forces and therefore, braced frames are not ideal for seismic areas with low intensity and frequent events and, moment resisting frames (MRFs) being more adequate owing to their high ductility. On the contrary, seismic areas where high intensity, seldom earthquakes occur, the higher stiffness of centrically braced frames (CBF) is an advantage. Eccentrically braced frames (EBFs) represent an intermediary solution, as function of the link length, different levels of ductility can be attained relative to the same stiffness.

The key aspect of MRFs (and of all steel structures actually) are the connections. The general practice is focused on designing and using either full strength, rigid or nominally pinned connections. In literature it has been proved that most connections are somewhere in between. Although accounting for this in the structural analysis might be more tedious, it is possible to design partial strength connections that have sufficient ductility and lead to lighter structural solutions (D'Aniello *et al.,* 2017). However, significant plastic damage is expected in the connection and therefore the structural repair costs once the structure undergoes severe earthquake events, are high.

In the framework of steel structures, it is easy to obtain easily-repairable structures starting from any of the consecrated systems. The key for sustainable seismic design is low-damage, localized in easily replaceable elements of the structure. In the recent years many reliable solutions have surfaced, devices which render the structure easily repairable or with low damage. However not all solutions are equal and although many provide the desired results, costs, requirements for specialized workmanship, design complexity as well as comparative performance must be accounted for.

The use of innovative structural devices which effectively replace the traditional ones undoubtedly reduce the post-earthquake repair costs. Selecting one solution depends on various constraints like the ability of the designer to implement it (some devices are patented or require complex design techniques), the availability of specialized workers for installation, the physical and design related changes to the structure, the initial and life-cycle costs or the social confidence in the solution

Most of the innovative devices render the structures repairable in the earthquake aftermath. However, viscous and hysteretic dampers, as well as BRBs tend to be expensive, protected by patents, require special design methodologies and qualified workers in most of the cases. The most suitable

solutions are the friction connections for MRFs and CBFs and the replaceable links for EBFs.

As a comprehensive complete study of easily repairable steel structures for different seismicity areas, it was deemed necessary to focus on a braced system (EBF) and MRF. In the framework of these two structures, the most effective innovative solutions were investigated: replaceable links for EBFs and friction connections for MRFs.

Converting traditional EBFs to an easily repairable solution was proved to be feasible by simply introducing a connection that separates the link (the dissipative element) from the beam containing it (Stratan et al. 2004). In this case the re-centrability of the EBF can be enhanced by combining it with MR bays leading thus to a D-EBF (Ioan *et al.*, 2016).

A friction connection is a type of partial strength connection designed in a way that disconnects the strength and stiffness of the moment resisting joint, changing the energy dissipation mechanism that eliminates most of the plastic deformation (being that localized in easily replaceable friction plates). The structure equipped with such connections could have significant inherent re-centrability because the framed members and the non-dissipative connections remain elastic and the residual drifts could be minimized by smartly replacing the friction devices.

The focus of this work is on these two types of connections that transform traditional structural systems with significant plastic damage concentrated in the members into structures that either have low damage (MRFs with friction devices) or into structures that have the damaged elements removable (EBFs with detachable links). Practically, the work will focus on traditional end-plate connections used in a special application and on innovative friction connection applied in typical MRFs.

*

1.1 MOTIVATION

The main motivation for the current work is to contribute to the general effort of the research community towards rendering low-damage, cost effective and easily repairable structural solutions more readily available and closer to being codified.

Although the idea has been around for a while and replaceable links have been studied in the last years (Stratan et al., 2003 and 2004, Dubina et al., 2007 and 2008, Fussell et al., 2014, Ioan et al,. 2016, Ji et al., 2016*b*, Tan & Christopoulos, 2016), it's not clear yet how the seismic links and the adjoining connections are to be designed. The research does not offer a definitive answer concerning the design forces (the shear overstrength, axial force) and there are no specific rules for the seismic design of the connection. In particular, the question needing an answer is whether the methodology available for the design of steel connections under static loads (EN1993 1-8) can be extended for the design of the seismic link's connection and if not, how to adapt it.

In what regards the friction connections, due to their relative novelty much more aspects need to be addressed. To start, the principal parameters that can be assumed to influence the friction response are the friction coefficient of the sliding interfaces and the normal force applied (Marsh & Pall 1981, Butterworth & Clifton, 2000, Latour et al., 2011*b*). While the latter is an issue that is common in steel industry (issues related to applying the correct force and the losses of preload are often studied), the friction properties of surfaces to be selected for the proposed friction device need to be investigated in depth for a representative range of materials and the best solution should be selected. Subsequently, it can be guessed that due to the newly proposed joint geometries, there are effects that need to be investigated (contact area, shear

capacity, cyclic behavior etc.) and the best joint solution is to be selected for ulterior developments. A comprehensive study of the devices developed is needed in order to confirm the validity of the concept, looking at all key factors and the seismic performance of frames equipped with friction devices will complete the assessment of the proposed solution.

The aim of the current work is to give an answer to questions raised for the two solutions and offer therefore a basis for the future codification. A correct connection design in the case of these two systems (the link connection for the D-EBF and the friction connection for MRFs) is key in attaining the goal of structural solutions that are easily repairable in the aftermath of severe seismic events.

*

1.2 OBJECTIVES

The main objective of the research is to perform an in-depth analysis of the two solutions and provide insight into the mechanism of the solutions and recommendations for the design. The set goals are achieved especially by using advanced finite element (FE) software to develop experimentally calibrated models able to accurately depict the steel connection response. Analytical methods for the design of connections and/or frames are discussed where it was the case. The work investigated both the local and global response (connections and structure – in the case of the friction devices).

A summary of the thesis, by chapters is hereinafter presented.

Chapter 1. Introduction

Chapter 2. State of the Art

Chapter 3. Bolted connections for detachable links

3.1 – Introduction and objectives

3.2 – DUAREM Research Project experimental campaign

This chapter briefly describes the DUAREM research project which focused on a full-scale test on a dual eccentrically braced frame equipped with detachable short links. The results of the experimental tests were used to calibrate the numerical models for the numerical study.

3.3 – European design of bolted moment-resisting connections

A general overview of the Component Method basic assumptions and methodology is described, as the main design procedure used in the European constructional steel practice. The chapter discusses the concepts of basic component, series and parallel component assembling, the T-stub, the connection moment-rotation characteristic and the design algorithm as implemented in the Eurocode.

3.4 – FE model assumptions and Validation

All the numerical modelling assumptions, general throughout the numerical analyses performed and presented in this first part of the thesis are summarized. The main aspects related to material modelling, boundary conditions and loading as well as meshing technique are discussed. The link-connection assemblies of the DUAREM mock-up frame were modelled in a manner simulating closely the real testing conditions, and the results were compared against the experimental results (in terms of shear-rotation response and deformed shape and plastic damage).

3.5 – Parametric study for the evaluation of the link connection design forces

This chapter presents the results of a large parametric study on short links (the models considering the link profile alone) in order to assess the actual design forces necessary for the design of the link end connections. Given that

the connection design forces are derived based on the links' capacity, the actual values of the shear overstrength and the axial force must be evaluated.

3.6 –Design and verification of bolted connection for links

The link end connection is special due to its location and type of loading it has to withstand. Therefore, the design methodology implemented in EN1993 1-8 must be tweaked in order to fit this particular case. In order to take into account the potential development of catenary action, two verification methods were presented and the results were discussed by comparing them with the results of the design method.

3.7 – Assessment of the bolted link connections response

Finally, the last chapter presents the result of numerical analyses on link-connection assemblies, looking at the shear overstrength and axial force in the link and the effect the connection mechanical parameters (strength and stiffness) have on them. The chapter introduces proposals for the evaluation of design forces and design recommendations in the case of link-connection assemblies.

Chapter 4. Bolted friction connections for MRFs

4.1 – Basic concepts of friction

As an introduction to the study of friction devices, this chapter presents a brief description of general tribology notions,

4.2 –Definition of friction device properties

Prior to the study of full-scale devices, the investigation of the main sub-component was performed. The experimental and numerical campaigns were aimed at the study of a number of friction materials and the impact of several parameters (normal force, contact area, distribution of the normal force, speed of load application) on the sliding behavior of sub-components.

4.3 – The FREEDAM Device

The answers obtained from the investigations on the sub-components were subsequently used for the beam-to-column joints. This chapter presents the response of full-size beam-to-column assemblies equipped with friction connections. The chapter is divided in two main parts: the first dealing with the experimental tests and the second presenting the results of numerical investigations on the influence of certain parameters on the device response as well as the mechanism of shear force transfer.

4.4 – Full scale test on Frame equipped with the FREEDAM friction device

In this chapter are presented the results of preliminary FE analyses of full-scale structures tested considering traditional partial strength connections, reduced beam section, and friction connections. The analyses are performed using both simplified and advanced numerical approaches in order to assess the capacity of the software to model the structural response.

4.5 – Design and Analysis of Frames equipped with Friction Devices

In order to be used in practice, the structures equipped with friction connections require a ready-to-use design procedure. Two methodologies are proposed and assessed in this chapter by designing two sets of structures and comparing their performance in terms of static and dynamic nonlinear response.

Chapter 5. Conclusions

Each of the two main parts have summaries of the research and they are reiterated in this final chapter, together with the general conclusions concerning easily repairable seismic resistant steel structures

2 STATE OF THE ART

Seismic resistant design

Structural design of buildings can be directed in three ways function of the destination and the architectural demands. The structures that are strategic for the society (nuclear power plants, hospitals, etc.) need to withstand earthquakes with high return periods remaining elastic. These structures fall within the first category of structural control i.e. hyper-resistant structures. The second category is comprised of active control systems which work by modifying the structural response at the occurrence of the seismic events. This kind of devices are effective however, the high cost is justified just in case of special structures (high-rise buildings, bridges etc.). The last category is the passive control systems which work by directing the seismic energy input into specific elements of the structure possessing enough capacity to dissipate it.

Given that the first two categories of seismic structural control are devoted to design of structures that represent a low percentage of the construction market and typically the design is not a strict code-compliant one, most of the efforts in improving and/or developing performant structural systems are focused on the third category.

The seismic base isolation systems studied in works like the ones by Kelly (1979), Aiken et al (1993) Christopoulos & Filiatrault (2000) Roy &

Chakraborty (2015) Cancellara & De Angelis (2017) are a special type of passive control systems that work as a barrier in between the soil and the superstructure, preventing the transfer of the seismic input and therefore limiting the demand on the structure. Although effectively used in practice, it constitutes a costly solution that has limitations.

The research conducted in the 20th century led to some, now consecrated, structural systems considering the largely favorite construction materials (reinforced concrete, masonr and steel). All the classical systems (being them frames or walls) assume that the seismic action is dissipated by plastic deformation of elements designed following the principles of the capacity design.

Capacity-based design

The capacity-based design principle is now at the base of all modern seismic design codes (EN 1998-1, ASCE 7-10, NZS 1170.5, BSLJ). The incorporation of the concept, as shown by Beatie *et al.* (2008) and Fardis (2018), followed several preliminary steps to seismic design regulations.

The first reference to the concept can be tracked back to the book by Blume, Newmark, and Corning, *Design of Multistory Reinforced Concrete Buildings for Earthquake Motions*, published in 1961. Mete Sozen contributed heavily to the work and the concept was included in the 1967 to 1968 revision of the Structural Engineers Association of California (SEAOC) recommendations. With the introduction of the new SEAOC rules in the 1968 New Zealand design code for public buildings, the term "capacity design" was born in the team surrounding Otto Glogau.

In New Zealand the concept was explained by Hollings (1969a and 1969b) for concrete structures (Figure 1) and as it gained attention and it was experimentally and theoretically developed, it was more comprehensively

explained in "*Reinforced Concrete Structures*" the book by Park and Paulay (1975). The principle was continually improved upon with ever extending applications. Works like the book by Paulay and Priestley (1992), containing detailing rules for reinforced concrete and masonry helped facilitate its implementation in practice.

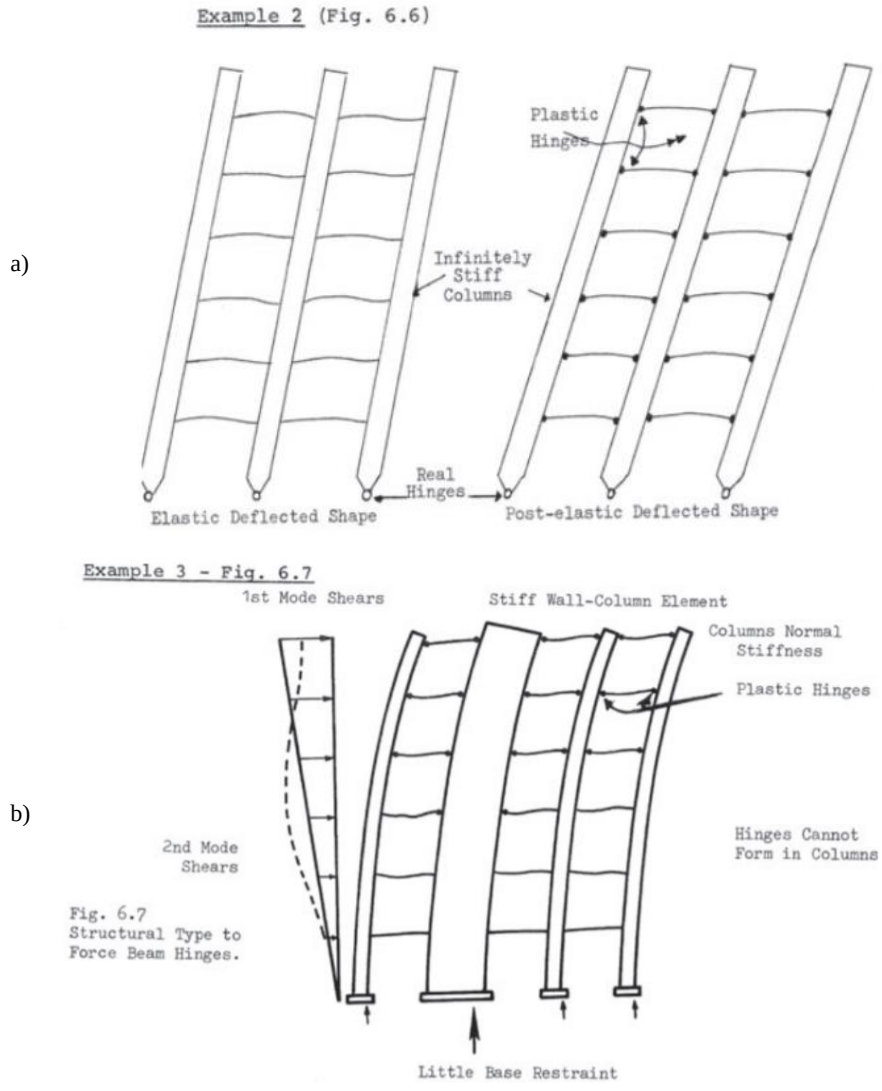

Figure 1 Plastic mechanisms, Hollings 1969a

The principle proposes the design of certain elements (so called dissipative or ductile elements) of the structure for lower design forces,

rendering them purposely weaker (Hollings, 1968). The amount by which the forces are reduced for the design of these elements depends of the reserve of ductility available (structural typology, material). On the other hand, the non-ductile elements must be designed with an overstrength with respect to the dissipative element, in order to allow the formation of the desired global plastic mechanism.

Damage in past earthquakes

The extent of the post-earthquake losses throughout the last century in Japan (Y. Ishiyama, 2011), and looking at recent seismic events like the one in Christchurch, New Zealand (Clifton *et al.*, 2011 and 2012, Kam and Pampanin, 2011) is sufficient proof to argue that there is always space for improvements in the seismic design and construction of structures.

The main causes for the extensive losses in terms of human lives and financial are not the same comparing the events at the beginning and the end of the past century. Moreover, tt stands to no doubt that the newer structures, designed according to modern regulations based on capacity design, have a better performance. During the events at the beginning of the century, the main culprit for the losses was the lack of knowledge with respect to seismic design, the poor constructional materials (timber, bricks) and the fires started by the earthquake and feeding onto the widely used timber structures (Kanto and San Francisco earthquakes). The events of the last decades surfaced problems of structural collapse related to detailing or poor implementation of the guidelines (Tremblay *et al.*, 1995, Youssef *et al.*, 1995, Nakashima *et al.*, 1995, Watanabe *et al.*, 1998). The basis for seismic design as well as the structural typologies are good, however, improvements are required at different levels (design rules, detailing rules, construction rules, etc.). Therefore, some of the collapse causes can be addressed without significantly altering the current design procedures.

Current design methodology

There is no doubt that the current practice is accustomed with the concept of capacity design but also to the specific types of structures that are by now consecrated systems i.e. MRFs, CBFs, EBFs, walls, etc., and when rationally applied the code guidelines lead to relatively economical solutions if only the initial cost is considered. The downside comes with the repair costs in the design-level earthquake aftermath. The ductile dissipative elements are usually structural members which undergo significant plastic damage, as intended, and must be replaced. In many cases this is no easy task, the repair costs being even larger than the complete replacement of the structure.

Traditional structural typologies

The simplest steel structures are composed of members connected in nodes which work together to transfer the vertical and horizontal forces. Several structural typologies can be identified for lateral resisting systems for seismic areas. The steel structural typologies are identified depending on the behavior of their primary resisting structure under seismic actions. In moment-resisting frames (MRF) members act primarily in flexure, concentrically-braced frames (CBF) have diagonal braces that act in tension and eccentrically-braced frame (EBF) transfer the forces by bending and/or shear deformation of links.

Each structural typology has its own structural features and applications, but the seismic design must adhere to two basic criteria: (1) sufficient stiffness to satisfy the serviceability limits and avoid damage to non-structural elements during events of low seismicity and (2) sufficient ductility to prevent collapse in the case of major seismic events.

MRFs and CBFs have been the default solutions for decades but they have widely opposite characteristics in terms of ductility and stiffness. It is not

relevant to compare the MRFs and any of the braced frames typologies, however EBFs represent a compromise solution. Khademi and Rezaie (2017) recently performed a comparison study of CBFs and EBFs bracing in steel structures using nonlinear Timehistory analysis. The EBF shows good seismic behavior in terms of lateral displacements and not surprisingly, almost double the energy absorption capacity compared to the other systems. Although CBFs are often used in areas with moderate seismicity, due to their simplicity in design and erection, Han (2008) made the case for the use of EBFs as a better alternative given its comparable stiffness but increased ductility

The seismic performance of MRFs is hugely influenced by the beam to column joints. As a matter of fact, many steel welded moment-frames exhibited a very poor behavior (brittle fracture of the welds) during the Northridge earthquake (Tremblay et al., 1995, Youssef et al., 1995, Yang and Popov, 1995) and owing to this, an extensive campaign for the pre-qualification of bolted beam to column joints was launched in the US (Sumner & Murray 2000 and 2002, Murray and Sumner 2004). A similar venture was recently concluded in Europe as the Equaljoints RFCS research project (RFSR-CT-2013-00021) (D'Aniello et al. 2017, Tartaglia et al. 2018a and 2018b).

The latter research project was aimed at the investigation of traditional moment-resisting connections typically used in the European constructional practice in seismic areas. The current design practice for steel joints is based on the Component method codified in Part 1-8 of EC3. The principle developed by Zoetemeier (1974) and refined by Jaspart (1991) works very well for static loading conditions (Bursi & Jaspart 1997a and 1997b, Jaspart et al., 2007 and 2008). Several research groups across Europe tested the typical moment-resisting joint configurations under cyclic loading (Dubina *et al*., 2001, Nogueiro *et al.,* 2006 and 2007, Diaz *et al.* 2011) and tried to fully

characterize their response and the one of the T-stub (Piluso *et al.*, 2001*a* and 2001*b*), the major component of the bolted steel connections.

In brief, the Equaljoints project (RFSR-CT-2013-00021) brought together some of the research groups that carried out research in this direction and, focusing on selected joint typologies, aimed at fully describing their seismic behavior, proposing improved design rules and pre-qualification charts for the design practitioners. Part of the project was also the investigation of partial strength and semi-rigid joints.

The partial-strength and semi-rigid behavior of joints and their effect on the frame response can be significant and must not be ignored in practice (Faella C., Piluso V. and Rizzano G. *"Structural steel semirigid connections: theory design and software"*). As it was highlighted in several studies (Elnashai & Elghazouli 1994 and 1998), the majority of steel joints are somewhere in between a fully-rigid and a pinned joint. The modelling of the joint semi-rigidity in practical applications is tedious, but many studies have proved that in many cases it is necessary, and it can be beneficial, from a design stand point (De Matteis *et al.*, 1999 and 2000, Calado *et al.*, 2000a, Della Corte *et al.*, 2000 and 2002).

The seismic design of steel MRFs according to EC8 leads to ineffective solutions due to the very stringent limitations in terms of drift and P-Δ effects. The Eurocodes are a relatively new set of design guidelines and owing to the complexity of the task of writing them and the continuous evolution of the available resources and information, it is obvious that improvements might be needed. As a matter of fact, the entire set of European codes is currently under revision in order to bring improvements and adjust the lacks, all based on the research and the experiences of designers from the last decades. As an alternative to the code Nastri et al. (2015) and Montuori et al. (2016), proposed

a design procedure based on the plastic mechanism theory, which shows potential in avoiding the code-related issues.

The Eurocode 8 revision made by Bosco *et al.*, (2014 and 2015) for the design of EBFs revealed additional issues regarding this structural typology. The problems are related mostly with the use of lateral force method in highly ductile EBF which leads to errors in the evaluation of the overstrength factor in links, the neglection of the structural overstrength in considering the P-Δ effects and the lack of a reliable control over the dissipative behavior of the structure, Furthermore, the authors emphasize that the link overstrength factor is discontinuous at a value of the mechanical length of links, the code neglects the presence of gravity loads does not seem adequate for structures with intermediate or long links. The rules for the application of the capacity design principles to braces, columns, and beam segments outside links are unconservative because of the underestimated bending moment

One of the major lacks regarding EC8 is that it does not cover innovative structural systems, outside of the consecrated typologies, although a larger variety of solutions are studied, and even implemented, and other international codes already codified them.

The argument for traditional structural systems stands, as they represent solutions which have been widely investigated and their response is known and predictable to a large extent. However, it is not difficult to imagine that by bringing small modifications to the structure, the seismic resilience can be improved, and the life-cycle cost mitigated.

Innovative structural solutions for seismic areas

The past couple decades have seen the tide change towards the use of passive structural controls that either localize the plastic damage in easily

replaceable elements or completely replace the dissipation mechanism. Anti-seismic devices have been around for much longer though.

Seismic damping devices are additional elements inserted into the structure with the task of absorbing the induced kinetic energy. The strategy of using such devices, as described by Kelly *et al.* (1972), is aimed at separating the load bearing capacity from the energy dissipation function of the structure. The 3 devices proposed and tested by the Authors were all based on steel plates working under different loading states (flexure, torsion) and performed well, demonstrating thus the effectiveness of steel plastic deformation in dissipating energy. Skinner et al. (1980) studied steel and lead hysteretic dampers for use in bridges and base-isolated structures.

More recently, triangular steel plate damping devices were proposed for steel MRFs (Saeedi et al. 2016). As it was shown by the Authors, the structural performance of MRFs has been significantly improved, in terms of stiffness and seismic performance.

Significant research has been performed in addressing detachable short links for EBFs, many of the results highlighting the combined benefits of high ductility and stiffness of the EBFs with the replaceable link solution (can be compared to a steel fuse) which rendered the structural system an easily repairable one (Stratan *et al.,* 2004, Dubina *et al.,* 2007, 2008, Mansour *et al.,* 2008, Fusell *et al.,* 2014, Ji *et al.,* 2016*b,* and Tan & Christopoulos, 2016),

Yet another dissipating mechanism that takes advantage of both high-strength steel and the plastic deformation capacity of mild steel are the reduced beam sections (RBS) used for MRFs with energy dissipation bays (EDBs) Ke & Chen (2016). Combining ductile bays, designed to undergo plastic damage in the RBS regions and MR bays of high strength steel members, the system has an adequate ductility, with reduced residual drift. However, the system is

not easily repairable as the damage is still distributed throughout the large part of the structure

Buckling restrained braces (BRBs) are devices which work like typical centrically braced frames (in tension) with the addition that the buckling is prevented when the element undergoes compression. This is managed by either additional steel profiles bolted to the brace or by encasing in RC (see Figure 2). Bosco & Marino (2013) studied and proposed a design method for frames equipped with BRBs, investigating also the behavior factor. Jian et al. (2015) used numerical methods to study the influence of design parameters on the performance of BRBs, concluding with recommendations for the core width-to-thickness ratio and the maximum gap. On the European market there are readily available, device-like patented BRBs, for example BRAD® produced by FIP Industriale S.r.l.

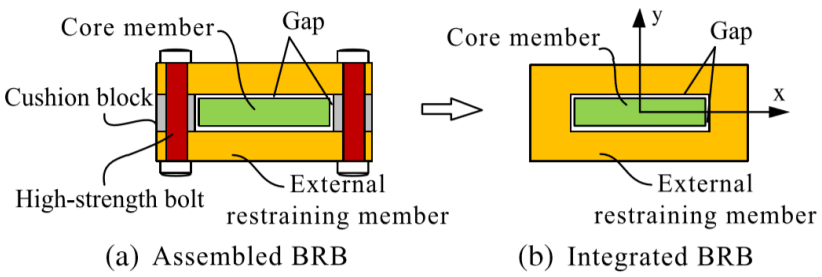

Figure 2 "Schematic diagram of BRB" Jiang et al. (2015)

As it does not rely on the dissipation of traditional connections or members, a type of seismic devices are the partial strength post-tensioned connections (see Figure 3). In a comparison between welded and post-tensioned connections, Reyes Salazar *et al.* (2016) demonstrated that the force reduction factors are larger and the ductility demands is smaller for the latter, concluding that the solution has a better seismic performance.

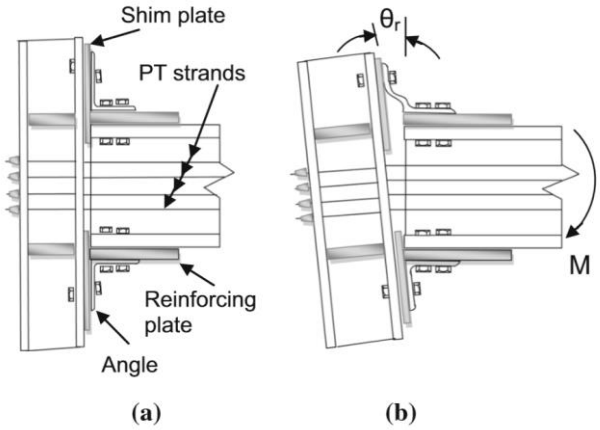

Figure 3 "Post-tensioned semi-rigid connection (PC). a No deformed, b Deformed" Reyes Salazar et al. (2016)

The introduction of the friction-based energy dissipation joint was made by Pall & Marsh (1979), like for most of the dissipative devices not for steel structures, but for concrete structures - for this case - large RC panels. The steel research community eventually caught up, and the solution which basically replaces the typical plastic deformation energy dissipation mechanism with a friction based one is now implemented successfully in practice (Butterworth & Clifton, 2000, Bruneau & McRae, 2017)

At an international level, many studies investigated the viscous dampers and their various applications (Symans *et al.*, 2008). Amongst them Climent (2006) and Guneyisi & Altay (2008) investigated the effectiveness of viscous dampers in RC buildings, while application of the same devices for steel MRF were investigated by Dong (2010), Abdi *et al.* (2015) Tsimas *et al.* (2016). The studies show marked improvements in MRF structural response but highlight also the need of an adjusted capacity design in order to avoid hinging of the columns (Karavasilis, 2016). In order to make the special devices usable in the US design practice, Whittaker *et al.* (2003) developed an equivalent lateral force and modal analysis methodologies for dissipative structures with damping devices.

The applicability of innovative seismic devices extends also to seismic upgrading of structures. Most of the devices previously discussed can be implemented successfully in both RC and steel structures, not only for frames but also for wall systems. De Matteis *et al.* (2005) showed the excellent energy dissipation capacity of low-yield metal shear panels while Formisano *et al*. (2010) gave insight into the behavior of RC structure upgraded with steel and aluminum shear panels. Other retrofitting solutions include hysteretic dampers (Oviedo-Amezquita *et al.*, 2010), friction dampers Guneyisi *et al*., (2014), Taghi Nikoukalam *et al.* (2015), passive energy dissipation systems (Constantinou *et al.*, 1998). Comparative to the use of regular steel braces for structural upgrading (CBFs: Mazzolani *et al.*, 2009, EBFs: Barecchia *et al.*, 2006, D'Aniello *et al.*, 2006) BRBs are much more versatile and integrate better with the demands of the structures to be upgraded (D'Aniello *et al.*, 2008, Guneyisi, 2012, Della Corte *et al.*, 2014).

Several research projects at European level have been focusing on some of the specific devices previously mentioned or similar ones: **INERD** – *Two innovations for Earthquake resistant design* (2001-2004 CEC Agreement No7210-PR-316); **FUSEIS** – *Dissipative devices for seismic resistant steel frames* (2008-2011 RFSR-CT-2008-00032); **DUAREM** – *Full-scale experimental validation of dual eccentrically braced frame with removable links* (FP7 2007-2013 SERIES Agreement No 227887); **STEELRETRO**. *STEEL solutions for seismic RETROfit and upgrade of existing constructions* (2007-2010 RFSR-CT2007-00050); **FREEDAM** – FREE from DAMage connections (2015-2018, RFCS (RFSR-CT-2015-00022) etc. **INNOSEIS** – *Valorization of innovative anti-seismic devices* (RFCS number) was a dissemination project which brought together several research groups that studied 12 devices, in an effort to circulate the acquired knowledge and to advance the new lateral-load resisting systems a step closer to being code-approved.

*

There is no doubt of the wide applications for innovative structural devices which can replace the traditional energy dissipation mechanism that leads to so large structural losses in the earthquake aftermath. However, there are some crucial aspects to be considered in the selection of the seismic device:

- ✓ The ability of the designer to implement it (whether it is a patented device or if it requires complex design techniques)
- ✓ The requirements in terms of specialized workers for installation
- ✓ The physical and design related changes it brings to conventional structural typologies (MRFs, CBFs, EBFs in the case of steel structures)
- ✓ The initial and life-cycle cost (including maintenance)
- ✓ The overall social confidence in the solution

Considering all of the above, it is not difficult to discern that there are few innovative seismic devices that simultaneously meet these requirements at the moment. To simplify matters, the discussion can be sub-divide in categories for the three main types of steel structural systems:

[1] **MRFs** can be designed with viscous dampers, hysteretic dampers, base isolation, shear panels, post-tensioned partial strength connections and friction connections.

[2] **CBFs** can be nowadays designed with BRBs, with dampers on the braces, friction connection between the brace and the beam (inverted V configuration)

[3] **EBFs** detailed with replaceable links or hysteretic dampers.

Most of the innovative devices render the structures repairable in the earthquake aftermath. However, viscous and hysteretic dampers, as well as

BRBs tend to be expensive, protected by patents, require special design methodologies and qualified workers in most of the cases. The most suitable solutions are the friction connections for MRFs and CBFs and the replaceable links for EBFs.

In the beginning of the section it was highlighted how the CBFs have a poor ductility and EBFs on the contrary, preserve the characteristic stiffness while having improved ductility. Also, the braced frames are not convenient in seismic areas with frequent low-intensity earthquake (premature buckling of braces) and rather MRFs are better choices.

Therefore, as a comprehensive complete study of easily repairable steel structures for different seismicity areas, it was deemed necessary to focus on EBF and MRF. In the framework of these two structures, the most effective innovative solution was investigated: replaceable links for EBFs and friction connections for MRFs. Due to the different research advances with regards to the two types of devices, a thorough review of the relative state of the art will hereby be presented separately.

Traditional EBFs and shear links

Ever since it surfaced in the 70s, the eccentrically braced frame (EBF) structural system has proved time and time again its feasibility. Amongst the many advantages, highlighted from the very beginning by its promoters (Roeder & Popov, 1978) are the almost ideal combination of stiffness of a braced frame with the superior energy dissipation capacity of a moment-resisting frame.

The EBFs with its diagonal bracing connected eccentrically to the beam leads to the isolation of a ductile fuse element called link. Function of the link length ratio, it will yield either in shear, moment or a combination of the two. The interaction of bending and shear was observed from the very beginning

as a negative effect, and the predominantly shear-based response short links have been favored. In 1984 Kasai and Popov proposed rules to design eccentrically braced frames under static loading and set limits for the link length in order to limit bending-shear interactions.

The initial studies in the 80s were very comprehensive and highlighted most of the critical points like the effect of web stiffening on preventing the web buckling and therefore enhancing the link ductility (Hjelmstad & Popov, 1983). Kasai and Popov (1986) subsequently brought more light into the influence of the compressive axial force, the interaction between bending moment and shear as well as the strain hardening and limits for short link length. Malley & Popov (1984) and Popov *et al.* (1987) highlighted the necessity for a proper lateral restraining of the link ends, as well as the problems that can occur in the beam containing the link, and even the benefits of combining EBFs and MRFs obtaining thus a dual system.

Practical applications, which did not fail to arise, provided further confirmation of the concept validity, indicating that the EBFs perform well exhibiting a theoretically predictable behavior during earthquakes. However, as brought to attention by Popov *et al.* (1992), the design must be correctly implemented, with attention also to the distribution of the links' strength on the height of the structure (very strong links on the higher levels induce large demands in the lower floors and limit frame ductility).

Applications of the system extended beyond buildings also to structures (McDaniel *et al.*, 2003). Recent studies by Dusicka et al (2010) underlined the fact that the shear overstrength exhibited by shear links is larger than the code recommended value, results confirmed by Ji et al. (2016*a*) in its summary of past tests on shear links (see Figure 4).

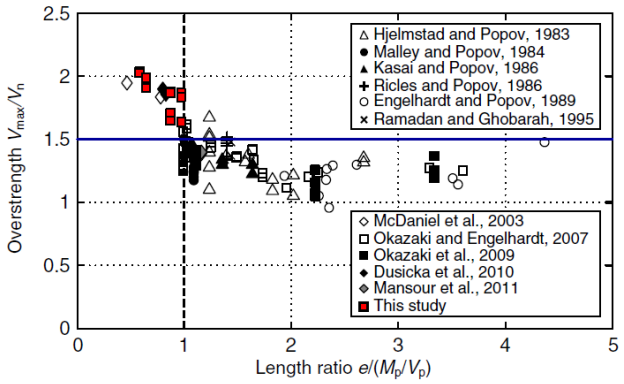

Figure 4. "Overstrength factors of link test data" Ji et al., (2016a)

The impact the RC slab, designed for most buildings, has on the steel frames was emphasized ever since Kasai & Popov (1984). In this regard, Ciutina et al. (2013) and Danku et al (2013) carried out both an experimental and numerical campaign to investigate the influence the slab would have on the dissipative link. The results demonstrated that simply disconnecting the slab from the dissipative zones (links) in D-EBFs does not lead to a response governed solely by the steel element, on the contrary, the overall strength and stiffness are improved while the ductility is preserved.

Further analyses on the effect of transverse web stiffeners were performed by Vataman et al., (2016) using numerical analyses calibrated on experimental tests. In a very comprehensive review of the research on EBFs and links, Azad & Topkaya (2017) considered also the observations made in the past on the web stiffeners and highlighted the unfavorable effect of improper stiffening but emphasizing the issue for intermediate links.

Azad & Topkaya (2017) brought up many of the lacks in the research concerning the topic: the link lateral bracing, lack of proper design rules for link-beam or link-column connections, the effect of tensile forces on the shear overstrength, a reliable way of accounting for the shear overstrength without under or over-estimating it, the progressive collapse capabilities etc. One of the largest and most urgent gaps that the Authors highlight is the need for

conclusive research towards the codification of design guidelines for link-to-beam connections, with the aim of proposing prequalified connections for replaceable links.

Replaceable links for EBFs

The design philosophy of eccentrically braced frames assumes the shear link as part of the same floor beam. In the design process the links are oversized because the beam outside the braces must resist the larger forces developed. Consequently, the whole chain of the capacity design is affected resulting in a more expensive solution. Mansour *et al.,* (2008) highlighted that by detaching the link, more control is gained in the design on the strength, stiffness and ductility, resulting in more cost-effective structures. The Authors investigated various details for replaceable shear links, out of which the bolted extended end-plate configuration displayed high ductility and stable behaviour making it suitable for practical applications.

The concept of EBFs with bolted short horizontal links which can be replaced after an earthquake was initially promoted by Stratan *et al.* (2003 and 2004), although the idea was not completely new (Yang, 1982, Seki et al., 1988, McDaniel et al., 2003). The preliminary investigations on the bolted flush end-plate connection revealed pinching and in order to obtain a stable cyclic response 80% of the link length ratio was proposed. Dinu et al (2010), Dubina et al. (2008 and 2011) further confirmed the solution's applicability highlighted its significant re-centering capabilities.

The DUAREM project was started with the aim of testing a full-scale D-EBF with replaceable short links. The pseudo-dynamic testing campaign, carried out at the Joint Research Center laboratory in Ispra, Italy, had the purpose of proving the re-centering capabilities of the proposed structural typology in the aftermath of design level earthquake events, as well as the

feasibility of the link replacement procedure tested by Ioan *et al*., (2013). In the paper summarizing most of the results, Ioan *et al,*. (2016) concluded that the D-EBFs with detachable links has significant potential as it exhibited optimal seismic performance while being easily repairable after the seismic event.

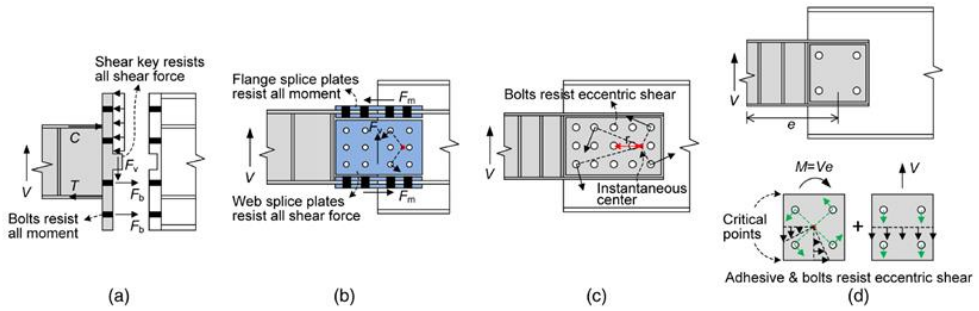

Figure 5 Free-body diagram of link-beam connections (a) CB1; (b) CB2; (c) CB3 (d) CB4 Ji et al., (2016b)

As a confirmation of the proper response of the D-EBF system with replaceable links stands the overview on the performance of structures during the Christchurch 2010 – 2011 series of earthquakes Clifton et al. (2012)

More recently, Ji et al., (2016b) analyzed several types of link-end connections. They observed that specimen CB1 (see Figure 5) representing the extended end plate connection with a shear key revealed a very stable and symmetric hysteretic response even for large values of inelastic rotation, while the other specimens exhibited pinching due to bolt slippage (CB2 and CB3) and premature brittle failure of connection (CB4). The shear key was designed to withstand the shear while the bolts and end-plate were designed for flexure.

An interesting investigation presented by Tan & Christopoulos (2016), focused on the response of four steel cast replaceable links and the global performance of EBF structures equipped with the best concept. Results show that the proposed links reach larger rotations and have better low-cycle fatigue life by distributing the flexural yielding uniformly and minimizing stress

concentrations. This result renders them a potential substitute for classical link profiles.

Past investigation on the axial force level and shear overstrength in the shear links (Della Corte *et al.*, 2007 and 2013) and the influence of the flange width/thickness ratio (Richards & Uang, 2005) are relevant also for the replaceable links. In fact, the presence of the end-connection makes the issue of establishing correct shear overstrength values and axial forces in the link even more pressing.

The link end-plate connections must remain elastic under the design level earthquake in order to facilitate the link replacement process. This is no easy task as the design forces derived based on the hierarchy of elements are very high. Connections for links which are very short can be more easily designed, as the bending is reduced, but the aspect that should not be forgotten is that the shear overstrength increases.

Limited research is available on the behavior of link end connections, as highlighted by Azad & Topkaya (2016). Zarsav *et al.*, (2016) carried out an investigation on the effect of stiffeners on the hysteretic behavior of the link-to-column connection, highlighting the benefits of trapezoidal stiffeners on the ductility and the beneficial effect of positioning the stiffeners close to the beam end.

Due to the lack of specific background research on the links' connections the aim is to analyze how bolted connections behave under loading conditions like what is expected in the link-beam splice. Flush end-plate (FEP) connections have gathered a solid reputation throughout the years, with applications mostly in non-seismic areas owing to their limited stiffness and strength (Aceti *et al.*, 2004, Aribert *et al.*, 2004, Atael *et al.*, 2014, Mohamadi-shooreh & Mofid (2013). The cyclic performance of such connections, when

compared to its monotonic level, was not very far of, showed Broderick et al., (2002). Although the connection exhibited significant rotational capacity, the severe pinching, low stiffness and strength makes it not the ideal solution for beam-to-column joints in seismic areas. The methodology for the assessment of the performance of FEP under seismic loading, results interesting when applied to FEP designed for gravity loading in the past and the structure is in an area that has an increased seismicity nowadays Cassiano *et al.,* (2018).

Owing t the expected high levels of axial force developing in the link, the analysis of FEP under column loss scenario is useful for the assessment of the connection (Guo *et al*., 2015, Cassiano *et al.,* 2017, Oosterhof & Driver, 2015 and Stylianidis *et al.*, 2015a, 2015b and 2016). Another loading situation which induces large catenary actions is the fire, and therefore the behavior of FEP at elevated temperatures is an important aspect (Yu *et al.*, 2011, Haremza et al., 2016)

Although the solution concerns shear links, the bending moment, although limited is present. And even if present in a limited extent, its effect combined with axial force can cause unwanted phenomena due to M-N interaction Chenaglou *et al.,* (2015*a* and 2015*b*). This effect was studied exhaustively for both FEP and extended end-plate (EEP) connections by Da Silva & Coelho (2001), Jaspart and Cerfontaine (2002), Da Silva *et al.,* (2004), Urbonas *et al.*, (2006), Nunes *et al.,* (2007), Del Savio *et al.,* (2009), Goudarzi *et al.* (2012), Shaker *et al.,* (2014).

As highlighted by Azad & Topkaya (2017), there is an urgent need for conclusive research towards the codification of design guidelines for link-to-beam connections, with the aim of proposing prequalified connections for replaceable links.

The work carried out and presented in the first part of this thesis (**Chapter 3. Bolted connections for detachable links**) is aimed at filling the gaps related to the actual forces in the link and the link-connection behavior, which will render this structural solution easily repairable and safe for application in practice.

Friction connections for MRFs

The idea of low or free from damage structures has become very appealing in the last decades (Marsh & Pall, 1981, Butterworth & Clifton, 2000, Soong & Spencer, 2002, Muala & Belev 2002, Christopoulos & Filiatrault 2006, Sato *et al.*, 2009). The use of friction connections is a viable and promising strategy to achieve this objective for steel structures and it has been studied and implemented in practice in New Zealand (Ono *et al.*, 1996, Clifton *et al.*, 2007, Khoo *et al.*, 2012a, 2012b, 2013 and 2014, Yeung *et al.*, 2013, Guneyisi *et al.*, 2014, Borzouie *et al.*, 2015*a* and 2015*b*).

In the framework of Eurocodes, this type of connections can be classified as partial strength according to EN1993:1-8 because their design resistance should be lower than the strength of the connected members to prevent any damage into the primary structural members. EN1998-1 allows the use of partial strength connections provided that their rotational capacity is properly demonstrated.

In the case of conventional partial strength joints the ductility can be designed by imposing local hierarchy rules among the components constituting the joints (Faella *et al.*, 1998 and 2000, Mazzolani 2000, Iannone *et al.*, 2011, Latour *et al.*, 2011a and 2012, D'Aniello *et al.*, 2017). Typical bolted joint configurations have been experimentally tested and verified by means of pre-qualification tests both in US and more recently in Europe (Murray 1990, Sumner and Murray 2000, 2002 Murray and Sumner 2004, Guo

et al. 2006, Shi *et al.* 2007a and 2007b, Abidelah *et al.* 2012, D'Aniello *et al.*, 2018, Tartaglia *et al.*, 2018a and 2018b). However, the classical partial strength connections are characterized by severe plastic damage concentrated in the connection which needs to be replaced, process which might be cost-wise inefficient.

Partial strength moment resisting friction connections are conceived to develop the dissipation mechanism by means of the relative slip into ad-hoc devices located between the lower beam flange and the outer cap plate connected to the column flange, while the upper flange of the beam is connected to a plate either bolted or welded to the column (Butterworth & Clifton 2000, Clifton et al., 2007). The cover plate connecting the upper beam flange may be subjected to some moderate plastic bending deformations to accommodate the joint rotation following the sliding of the device, thus enforcing the formation of an ideal center of rotation that prevents the damage of the slab.

The friction device is composed of a stack of steel plates that are clamped together by means of tightened high strength bolts, which are inserted in the slotted holes of the plates to allow the relative sliding (Figure 6). To increase the moment capacity, friction devices can be also adopted for the beam web (Khoo et al., 2013). In addition, the resistance of the joint can be modulated keeping the same assembly but varying the friction resistance that changes with the clamping force used for the bolts (Butterworth & Clifton, 2000). Except for the friction coefficient and the bolt preload, another way of controlling the friction connection flexural capacity is by adding a haunch (Latour at al., 2018b)

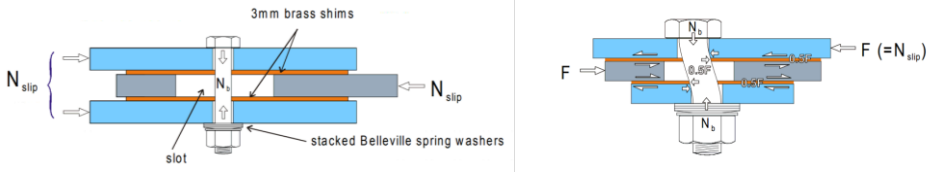

a) Symmetric sliding hinge joint b) Asymmetric sliding hinge joint

Figure 6 "Basic sliding hinge connection" (Butterworth & Clifton, 2000)

Butterworth & Clifton (2000) highlighted the economical and behavioral advantages which can be obtained by implementing friction devices in K or X-braced frames. The idea for such applications initially presented in the works like the ones of Pall & Marsh 1982 and Popov *et al.,* 1995 for different interfaces (brake lining and steel/brass, respectively) proved to be promising and a similar assembly was subsequently tested by Clifton *et al.* (1998).

The nonlinear response of these connections depends on the type of friction mechanism, which can be either asymmetric or symmetric. The asymmetric friction connection (AFC) has been thoroughly investigated (Butterworth *et al.*, 2000, Yeung *et al.*, 2013, Khoo *et al.*, 2014, Borzouie *et al.*, 2015*a*) and even successfully implemented in recent practice (Bruneau *et al.*, 2017). In this configuration the force is transferred by an external plate and resisted by the internal plate (Butterworth *et al.*, 2000). Figure 6*b* depicts a classical AFC example given by Butterworth *et al.* (2000). However, the bolts that clamp the friction pad of AFCs can experience yielding due to large bending moment, shear and axial force interaction, which can induce clamping loss of the bolts and consequently pinching and loss of strength of the connections.

On the contrary, these phenomena can be mitigated with the use of a symmetric friction connection (SFC) (Latour *et al.*, 2011*b*, 2013, 2014*a*, 2014*b*, 2015 and 2018). For this configuration the inner plate represents the mobile part detailed with slotted holes and the outer parts are both fixed to the column. The geometrical particularities make the response more stable. The

resulting hysteretic loops are ideally rectangular; however, this is relative to the material used for the siding interfaces.

Experimental investigations performed in the past for both asymmetric and symmetric friction sub-assemblies (Khoo *et al.*, 2012 and Latour *et al.*, 2014b, respectively) highlight the importance of the relative material hardness of the surfaces in contact.

Latour *et al.* (2018*b*) recently carried out an experimental study on SFCs with the friction damper applied by means of an additional haunch welded to the lower flange of the beam. The friction pad was located at the interface between the haunch and L-stubs that are connected to the column flange. It was composed by a steel plate coated with a thin layer of sprayed of aluminum to improve the friction resistance with low cost of the raw material, as also shown by Ferrante-Cavallaro *et al.* (2017).

The tests showed that this solution is very effective, because the allowable flexural strength of the connection at column face is greater than the plastic resistance of the connected beam. Hence, full-strength connections can be also obtained without requiring any damage to the beam. In addition, the use of a haunch increases the stiffness of the connection, since its internal lever arm is larger than the beam cross section depth, thus obtaining rigid connections prior the sliding of the device. These features are very important from design point of view because the structural models adopted for the seismic analysis do not need to account for the deformability of the joints.

The geometry of these connections is similar with a split tee connection with the particularity of the friction pads needed in order to ensure specific friction properties. The resistance of the connection is dictated by the friction damper but, once the design resistance is established, the design of such connection can be carried out entirely according to EC3 Part 1-8. In addition,

the constructional costs for such connection are marginally different compared to traditional steel bolted connections.

The economic advantages of the MRFs equipped with friction connections include also the limited extent of the damage that is localized at the level of the joint components, this further simplifying the rehabilitation work in the earthquake aftermath. Although the friction connections themselves do not particularly enhance re-centering, the fact that the beams and columns of the MRF remains elastic, they can re-establish verticality when the bolts of the friction connections are untightened (Khoo *et al.* 2012, Piluso *et al.,* 2014).

However, after severe seismic events the friction pad and bolts require substitution, and the surface of the haunch should be treated to restore its initial roughness. These types of interventions can arise some operational difficulties especially concerning the tightening of the bolts that clamp the friction device. Indeed, as shown by Latour *et al.,* 2018*b* and Ferrante Cavallaro *et al.,* 2017 it is crucial to control and guarantee the level of bolt pre-loading to ensure the design value of friction resistance. An excessively large clamping force may lead to the failure of the hierarchy of resistance among the connection and the adjacent members. On the contrary, lower preloading may either anticipate the sliding of the connections under serviceability non-seismic loading or weaken the global structural capacity under the design earthquake that may induce disproportionate rotation demand of the connections.

A viable solution to solve these issues can be the use of removable friction dampers that can be easily detached from both the lower beam flange and the column face by means of bolted connections, thus simplifying the reparability of the friction device. By conceiveing the whole friction damper as a demountable kit containing both the friction pad and the relevant steel supports, this option allows tightening the bolts in the shop with the reliable control of the applied torque. In addition, the friction kit can be entirely

substituted in the aftermath of severe earthquake without the need to perform superficial treatments of the beam flange on site.

These considerations motivated the research activity presented in the second part of this work (**Chapter 4. Bolted friction connections**), which is devoted at completely developing easily repairable friction connections for MRFs.

3 BOLTED CONNECTIONS FOR DETACHABLE LINKS

Introduction

Detachable short links require special attention in design due to the key role they pay in the response of the eccentrically braced frames (EBFs) and even much more so the end connections (Azad & Topkaya, 2017). EC8 specifies design rules for the design of EBFs, but with no mention for replaceable links. Furthermore, the code has been shown to have gaps while it ignores certain aspects. In particular, the code gives a unique value for the shear overstrength of short links, which can lead to either over-conservative or un-conservative results. In addition, there is no mention of the presence of axial force which has been shown to develop in short links under large deformation demands.

On the other hand, the design of end-plate connections is covered by the EN1993 1-8, but these rules are tailored for design under static loads only. It is assumed however that the connection of the link will undergo severe cyclic actions, at the occurrence of the design seismic events. The connections must be designed to remain elastic to facilitate the link replacement and therefore, an evaluation of the code design rules for the specific case of link end connections is necessary

Objectives

Within this Chapter the work carried out and presented was aimed at resolving some of the issues highlighted above and for the attainment of this goal, the following objectives were set:

1. Discuss possible design approaches and their validity (Component Method, way of accounting for the shear overstrength, disregarding the axial force)
2. Check the validity of the shear overstrength coefficient proposed in EN1998-1 and the level of axial force developed in short links under varying boundary conditions
3. Propose more accurate evaluation of design forces for the capacity design, based on the shear overstrength obtained numerically and considering the axial force
4. Asses the performance of the link-connection assemblies designed in accordance with the methods and using the design forces obtained as proposed
5. Propose empirical curves/equations for the evaluation of the design axial force and shear overstrength function of the link/connection utilization factor (m_j) and other mechanical characteristics of the assemblies.
6. Propose design guidelines for both the detachable link and its connection

3.1 DUAREM RESEARCH PROJECT EXPERIMENTAL CAMPAIGN

1.1.1 Scope and Objectives

The research project was aimed at investigating and validating the re-centering capabilities of a dual-eccentrically braced frame (D-EBF) with replaceable links. The dual solution combines the stiffness and energy dissipation capacity of eccentrically braced frames (which will engage at the occurrence of design seismic events) with the flexibility of moment resisting frames (which will provide the necessary elastic re-centering force once the damaged links are removed) in order to obtain a performant structural system that mitigates the life-cycle cost of the building.

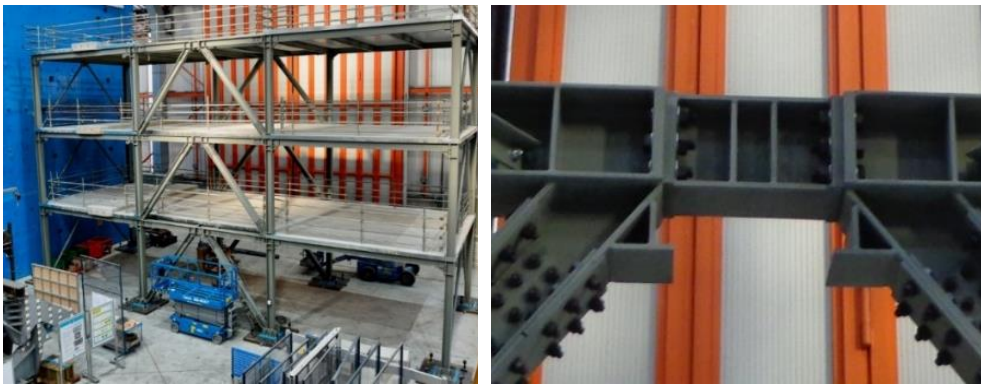

a) Full-scale test building b) Link and end connections

Figure 7 The tested structure (Ioan et al. 2016)

The research objectives set prior to the experimental campaign were, as presented by Ioan *et al.* (2016) to validate the re-centering capability of dual structures with removable links, to investigate the interaction between the concrete slab and steel link and to assess the seismic performance of D-EBFs with removable links, including the replacement of damaged links.

To attain the desired goals, full-scale tests on a D-EBF structure have been performed at the JRC (Joint Research Center) Laboratory in Ispra, Italy. All

relevant information and results were presented in detail in the final report of the project (DUAREM Final Report, 2016) and journal articles (Ioan *et al.* 2016), hence only a summary will be presented hereinafter.

3.1.1 Tested structure

The tested structure consisted in two perimetral frames (see Figure 7), extracted from a larger structure, reducing thus the total cost and simplifying the test procedure. The fundamental difference between the two frames (identified as the North and South frame) is represented by the link-slab interaction. In particular, the North frame was detailed with the reinforced concrete slab cast over the beam and link (the beam being connected to the slab with shear studs), while the South frame had the link and beam separated from the slab.

The structural design followed the Eurocode recommendations considering the basic design assumptions presented in Table 1. The masses assigned to the test specimen correspond to the entire prototype structure, as computed from the load combination:

Table 1 Structural design assumptions

Dead load G_k	**Live load Q_k**	**Soil type**	**PGA**	**Ductility class**	**Behaviour factor q**	**Return period**		**δ_{adm}**
						ULS (SD)	**SLS (DL)**	
[kN/m^2]	*[kN/m^2]*	*[-]*	*[g]*	*[-]*	*[-]*	*[years]*	*[years]*	*[-]*
4.9	3	C	0.19	M	4	475	95	*0.0075* h_{storey}

$$\sum G_{k,i} + \sum \psi_{2,i} \cdot Q_{k,i} \tag{3.1}$$

Where $G_{k,i}$ represents the permanent load, $Q_{k,i}$ represents the variable load, and $\psi_{2,i}$ is the factor for the quasi-permanent value of the variable action (considered to be 0.3).

The dual characteristic of the structure was obtained by allowing the MRFs to resist at least 25% of the total seismic force, as recommended by

seismic design codes (FEMA 450, P100). The plastic engagement of MRFs prior to the achievement of the ultimate deformation capacity in the EBFs was restricted by checking that the ultimate displacement of the EBFs was smaller than the yield displacement of the MRFs (Ioan *et al.* 2016).

The EBFs were detailed with short links, characterized by a predominantly shear energy dissipation mechanism. The links were stiffened considering high ductility demands and the added flexibility of the detachable links was accounted for in the global analysis (Stratan *et al.* 2004). The link-beam flush end-plate connections were designed to remain elastic under ULS conditions to facilitate the link replacement. The link and other frame elements sections and materials are detailed in Table 2.

Table 2 Structural members details

Member	Material	Profile type	Dimensions
Beams MRFs	S355	Hot rolled	IPE240
Beams EBFs	S355	Hot rolled	HE 240A
Columns	S460	Welded	230x240x12x8
Braces	S355	Hot rolled	HE 200B
Links (1st and 2nd floor)	DOMEX 240 YP B	Welded	230x170x12x8
Links (3rd floor)	(S235 equivalent)	Welded	230x120x12x4

The feasibility of the replacement procedure was verified using numerical methods prior to the tests and solutions regarding the order in which the bolted links would be replaced were proposed (Ioan *et al.* 2013).

3.1.2 Experimental campaign

Pseudo-dynamic tests were performed to evaluate the structural performance of the structure. The ground motions used throughout the experimental campaign were selected using preliminary numerical simulations on planar models, starting from a set of 7 records selected from the RESORCE database (Akkar *et al.* 2014) scaled to match the elastic response spectrum for soil Type C and a peak ground acceleration of 0.19*g*.

Four seismic intensity levels were considered: Damage Limitation limit state (DL) corresponding to 95 years return period, Significant Damage limit state (SD) corresponding to 475 years return period and Near Collapse limit state (NC) –2475 years return period. The fourth limit state, Fully Operation (FO), corresponds to a very weak earthquake that would leave the structure elastic.

The first two seismic intensity levels correspond to limit states used in the design (Dl corresponds to SLS and SD to ULS), therefore they are highly relevant to assess the performance of the building globally and locally, as well as the link replacement process and the re-centering capabilities. The NC test was considered for the verification of the structural safety under a very destructive seismic event.

Three sets of pseudo-dynamic tests were performed, starting with the less damaging to the most damaging limit state. For each of the three limit states (DL, SD and NC) a FO (a_g = 0.02 g) test was performed in order to calibrate the numerical model and assess the elastic response of the structure. After each set of tests, the links were replaced:

Damage Limitation (DL) tests:

- Full-operation (FO1) earthquake
- DL earthquake (a_g = 0.191 g)

Significant Damage (SD) tests:

- Full-operation (FO2) earthquake
- SD earthquake (ag = 0.324 g)
- Pushover (PO1) test (displacement of 55 mm)

Near Collapse (NC) tests:

- Full-operation (FO3) earthquake (a_g = 0.02 g)
- NC earthquake (a_g = 0.557 g)

The structural behavior of the two frames was monitored by means of local transducers (which monitored the link and the slip in the relevant connections), global displacement transducers (for the monitoring of global structural displacements), inclinometers (to monitor the beam to column and column base-joints rotations) and strain gages (tor the yield at the middle of the braces and at the end of the MRF beams).

3.1.3 Results

A brief summary of the tests are hereby described. The main results in terms of maximum link rotations and residual drifts of the tests are depicted in Table 3.

3.1.3.1 The damage limitation (DL) test

During this test, no yielding was observed in the elements outside the links (which had only limited plastic deformations as showed in Figure 9a), all the other elements remaining elastic while the beam to column and column base joint zones exhibited small rotations (see Table 3).

3.1.3.2 The significant damage (SD) test

No plastic deformations were observed in the structural elements during this test, except for the links which suffered moderate damage (see Figure 9b). The beam to column and column base joints exhibited, as expected, slightly larger rotations and moderate cracks were observed in the concrete slab (see Figure 9b). The links developed stable cyclic loops during the SD test (Figure 8), reaching the maximum and residual deformation demands in Table 3.

Given that after the SD test the residual displacements were still small, a monotonic pushover test (PO1) was proposed and performed in order to get larger values, required for the validation of the link replacement procedure. All the structural elements remained elastic throughout the test, except for the

links and the concrete slab which underwent higher damage levels (see Figure 9c). All the deformation values are presented in Table 3.

3.1.3.3 The near collapse (NC) test

This pseudo-dynamic test had to be stopped prematurely because of the insufficient actuator capacity. Another cyclic pushover test (PO2) was performed with a maximum displacement amplitude of 150 mm, followed by a final cyclic pushover test (PO3) with a maximum displacement amplitude of 400 mm (Ioan *et al.* 2016).

The last three tests produced extensive plastic deformation throughout the entire structure. Very large plastic deformations occurred in the links, with the complete failure of the links-to-end-plates welds and the ones between the link webs and flanges, the column bases zones and at the MRF beams ends. The concrete slab was heavily compromised in the north frame (see Figure 9d).

Table 3 Summary of experimentally obtained values

Test	γ_{max}	γ_{res}	$\delta_{res,storey}$	$\Delta_{res,top}$	θ
	Maximum link rotation	*Maximum residual link rotation*	*Maximum residual interstorey drift*	*Residual top drift*	*Beam-column and column base rotation*
	[rad]	*[rad]*	*[%]*	*[%]*	*[mrad]*
DL	0.032	0.014	0.10	0.05	9
SD	0.061	0.022	0.14	0.12	13
SD (PO1)	0.075	0.066	0.50	0.43	20
NC (PO3)	0.38	-	-	-	90

3.1.3.4 Validation of re-centering capacity

The links were replaced twice, first after the damage DL test and the second time, after the PO1 test. The limited residual top displacement after the DL test and low residual drift allowed for the damaged links to be replaced by simply removing the bolts. With the link removal, the residual drifts were significantly reduced, and additional re-centering was observed during the replacement of the links, leading to residual drifts smaller than the limit H/300.

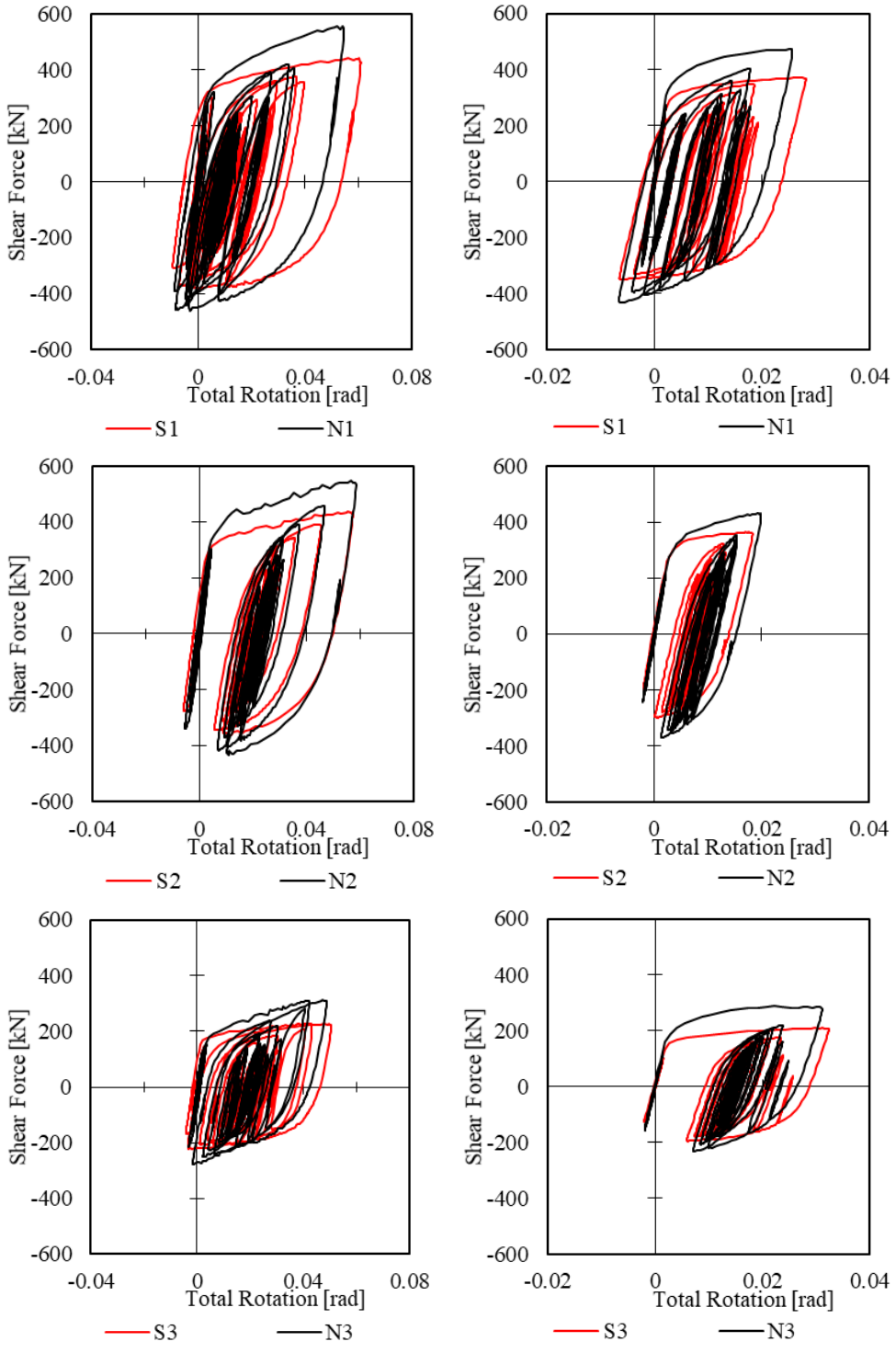

a) ULS test b) SLS tests

Figure 8 Shear force – link rotation for ULS and SLS tests (Ioan et al. 2016).

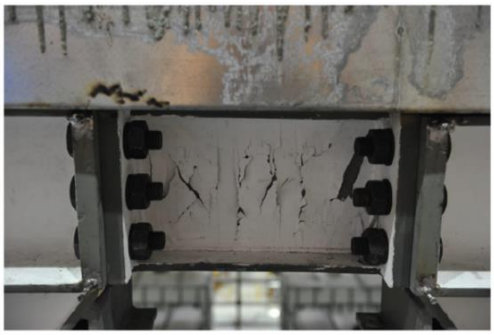


a) Link plastic deformation and slab crack distribution after DL test

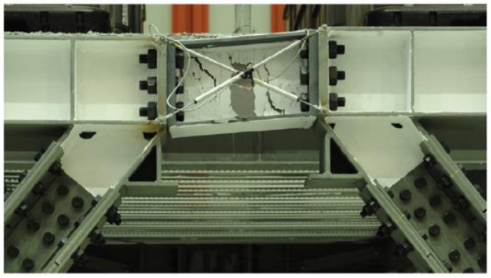


b) Link plastic deformation and slab crack distribution after SD test

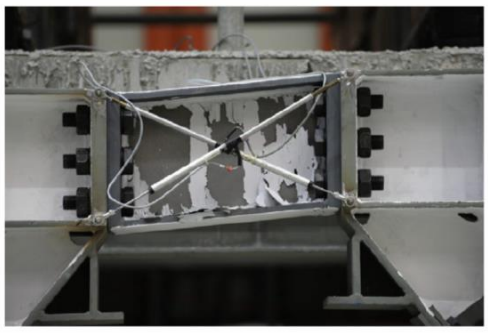
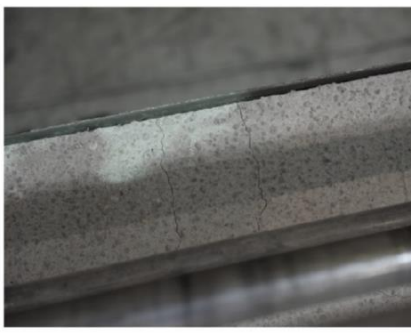

c) Link plastic deformation and slab crack distribution after SD(PO1) test


d) Link and slab after NC(PO3) test

Figure 9 Link and slab deformations after each test set (Ioan et al. 2016)

Larger drifts were obtained after the SD(PO1) test (see Table 3); therefore the links were flame-cut in order to be removed. Again, better re-centering was observed in the south frame. Although it was not necessary to use a hydraulic jack to remove the links, it was needed to place the new set of links in the structure. An additional small re-centering was also observed after the replacement of the links. In Figure 10, it can be observed that at the end of the second replacement procedure only very small residual drifts were measured, H/5250 for the south and H/1750 for the north frame - lower than erection tolerances H/300. Based on this it was concluded that the structure has re-centering capabilities.

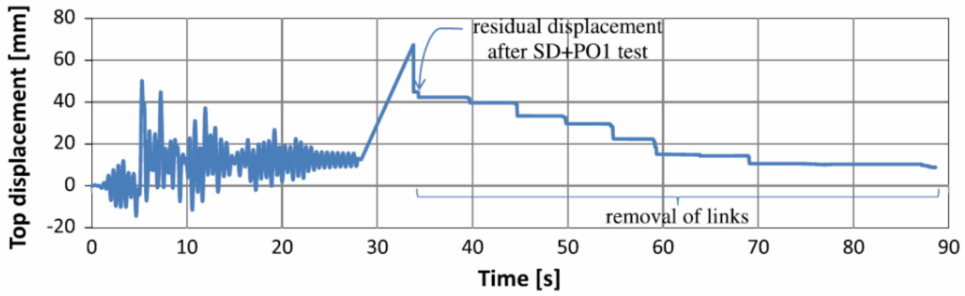

Figure 10 Top displacement time history for south frame during second link removal process (Ioan et al. 2016)

3.1.3.5 Influence of concrete slab

The test results showed that the concrete slab increases the link's shear capacity however, considering that with larger link deformations the damage in the concrete slab increases, this goes against the idea of localizing the damage in the replaceable link only.

Another downside in having the slab over the links, like in the case of the north frame, is the higher stiffness and larger capacity which makes re-centering more difficult compared to the south frame (Figure 8). The presence of the slab (in the North frame) leads to a 7%, increase of yield force, a 5%

initial stiffness increase and the most important, a significant increase of the post-yield stiffness with 24%.

Nevertheless, for the SD seismic input level and the subsequent PO1 test (corresponding to design level events), only minor to moderate cracking of the concrete slab was observed. Keeping in mind that the cracks in the slab can be repaired locally, and assuming that the reinforcement and corrugated steel sheet retain their integrity, the solution is still feasible given that the residual drift after the link replacement was lower than the erection tolerances.

3.1.4 Summary

The DUAREM research project confirmed that the Dual frames with removable links represent a structure with re-centring capability and can greatly reduce the costs and manpower required for post-earthquake repair.

The tests showed that the structure exhibited excellent performance when subjected to DL and SD earthquakes. Small permanent deformations were recorded for both seismic intensity levels, and after the link replacement the residual deformations were almost completely removed (within the erection tolerance limits defined in EN 1090). This means that the structure is self-centering to a certain degree, and that it can be easily repaired in the earthquake aftermath.

Very good re-centering of the frame for which the links are not connected to the slab was observed after the DL earthquake. Provided the permanent plastic deformation after an earthquake is small, the shear links can be removed simply by unbolting. If a larger permanent drift occurs, flame cutting of links is recommended. The damage in the slab zone above the link of the north frame was limited for both DL and SD tests and it could potentially be repaired, rendering also this solution feasible for practice.

3.2 EUROPEAN DESIGN OF BOLTED MOMENT-RESISTING CONNECTIONS

3.2.1 Basic principles of the Component Method

The current European practice used for the design of joints in steel constructions is based on the Component Method. Although Part 1-8 of the steel Eurocode provides a limited number of components, it is possible to design any joint typologies following the basic principles of the above-named method.

The Component method calculation procedure starts with the identification of the joint basic components and the description of their behavior. On a theoretical level, the components are considered as linear springs whose behavior is completely defined by a Force – Deformation curve ($F - \Delta$). The following step requires the assemblage of the components. Finally, the characterization is complete once the joint capacity in terms of resistance, stiffness and deformation is defined. A brief description of the Component Method will be discussed in the first part of this chapter.

Flush and extended end-plate connections, like the ones used for the replaceable links, are designed for shear and bending, neglecting the influence of the axial force. It was observed however that for large link rotations, large tensile force can occur due to catenary effect. A revision of the design methodology is therefore due.

3.2.1.1 Basis of Component Method

Steel connections are subjected to various loading conditions, i.e. axial force (N), shear (V), bending moment (M) or their combinations. The Component Method used in design of joints involves an iterative procedure

that requires an initial joint geometry that will be adjusted such that the safety criteria will be satisfied.

The evaluation of the joint characteristics (strength, stiffness and deformation capacity) begins with the identification of the load transfer mechanisms. Flush end-plate connections are most often designed to transfer uniaxial bending and shear forces. In general, the design for the two is conducted independently. The bending moment is transferred like a couple of forces that act in the center of tension zone and compression zone, respectively. The shear is transferred by the bolts' shank.

Some of the main components of an end-plate connection identified according to EC3 1-8 are presented in Table 4. Each component is characterized by a nonlinear $F - \Delta$ response which can be analytically or experimentally obtained. All the components are afterwards assembled together (in series or in parallel) in order to obtain one equivalent component that will give the Moment – Rotation ($M - \varphi$) characteristic of the joint.

3.2.1.2 Characteristics of the component

The basic components are modelled by means of linear springs with an elastic-plastic behavior (Figure 11*a*). Basically, the complex response of such spring can be described by a bilinear elastic-perfectly-plastic relationship like in Figure 11*b*. The two characteristics allow for the spring to be modelled as a function of the axial stiffness K and the plastic resistance F_{Rd}, respectively.

According to the model adopted in EN 1993 1 – 8, the hardening and the effects due to geometrical nonlinearities are neglected. With regards to the ductility of the component (length of the plastic range), the code provides only quantitative measures, with only basic principles for most of the components. For example, the beam web in tension is considered ductile, while the bolts in tension are considered fragile elements so no plastic deformation is assumed.

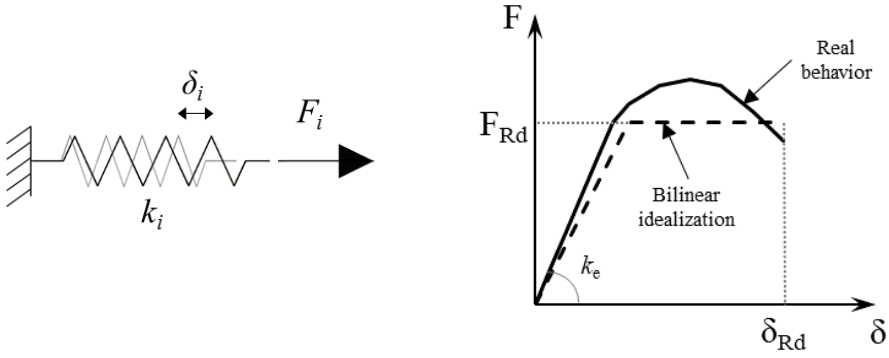

a) Model of an axially loaded component *b) The equivalent spring response*

Figure 11 Component idealization and tensile response curve

3.2.1.3 Assembling the components

First step in finding the components of a joint is the identification of the group of elements connected in series/parallel. The stiffness, resistance and plastic deformation capacity are considered separately and obtained by assembling the characteristics of all components (Figure 13 and Figure 14).

The flexural resistance is evaluated considering a plastic distribution of the tension forces (allowed by EN 1993 1-8) corresponding to the bolt rows in tension and is obtained by summing the products between these forces and their respective lever arm calculated from the center of compression (for simplicity it's assumed in the center of the bottom flange for unstiffened end plate connections).

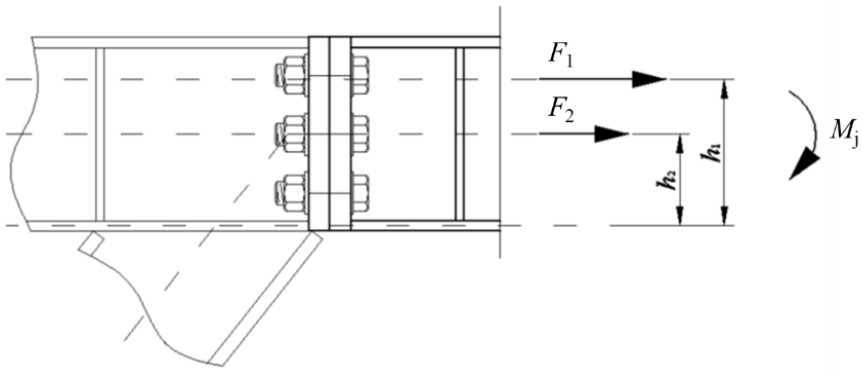

Figure 12 Computation of the bending resistance

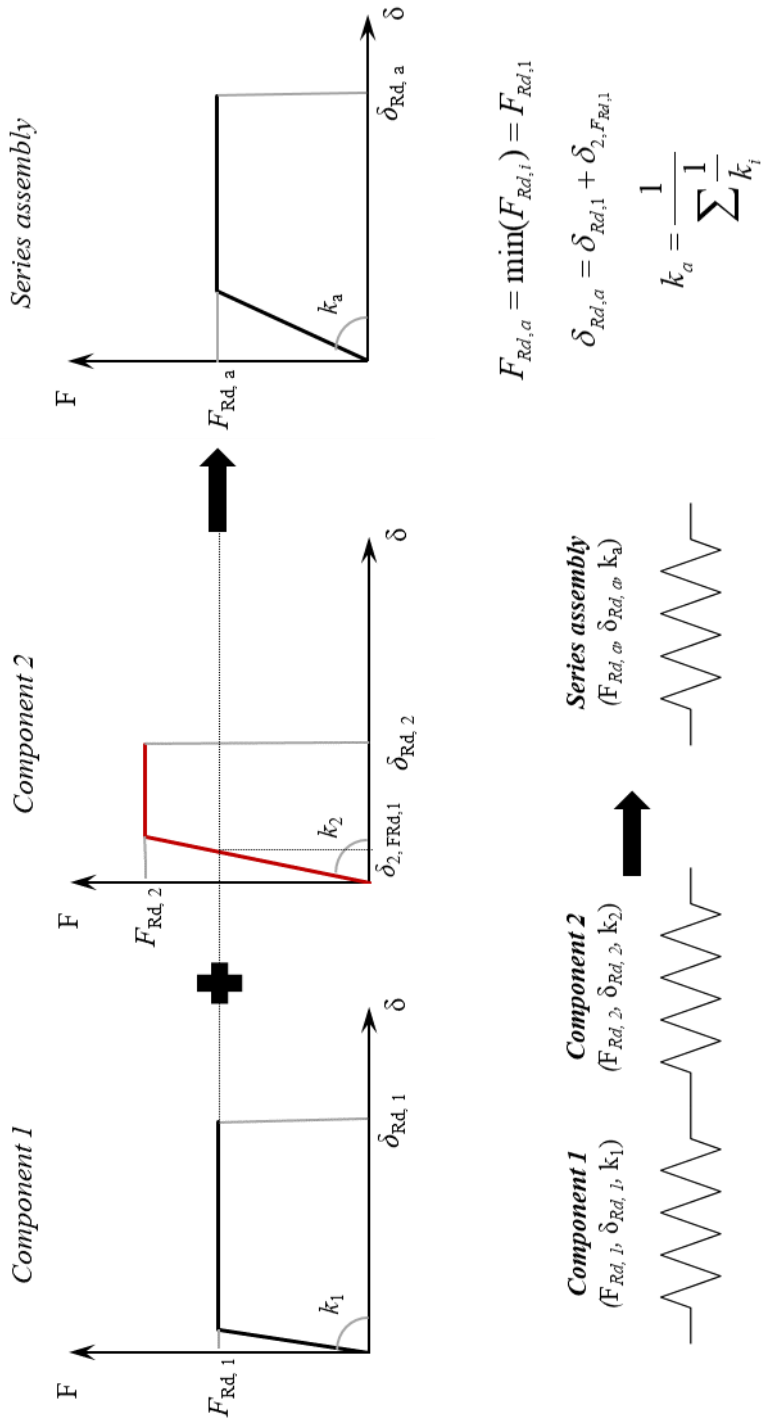

Figure 13 Linear series assembling

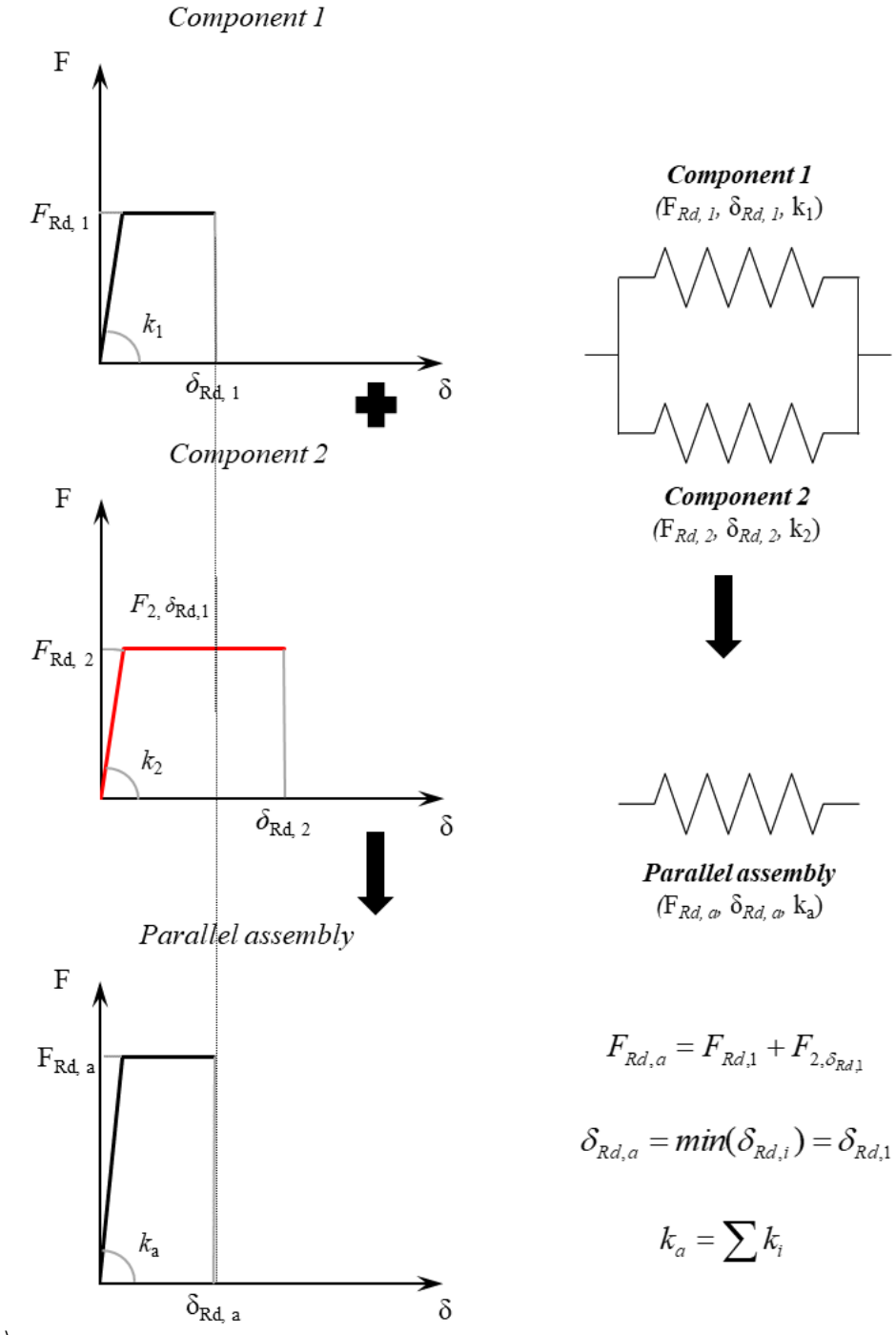

Figure 14 Linear parallel assembling

$$M_{Rd} = \sum F_{t,i,Rd} h_i \tag{3.2}$$

In order to achieve equilibrium at the joint level, the sum of tension forces $F_{T,Rd}$ has to be smaller than the resistance of the compressed region $F_{C,Rd}$. If this condition is satisfied for bolt row *i*, then the contribution of the lower rows to the bending moment resistance is neglected.

Detailed computation of some basic components that appear in a common beam to column bolted end-plate joint are presented in Table 4.

Table 4 Strength evaluation for basic components according to EN 1993 1-8

Component	Strength evaluation
5. End plate in bending	The design resistance and failure mode of an end-plate in bending, together with the associated bolts n tension, should be taken as equal to those of an equivalent T-stub flange for: - each individual bolt-row required to resist tension; - each group of bolt-rows required to resist tension.
7. Flange and web of beam or column in compression	$F_{c,fb,Rd} = \frac{M_{b,Rd}}{h - t_{fb}}$ $M_{b,Rd}$ – is the design moment resistance of the beam cross-section, reduced if necessary to allow for shear, see EN 1993-1-1. For a haunched beam $M_{b,Rd}$ may be calculated neglecting the intermediate flange, h – is the depth of the connected beam, t_{fb} – is the beam flange thickness
8. Beam web in tension	$F_{t,wb,Rd} = \frac{b_{eff,t,wb} t_{wb} f_{y,wb}}{\gamma_{M0}}$ $b_{eff,t,wb}$ is the effective width of the beam web in tension; should be taken as equal to the effective length of the equivalent T-stub representing the end-plate in bending, for an individual bolt-row or a bolt row-group, t_{wb} – is the beam web thickness.

For steel joints the initial stiffness is determined by combining the stiffnesses of each component. Provided that the axial force is not higher than 10% of the plastic resistance of the cross section, the initial stiffness of the joint $S_{j,ini}$ is computed using the following formula:

$$S_{j,ini} = \frac{Ez^2}{\sum_i \frac{1}{k_i}} \tag{3.3}$$

Where E is Young's modulus for steel, k_i is the stiffness coefficient associated to component i (Table 6.11 from EN 1993 1-8); and z is the lever arm of the components from the center of compression.

For the bolt rows in tension the stiffness coefficients can be grouped by considering a series assembling, resulting in the end only one equivalent coefficient:

$$k_{eff,r} = \frac{1}{\sum_i \frac{1}{k_{i,r}}} \tag{3.4}$$

Where $k_{i,r}$ are the stiffness coefficients of the components i of bolt row r.

For each bolt row in tension, in a stiffened joint, there are the following stiffness coefficients to be combined using formula (3.4):

- stiffness coefficient of the end-plate in bending:

$$k_5 = \frac{0,9 l_{eff} t_p^{\ 3}}{m^3} \tag{3.5}$$

Where: l_{eff} is the smallest of the effective lengths (individually or as part of bolt rows); m is generally as defined in Figure 6.11 (EN1993 1 – 8) but for bolt rows outside the tension flange $m = m_x$, where m_x is defined in Figure 6.10 (EN1993 1 – 8); t_p is the thickness of the end-plate.

- stiffness coefficient of bolts in tension

$$k_{10} = \frac{1,6A_s}{L_b} \tag{3.6}$$

Where A_s is the nominal area of the bolt cross section and L_b is the tightening length.

When in a joint two or more bolt rows are in tension, the stiffnesses of all the named bolt rows are assembled in parallel. This leads to the introduction of k_{eq} which is used for the evaluation of the initial stiffness. The equivalent lever arm z_{eq}, used for $S_{j,ini}$ instead of z, is computed function of the lever arms of the components in tension.

$$k_{eq} = \frac{\sum k_r h_r}{z_{eq}} \tag{3.7}$$

$$z_{eq} = \frac{\sum k_i z_i^{\,2}}{\sum k_i z_i} \tag{3.8}$$

Where k_r is the effective stiffness of bolt row r and h_r is the lever arm of the same bolt row r.

3.2.1.4 Design moment-rotation characteristic (EN 1993 1-8 6.1.2)

In the end, using the value of the bending resistance and initial stiffness computed above the design moment – rotation characteristic of the joint can be put together (see Figure 15). This can further be used in the global analysis of the structure, where the joints can be approximated with rotational springs, having the characteristics described above.

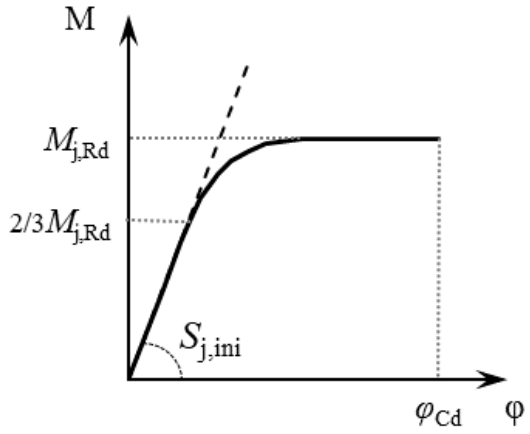

Figure 15 Design moment-rotation of a joint

For a given value of $M_{j,Sd}$ applied on the joint, lower or equal than the flexural resistance $M_{j,Rd}$, the stiffness is given by:

$$S_j = S_{j,ini} \quad \text{for} \qquad M_{j,Sd} \le \frac{2}{3} M_{j,Rd} \tag{3.9}$$

$$S_j = \frac{S_{j,ini}}{\mu} \quad \text{for} \qquad \frac{2}{3} M_{j,Rd} < M_{j,Sd} \le M_{j,Rd} \tag{3.10}$$

$$\mu = \left(1,5 \frac{M_{j,Sd}}{M_{j,Rd}} \right)^{2.7} \tag{3.11}$$

The design of a joint using the component method must consider the following:

- the joint resistance is determined by the weakest component. It is advisable for this component to have a ductile behavior, to allow stress redistribution in the connection. Usually, the bolts and the welds exhibit brittle failure modes that are to be avoided by providing these components with sufficient overstrength with respect to the more ductile components.

- the stiffness is given by a weighted average of the components, some of them having a larger contribution than others;

- the rotation capacity of the joint is dependent on the capacity of the weakest component. On the other hand, the deformability of different components can generate stress concentration that should be avoided (for example large stress concentration in the welds)

3.2.1.5 Behavior of the T – stub and evaluation of its resistance

In order to define all the components above mentioned (especially end plate in bending) one of the fundamental things to be clarified is the T–stub behavior and the way its resistance is obtained starting from the yielding patterns. A T–stub represents the assembly of two rigidly connected plates (see Figure 16), out of which one is called the flange of the T-stub and is characterized by the fact that it's connected with another member through one or more bolt rows.

The resistance of a bolt row is the minimum of all the components that develop at the level of the given bolt row and the parameter influencing these components is the effective length (l_{eff}) of the T-stub. The resistance of each T – stub is given by the minimum of the three possible failure modes described in Figure 17.

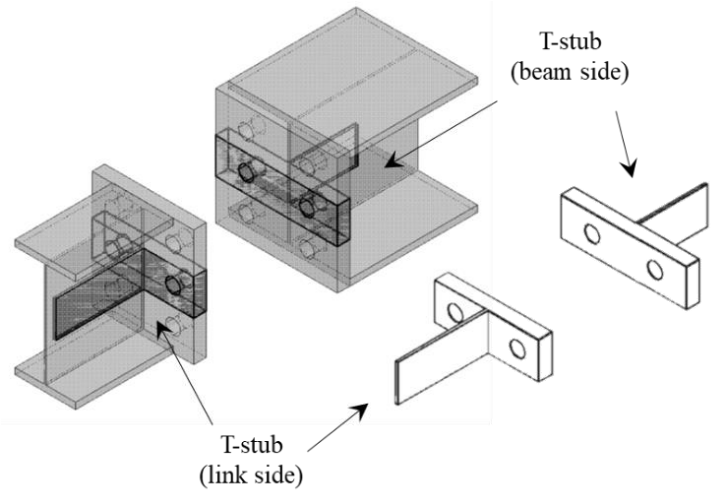

Figure 16 T-stub examples for the flush end-plate connection of detachable links

Mode 1 – considered a very ductile failure mode; occurs by complete plasticization of the flange and the bolts are not involved in the failure mechanism.

Mode 2 – the failure is characterized by a combined mechanism of flange plasticization and failure of the bolts.

Mode 3 - represents the brittle failure of the bolts and it doesn't involve any plastic engagement of the T-stub flange.

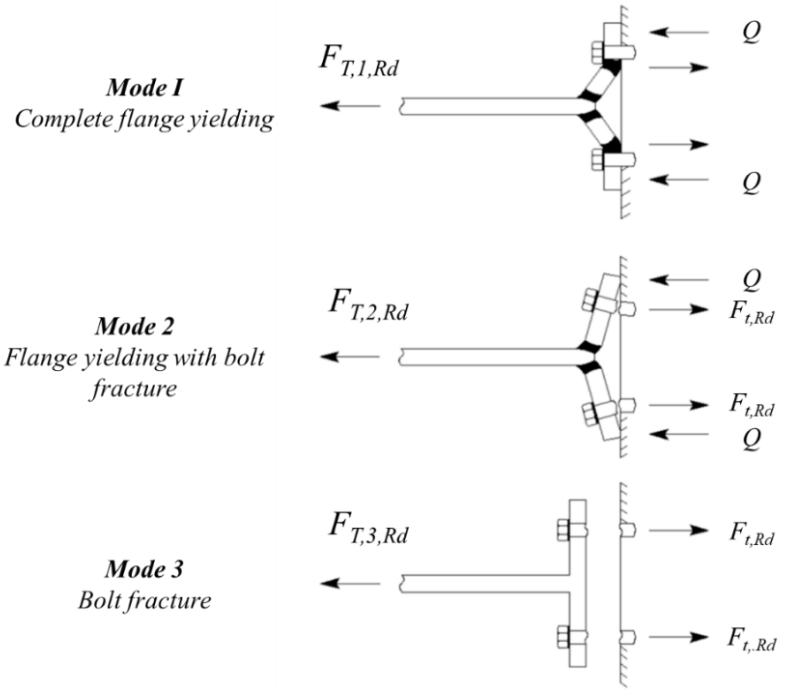

Figure 17 T-stub failure modes

In order to obtain the effective length for the first two failure modes, all the possible yielding cases must be considered. Figure 18 shows the most common types of circular and non-circular yield patterns for individual bolt rows while Figure 19 depicts the same patterns, for bolt rows as groups. The minimum length obtained is to be considered for further calculations, i.e. the resistance and stiffness of the components. The effective length for Mode 1 will be the minimum of $l_{eff,cp}$ and $l_{eff,nc}$ and for Mode 2 it will be $l_{eff,nc}$.

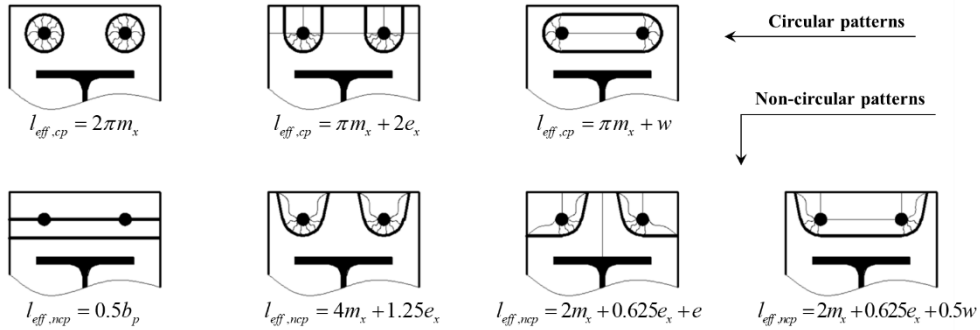

Figure 18 Typical examples of effective lengths for bolt rows acting alone

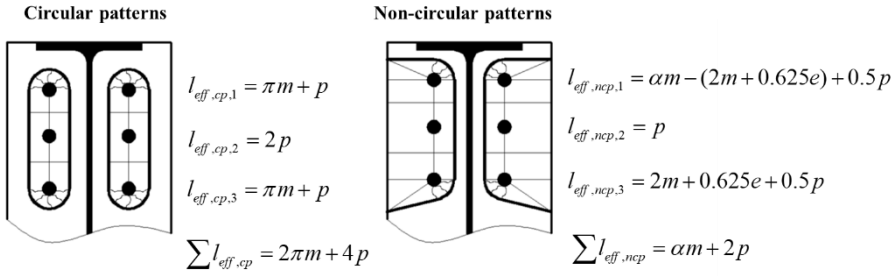

Figure 19 Typical examples of effective lengths for bolt rows acting in combination

Depending on the position of the bolt row relative to existing stiffeners and the component considered there are different values to be considered. Examples of evaluation formulas for the bolt row effective lengths are illustrated in Figure 18 (considering a single bolt row) and Figure 19 (considering bolt rows acting in combination).

3.2.2 Design of link end connections according to EC3 1-8

The design forces are estimated based on the capacity design principle, namely the connection must withstand the link ultimate plastic rotation (assumed as 0.08*rad* for short links). According to EN1998-1, the link strength associated to this condition are the following:

$$V_{j,Ed} = 1.1 \cdot \gamma_{ov} \cdot 1.5 \cdot V_{pl,link} \quad (3.12)$$

$$M_{j,Ed} = V_{Ed,j} \frac{e_{link}}{2} \quad (3.13)$$

Where: $V_{j,Ed}$ and $M_{j,Ed}$ are the design shear force and bending moment, respectively; *1.1* is the coefficient accounting for additional source of overstrength (N.B. this factor is questionable); γ_{ov} is the coefficient accounting for the material yield strength variability, which has been assumed equal to 1.25 in this study; $V_{pl,link}$ is the plastic shear strength calculated according to EC8 and *e* is the geometrical length of the link.

The links adopted in the DUAREM mock-up were very compact, thus the corresponding bending demand on the connection is significantly low. On the contrary, when the length of the links is close to the limit length of short links (e_s) the flexural demand increases, especially for links with thick web (higher shear capacity). This issue makes designing flush end plate connections nearly impossible. Therefore, under such conditions extended end-plate connections are considered as well (see Figure 20)

Table 5 Characteristics of experimental links

Link	$V_{pl,link}$	$M_{pl,link}$	e	e_s	e/e_s
	[kN]	*[kNm]*	*[mm]*	*[mm]*	*[-]*
S1	303	154	350	814	0.43
S2	303	154	350	814	0.43
S3	152	109	350	1146	0.31

$$V_{pl,link} = (d - t_{fl}) t_w \, f_y / \sqrt{3} \quad (3.14)$$

$$M_{pl,link} = b_{fl} t_{fl} (d - t_{fl}) f_y \quad (3.15)$$

$$e_s = 1.6 \frac{M_{pl,link}}{V_{pl,link}} \quad (3.16)$$

Figure 20*a* depicts the flush end plate connection that can be used for very short links (i.e. $e < 0.5e_s$) while Figure 20*b* shows the layout of an extended

end-plate connection applicable for most short links. The case of narrow flange profiles (IPE) accommodates the solution of flush end-plate connection also for links with lengths up to e_s while wide flange profiles like HE A and HE B do not (in these cases only extended end-plate connections can be designed).

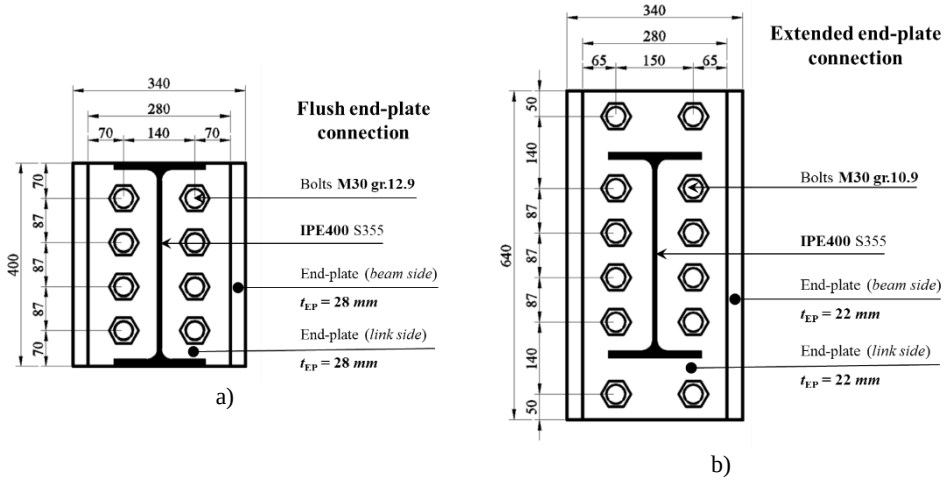

Figure 20 Connection layout: a) Flush end-plate connection, b) Extended end plate connection

3.2.2.1 Main components and their evaluation

The capacity of the connection is determined based on the component method as recommended by EC3 1-8. For the evaluation of the bending resistance, the joint is considered as composed of two parts: the link side and the beam side connection. A summary of the components in tension and compression is presented in Table 6.

Table 6 Link connection components

	Link side	***Beam side***
Flush end-plate connection	End plate in bending	End-plate bending Beam web in tension Beam flange and web in compression
Extended end-plate connection	End plate in bending	End plate in bending Beam web in tension Beam flange and web in compression

The components accounted for the two connection typologies are similar, with the difference that the extended end-plate connection has an additional bolt row outside the flanges of the link and/or beam respectively. The link web in tension and link web and flange in compression are disregarded as they are involved in the plastic dissipation mechanism (yielding is expected in the link web and flange). The compression resistance assumed to verify the internal equilibrium is the compression strength of beam web and flange. The evaluation of the effective T-stub length was conducted based on Table 7.

In both joint typologies the last bolt row in between the flanges is considered as a bolt row adjacent to a stiffener and has the effective length calculated as for the first bolt row below the tension flange. The resistance of the T-stub was evaluated considering the 3 possible failure modes, with no backing plates and Method 1 for the evaluation of $F_{T,1,Rd}$.

In both joint typologies the last bolt row in between the flanges is considered as a bolt row adjacent to a stiffener and has the effective length calculated as for the first bolt row below the tension flange. The resistance of the T-stub was evaluated considering the 3 possible failure modes, with no backing plates and Method 1 for the evaluation of $F_{T,1,Rd}$.

Table 7 Effective length of the T-stub

	Bolt row considered individually		*Bolt row as part of a group*	
	$l_{eff,cp}$	$l_{eff,ncp}$	$l_{eff,ncp}$	$l_{eff,ncp}$
Bolt row outside tension flange	Smallest of: $2\pi m_x$ $\pi m_x + w$ $\pi m_x + 2e$	Smallest of: $4m_x + 1.25e_x$ $e + 2m_x + 0.625e_x$ $0.5b_p$ $0.5w + 2m_x + 0.625e_x$	-	-
First bolt row below tension flange	$2\pi m$	αm	$\pi m + p$	$0.5p + \alpha m - (2m + 0.625e)$
Other inner bolt row	$2\pi m$	$4m + 1.25e$	$2p$	p

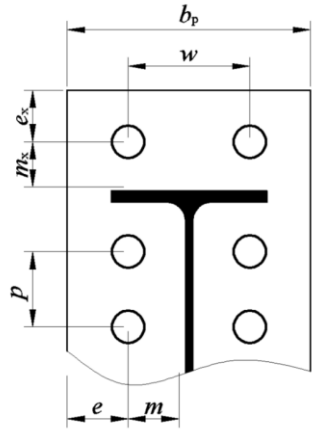

Figure 21 Definition of values for the T-stub effective length evaluation

Table 8 Formulas for the calculation of the three failure modes

	Prying forces may develop, i.e. $L_b \leq L_b^*$	No prying forces
Mode 1	$F_{T,1,Rd} = \frac{4M_{pl,1,Rd}}{m}$	$F_{T,1-2,Rd} = \frac{2M_{pl,1,Rd}}{m}$
Mode 2	$F_{T,2,Rd} = \frac{2M_{pl,2,Rd} + n\sum F_{t,Rd}}{m+n}$	
Mode 3	$F_{T,3,Rd} = \sum F_{t,Rd}$	

Where:

$$L_b^* = \frac{8.8m^3 A_s}{\sum l_{eff,1} t_f^3} \tag{3.17}$$

$$M_{pl,1,Rd} = \frac{0.25\sum l_{eff,1} t_f^2 f_y}{\gamma_{M0}} \tag{3.18}$$

$$M_{pl,2,Rd} = \frac{0.25\sum l_{eff,2} t_f^2 f_y}{\gamma_{M0}} \tag{3.19}$$

L_b is the bolt elongation taken equal to the grip length (total thickness of material and washers), plus half the sum of the height of the bolt head and the height of the nut, A_s is the bolt tensile area, $\sum l_{eff}$ is the effective length of the T-stub, t_f is the thickness of the T-stub flange, $F_{T,Rd}$ is the resistance of the T-stub $\sum F_{t,Rd}$ is the total tensile resistance of the bolts in the T-stub, *n* is the minimum between $e_{\min}$ and $1.25m$. Additionally, there is:

Table 9 Formulas for the evaluation of the components

End-plate in bending	$F_{T,Rd} = \min(F_{T,1,Rd}, F_{T,2,Rd}, F_{T,3,Rd})$
Beam web in tension	$F_{t,wb,Rd} = \frac{b_{eff,t,wb} t_{wb} f_{y,wb}}{\gamma_{M0}}$
Beam flange and web in compression	$F_{c,fb,Rd} = \frac{M_{b,Rd}}{h - t_{fb}}$

The individual components are evaluated as given in Table 9. For the link side the only component considered is the end-plate in bending, thus the resistance of the connection is given by the named component. On the beam side, the minimum between the end-plate in bending and the beam web in tension will give the resistance of the bolt rows and connection, respectively.

3.2.2.2 The strength and stiffness assembly

The flexural resistance ($M_{j,Rd}$) and initial stiffness ($S_{j,ini}$) of the connection are evaluated based on the steps previously discussed. The flexural stiffness is calculated considering k_5, the stiffness of the end-plate in bending (both for link and beam side) and k_{10}, the stiffness of the bolt.

In general, flush end-plate and extended end-plate connections will result to be semi-rigid and full-strength joints i.e. the Moment-rotation curve will fall in between the limits for rigid and pinned joints (as detailed in Figure 22).

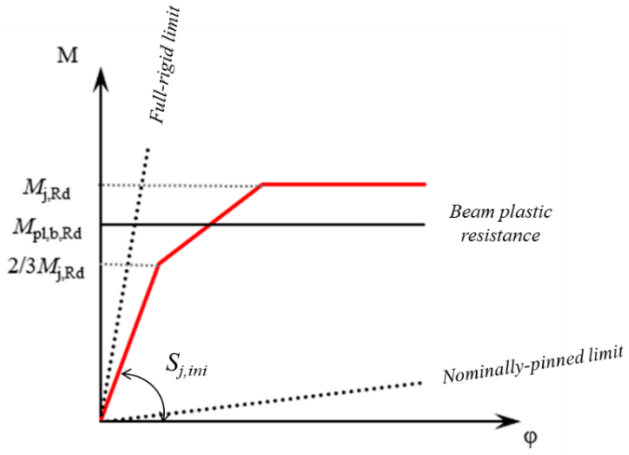

Figure 22 Analytical moment-rotation curve

The shear strength is evaluated considering the full shear capacity of the bolts in compression and a percentage (28.5%) of the ones in tension.

$$V_{Rd} = n_c F_{v,Rd} + \frac{0.4}{1.4} n_t F_{v,Rd} \tag{3.20}$$

Where: n_c is the number of bolts in compression; n_t is the number of bolts in tension; $F_{v,Rd}$ is the shear strength of a single bolt.

In order to design a set of case study connections for the investigation on the link-connetion assembly behavior, the numerical model assumptions as well as its calibration are presented.

3.3 FE MODEL: ASSUMPTIONS AND VALIDATION

3.3.1 Numerical assumptions

In order to obtain accurate results using a FE software, validation against experimental results is compulsory. Based on the results of the full-scale test performed within the DUAREM research project (FP7 2007-2013 SERIES Agreement No 227887), the numerical model hereby presented was calibrated using Abaqus. In the following paragraphs the modelling details and basic assumptions considered for the numerical analyses are presented.

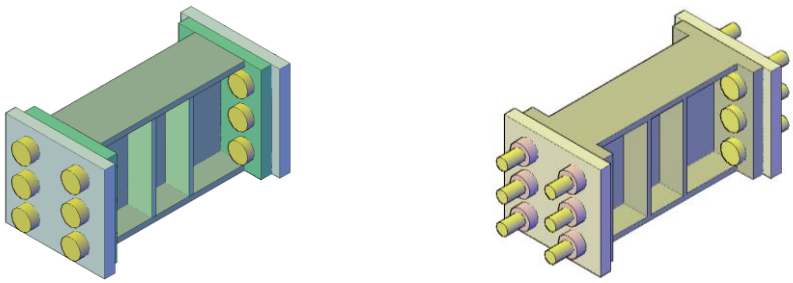

a HR model *b) HV model*

Figure 23 Link assembly models with the two bolt typologies

3.3.1.1 Model Geometry and Materials

The ABAQUS model represents the link with both side flush end-plate connections. The link assembly elements (link, stiffeners and end-plates) were modelled as solid parts depicting the respective nominal geometry. Two possible modelling solutions were considered for the bolts, in accordance with the bolt assemblies available and their respective failure mechanisms (see Figure 23). The HR British/French system (HR is the acronym for '*High Resistance*') and the German system HV (German acronym of *'Hochfeste Bolzen mit Vorspannung'*, which in English is '*high resistance bolts for pretension'*) are characterized by different failure i.e. the former by necking of the shank while the latter by thread plastic deformation and nut stripping.

The HR bolt modelling consists of a unique solid part that combines the bolt and nut while in the case of HV bolts a combination of solid and beam elements is used. The solid parts of the HV bolts (head and shank) are modelled separately from the nut and they are connected by the beam element. Simplified cylindrical shapes for the bolt's shank, head and nut are used in all cases and the nominal dimensions are considered.

The parametric study on the links was carried out considering only the profile and stiffeners while the assessment of the link connection assemblies was performed on models like the DUAREM links used for the FE model calibration.

3.3.1.2 Units

The units used throughout the numerical study were chosen such that no inconsistencies occur. The units for the main measures used for the input procedure are presented in Table 10.

Table 10 Units for ABAQUS

	Length	**Force**	**Stress**	**Density**	**Elastic Modulus**
Unit	*mm*	*N*	*N/mm²*	*Ton/mm³*	*N/mm²*

3.3.1.3 Material property

The experimental program of DUAREM included material tests on most elements of the structure, therefore the true stress-strain curves used in the FE models were obtained from the tensile test results. The ready to use material curves were derived from the engineering curves using the following relationships:

$$\varepsilon_{true} = \ln(1+\varepsilon_{eng}) \tag{3.21}$$

$$\sigma_{true} = \sigma_{eng} \cdot e^{\varepsilon_{true}} = \sigma_{eng}(1+\varepsilon_{eng}) \tag{3.22}$$

The plastic stress-strain material properties are introduced using the "Half-cycle" input method. Combined Isotropic and Kinematic hardening model is used. The material properties for the steel elements and bolts present certain particularities that must be considered individually.

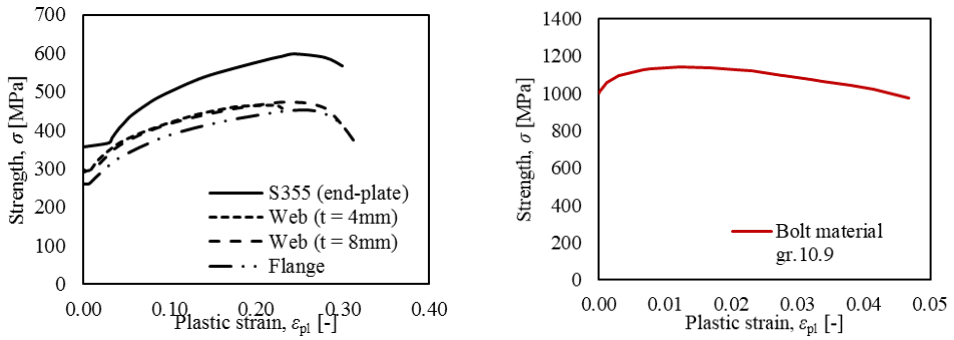

a) Steel elements *b) Bolts*

Figure 24 Modelled materials

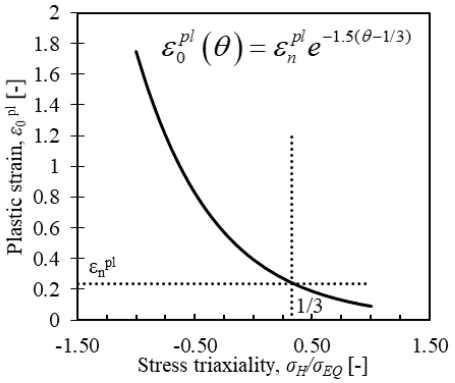

Figure 25 Ductile Damage model

3.3.1.4 Steel material property

The elastic domain of the steel constitutive law is defined by the nominal Young's modulus (E = 210 *GPa*) and the Poisson ratio (v = 0.3). As for the plastic range, apart from the true stress – plastic strain curve (showed in Figure 24*a*), the steel fracture was modeled using the *'Ductile Damage'* input method (from Damage for Ductile Metals). This method allows the user to provide the fracture strain (ε_0^{pl}) as function of the stress triaxiality $(\theta = \sigma_H/\sigma_{EQ})$ and strain rate. The ductile damage failure model by Lemaitre (1992) leads to the curve

in Figure 25 i.e. for pure tension the stress triaxiality is equal with 1/3, therefore the plastic strain is equal with the necking plastic strain (ε_n^{pl}) measured experimentally during the tensile test.

3.3.1.5 Bolt material property

As previously specified, two bolt typologies were considered, HR and HV. The resistance and stiffness of the HR bolt assemblies is corrected by altering the shank's material strength and elastic modulus. The effective resistance was obtained starting from the grade 10.9 plastic stress-strain material curve in Figure 24*b* which was scaled by the ratio of nominal to net area of the shank (A_{nom}/A_s) in accordance with the bolt diameter (see Figure 26). As for the stiffness, an effective Young's modulus had to be used, calculated based on the elastic stiffness of the bolt k_b evaluated according to the equation proposed by Swanson and Leon (2001).

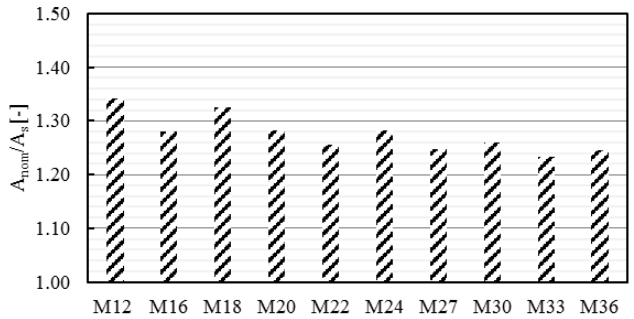

Figure 26 The nominal/net area for typical range of bolt diameters

$$\frac{1}{k_b} = \frac{f \cdot d_b}{A_b \cdot E} + \frac{L_s}{A_b \cdot E} + \frac{L_{tg}}{A_{eb} \cdot E} + \frac{f \cdot d_b}{A_{be} \cdot E} \tag{3.23}$$

Where f is the stiffness correlation factor taken as 0.55; d_b is the nominal diameter of the bolt; A_b is the nominal area of the bolt shank; A_{be} is the effective area of the threads; L_s is the shank length of the bolt; L_{tg} is the length of the threaded portion included in the bolt's grip; and E is the modulus of elasticity.

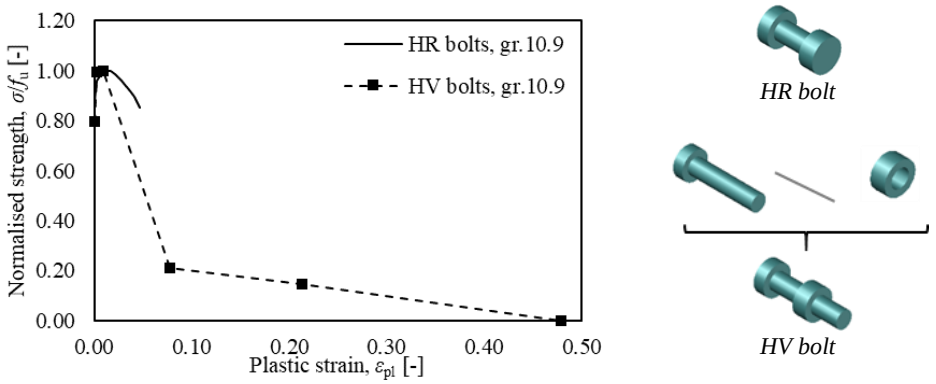

Figure 27 HV vs. HR constitutive law model

The HV bolts were modelled following the procedure described by Cassiano et al. (2017), who modelled the thread stripping by defining a wire element characterized by the real failure mechanism of the bolt-nut assembly. The non-linear law describing the wire response is presented in Figure 5.

The ductile damage was considered also for the bolts. The adopted equivalent plastic strain at damage onset curve as a function of triaxial stress state was defined according to Pavlovic *et al.* (2015) and assumed independent from strain rate.

The parametric study and the link assessment were performed considering similar material definition, with the distinction that the link had the same material for the web and flanges, as the profiles were hot rolled. The material properties used for design and the numerical investigation are the average curve of S355 steel, and the gr.10.9 and 12.9 for bolts.

3.3.1.6 Step setting

Dynamic Implicit analysis was employed. A two-step procedure was used, in order to separate the clamping of the bolts from the loading protocol applied. The load application method is "Quasi-Static" and the nonlinear effects of large displacements are included. The maximum increment was limited to the minimum value of the loading history.

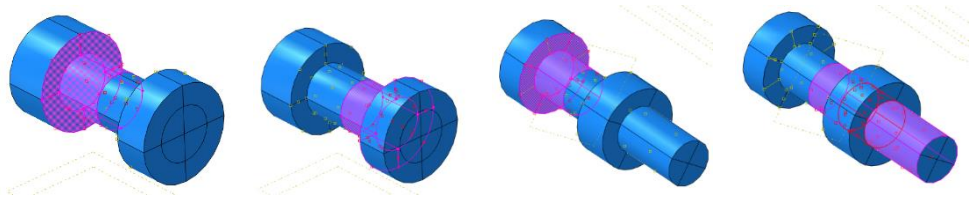

Figure 28 Bolt interaction definition

3.3.1.7 Interaction

The contact between various surfaces, such as bolt to end-plates or between the end-plates, was defined considering an interaction property that accurately describes the frictional behavior of the respective surfaces. *'Coulomb friction'* was used for the tangential behavior, with a friction coefficient equal to 0.4, and *'Hard contact'*, to characterize the normal behavior of the surfaces. This was the case for the models with HR bolts (Figure 28).

In the case of HV bolts, the contacts between the end-plates, and the bolt-nut assembly with the adjacent surfaces was treated separately. The former was modeled as previously seen (considering both tangential and normal behavior) while the latter was modelled considering just the normal behavior. This was necessary in order to allow the wire to transfer the loads while the solid parts provide stable supports and shear resistance.

3.3.1.8 Boundary Conditions and Loads

Appropriate boundary conditions were used at the link ends. *Coupling* restraints with a *'Structural distribution'* were used to simulate the beam section at the connection face. In the case of HV model, the wires were connected to the solid bolt head and nut using *MPC Tie* constraints.

The axial and flexural stiffness of the frame was calculated, based on the static scheme in Figure 29 and applied as extensional and rotational springs at the connection-beam interface. The DOFs along which the deformation was

allowed were selected in accordance with the global coordinates system of the model (DOF 1 for axial deformation and DOF 5 for flexure about y axis).

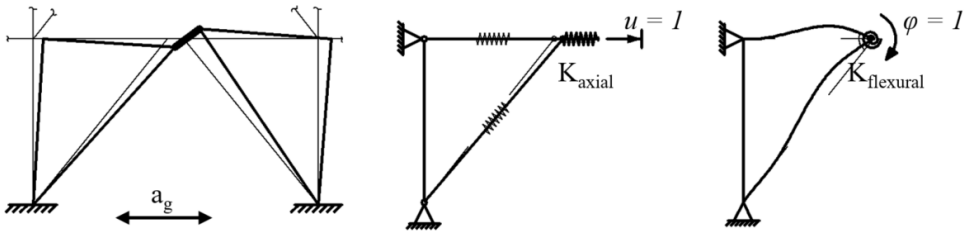

Figure 29 Static scheme for the evaluation of the frame stiffness

The bolts are preloaded using the *'Bolt Force'* option in Abaqus. The pretension force was calculated according to EN 1993 1-8, considering 70% of the bolt ultimate strength.

$$F_{p,Cd} = 0.7 A_s \cdot f_{ub} / \gamma_{M7} \tag{3.24}$$

Where $F_{p,Cd}$ is the preload force for a bolt, f_{ub} is the ultimate strength of the bolt material, A_s is the tensile stress area, and γ_{M7} is the partial safety coefficient for preloading.

The analyses were carried out in displacement control considering the cyclic protocols derived from the experimental tests for the calibration, and monotonically increasing displacement up to 10% link rotation for the parametric studies performed.

3.3.1.9 Element type

The model was meshed using 3D solid elements. The finite element type C3D8R (an 8-node linear brick, reduced integration, hourglass control) is adopted for all the solid parts of the model. A minimum of wo elements per plate thickness were enforced in order to prevent shear locking.

3.3.1.10 ABAQUS Output

To calibrate the response of a numerical model based on the experimental tests, the most important results were the shear vs. link rotation curves at the beam side interface of the connection. The desired results are obtained from the reaction force along z (reaction force 3 - RF3) and the displacement along the same direction (U3) in the reference point where the loading history was applied. Other results include the equivalent plastic strain (PEEQ), rotation of the nonlinear spring (UR) and the axial force (obtained as integration of the normal stress in the section), for the parametric studies.

3.3.2 Calibration of the FE input method on experimental tests

3.3.2.1 General

The input numerical method is calibrated based on the detachable links of the south frame of the DUAREM structure. Details of the test sequence were presented in the project description at the beginning of the chapter.

Table 11 DUAREM experimental links geometry details (South Frame)

Specimen	Link length (e_{link})	Assembly length ($L_{assembly}$)	Height (h)	Width (b_{fl})	Flange thickness (t_{fl})	Web thickness (t_w)
	mm	*mm*	*mm*	*mm*	*mm*	*mm*
S-1	350	450	230	170	12	8
S-2	350	450	230	170	12	8
S-3	350	450	230	120	12	4

Table 12 DUAREM links connection geometry details

Specimen	**Bolts**	$h_{EP\text{-}link/beam}$	$t_{EP\text{-}link/beam}$	$b_{EP\text{-}link}$	$b_{EP\text{-}beam}$	e_1	p_1	$e_{2\text{-}link}$	$e_{2\text{-}beam}$	p_2
		mm	*mm*	*mm*	*mm*	*mm*	*mm*	*mm*	*mm*	*mm*
S-1	M27	230	25	220	240	45	70	50	60	120
S-2	M27	230	25	220	240	45	70	50	60	120
S-3	M27	230	25	220	240	45	70	50	60	120

The joint configuration is that of a classical flush end-plate connection for splices. The detailed geometry of the link assembly and joint are described in Figure 30, Table 11 and Table 12. To be noted that the geometry of the link on 1st and 2nd floor (S1 and S2) is identical but the loading protocol applied is different. The stiffness of the frame was evaluated as previously shown in Figure 29 and modelled by means of nonlinear flexural and axial springs. The values modelled are presented in Table 13

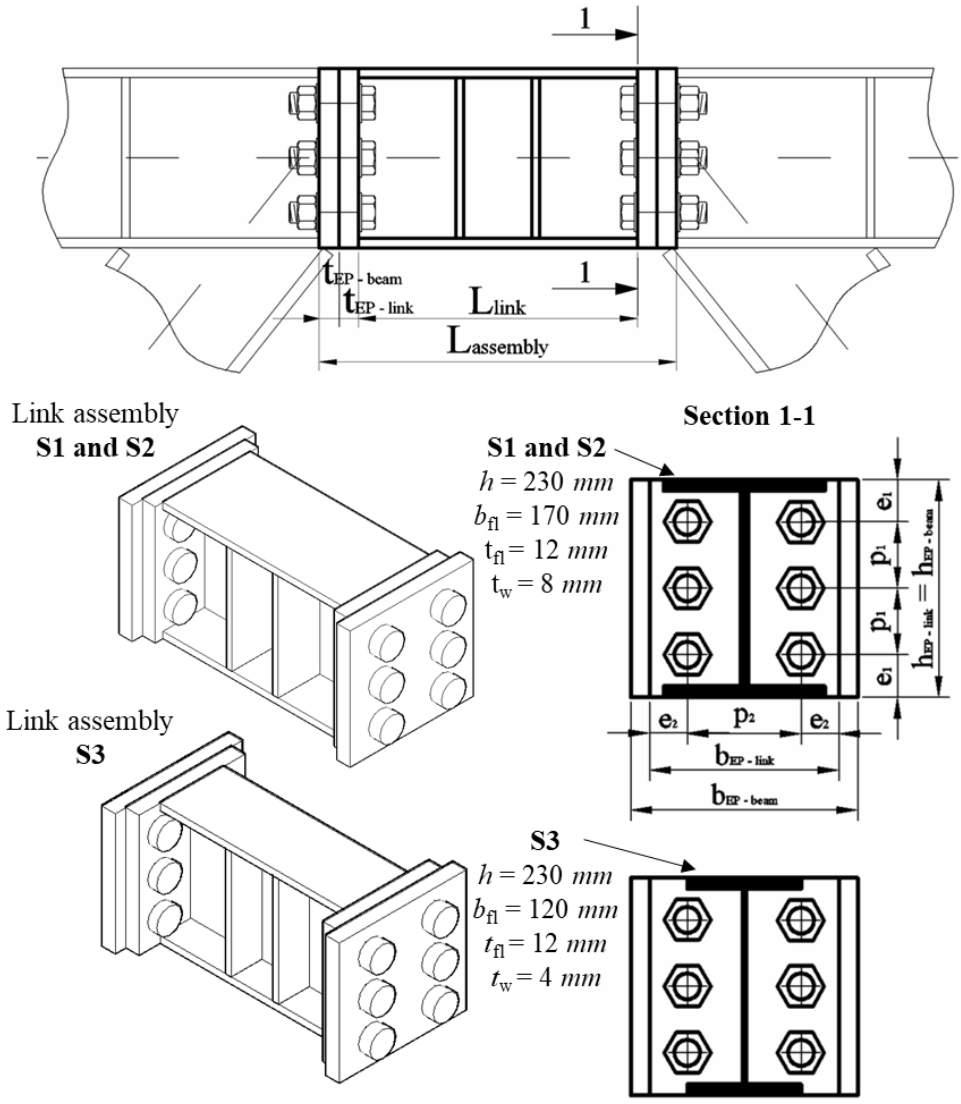

Figure 30 DUAREM links and connections to beam

Table 13 Evaluation of the frame flexural and axial stiffness

	Section	A	I_y	L	E	α	$K_{rotational}$	K_{axial}
		mm^2	mm^4	mm	N/mm^2		Nmm/rad	Nmm/rad
Column	HEA240	7680	7.76E+07	3500	210000			4.61E+05
Beam	HEA240	7680	7.76E+07	2780	210000	51.54	2.35E+10	5.80E+05
Brace	HEB220	9100	8.09E+07	4469.7	210000		1.52E+10	4.28E+05
Assembly							3.87E+10	7.46E+05

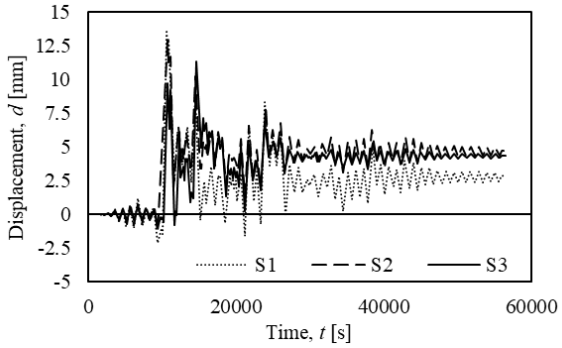

Figure 31 Cyclic loading protocol for DUAREM south frame links (Ioan et al., 2016)

The cyclic protocol was derived from the experimental curves, for the links at each level, by multiplying the rotation with the link length. The displacement histories for all three links are plotted in Figure 31. All the other assumptions made above were applied in the modelling phase. The materials were properly defined accounting for the damage and cyclic hardening. The surface interactions and the boundary conditions were carefully attributed, so that the fidelity of the FE model to the real link is as good as possible. Finally, the mesh was properly defined using the solid 3D finite elements described above.

3.3.2.2 Results

The comparison of the numerical and experimental cyclic response is presented in Figure 32. The shear force – total rotation cures for the simulations considering the HR bolts give an accurate approximation of the experimentally measured results.

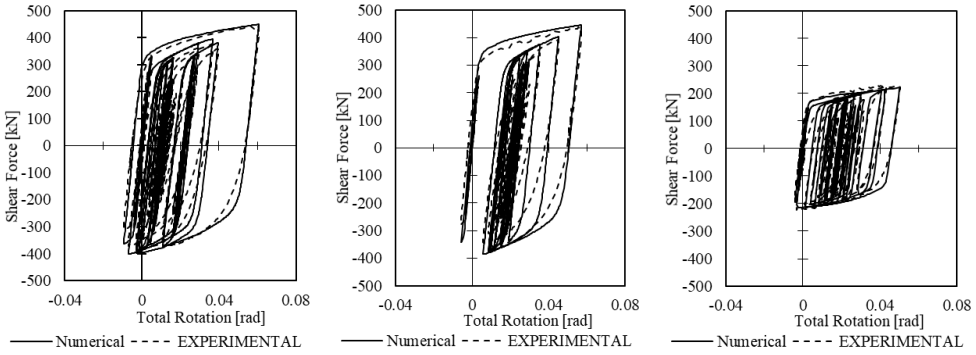

S1 S2 S3

Figure 32 Experimental vs Numerical Shear Force-Rotation Curves

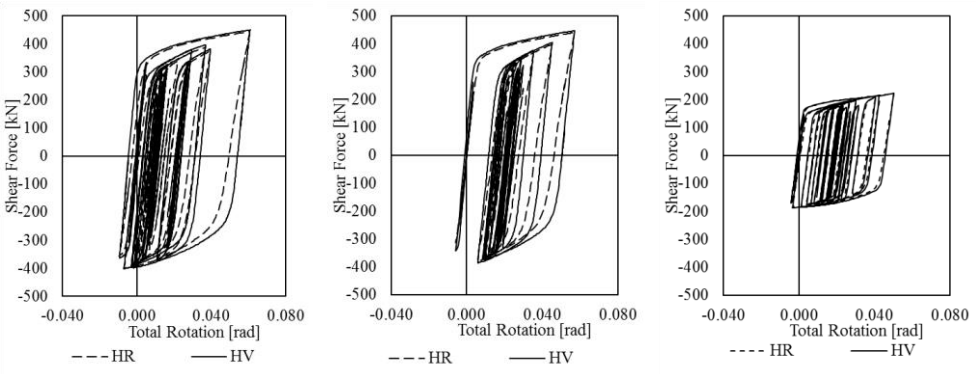

S1 S2 S3

Figure 33 Experimental vs Numerical ShearForce-Rotation Curves

Modelling the bolts using the wire element (with HV bolt model) gives a more realistic approximation of the link assembly response. However, the differences between HR and HV models is not significant (see Figure 33), as the connection does not undergo serious plastic damage and the bolts remain elastic.

In terms of plastic damage, the results can be compared only qualitatively based on the pictures in Figure 34 which depicts the links of the south frame of the structure tested at JRC, in Ispra (the DUAEM Research project) and the screenshots of the equivalent plastic strain (PEEQ) for the corresponding models, considering the HR bolts. The areas of concentration of damage are similar as well as the residual deformation.

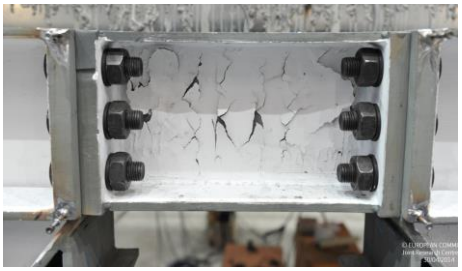

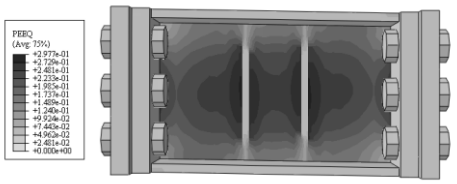

S1

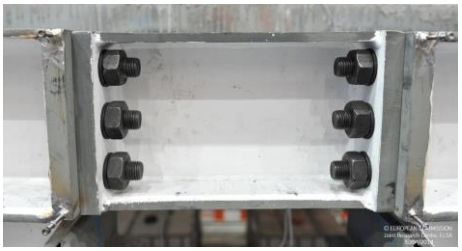

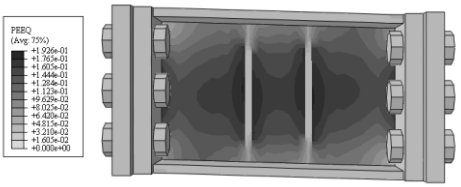

S2

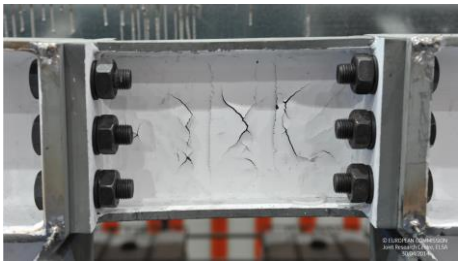

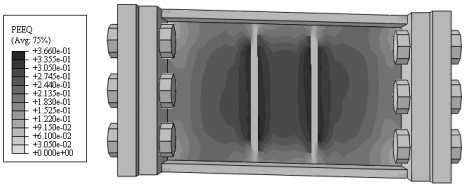

S3

Figure 34 Comparison of the cumulative plastic damage in the links of the tested structure and the PEEQ for the numerical models

3.4 PARAMETRIC STUDY FOR THE EVALUATION OF THE LINK CONNECTION DESIGN FORCES

The link end connections should be designed to remain elastic under Ultimate Limit State earthquake levels. According to EN1998-1, this can be achieved by making sure the connection can withstand the link ultimate plastic rotation by overdesigning it with respect to the link plastic shear and bending capacity ($V_{\text{pl link}}$ and $M_{\text{pl,link}}$) as defined in the equations below).

$$V_{pl,link} = (d - t_{fl}) t_w \, f_y / \sqrt{3} \tag{3.25}$$

$$M_{pl,link} = b_{fl} t_{fl} (d - t_{fl}) f_y \tag{3.26}$$

$$e_s = 1.6 \frac{M_{pl,link}}{V_{pl,link}} \tag{3.27}$$

Where d is the link section depth, t_{fl} is the flange thickness, t_{w} is the web thickness, f_{y} is the yield strength of the steel and b_{fl} is the flange width. The design values for $V_{\text{j,Ed}}$ and $M_{\text{j,Ed}}$ according to EC8 are given by *Eq.* 1.3 and 1.4.

$$V_{j,Ed} = 1.1 \cdot \gamma_{ov} \cdot 1.5 \cdot V_{pl,link} \tag{3.28}$$

$$M_{j,Ed} = V_{j,Ed} \frac{e}{2} \tag{3.29}$$

Where: $V_{\text{j,Ed}}$ and $M_{\text{j,Ed}}$ are the design shear force and bending moment, respectively; *1.1* is the coefficient accounting for additional sources of overstrength; γ_{ov} is the coefficient accounting for the material yield strength variability; $V_{\text{pl,link}}$ is the plastic shear strength calculated according to EC8 and e is the geometrical length of the link.

As it can be noted, the design shear force $V_{\text{j,Ed}}$ is significantly higher than the link plastic capacity $V_{\text{pl,link}}$ owing to the material strength uncertainty

(coefficient γ_{ov}), the additional sources of overstrength (the *1.1* factor) but mainly due to the shear overstrength that has a recommended value of 1.5.

The link shear overstrength depends on a variety of factors like the link length, boundary conditions, section compactness, stiffening or axial forces (Azad and Topkaya, 2017)

According to the provisions of EN1993 1-8 the axial force can be disregarded in the connection design as long as it amounts for less than 5% of the member tensile capacity ($N_{pl,Rd}$). It was proved in past research (Della Corte et al. (2007 and 2013) that axial forces can develop in the very short links under large deformations. Therefore, the level of axial forces developing in the link must be assessed for a correct connection design.

A parametric study on the most commonly used hot rolled steel profiles has been carried out. The main parameters of the study are hereinafter presented.

3.4.1 Parametric study

The numerical models analyzed under monotonic loading, consisted only in the link profile itself and the stiffeners (spaced in accordance with the EC8 recommendations). The parameters selected for the numerical investigation are the profile type (narrow or wide flange), the section depth, the link length (function of the limit for short links e_s) and the boundary conditions.

The detailed parameters are:

1. **Type of hot-rolled profile**: IPE, HE A and HE B
2. **Depth of the profile**: 200, 300, 400, 500 and 600 mm
3. **Link length**: e_s, $0.75e_s$ and $0.50e_s$

The boundary conditions considered:

1. Fully restrained (all six degrees of freedom are blocked);
2. Axial release at one end (all degrees of freedom are blocked apart from the axial deformation at one end);
3. Deformable restraints (axial and in plane flexural stiffness of the frame and connection are modelled while all other DOF are blocked).

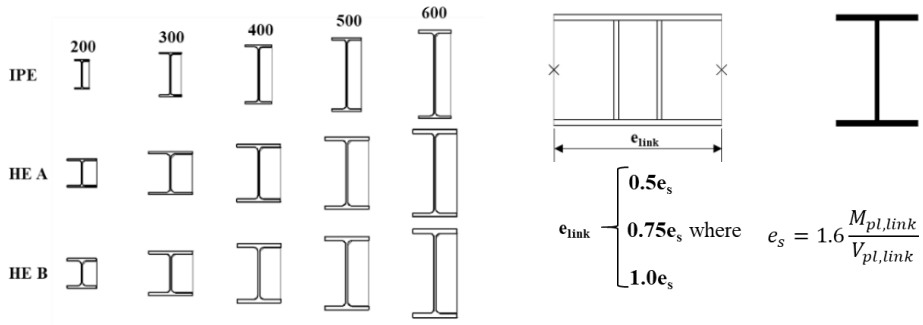

a) Link profile sections *b) Length definition*

Figure 35 Hot-rolled profiles investigated

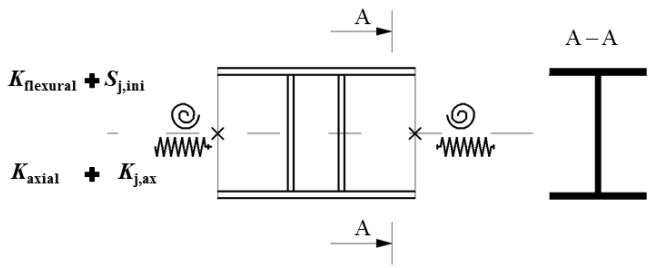

Figure 36 Deformable restraints (DR) boundary conditions definition

The symbols in Figure 36 represent as it follows: K_{flexural} is the flexural stiffness of the braced bay, K_{axial} is the axial stiffness of the braced frame, $S_{\text{j,ini}}$ is the joint initial stiffness and $K_{\text{j,ax}}$ is the joint axial stiffness. The values were evaluated as presented in the chapter describing the numerical model (for the frame stiffness) and in the chapter describing the design of connections, respectively. Table 14 presents the values for the $0.50e_s$ set of links.

Table 14 Frame and connection stiffness for $0.50e_s$ set of links

Length **$0.50e_s$**	**$K_{flexural}$** *[Nmm/rad]*	**K_{axial}** *[Nmm/mm]*	**$S_{j,ini}$** *[Nmm/rad]*	**$K_{j,ax}$** *[Nmm/mm]*
IPE 200	1.9E+10	5.0E+05	3.3E+10	3.0E+06
IPE 300	9.0E+10	1.0E+06	7.3E+10	2.8E+06
IPE 400	1.3E+11	1.1E+06	3.2E+11	6.8E+06
IPE 500	2.6E+11	1.4E+06	5.0E+11	6.7E+06
IPE 600	3.7E+11	1.6E+06	1.2E+12	8.6E+06
HE 200 A	2.5E+10	6.6E+05	3.8E+10	3.8E+06
HE 300 A	1.1E+11	1.3E+06	1.1E+11	4.8E+06
HE 400 A	1.6E+11	1.3E+06	2.6E+11	5.8E+06
HE 500 A	3.1E+11	1.7E+06	5.3E+11	7.4E+06
HE 600 A	4.4E+11	1.8E+06	9.9E+11	9.5E+06
HE 200 B	7.1E+10	1.1E+06	3.2E+10	3.0E+06
HE 300 B	2.0E+11	2.3E+06	1.5E+11	6.0E+06
HE 400 B	2.5E+11	2.0E+06	3.5E+11	8.0E+06
HE 500 B	4.2E+11	2.2E+06	6.6E+11	8.5E+06
HE 600 B	5.8E+11	2.3E+06	1.1E+12	1.1E+07

The links are designed with intermediate web stiffeners to guarantee ductility and prevent buckling or fracture of the web prior to the plasticization of the link. EN 1998-1 6.8.2(10) provides the following guidelines in designing intermediate web stiffeners for short links:

- for a link rotation of 0.08*rad*, the maximum interval of the stiffeners should not exceed $(30t_w - d/5)$
- intermediate web stiffeners should be full depth. For links that are less than 600*mm* in depth, stiffeners are required on only one side of the link web. For links that are 600*mm* deep or greater, the stiffeners should be placed on both sides of the web
- the thickness of one-sided stiffeners should not be less than t_w or 10 mm, whichever is larger
- the width of the stiffener should not be less than $b/2 - t_w$

3.4.2 Shear Overstrength

The shear overstrength represents the ratio between the shear force V and the plastic shear resistance $V_{pl,link}$ evaluated according to EC8, at a link rotation equal to 0.08 radians.

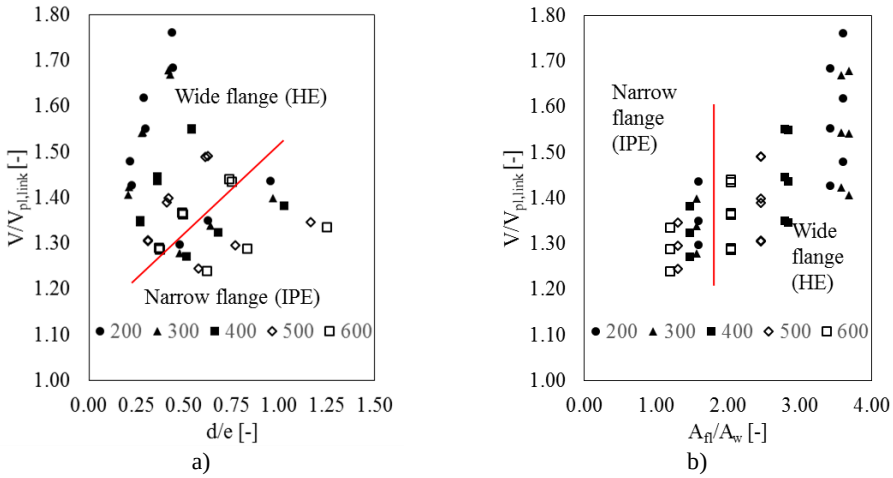

Figure 37 Shear overstrength for fully restrained (FR) links

The type of profile used for the link has proved to greatly influence its shear overstrength. As shown in Figure 37 the wide flange profiles (HE A and HE B) exhibit significantly larger values of shear overstrength with respect to the narrow flange profiles (IPE) and this is true regardless of the web thickness. Indeed, even though both the HE A and IPE have comparable web thicknesses for the same depth, the difference is compelling.

Furthermore, regarding the wide flange HE profiles, it is to be noted that the differences between same depth profiles is negligible, except for very shallow sections for which small variations are visible. This is so because both the flange and web areas proportionally increase from HE A to HE B profiles. The curves in Figure 37 are plotted for the fully restrained links, but the previous observations are valid also for links modelled considering the frame and connection stiffness, as depicted in Figure 38*c* and *d.*

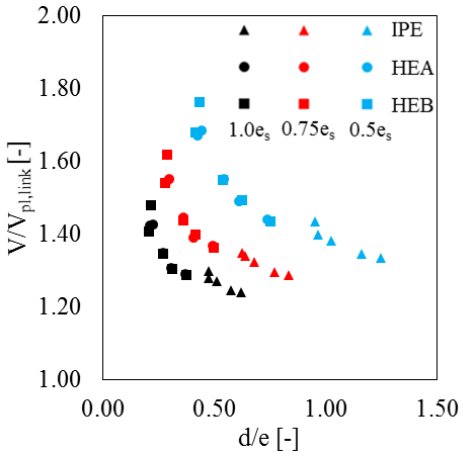

a) Fully restrained (FR)

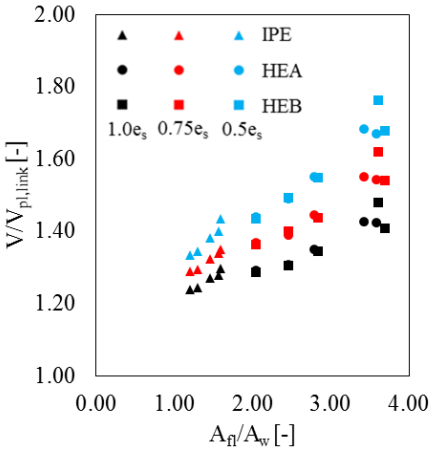

b) Fully restrained (FR)

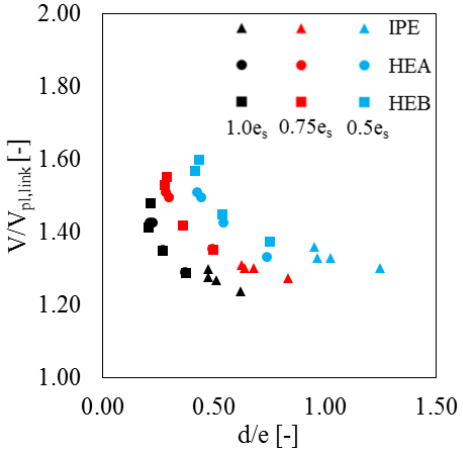

c) Deformable restraints (DR)

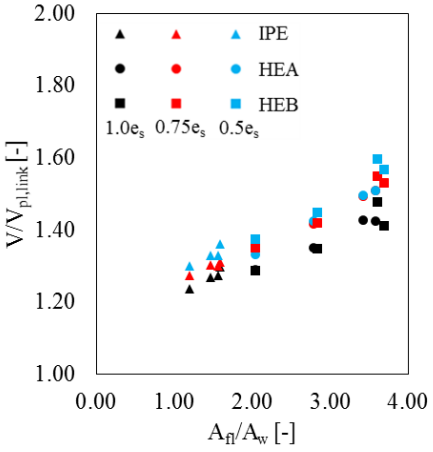

d) Deformable restraints (DR)

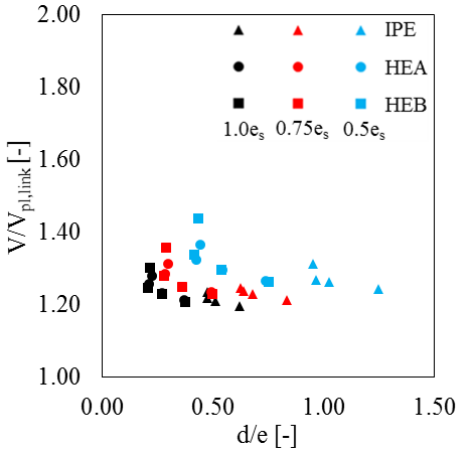

e) Fully restrained with axial release

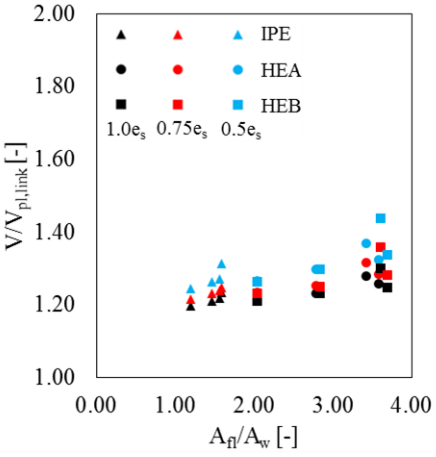

f) Fully restrained with axial release

Figure 38 Shear overstrength

The influence of the section depth is also shown in Figure 37 , where the difference between the ranges of profiles are highlighted. Indeed, at both section groups (wide and narrow flange), it can be observed that the trend is very similar, namely the small and more compact sections exhibit the higher overstrength. Conversely, the shear overstrength reduces appreciably with the depth increase.

Moreover, the boundary conditions of the profiles have a significant impact as well. In Figure 38 it can be noted that fully axial restrained links (Figure 38*a* and *b*) exhibit overstrength 10% higher with respect to the models with deformable restraints in which the flexural and axial stiffness of the frame and connection was considered (Figure 38*c* and *d*). For the links without axial restraints (Figure 38*e* and *f*), the shear overstrength is the lowest because no catenary action can be developed and, therefore, no second order shear and bending moment can occur.

For what concerns the length of the link, it can be observed that for the same profile, the shorter links ($0.50e_s$) have the highest shear overstrength and the values decrease with the length increase. This is because the shorter is the link, the larger are the nonlinear effects developing at the same rotation demand. Comparing the obtained values with the shear overstrength $V/V_{p,link}$ equal to 1.5 as recommended by EC8, it can be observed that this value can be significantly non-conservative.

Based on the results obtained from finite element analyses, polynomial regressions have been developed to estimate the shear overstrength as function of both link length and type of profile. Figure 39*a* shows the relationship between $V/V_{p,link}$ and link depth/length (d/e) ratio for each link length (e_s, $0.75e_s$ and $0.5e_s$). The regressions satisfactorily match the numerical data, with R^2 indexes close to 1. Regressions have been made also with respect to the flange area/web area (A_{fl}/A_w) ratio and even in this case very good dependency

can be observed (see Figure 39*b*). It is worth mentioning that the results for HE A and HE B overlap in both curves and that there is a clear difference between the trends of the IPE and HE sections.

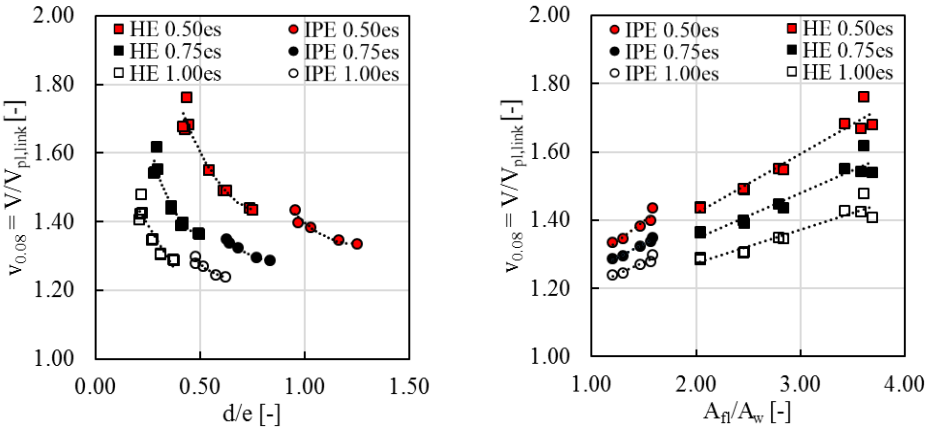

a) Link depth/length ratio b) Section flange/web area ratio

Figure 39 Dependency between the shear overstrength and geometrical parameters (FR)

The evaluation of the shear overstrength at 0.08*rad* link rotation for the fully restrained (FR) boundary conditions ($v_{0.08,FR}$) can be obtained using a linear regression function of the depth/length ratio *d/e* and of the flange/web area ratio A_{fl}/A_w. The equations are the following:

$$v_{0.08,FR} = p_1\left(\frac{d}{e}\right) + p_2\left(\frac{A_{fl}}{A_w}\right) + p_3 \tag{3.30}$$

Table 15 Polynomial regression coefficients

Profile type	Length	p_1	p_2	p_3	R^2
IPE	**0.50*e*s**	0.70	0.77	-0.47	0.94
	0.75*e*s	0.30	0.31	0.67	0.99
	1.0*e*s	0.63	0.37	0.41	0.97
HE	**0.50*e*s**	0.23	0.22	0.82	0.95
	0.75*e*s	0.68	0.22	0.58	0.93
	1.0*e*s	0.76	0.17	0.65	0.91

3.4.3 Axial force

The results in terms of axial force are presented as the values at 0.08*rad* link rotation, normalized with respect to the axial capacity of the flange $N_{pl,fl}$ evaluated as:

$$N_{pl,fl} = 2b \cdot t_{fl} \cdot f_{y,fl} \tag{3}$$

Where $\underline{b}$ is the width of the link flange, t_{fl} is the thickness of the link flange and $f_{y,fl}$ is the strength of the flange steel.

From the plots in Figure 40 it can be observed that the level of axial force developed in the link is mostly independent with respect to the type of profile, only small differences can be observed for HE B profiles. The same results can be noted varying the section depth, namely the normalized axial force is constant for all section depths. As a matter of fact, no correlation between the axial force and any geometrical parameters (e.g. d/e, A_{fl}/A_w) can be recognized.

The boundary conditions play a fundamental role in the level of axial force of the replaceable links. As possible to see in Figure 40, the fully restrained links show axial forces up to 50% larger than the links with deformable restraints. Another consequence of using DR is the loss of dependency between the axial force and the link length. This suggests that modelling the connection will lead to lower axial forces developing in the assembly.

Figure 41 presents the full curve for the axial force evolution with the link plastic rotation for the HE A links. It is trivial to observe that relaxing the axial stiffness of the restraints leads to the reduction of the axial force developed in the link. Indeed, although there is a clear difference between the different groups of link lengths at 8% rotation for the fully restrained links, this difference shades off for the models with deformable restraints.

The values of $n_{fl,T\,max}$ at 0.08*rad* link rotation are presented in Table 16.

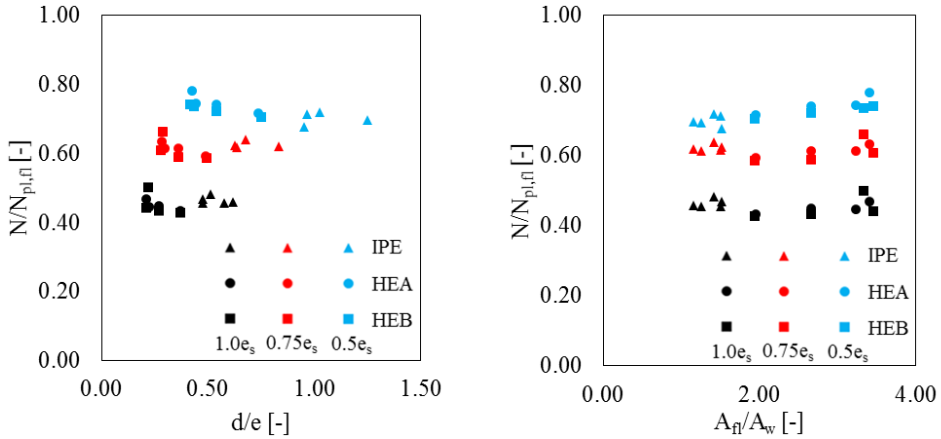

a) Fully restraints (FR)

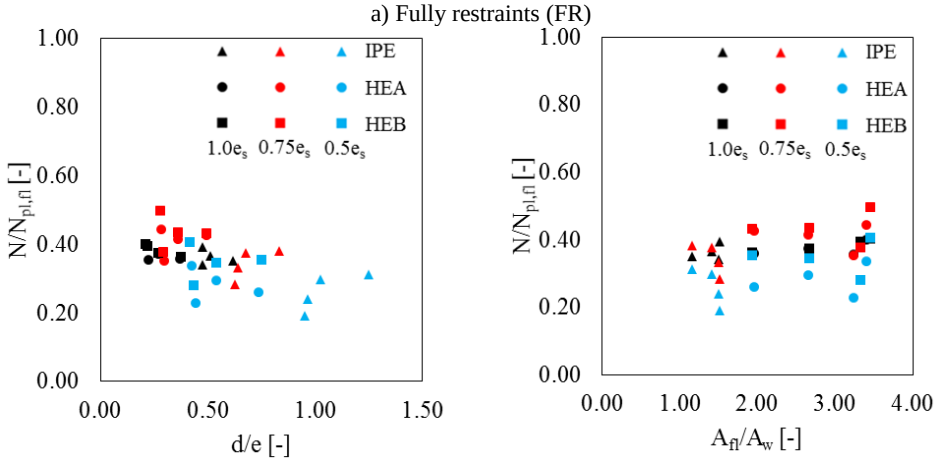

b) Deformable restraints (DR)

Figure 40 Axial force in the link

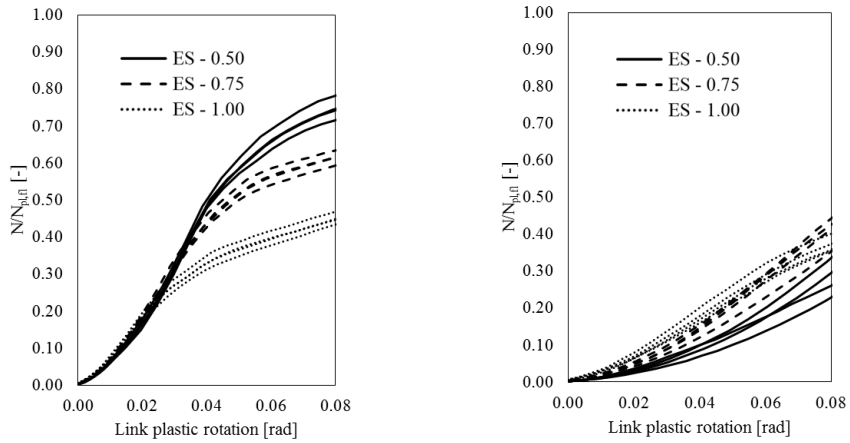

a) Fully restrained (FR)

b) Deformable restraints (DR)

Figure 41 Normalized axial force curves for HE A links

Table 16 Links normalized tensile forces at 0.08rad link rotation

FR	$N/N_{pl,fl}$		
Section/Length	**$0.50e_s$**	**$0.75e_s$**	**e_s**
IPE200	0.678	0.624	0.469
IPE300	0.712	0.618	0.456
IPE400	0.720	0.639	0.483
IPE500	0.693	0.613	0.455
IPE600	0.696	0.620	0.459
HE 200 A	0.745	0.614	0.446
HE 300 A	0.782	0.634	0.469
HE 400 A	0.742	0.615	0.449
HE 500 A	0.728	0.596	0.438
HE 600 A	0.716	0.593	0.434
HE 200 B	0.737	0.662	0.501
HE 300 B	0.741	0.609	0.442
HE 400 B	0.722	0.590	0.434
HE 500 B	0.702	0.587	0.424
HE 600 B	0.705	0.586	0.428

Given the lack of correlation between the level of axial force with other geometrical parameters, constant values can be assumed for varying link lengths. Table 17 presents the mean and standard deviation for the IPE and HE profiles separately, as well as the global values for all profiles. These values can be used as a design value for regular links in EBFs and as a starting point for the evaluation of the actual axial force in the link-connection assemblies

Table 17 Tensile force at 0.08rad link rotation for links only and FR boundary conditions ($n_{fl,T\,max}$)

Section	Value	**$0.5e_s$**	**$0.75e_s$**	**e_s**
		[-]	[-]	[-]
IPE	Mean:	0.70	0.62	0.46
	St. Dev:	0.017	0.010	0.012
HE	Mean:	0.73	0.61	0.45
	St. Dev:	0.023	0.024	0.023
All	Mean:	0.72	0.61	0.45
	St. Dev:	0.024	0.022	0.022

3.5 DESIGN AND VERIFICATION OF BOLTED CONNECTIONS FOR LINKS

The regular design according to EC3 1-8 is mostly concerned with static loading conditions. Although the link connection is a typical bolted connection it requires additional considerations, the main concerns being:

1. Regular design for M and V ignores the presence of axial force (which can be larger than 5% of the link tensile capacity, the limit below which it can be ignored according to EC3 1-8). However, significant axial forces can develop in short links under large deformation (Della Corte *et al.*, 2013)
2. The design shear force and bending moment are severely amplified for the local hierarchy, however the shear overstrength is assumed with a constant value which could be over or under-conservative (function of link length, type of section, connection etc.).
3. The design methods for connections need not further complicate the design process, but this should not go against the safety requirements.

Three methods are used to design and/or check the link connections. Each link connection is designed to satisfy Method 1 (design according to EN1993 1-8), and the obtained connections are checked for Methods 2 and 3.

3.5.1 Considered design and verification methods

3.5.1.1.1 Method 1 – Design for M and V, disregarding N

In terms of bending resistance, this method neglects the influence of axial force. For the evaluation of the shear resistance, the contribution of the bolts in tension are reduced to 28% while those in compression are considered with 100% of their shear capacity.

The joint is designed to satisfy the following condition, according to EC3 Part 1-8:

$$M_{j,Ed} = 1.1 \cdot \gamma_{ov} \cdot 1.5 \cdot V_{pl,link} \cdot \frac{e_{link}}{2} \leq M_{j,Rd} \qquad (3.31)$$

Where $M_{j,Ed}$ is the design bending moment of the connection and $M_{j,Rd}$ is the bending resistance of the connection according to EN1993 Part 1-8

The shear resistance is then checked to be above the demand

$$V_{j,Ed} = 1.1 \cdot \gamma_{ov} \cdot 1.5 \cdot V_{pl,link} \leq V_{j,Rd} = n_c F_{v,Rd} + \frac{0.4}{1.4} n_t F_{v,Rd} \qquad (3.32)$$

Where $V_{j,Ed}$ is the design shear force of the connection, $V_{j,Rd}$ is the connection shear capacity, n_c is the number of bolts in compression, n_t, is the number of bolts in tension and $F_{v,Rd}$ is the shear resistance of a single bolt.

The tensile force developed within the link is ignored and models designed for M+V will be created in order to observe the behavior of the connection under the *M - V - N* loading conditions.

3.5.1.1.2 Method 2 – Check for combined M – N and ulterior V check

The calculation of the resistance considers the combined influence of bending and axial force. For the shear resistance, all bolts are assumed to be in tension).

For this method, the *M-N* combined resistance is checked according to the EN 3 Part 1-8 for cases when the axial force in the connected beam N_{Ed} is larger than 5% of the design plastic resistance $N_{pl,Rd}$.

$$\frac{M_{j,Ed}}{M_{j,Rd}} + \frac{N_{j,Ed}}{N_{j,Rd}} \leq 1 \qquad (3.33)$$

Where $M_{j,Rd}$ is the design moment resistance of the joint, assuming no axial force and $N_{j,Rd}$ is the design tensile resistance of the joint, assuming no applied bending moment. $N_{j,Ed}$ in this case would be the tensile force in the link at 8% link rotation from analyses already performed, considering fully restrained BCs.

The shear capacity of the connection is then checked assuming that all bolts are in tension.

$$V_{j,Ed} = 1.1 \cdot \gamma_{ov} \cdot 1.5 \cdot V_{pl,link} \leq V_{j,Rd} = \frac{0.4}{1.4_t} \sum F_{v,Rd} \qquad (3.34)$$

3.5.1.1.3 Method 3 – Check using the M-N interaction curve

The third method of verification requires building the M-N interaction curve and checking the actual ($M_{j,Ed}$, $N_{j,Ed}$) position with respect to the capacity curve. The shear capacity is then checked assuming that all the bolts are in tension as shown for Method 2.

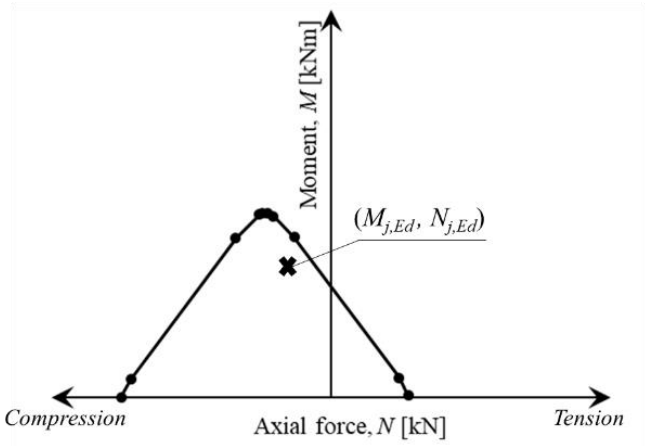

Figure 42 M-N Interaction curve for the link EEP connection

3.5.2 Verification of bolted link connections

3.5.2.1 Flush end-plate connections (FEP)

From the link profiles investigated in the parametric study on the link profiles, only the ones highlighted in Table 18 were selected and flush end-plate (FEP) and extended end-plate (EEP) connections were designed.

Table 18 Summary of designed and analyzed connections

Connection:		***Flush End-Plate connection (FEP)***			***Extended End-Plate connection (EEP)***		
Relative length		$0.50e_s$	$0.75e_s$	$1.00e_s$	$0.50e_s$	$0.75e_s$	$1.00e_s$
IPE	200	x	x	x	x	x	x
	300	x	x	x	x	x	x
	400	x	x	x	x	x	x
	500	x	x	x	x	x	x
	600	x	x	x	x	x	x
HE A	200	x					
	300	x					
	400	x					
	500	x					
	600	x					
HE B	200	x					
	300	x					
	400	x					
	500	x					
	600	x					

As previously mentioned, the first method was used for the design of the connections. The design of FEP connections proved to be difficult as the design forces were significant, especially for HE profiles. In effect, the FEP connections were designed only for the very short HE links ($0.50e_s$), and even in these cases, the connections for the HE B links do not meet the design requirements and are investigated as partial strength connections. Table 19 presents all the results for Method 1.

The verification of the connection according to Method 2 (considering the combined effect of M and N) using the values of axial force obtained in the previous chapter (Table 16), it is possible to observe that none of the connections satisfies the requirement (Table 20). This is trivial given that most of the connections are designed close to their flexural capacity limit and they

are all subjected to significant tensile forces. Considering this method and assuming that indeed the level of axial force is the one previously derived, Figure 43 shows that the connections are severely above the limit of 1, and therefore are very weak, contrary to the design method which ignores the tensile forces and gives a reasonable utilization factor.

Table 19. Design force to resistance ratio according to Method 1 (FEP)

Link	**e/e$_s$=1.0**		**e/e$_s$=0.75**		**e/e$_s$=0.5**	
	$\frac{M_{j,Ed}}{M_{jRd}}$	$\frac{V_{j,Ed}}{V_{jRd}}$	$\frac{Mj_{,Ed}}{M_{jRd}}$	$\frac{V_{j,Ed}}{V_{jRd}}$	$\frac{M_{j,Ed}}{M_{jRd}}$	$\frac{V_{j,Ed}}{V_{jRd}}$
IPE200	0.92	0.65	0.78	0.65	0.88	0.45
IPE300	0.95	0.85	0.92	0.32	0.96	0.46
IPE400	0.99	0.76	0.89	0.91	0.59	0.91
IPE500	0.95	0.80	0.75	0.80	0.67	0.81
IPE600	0.98	0.85	0.89	0.87	0.62	0.87
HEA200					0.97	0.59
HEA300					0.93	0.97
HEA400					0.97	0.78
HEA500					0.98	0.91
HEA600					0.97	0.74
HEB200					1.10	1.22
HEB300					0.99	1.28
HEB400					1.11	0.84
HEB500					1.09	0.96
HEB600					1.18	0.90

Table 20. Design force to resistance ratio according to Method 2 (FEP)

Link	**e/e$_s$=1.0**		**e/e$_s$=0.75**		**e/e$_s$=0.5**	
	$\frac{M_{j,Ed}}{M_{j,Rd}}+\frac{N_{j,Ed}}{N_{j,Rd}}$	$\frac{V_{j,Ed}}{V_{j,Rd}}$	$\frac{M_{j,Ed}}{M_{j,Rd}}+\frac{N_{j,Ed}}{N_{j,Rd}}$	$\frac{V_{j,Ed}}{V_{j,Rd}}$	$\frac{M_{j,Ed}}{M_{j,Rd}}+\frac{N_{j,Ed}}{N_{j,Rd}}$	$\frac{V_{j,Ed}}{V_{j,Rd}}$
IPE200	1.30	1.49	1.41	1.49	1.54	1.49
IPE300	1.22	1.06	1.36	1.06	1.74	1.54
IPE400	1.47	1.51	1.60	1.87	1.39	1.87
IPE500	1.41	1.60	1.41	1.60	1.42	2.25
IPE600	1.46	1.57	1.53	2.16	1.36	2.16
HEA200					2.22	1.40
HEA300					1.76	1.21
HEA400					2.22	1.76
HEA500					2.32	1.82
HEA600					2.10	2.07
HEB200					1.92	1.25
HEB300					2.13	1.33
HEB400					2.26	1.91
HEB500					2.21	1.94
HEB600					2.15	1.99

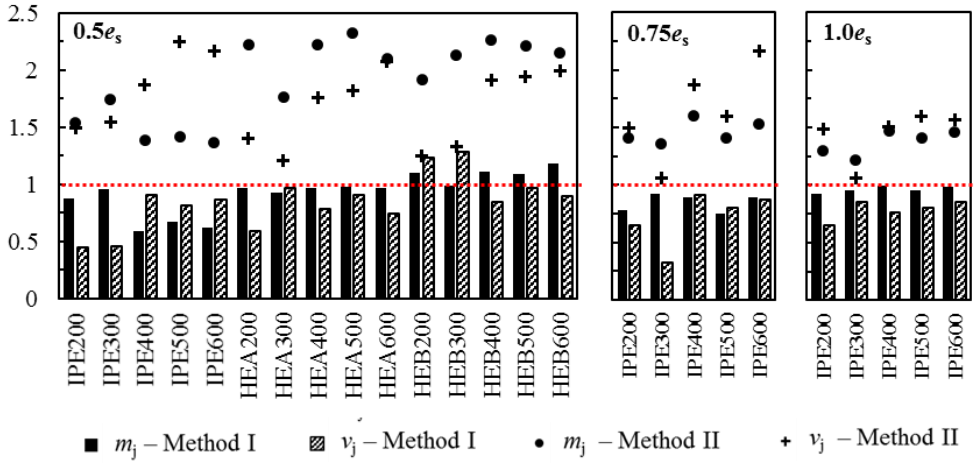

Figure 43. Design ratios for FEP assemblies

Given that it would be very difficult to design anew the connections (to consider also the presence of the axial force) a different approach was considered and the original design according to Method I was preserved. It is assumed that the response of the connections designed for bending moment and shear (method I) could be assessed by means of FEAs and based on the results obtained, the design procedure can be adjusted. Furthermore, the results obtained using Method II are very conservative and in order to better assess the resistance of the link connection under combined flexure and axial force, the third method is deemed more appropriate.

Method 3 implies the derivation of the *M-N* interaction curve for each link connection. The evaluation process is exemplified for IPE400 0.75e_s.(Figure 44 and Table 21). The curve is obtained by evaluating the ($M_{j,Rd}$, $N_{j,Rd}$) pairs considering a sequential shift of the neutral axis (NA) with respect to the axis of the components resistance (the bolt rows in tension and the beam flange and web in compression). Figure 45 details the *M-N* curve and the points obtained considering the variation of the position of the neutral axis (NA).

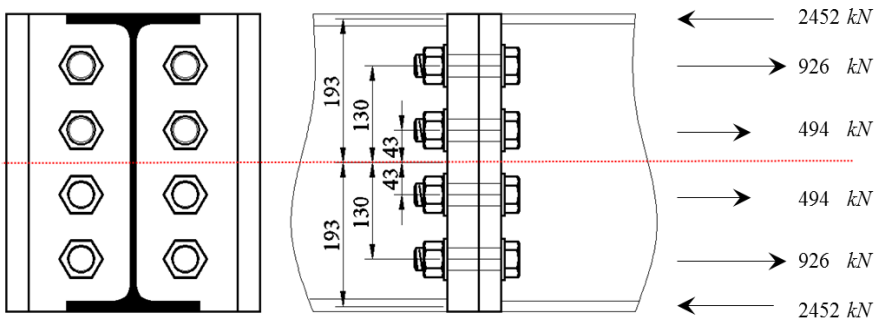

Figure 44 Distribution of forces in the bolt rowsfor FEP connection IPE400 0.75e_s

Table 21 Component information (force and lever arm) for the beam and link side for IPE400 0.75e_s

	F_{beam}	z_{beam}	F_{link}	z_{link}
	[kN]	*[mm]*	*[kN]*	*[mm]*
$F_{c,fb,Rd}$	2452	193	2452	193
$F_{T,1}$	985.6	130	925.6	130
$F_{T,2}$	494.3	43	494.3	43
$F_{T,3}$	344.2	43	309.2	43
$F_{T,4}$	925.6	130	925.6	130

The first point of the curve (a) represents the maximum negative axial force on the joint associated to zero bending moment, which occurs when the NA is at the top edge, therefore both beam flanges are in compression. At point (b), only the bottom flange is in compression so the axial force is given by the its compressive resistance while the corresponding bending moment is obtained by multiplying it with its lever arm. Point (c) is obtained when the NA is below the first bolt row (BR) which is now in tension so the axial force is given by imposing the translation equilibrium equation. The corresponding bending moment capacity is given by imposing the rotation equilibrium equation relative to the NA. The remaining points are obtained by considering the resistance of the succeeding bolt rows. For bolt rows in compression in which the resultant force is negative, the minimum positive resistance is used. The same process is done on the beam side and the results are plotted below.

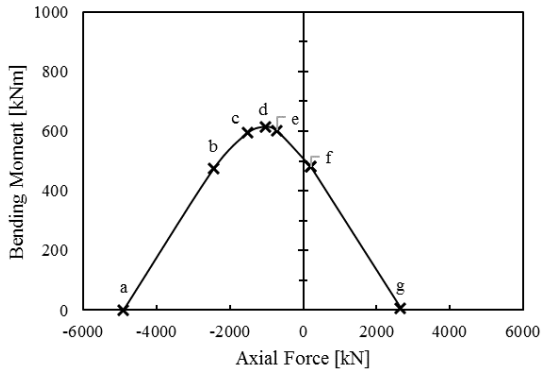

a – NA at the top edge (top and bottom flanges in compression)

b – NA between top flange and BR1 (bottom flange in compression)

c – NA between BR1 and BR2 (bottom flange in compression and BR1 in tension)

d – NA between BR2 and BR3 (bottom flange in compression, BR1 and BR2 in tension)

e – NA between BR3 and BR4 (bottom flange in compression, BR1, BR2 and BR3 in tension)

f – NA between bottom flange and BR4 (bottom flange in compression)

g –NA at top flange (all BR in tension)

Figure 45 M-N interaction curve for IPE400 0.75e_s

Table 22 M-N curve points for FEP connection IPE400 0.75e_s

Link	**a**	**b**	**c**	**d**	**e**	**f**	**g**
N (kN)	-4902.6	-2451.3	-1525.6	-1030.8	-721.6	204.4	2655
M (kNm)	0.00	473.7	594.1	615.3	601.7	480.4	0

Beam	**a**	**b**	**c**	**d**	**e**	**f**	**g**
N(kN)	-4902.6	-2451.3	-1465.72	-974.4	-629.8	356.2	2807
M (kNm)	0.00	454.7	582.9	604	588.8	459.6	0

In order to get the relative position of the design bending moment axial force pair ($M_{j,Ed}$, $N_{j,Ed}$) with respect to the *M* - *N* curve derived, the deviation is evaluated based on Figure 46. Two intersecting lines are considered: (1) the line where the design forces will intersect with the curve upon its projection from the origin (2) the line formed by the two relevant points in the *M* - *N* interaction curve. The intersection points of these two lines are calculated based on the equations of the line.

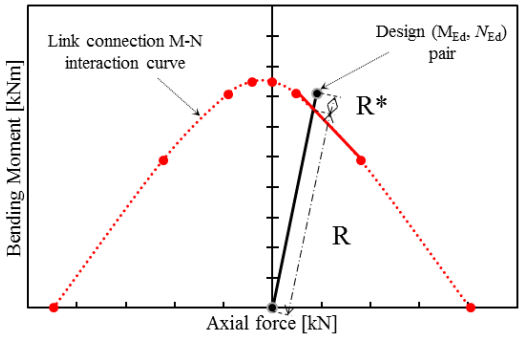

Figure 46 Deviation of design forces from the resistance curve

Table 23 Design ratios for FEP connections

e/e_s = 1.0					
Section		**FR**		**DR**	
	$M_{j,Ed}/M_{j,Rd}$	$N_{j,Ed}/N_{j,Rd}$	(R+R*)/R	$N_{j,Ed}/N_{j,Rd}$	(R+R*)/R
IPE200	0.92	0.38	**0.99**	0.32	**0.94**
IPE300	0.95	0.27	**0.80**	0.20	**0.77**
IPE400	0.99	0.47	**1.08**	0.35	**1.04**
IPE500	0.95	0.46	**1.08**	0.35	**1.04**
IPE600	0.98	0.47	**1.09**	0.36	**1.05**

e/e_s = 0.75					
Section		**FR**		**DR**	
	$M_{j,Ed}/M_{j,Rd}$	$N_{j,Ed}/N_{j,Rd}$	(R+R*)/R	$N_{j,Ed}/N_{j,Rd}$	(R+R*)/R
IPE200	0.78	0.63	**0.92**	0.2859	**0.80**
IPE300	0.83	0.45	**0.79**	0.2398	**0.70**
IPE400	0.89	0.71	**1.10**	0.4168	**0.95**
IPE500	0.75	0.66	**0.97**	0.4172	**0.87**
IPE600	0.90	0.63	**1.07**	0.3889	**0.93**

e/e_s = 0.5					
Section		**FR**		**DR**	
	$M_{j,Ed}/M_{j,Rd}$	$N_{j,Ed}/N_{j,Rd}$	(R+R*)/R	$N_{j,Ed}/N_{j,Rd}$	(R+R*)/R
IPE200	0.88	0.66	**0.76**	0.19	**0.56**
IPE300	0.96	0.78	**0.98**	0.27	**0.72**
IPE400	0.59	0.80	**0.90**	0.33	**0.67**
IPE500	0.67	0.75	**0.90**	0.34	**0.68**
IPE600	0.62	0.75	**0.91**	0.33	**0.68**
HEA200	0.97	1.25	**1.39**	0.39	**0.92**
HEA300	0.93	0.83	**1.64**	0.34	**1.14**
HEA400	0.97	1.25	**1.39**	0.50	**1.03**
HEA500	0.98	1.33	**1.51**	0.62	**1.13**
HEA600	0.97	1.13	**1.34**	0.41	**0.96**
HEB200	0.99	0.92	**1.80**	0.35	**1.17**
HEB300	0.92	1.21	**1.33**	0.58	**0.99**
HEB400	0.99	1.27	**1.45**	0.61	**1.10**
HEB500	0.98	1.23	**1.50**	0.61	**1.15**
HEB600	0.98	1.17	**1.48**	0.61	**1.21**

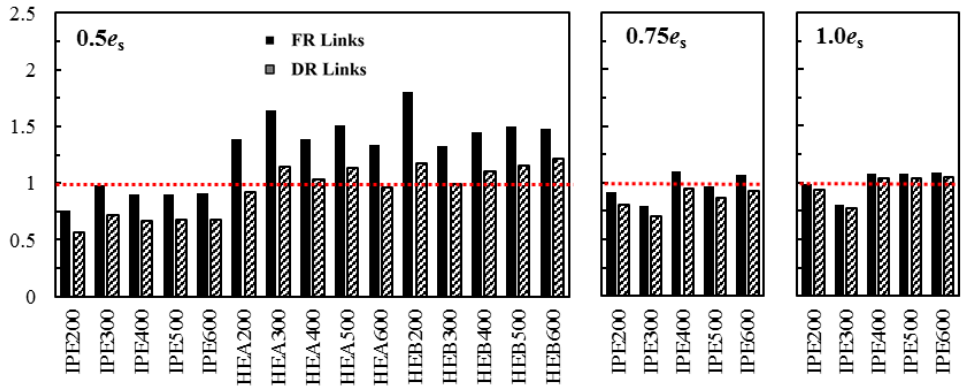

Figure 47 The deviation from the M-N interaction curve considering the axial force obtained using FR and DR boundary conditions

As presented in Table 23 and Figure 47, for longer links (e/e_s = 1.0), the deviation of the design forces when considering the N_{Ed} from the analyses on links considering fully-restrained (FR) boundary conditions are limited to 1.09 when the $M_{Ed}/M_{j,Rd}$ ratios are as close to 1.0 as possible. Higher axial forces develop in shorter links hence, links with e/e_s = 0.5 have the highest deviation, reaching 1.8 for $M_{Ed}/M_{j,Rd}$ of 0.99. Most of the IPE links with e/e_s = 0.5 have design forces within the *M - N* curve while HE A and HE B profiles have ratios significantly higher than 1.0. Comparing the results from the fully rigid (FR) boundary conditions analyses with the ones with deformable restraints (DR), there is a significant reduction in the axial force and consequently, in the deviation of the design forces from the *M-N* curve (Table 23 and Figure 47).

3.5.2.2 Extended end-plate connections

The design of extended end-plate connections proved to be simpler due to the more relaxed geometrical limitations. Or the current study only the IPE link-connections are presented. All assemblies are designed to satisfy Method 1 with the design ratios shown in Table 24. The assemblies are then checked according to Method 2 (results summarized in Table 25) and the results are comparatively presented for the first two methods in Figure 48.

Table 24. Design force to resistance ratio according to Method 1 (EEP)

Section	**e/e_s=1.0**		**e/e_s=0.75**		**e/e_s=0.5**	
	$\frac{M_{j,Ed}}{M_{j,Rd}}$	$\frac{V_{j,Ed}}{V_{j,Rd}}$	$\frac{M_{j,Ed}}{M_{j,Rd}}$	$\frac{V_{j,Ed}}{V_{j,Rd}}$	$\frac{M_{j,Ed}}{M_{j,Rd}}$	$\frac{V_{j,Ed}}{V_{j,Rd}}$
IPE200	0.82	0.56	0.91	0.81	0.82	0.56
IPE300	0.99	0.85	0.96	0.85	0.81	0.85
IPE400	0.87	0.85	0.89	0.85	0.59	0.85
IPE500	0.93	0.94	0.90	0.94	0.80	0.94
IPE600	0.93	0.88	0.69	0.88	0.47	0.88

Table 25. Design force to resistance ratio according to Method 2 (EEP)

Section	**e/e_s=1.0**		**e/e_s=0.75**		**e/e_s=0.5**	
	$\frac{M_{j,Ed}}{M_{j,Rd}}+\frac{N_{j,Ed}}{N_{j,Rd}}$	$\frac{V_{j,Ed}}{V_{j,Rd}}$	$\frac{M_{j,Ed}}{M_{j,Rd}}+\frac{N_{j,Ed}}{N_{j,Rd}}$	$\frac{V_{j,Ed}}{V_{j,Rd}}$	$\frac{M_{j,Ed}}{M_{j,Rd}}+\frac{N_{j,Ed}}{N_{j,Rd}}$	$\frac{V_{j,Ed}}{V_{j,Rd}}$
IPE200	1.21	1.17	1.71	1.69	2.07	1.17
IPE300	1.50	1.72	1.78	1.72	1.94	1.72
IPE400	1.24	1.52	1.53	1.52	1.32	1.52
IPE500	1.27	1.57	1.48	1.57	1.74	1.57
IPE600	1.44	1.88	1.38	1.88	1.29	1.88

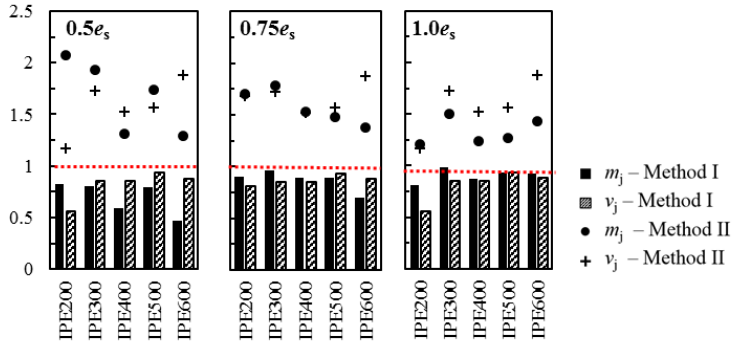

Figure 48. Design ratios for EEP assemblies according to Method 1 and Method 2

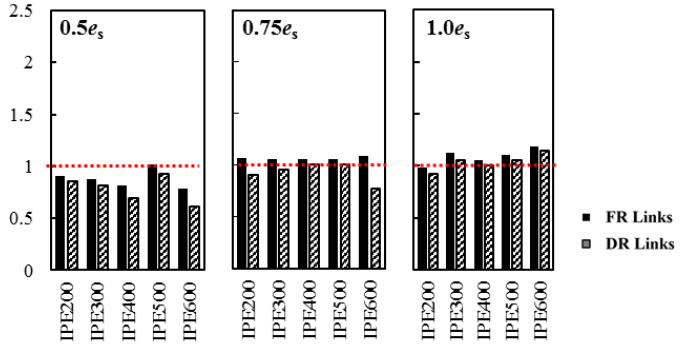

Figure 49. Deviation of design forces from M-N curves of EEP assemblies

Similar to the cases of flush end-plate connections, the EEP connections were designed close to the limit. Owing to this and the important tensile forces resulting from the FEAs on the links, the limits for Method II, in terms of shear and combined bending-axial force, are not satisfied (Figure 48). It is deemed however that the second method is highly conservative, and as proved by the analyses on links considering the links with deformable restraints, modelling the connection response, leads to significantly axial force reduction. It is expected that when the connection is modelled, a further reduction will occur due to the compressive arch, which cannot be observed in the models without the physical connection modelled.

With regards to the third method (*M* - *N* interaction curves), a less severe effect on the verification is obtained, compared to Method II. Figure 49 shows that the limit is reached only for the longer links (e/e_s = 1.0) and especially when the axial force is based on the very conservative case of fully restrained (FR) links.

The connection design according to Method I will be preserved, and the assessment of the connection will be performed using numerical models which were calibrated, as shown in the previous chapters.

3.6 ASSESSMENT OF THE BOLTED LINK CONNECTIONS RESPONSE

This chapter discusses the results of numerical analyses on the link-connection assemblies (Figure 50*c* and *d*). The link profiles are the same as those defined in the "*Parametric Study for the evaluation of the link connection design forces*" chapter (Figure 50*a* and *b*) and the connections designed according to the methodology presented in the chapter "*Design and verification of end-plate connections for links*" (Figure 50*e* and *f*).

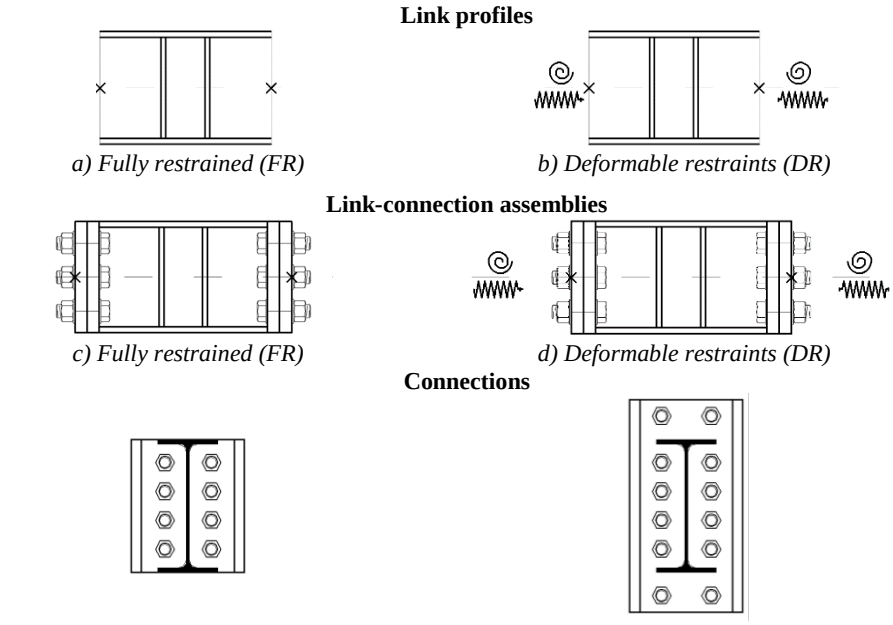

Figure 50 The boundary conditions (BC) for all analyzed models

Two types of connections modelled are:

- Flush end-plate (FEP - Figure 50*e*)
- Extended end-plate (EEP - Figure 50*f*)

All IPE profiles are modelled considering the two types of connections and the three lengths proposed, namely $0.5e_s$, $0.75e_s$, and $1.0e_s$ while HEA and HEB profiles are only modelled with flush-end plate connections, $0.5e_s$. In

addition, all models are analyzed with two boundary conditions: the first neglecting the deformation of the frame (Figure 50*c*) by imposing fully-rigid restraints at the face of the connection, hereafter referred to as fully-restrained or FR, and the second one considering the frame's deformability by imposing springs with axial and rotational stiffness i.e. deformable restraints or DR (Figure 50*d*).

Table 26. Models used for parametric analysis of seismic links

	Flush-end-plate			**Extended-end-plate**
Link length	**IPE**	**HE A**	**HE B**	**IPE**
$0.5e_s$	✓	✓	✓	✓
$0.75e_s$	✓			✓
e_s	✓			✓

The results are presented in contrast to the link profiles analyses considering FR boundary conditions, which represent the case of links in traditional EBFs where the link is continuous with the beam and the link profiles considering DR which represent a simplified modelling strategy for the actual link-connection assemblies representing the focus point of this chapter.

The curves hereby presented are in terms of normalized forces:

- Normalized shear force:

$$v = \frac{V}{V_{pl,link}} \tag{3.35}$$

$$V_{pl,link} = (d - t_{fl}) t_w \, f_y / \sqrt{3} \tag{3.36}$$

- Normalized axial force:

$$n_{fl} = \frac{N}{N_{fl,link}} \tag{3.37}$$

$$N_{fl,link} = 2bt_{fl} f_y \tag{3.38}$$

Where V and N are the shear and axial force in the link numerically obtained, $V_{pl,link}$ is the link plastic capacity according to EC8, d is the profile depth, t_{fl} is the thickness of the flange, t_w is the thickness of the web f_y is the material strength, $N_{fl,link}$ is the link axial capacity considering only the flanges and b is the flanges width.

The evaluation of the link rotation is based on the diagonal springs defined from one end of the link to the other (see L_1 and L_2 in Figure 51*a*). The following equations is used to determine the link rotation:

$$\gamma_{link} = \frac{\sqrt{d^2 + e^2}}{2de}\left(L_1 - L_2\right) \tag{3.39}$$

The connection rotation is evaluated as the gap-opening rotation (Figure 51*b*), based on the following equation:

$$\gamma_{connection} = \frac{u_{gap}}{z} \tag{3.40}$$

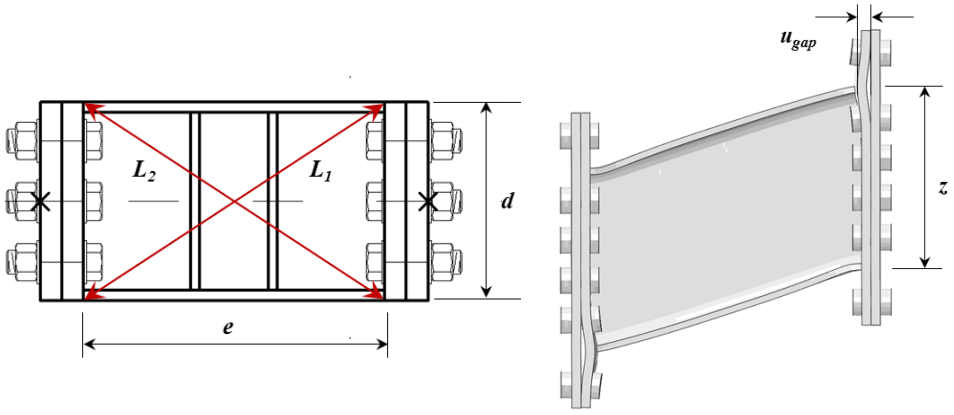

a) Link rotation b) Connection rotation

Figure 51 Rotation evaluation measurements

Other values of interest for the current chapter are the link-connection relative strength and stiffness ratios defined as:

$$m_j = \frac{M_{j,Ed}}{M_{j,Rd}} \tag{3.41}$$

$$v_j = \frac{V_{j,Ed}}{V_{j,Rd}} \tag{3.42}$$

$$k_{j,fl} = \frac{S_{j,ini}}{K_{fl,link}} = \frac{S_{j,ini}}{EI_{y,link}} \cdot e \tag{3.43}$$

$$k_{j,ax} = \frac{K_{j,ax}}{K_{ax,link}} = \frac{K_{j,ax}}{EA_{link}} \cdot e \tag{3.44}$$

Where $M_{j,Ed}$ is the joint design bending moment evaluated based on the link shear plastic capacity $V_{pl,link}$ (also defined in the chapter "*Design and Verification of Bolted connections for links*") , $M_{j,Rd}$ is the joint bending resistance, $V_{j,Ed}$ is the joint design shear force (defined as well in the previous chapter function of $V_{pl,link}$), $V_{j,Rd}$ is the joint shear resistance, $S_{j,ini}$ is the joint initial stiffness, $K_{fl,link}$ is the link flexural stiffness, $I_{y,link}$ is the link second moment of inertia, E is Young's modulus, e is the link length, $K_{j,ax}$ is the joint axial stiffness and $K_{ax,link}$ is the link axial stiffness, A is the section area.

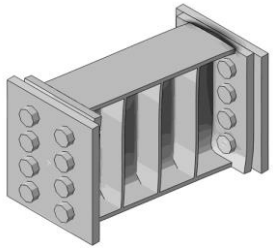

a) Flush-end-plate (FEP) connection link assembly

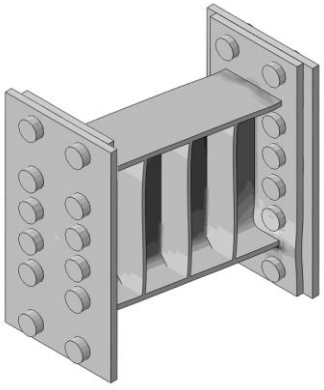

b) Extended end-plate (EEP) connection link assembly

Figure 52 Assembly typology

The chapter is subdivided into two main parts. First, the results of the numerical models with the flush end-plate connections (Figure 52*a*) will be presented, followed by the ones of the extended end-plate (Figure 52*b*). For a clearer discussion, the behavior of the link in terms of shear overstrength and the axial force developed is separated, but the two aspects and their interconnectivity will be treated in the final section.

3.6.1 The flush-end plate connections (FEP)

3.6.1.1 Shear overstrength

From the graphs in Figure 53, Figure 54 and Figure 55, it can be seen that different seismic links have very close response in the elastic region. All link assemblies reach their full plastic capacity and significant overstrength for large rotational levels (all web stiffeners are designed as prescribed by the Eurocode with a maximum tolerance of 6 mm). Figure 53 and Figure 54 show the results for the IPE link assemblies for all lengths and both boundary conditions.

The shear response of the link is independent from boundary conditions, at a first glance. Comparing the results for FR and DR for the same assembly, all links have similar responses, as exemplified in Figure 56.

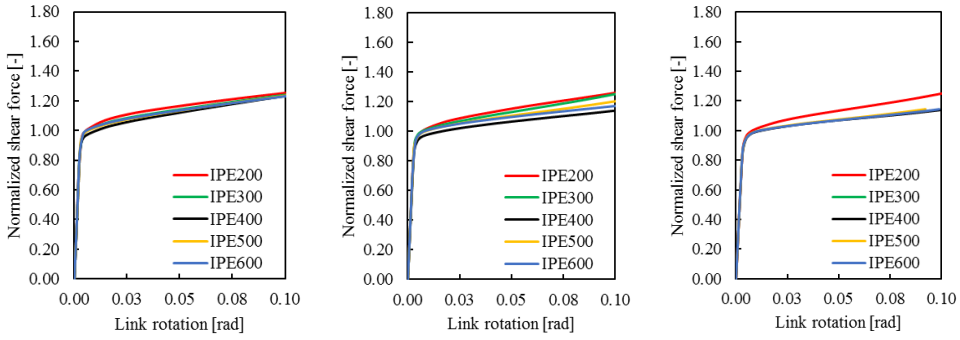

a) 0.5 e_s b) 0.75 e_s c) 1.0 e_s

Figure 53 Normalized shear force curves for IPE link assemblies with FR boundary conditions

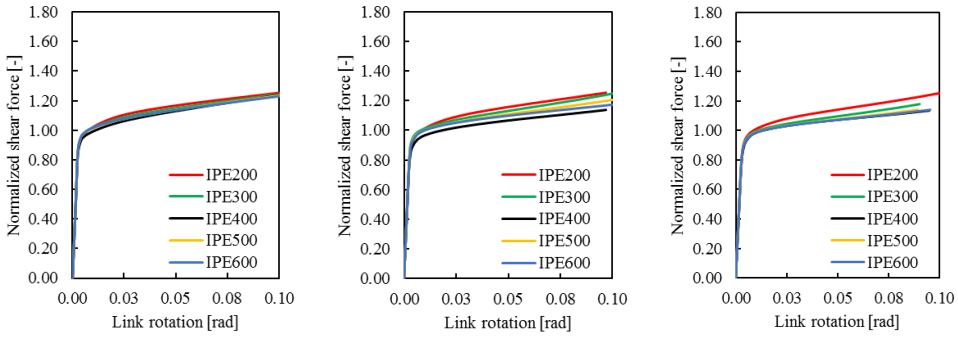

a) 0.5 e_s b) 0.75 e_s c)1 e_s

Figure 54 Normalized shear force curves for IPE link assemblies with DR boundary conditions

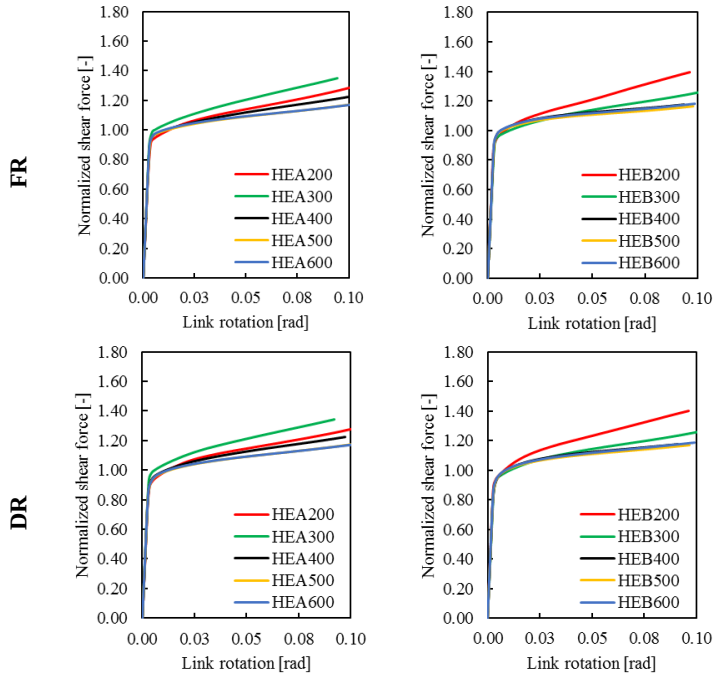

Figure 55 Normalized shear force curves for 0.5e_s HE A and HE B link assemblies

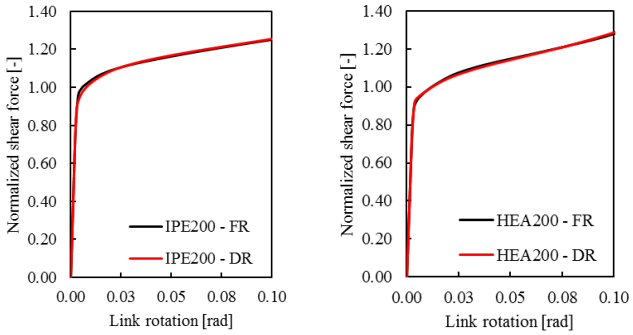

Figure 56. Shear response considering different boundary conditions

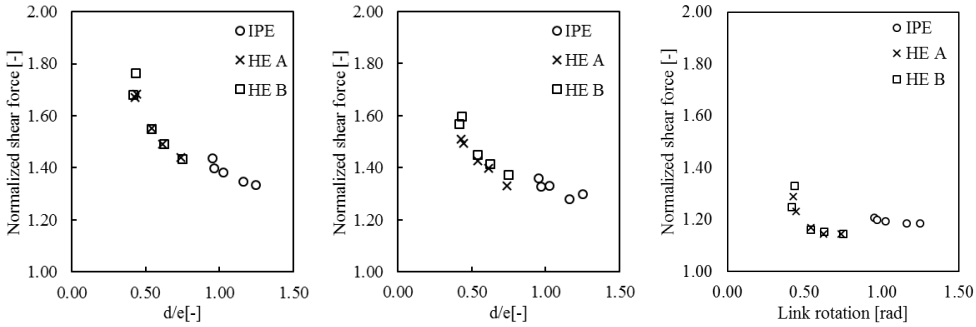

a) Link only (FR) b) Link only (DR) c) Link assembly (DR)

Figure 57 Shear overstrength at 8% link rotation vs. link depth/length ratio for the 0.5e_s links

In the case of the link-connection assemblies (Figure 50*c* and *d*) it is difficult to distinguish a clear correlation between the shear overstrength and the *d*/*e* ratio. Comparing the values obtained previously for the link profile investigation (Figure 57*a* and *b*) with the values obtained considering the link assemblies (Figure 57*c*), lower values can be observed and the previous trend is lost.

From the characteristics of the model, it is believed that the connection strength and stiffness might play a role in the link response.

In order to investigate this aspect, a set of analyses was performed by varying the ratio between the connection design bending moment ($M_{j,Ed}$) which is a function of the link strength, and the connection flexural resistance ($M_{j,Rd}$). As the design of connection results complex, the variation in relative strength was obtained by scaling the link material. The ratio (identified as m_j was defined with values ranging from 0.1 to 2 with a step of 0.1 up to 1.4, and 0.2 beyond 1.4. The values larger than 1.0 were used to observe the behavior of the assembly in case of a partial strength joint.

Figure 58 and Figure 59 show the normalized shear – link rotation curves (*a*) and the value of the shear overstrength at 0.08*rad* (*b*) for the analyses considering the specified m_j values for the 400*mm* IPE and HE assemblies,

respectively. All the analyses were performed considering fully-restrained (FR) boundary conditions for the assemblies (see Figure 50*c*).

In the left side (*a*) the curves depict evident variation of the shear at the variation of the link/connection strength ratio. The lower m_j, the higher the stiffness and the shear overstrength achieved at higher rotational levels.

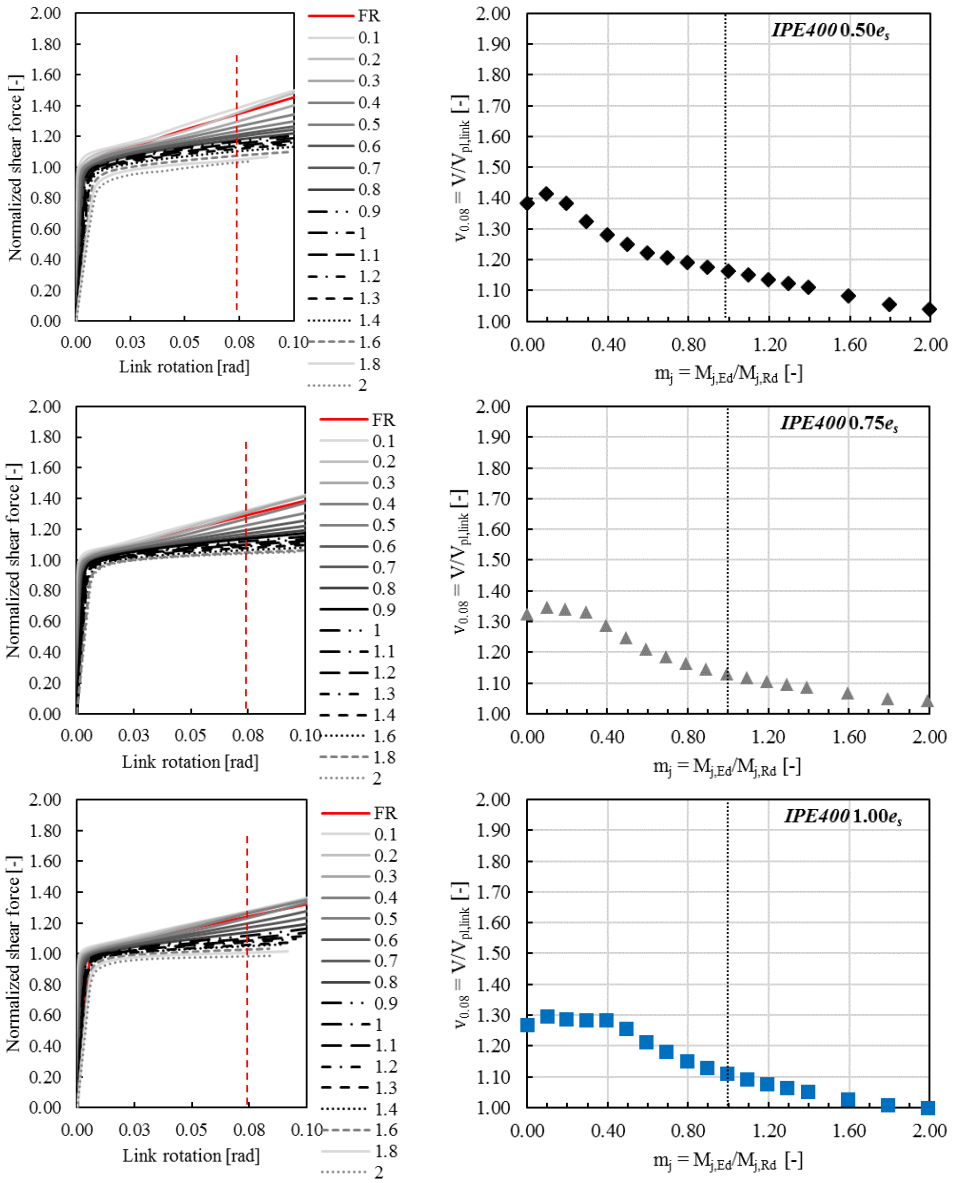

Figure 58. Shear response for 400 mm, IPE assemblies considering the variation of m_j

Considering only the shear overstrength of interest in design (at 0.08*rad* link rotation) the graphs in the right side of Figure 58 and Figure 59 (*b*) show an evident decrease of the overstrength the closer the connection resistance gets to the limit design value (m_j = 1.0). The difference between the shear overstrength for m_j = 0.10 and m_j = 1.0 ranges from 13% to 18% function of the type of section and the link length ratio (in less of a measure). The very small ratios (m_j = 0.1 … 0.3) give results which are very close to the FR case which represents the case of the fully restrained link profile (Figure 50*a*). For values larger than 1.0, the reduction in shear overstrength is more pronounced, reaching at limit values of 1.0 (no shear overstrength).

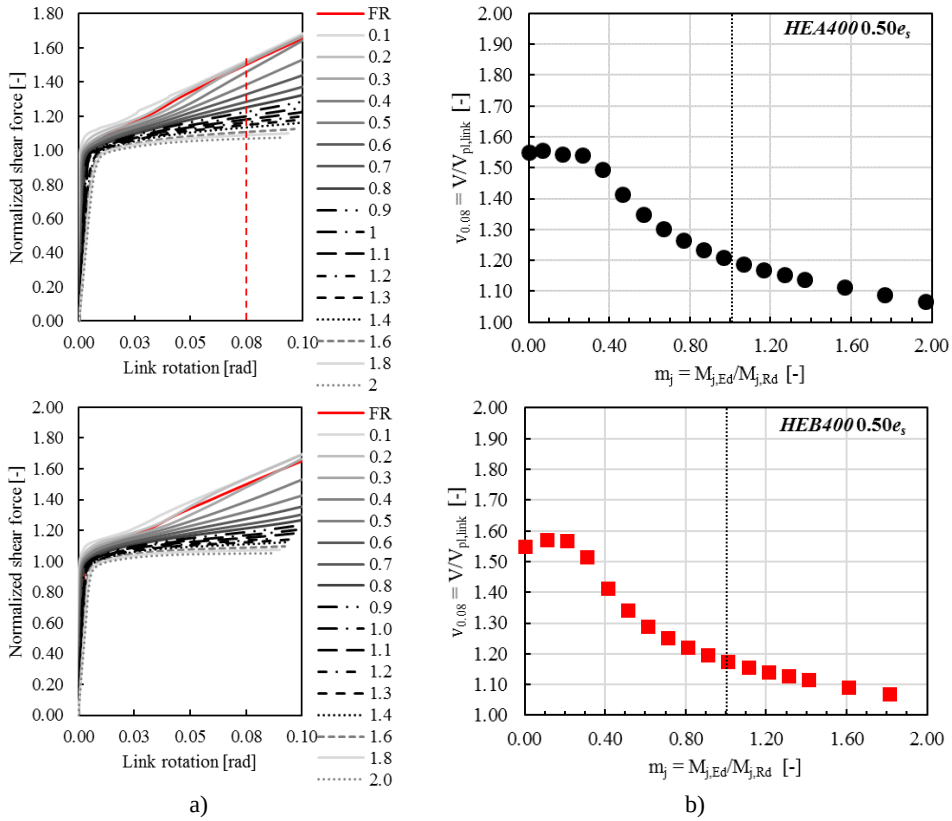

Figure 59. Shear response 400 mm HE assemblies considering the variation of m_j

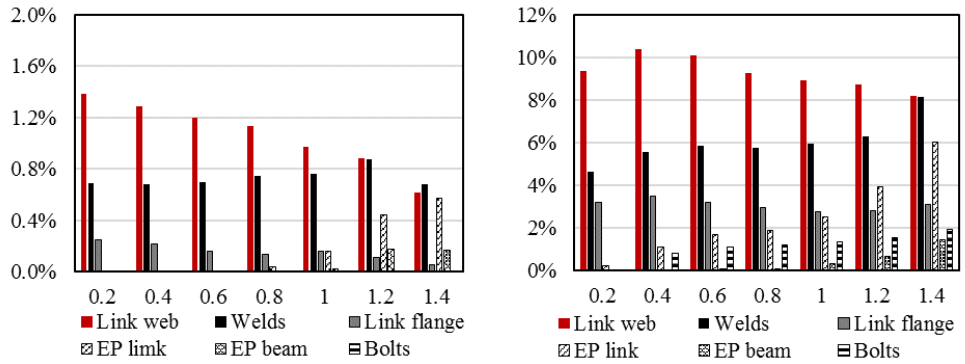

a) 0.01*rad* link rotation b) 0.08*rad* link rotation

Figure 60 PEEQ in the link assembly IPE400 0.75e_s FR

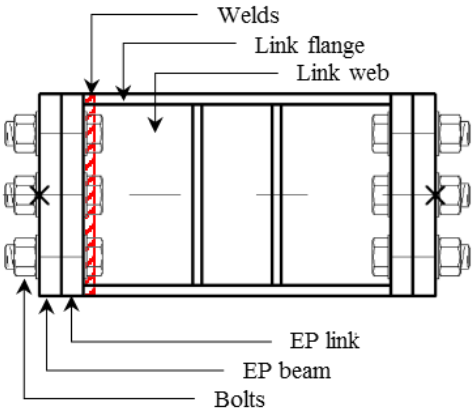

Figure 61 Areas selected for the level of PEEQ

The reduction in connection strength leads to a reduced stiffness due to early onset of plastic damage. Figure 60 shows the equivalent plastic strain (PEEQ) in the assembly components defined in Figure 61. In particular, by "Welds" it is intended the link-to-end-plate welds and the heat affected area around them. In Figure 60 *a* is evident that even at small rotational levels (0.01*rad* link rotation) the level of cumulative plastic damage (PEEQ) in the connection components is ever increasing for larger m_j values. The plastic involvement of the connection at link rotations corresponding to the achievement of $V_{pl,link}$, explains the reduction of the assembly stiffness.

Another trend, observed also for larger rotation levels (Figure 60 *b*), is the decrease in the link web PEEQ while larger values are observed for the welds,

end plate on the link side (EP link) and beam side (EP beam) and bolts. Therefore, the larger plastic contribution of the connection leads to a limitation in the capacity of the link to develop the maximum shear overstrength. The connection rotation increases at a faster rate for m_j ratios larger than 1.0 for IPE profiles, especially for the longer ones (Figure 62 *a*). The short link assemblies exhibit very similar trends regardless of the section type (Figure 62*b*).

Overlapping the curves for the same IPE400 profile considering the various lengths (Figure 62 *c*) it can be observed that the decrease is quite proportional and more interesting, the similarity of values is correlated to the similarity of connection rotation. A clear distinction between the IPE and HE assemblies is highlighted in Figure 62 *d*, the HE A and HE B models having very similar responses.

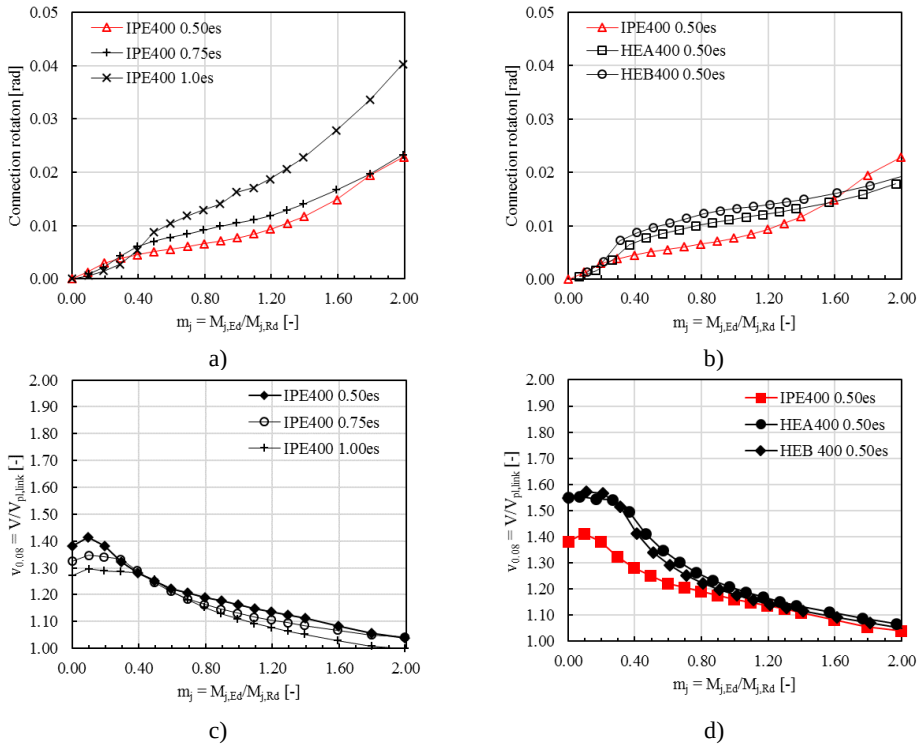

Figure 62 Connection rotation contribution at 0.08rad link rotation

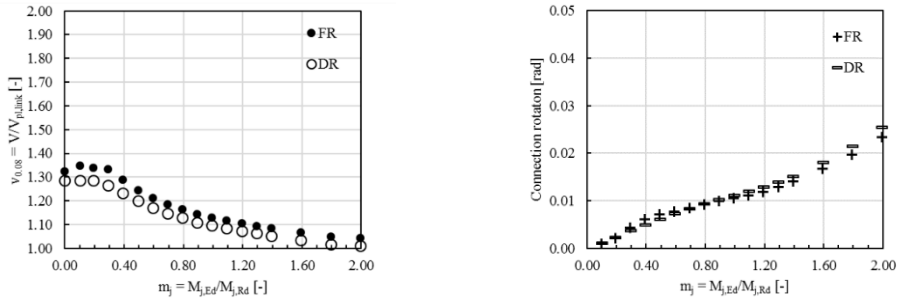

a) Variation of shear overstrength b) Variation of connection rotation

Figure 63 Influence of FR and DR boundary conditions for IPE400 0.75e_s

Using only one model (IPE400 0.75e_s), the previous analyses were repeated considering the DR boundary conditions (see Figure 50*d*). This was done so due to the timely and computationally demanding process required to perform the analyses and extract the desired results. Figure 63*a* shows that the differences are insignificant for all the analyses performed in terms of shear overstrength.

Based on these observations it can be concluded that the shear overstrength not only depends on the link length and type of profile, as shown in the previous investigation on the link only, but also on the relative connection/link strength. Using the information from the performed analyses, both on link profiles and link assemblies, equations can be proposed for the accurate definition of the shear overstrength.

3.6.1.2 Axial force

In the previous investigation (on the link profile only - Figure 50*a*) the axial forces were always positive i.e. tensile forces, as the physical connections were missing. The models in which the connection and frame deformability were modelled by means of axial and flexural springs (DR - Figure 50*b*) were characterized by a reduced magnitude of the tensile forces.

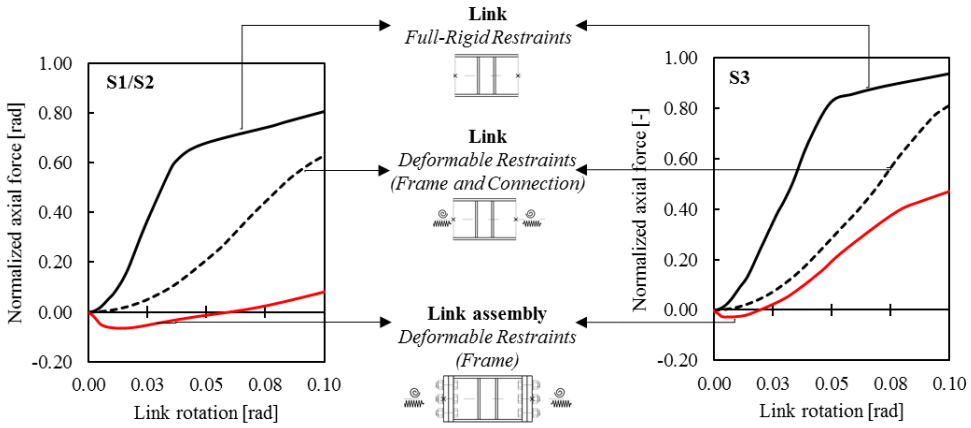

Figure 64 Variation of axial force in the link with the boundary conditions

However, based on the numerical results of the three links used for the FE model calibration, it was expected that modelling the connection would lead to the occurrence of the so-called compressive arch in the link and a consequential reduction of the tensile axial force at 0.08*rad* link reduction. The compressive arch refers to the compressive stresses developing in the axially restrained link assembly at low levels of rotation when displacement is applied at both ends in order to induce a uniform shear force.

Figure 64 shows the clear distinction between the three cases, namely the large tensile forces developed when assuming fully-restrained boundary conditions, the reduction in tensile forces when modelling the connection by means of nonlinear springs and the occurrence of compressive arch only when the connection is modelled.

The level of axial force, normalized with respect to the axial capacity of the link considering only the area of the flanges, up to 10% of link rotation is plotted in Figure 65 to Figure 67 for all the FEP assemblies investigated. It can be observed that the compressive arch is larger than presumed and that the tensile forces develop only at levels of rotation greater than 10%.

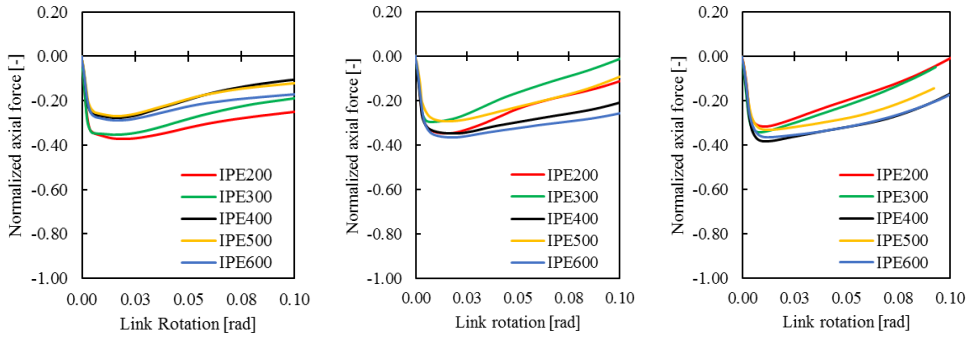

a) 0.5 e_s b) 0.75 e_s c) 1.0 e_s

Figure 65 Normalized axial force curves for IPE link assemblies with FR boundary conditions

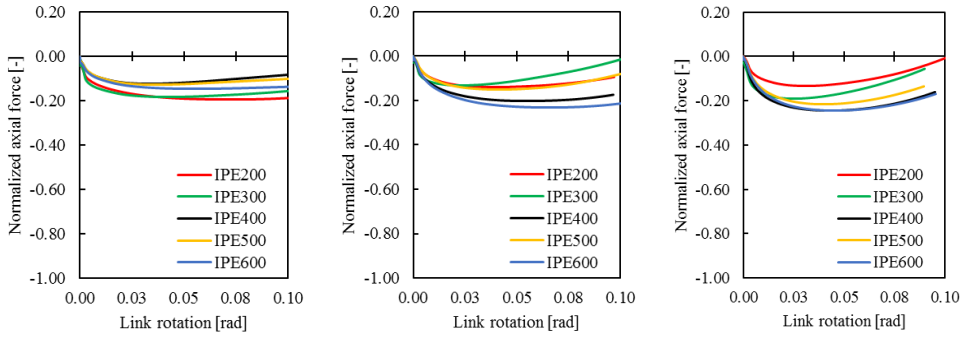

a) 0.5 e_s b) 0.75 e_s c)1.0 e_s

Figure 66 Normalized axial force curves for IPE link assemblies with DR boundary conditions

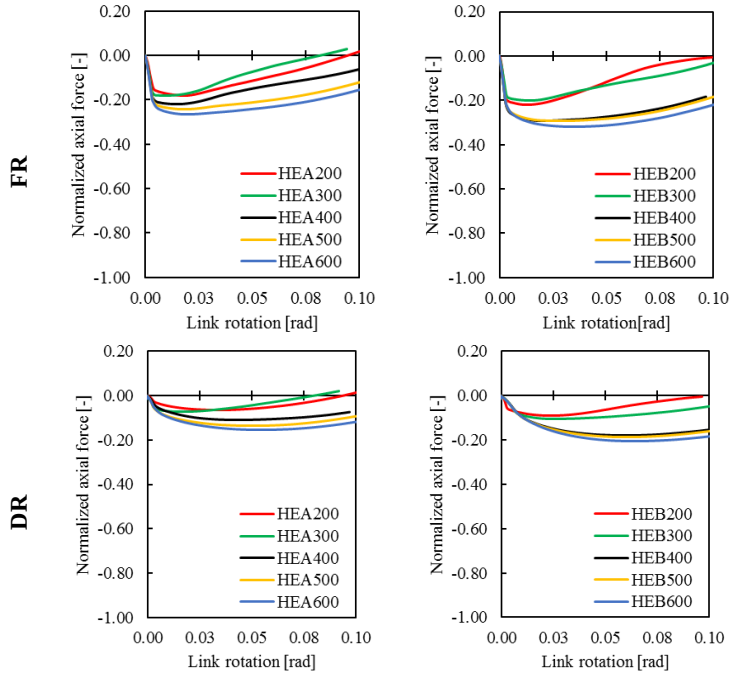

Figure 67 Normalized axial force curves for 0.5e_s HE A and HE B link assemblies

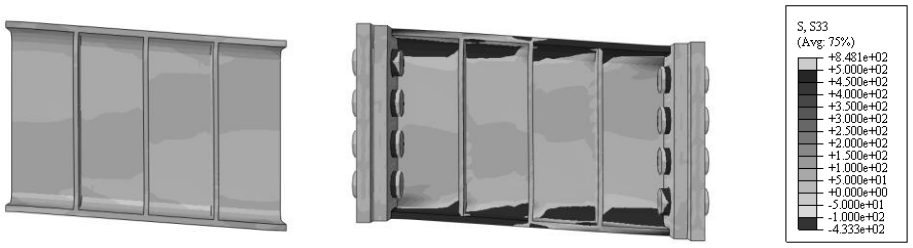

a) Just link (DR) b) Link-Connection assembly

Figure 68 The normal stress for IPE400 0.75e$_s$

In effect, when looking at the normal stresses in the link of the two types of models (the link and the link-connection assembly) presented in Figure 68 for a sample case, it is evident that at the same rotational level, the first is undergoing tensile forces while the latter compression. Therefore, while the models with only the link profiles have ever increasing tensile forces and the tension force at 0.08*rad* can be assumed as the maximum axial force ($N_{max} = N_{0.08}$), in the case of the link-connection models, N_{max} corresponds to the maximum compressive force developing at lower rotations.

In Figure 64 it can be clearly noted for the links of the South frame (S1, S2 and S3) that the analysis of only links with fully restrained (FR) boundary conditions leads to severe over-estimation of the tensile forces. This case is representative for the link in a traditional EBF, which is continuous with the beam and therefore can be assumed to have fixed ends. Modelling the flexural and axial stiffness of the connection and frame, imposing thus deformable restraints (DR), reduces the obtained values and when compared to the complete link-connection assembly model, it offers a closer approximation. Nevertheless, the DR link profile model cannot capture the initial compressive arch and leads to significant force over-estimation in most cases.

The link-connection assembly model combined with restraints modelling the frame deformability (the model which calibrates well the cyclic response

of the experimental results Figure 50*d*), gives the best approximation of the axial force, including the compressive arch and a realistic level of tensile forces at 8% link rotation. However, as it can be observed in Figure 65 and Figure 66 for all IPE link lengths and in Figure 67 for the $0.50e_s$ HE compact links, modelling the deformable support conditions reduces the compressive arch in terms of maximum compressive force, but not in terms of the extent (the tensile forces appear after more or less the same rotation level).

Looking on the S1, S2 and S3 calibrated models with FR and DR (ignoring or accounting the frame deformability, respectively) in Figure 69, the same is observed – reduction of the maximum forces with the introduction of the deformable BC, but no change in the rotation level at which the link goes in tension.

A clear discrepancy between the values of the tensile force at 0.08*rad* link rotation is observed for the two link assemblies. Looking at the geometrical and mechanical characteristics of the two assemblies, it was observed that the main difference between the S1/S2 and S3 links was the connection design ratios. Namely, the connection was identical for the 3 storeys but the link on the third storey had a smaller section.

As it was shown in the chapter dedicated to the calibration of the numerical model, the section of the links on the first two floors (S1 and S2) were wide flange sections close to a HEA 240 profile and the link on the last floor was a slenderer section, close to an IPE240 profile. This difference leads to different levels of connection overstrength, and as depicted in Table 27, the connection for the S3 link has a larger strength margin and is more rigid with respect to the link, which allows for the development of tensile forces in the link at lower rotation levels.

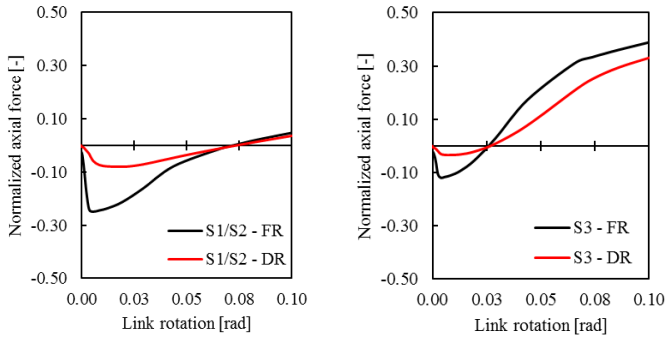

a) Link assemblies S1/S2 b) Link assemblies S3

Figure 69 Normalized axial force curves for 0.5e_s links comparison of FR vs DR boundary conditions

Table 27 Design forces and resistance in the links of the tested frame (Ioan et al 2016)

	e/e_s	$V_{Ed,j}$	$M_{Ed,j}$	$V_{Rd,j}$	$M_{Rd,j}$	$S_{j,ini}$	$K_{fl,\ link}$	v_j	m_j	$k_{j,fl}$
	[-]	*[kN]*	*[kNm]*	*[kN]*	*[kNm]*	*[kNm/rad]*	*[kNm/rad]*	*[-]*	*[-]*	*[-]*
S1/S2	0.43	625	125	931	166.8	15022	92512	0.67	0.75	0.16
S3	0.31	313	63	931	166.8	14643	58702	0.34	0.38	0.25

It can be summarized that the level of axial force at 0.08*rad* link rotation, as well as the trend of the axial force – link rotation curve is directly correlated with the following parameters:

- Boundary conditions (full-rigid vs. deformable restraints)
- Link profile geometry (wide/narrow flange section, d/e ratio)
- Connection/Link strength and stiffness ratio (flexural/ shear/ axial)

The following sections are dedicated to the investigation of these parameters on the axial force development in the link-connection assembly.

3.6.1.2.1 Influence of the boundary conditions on the axial force

Considering the same assembly, the difference in boundary conditions only causes a change in the area of the compressive arch due to the increase in maximum compression, the link rotation at which tension is reached remaining the same. Figure 70 depicts an example for the 0.5e_s 200*mm* deep profiles.

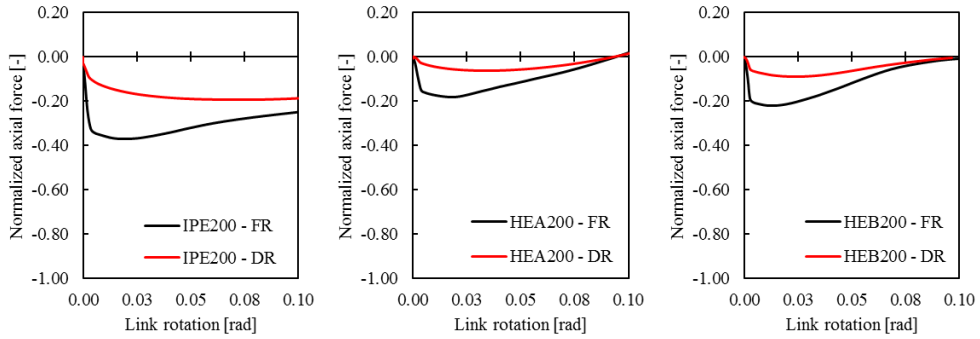

Figure 70 Normalized axial force curves for 0.5e_s links comparison of FR vs DR boundary conditions

There is an average decrease of 47% in maximum compressive force (Figure 71) when the same model is analyzed using FR and DR. This decrease is more significant for shallow links, and it decreases with depth and the same is true also for the link length i.e. shorter links exhibit a larger decrease in compression force when the DR are applied (see Figure 72).

Considering the deformability of the frame to which the link is connected greatly influences the compressive arch, and therefore, the axial demand on link connections and the adjoining beam. However, assuming FR boundary conditions leads to a conservative evaluation of the design forces, which is beneficial especially for the beam side components (beam web and flange in compression). Moreover, a larger compression force in the joint is not as detrimental for the bending resistance compared with tensile forces.

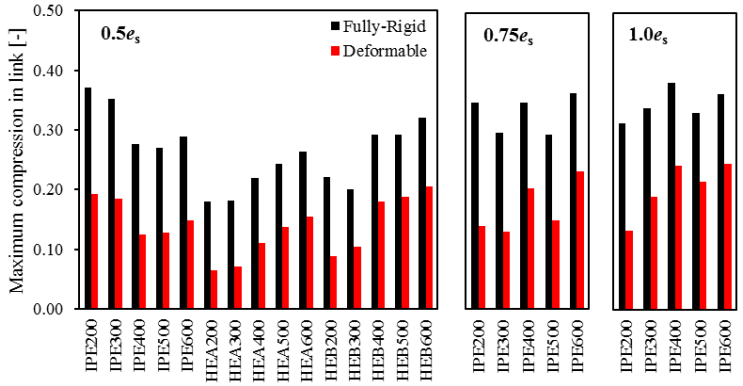

Figure 71 Maximum compression force for the investigated link assemblies

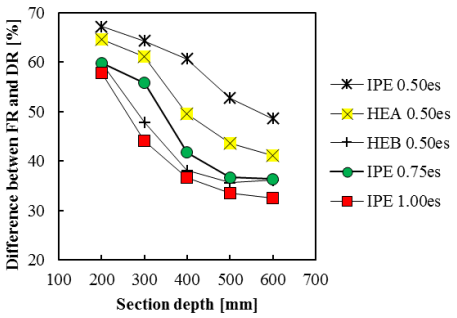

Figure 72 Difference between the maximum compression force for models with FR and DR

Referring to Method 3 of link verification, the M-N curves generated are not perfectly symmetrical along the moment axis (y-axis) but are slightly translated to the left. This means that for the same magnitude of axial force the corresponding bending resistance under the presence of a tensile force is significantly lower than the bending resistance for a compressive force. Caution must be used as the difference between the case with FR and DR leads to a scaling of the entire curve, so tensile forces the same as compressive forces will be larger when assuming fully rigid BCs.

3.6.1.2.2 Influence of the profile geometry on the axial force

The section compactness seems to have no influence on the axial force developed in the link assemblies. In the previous chapter it was shown that the axial force for the link profiles was identical for same depth IPE and HE profiles, as it can be seen also in Figure 73*a* and *b.*

The shallower (200 and 300*mm*) IPE link-connection assemblies exhibit larger axial forces compared to the wider HEA counterparts (FR assemblies in Figure 73*c* and DR assemblies in Figure 73*d*). However, because the change from the models of the link profiles to the link assemblies is the connection, it can be assumed that this difference is related to the different relative connection strength and stiffness, aspect which will be discussed more in depth in the subsequent section.

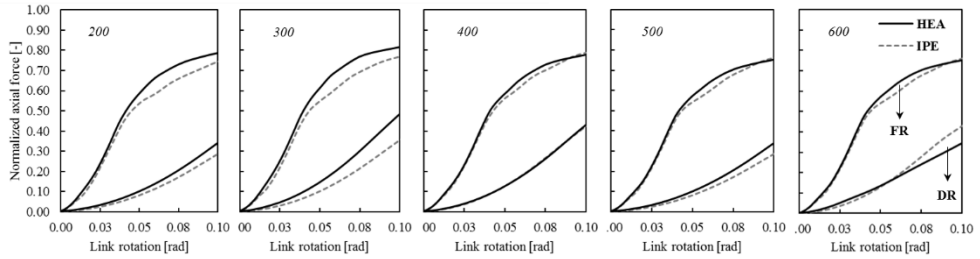

a) Link profiles fully restrained (FR) and b) considering deformable restraints (DR)

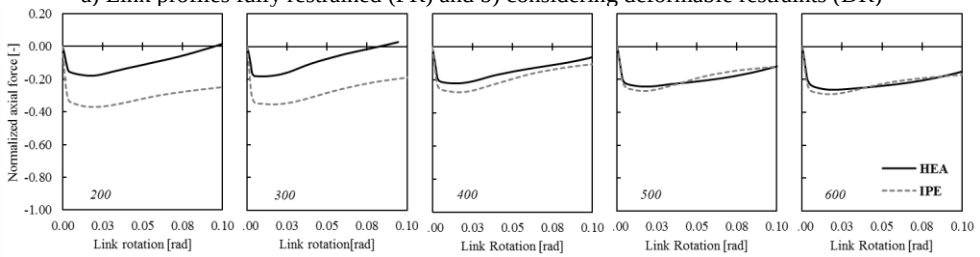

c) Link assemblies fully restrained (FR)

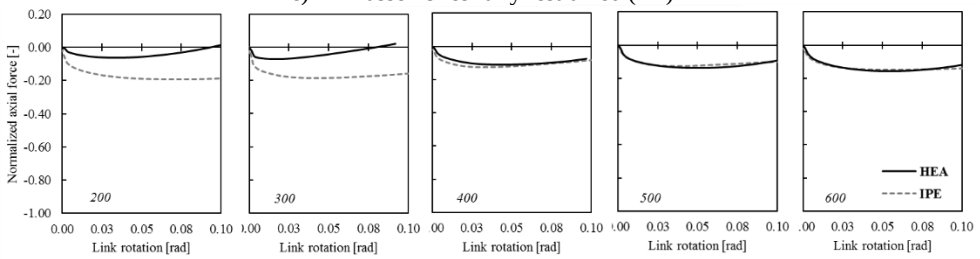

d) Link assemblies considering deformable restraints (DR)

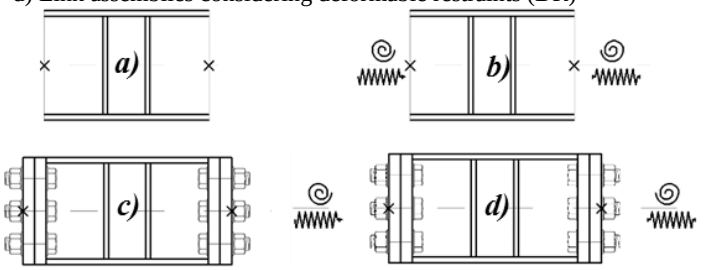

Figure 73 Influence of section compactness

Figure 74 shows the difference in terms of m_j ratios and $k_{j,fl}$ (parameters defined at the beginning of the chapter) for the two types of sections (IPE and HEA) of link-connection assemblies. Indeed, while for the HEA assemblies m_j is close to 1 for all profile depths, for the IPE, the ratio is significantly lower for the 400, 500 and 600 *mm.* The $k_{j,fl}$ is different for the 200 and 300 *mm* profiles due to significant difference of the joints' $S_{j,ini}$ (the link stiffness is similar – the HEA tend to have larger e while the IPE larger I_y, effects

compensating each other). These two connection-link related parameters have already been shown to influence the magnitude of the compressive arch and they will further be discussed.

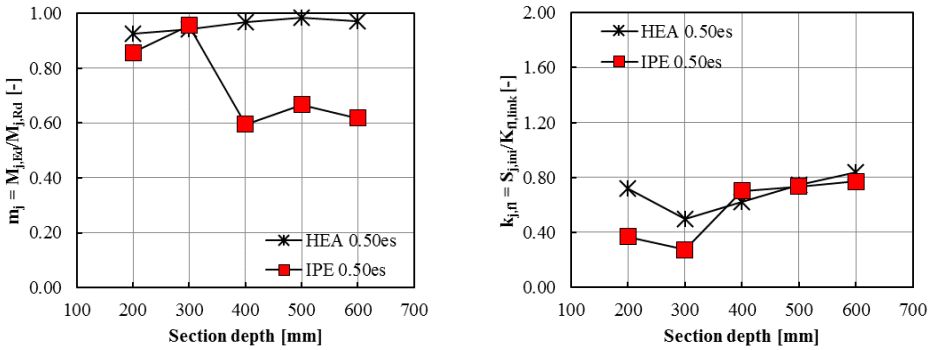

a) *Resistance* b) Stiffness

Figure 74 Connection/Link ratios for IPE and HEA 0.50e_s assemblies

The link length seemed to play a very significant role in the magnitude of the axial force in the link profiles for the FR boundary conditions (Figure 75 *a*) but less for DR boundary conditions (Figure 75 *b*). However, the link assemblies do not preserve the order (Figure 75 *c* and *d*), and as observed in the comparison between IPE and HEA, the shallow profiles (200 and 300 *mm*) exhibit different axial force distribution (larger compression for the shorter 0.50e_s link assemblies).

When comparing the connection strength, expressed as m_j in Figure 76*a*, for the same-depth IPE links for the 3 considered lengths, the trend is identical to the one in Figure 74*a*. The sets of longer IPE links, namely 0.75e_s and 1.0e_s have similar values of m_j while, as already shown, the 0.50e_s set has varying values (closer to 0.9 for shallow sections and approximately 0.6 for the other). Figure 76*b* shows that the shorter set has the least rigid connections, especially for the shallow links. However, as the difference between the $k_{j,fl}$ for varying link lengths, remains practically constant, it is assumed that it's the larger connection resistance which leads to the reduction in compressive arch for the IPE400, 500 and 600 0.50e_s.

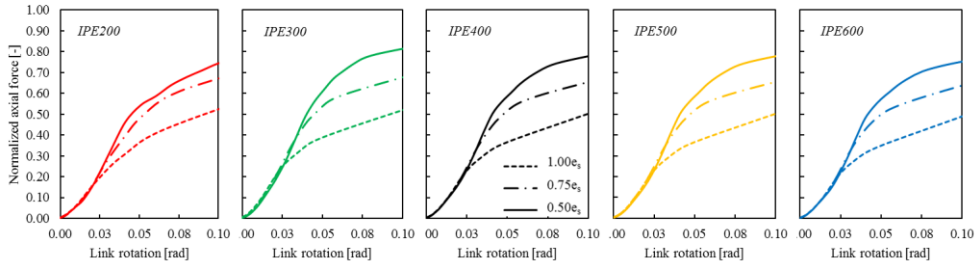

a) IPE link profiles fully restrained (FR)

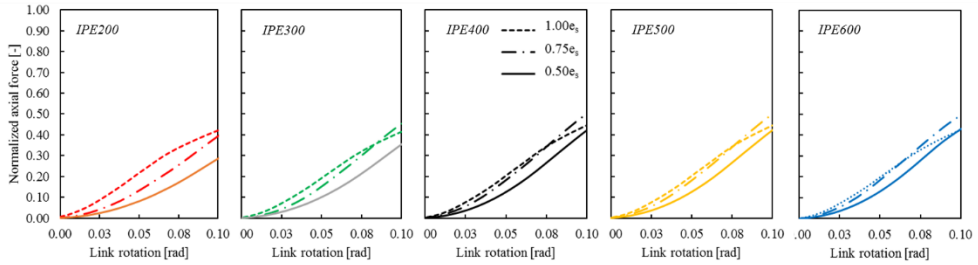

b) IPE links profiles considering deformable restraints (DR)

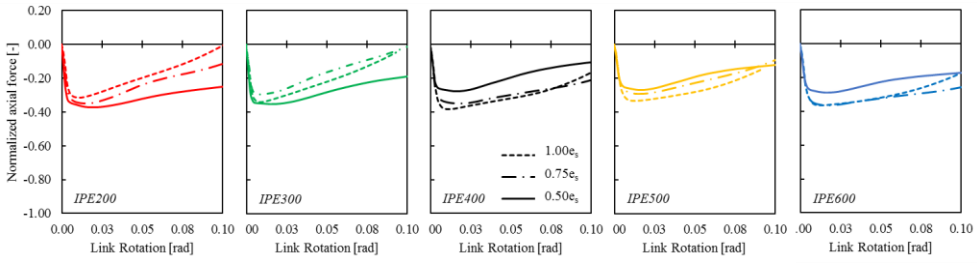

c) Links assemblies fully restrained (FR)

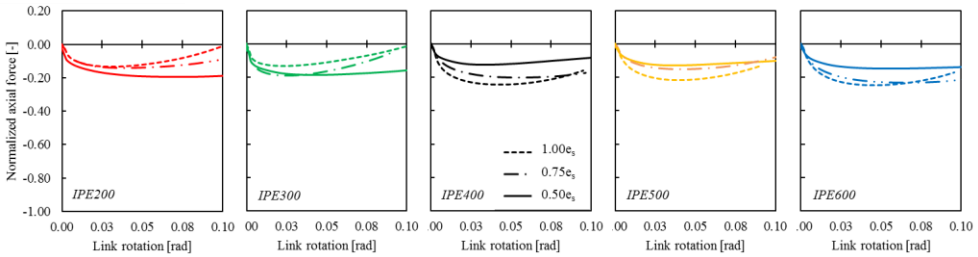

d) Link assemblies considering deformable restraints (DR)

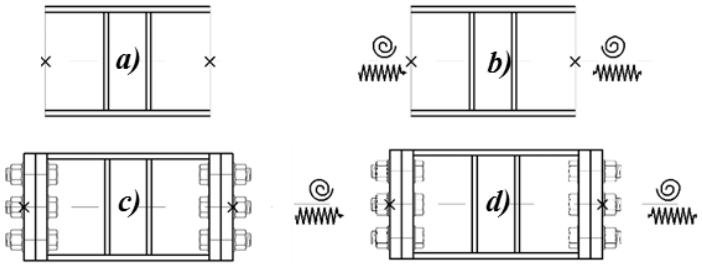

Figure 75 Influence of depth and length

Indeed, different compared to the comparison between IPE and HEA, the strength and stiffness are separated, and it can be highlighted that both parameters influence the axial response.

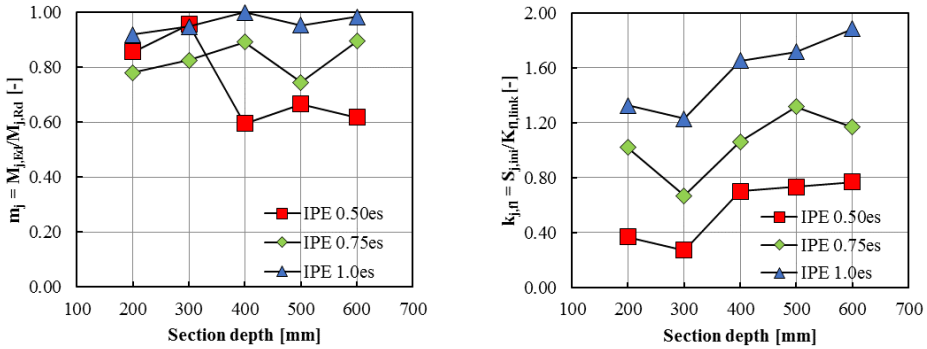

a) *Resistance* b) Stiffness

Figure 76 Connection/Link ratios for IPE assemblies

3.6.1.2.3 Influence of the connection/link strength and stiffness ratio

The remarks based on the axial response of the calibrated links (Figure 69) relative to the connection properties (Table 27) and the ones from the previous paragraphs (Figure 74 and Figure 76) highlight how, aside from the assembly boundary conditions (FR or DR) which alter the magnitude of the compressive arch, another significant contribution to the axial force in the link is the connection, in particular its strength and stiffness.

The influence of the connection strength and stiffness was verified separately by designing different connections for one of the link-connection assemblies, starting from the original one. Table 28 summarizes two cases: (i) Case I: strength is reduced, and stiffness is kept constant, (ii) Case II: stiffness is increased while strength is kept constant.

The choices made for the strength and stiffness variation was based on the limiting geometrical constraints. It was simpler to reduce the strength rather than increase it and this was achieved by changing the bolt grade. Similarly, the stiffness was increased by adjusting the bolt spacing.

Table 28 Strength and stiffness ratios for the IPE200 0.75e_s

	Original joint (FR, DR)	Modified joint (FR*, DR*)	Difference
Case I. Strength influence			
m_j	0.78	0.89	~15% reduction
v_j	0.65	0.99	~35% reduction
Case I. Stiffness influence			
$k_{j,fl}$	1.02	0.87	~15% increase
$k_{j,ax}$	1.85	1.75	~6% increase

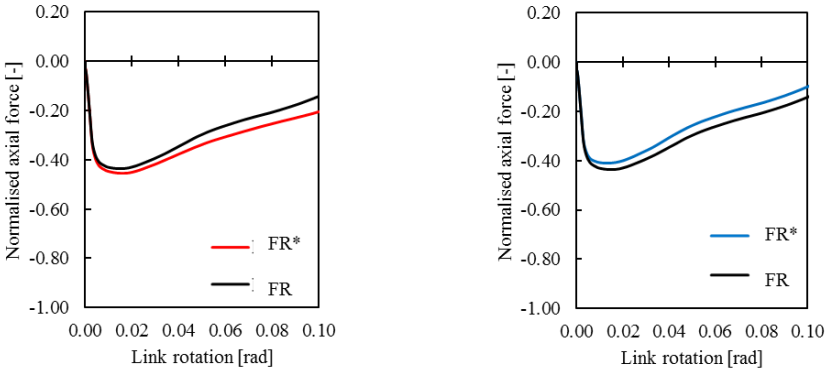

Figure 77 Influence of joint properties variation on link forces (example for IPE200 0.75e_s)

The IPE200 0.50e_s link-connection assembly was used as a base and for the simple check of these 2 parameters' influence, the resistance was reduced with 15% (Case I) while the stiffness was increased by 15% (Case II). The results are eloquent, showing that indeed a lower connection resistance leads to an increased axial force (Figure 77*a*). Similarly, increasing the stiffness, leads to a reduction in the compression developed (Figure 77*b*)

To verify these results by re-designing all the link FEP connections to have a larger overstrength is tedious, if not impossible, owing to the important design forces and the limiting geometrical constraints i.e. bolt spacing, depth of the end-plate etc. A reversed strategy can be adopted by reducing the link capacity (and therefore the design forces), using a material with a reduced

yield strength i.e. a S235 steel instead of the S355 used. As a result, the same connection has a relative larger strength (Figure 78) for the same elastic stiffness (the reduction in m_j is 30%). During the design process it was not possible to design full-strength connections for some of the HE B links (Figure 78*a*), and by using a lower grade material for the link, the m_j ratios for these connections are reduced sufficiently (less than 1 – see Figure 78*b*).

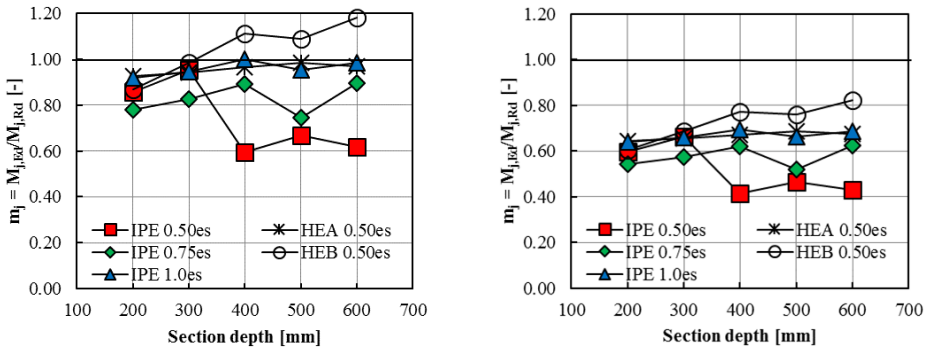

a) Links S355 b) Links S235

Figure 78 Connection/Link strength ratios for all FEP assemblies

The results are comparatively presented in Figure 79, Figure 80 and Figure 81. As it can be observed, the reduction of the m_j ratio leads to the transition from compression to tension at a lower link rotation (in all cases), but the maximum compressive force is not significantly affected.

This could be a confirmation that the shape of the axial force curve could be predicted based on the link geometrical properties, the relative link/connection strength and stiffness and, the boundary conditions. However, with regards to the connection influence, more analyses are needed for each assembly in order to get the extent to which the m_j ratio influences the assembly response.

The same set of analyses previously presented for the shear overstrength are used to attain this goal. The plots for the 400*mm* deep profiles are depicted in a similar style.

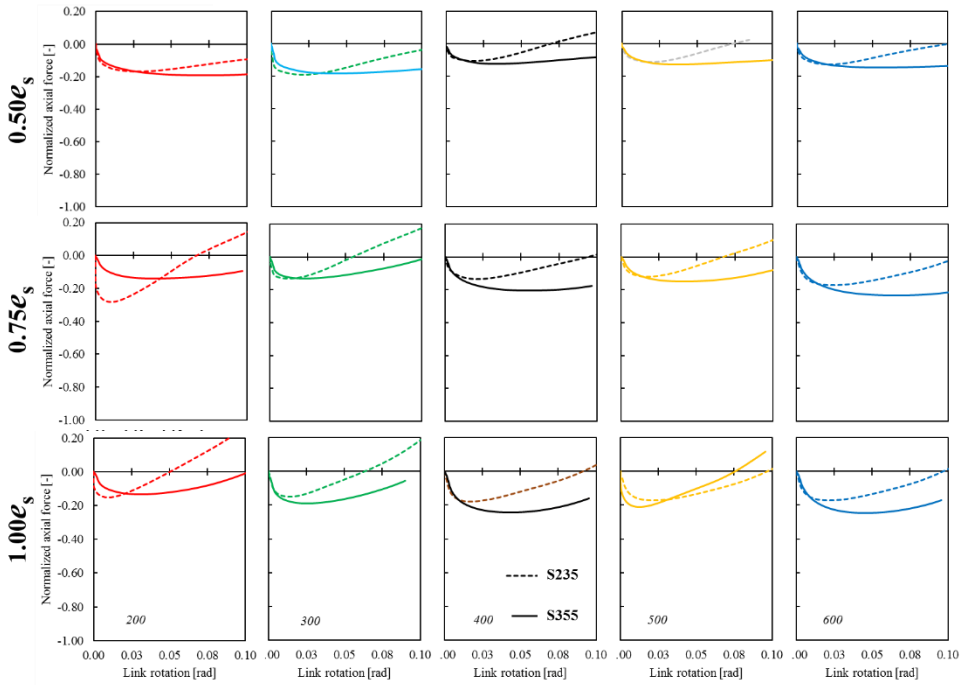

Figure 79 Normalized axial force curves for IPE link assemblies with DR boundary conditions

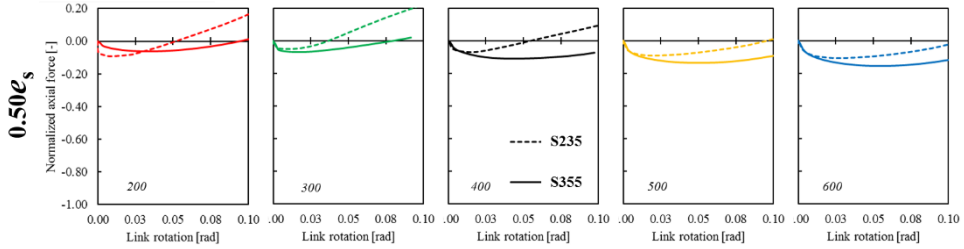

Figure 80 Normalized axial force curves for0.5e$_s$ HEA link assemblies with DR boundary conditions

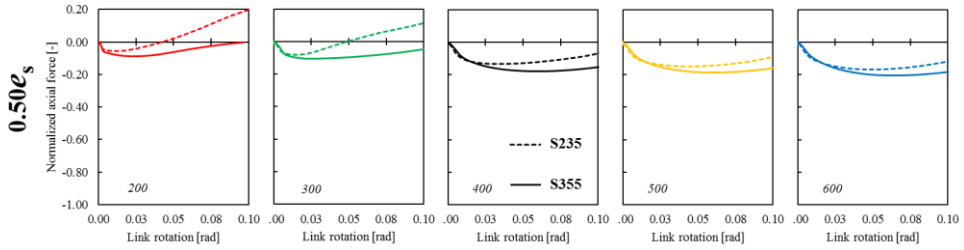

Figure 81 Normalized axial force curves for 0.5e$_s$ HE B link assemblies with DR boundary conditions

On the left of Figure 82 and Figure 83 (*a*) are the normalized curves in terms of axial force – link rotation, which show a clear dependence to the connection's relative strength. At the superior limit (denoted as FR) is the

curve representing the case of the link profile assuming FR boundary conditions (Figure 50*a*) and with ever decreasing tensile forces, below are the curves considering higher values of m_j. The maximum compression force is achieved at low levels of link rotation and this is not significantly dependent on the m_j.

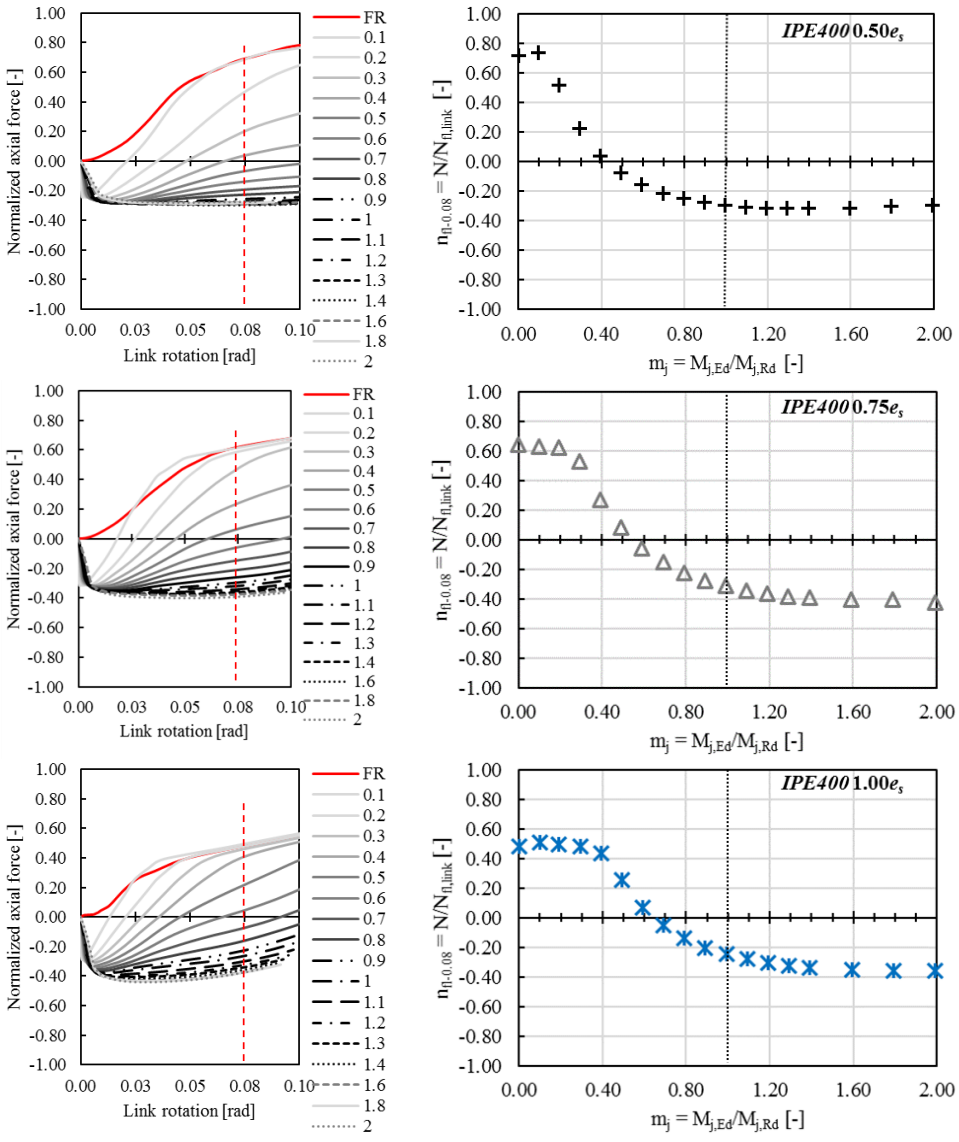

Figure 82. Axial force for 400 mm, IPE assemblies considering the variation of m_j

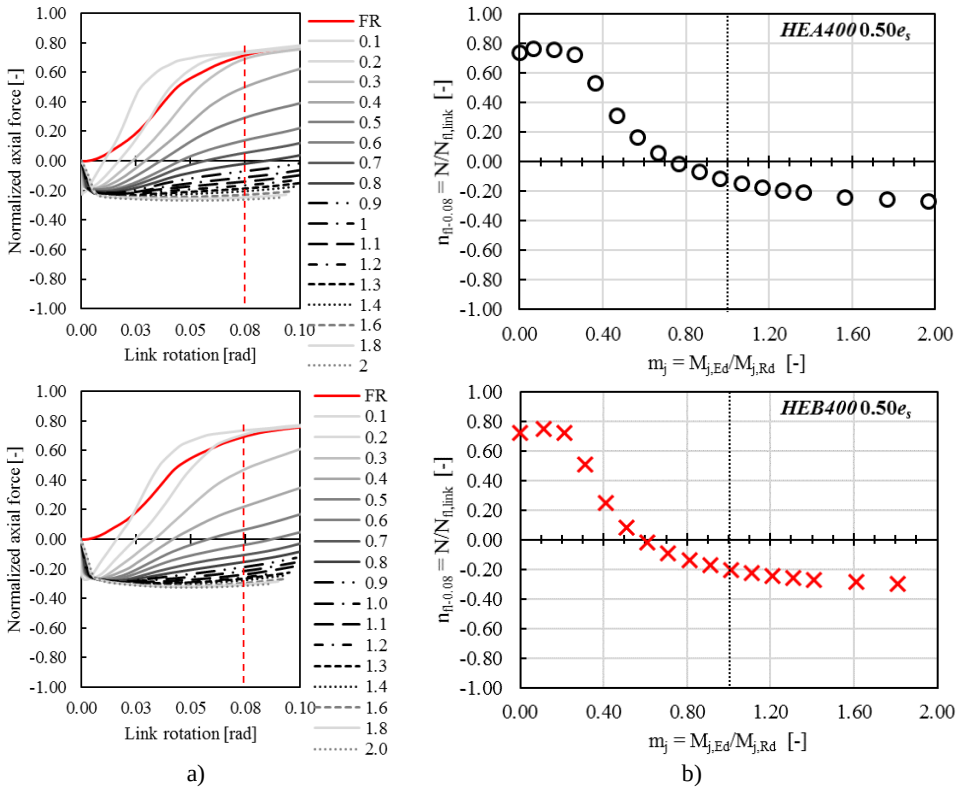

Figure 83. Axial force for 400 mm HE assemblies considering the variation of m_j

On the righthand side of Figure 82 and Figure 83 (*b*) is depicted the normalized axial force at 0.08*rad* link rotation function of m_j. Very significant correlation can be observed. For lower values of m_j the link is able to develop significant tensile forces, comparable to the ones of the fully-restrained isolated link profile. For a medium range of values (m_j = 0.4 … 1.0) the axial forces are reduced and tend to shift towards compression as m_j gets closer to 1.0. For values larger than 1.0 (partial strength connections), the link assemblies remain in compression as the connection develops significant plastic damage.

A very expressive way of depicting the difference between the extreme cases analyzed is the distribution of the normal stress in the link as depicted in Figure 84. The two pictures show the clear difference between the analyses

considering m_j = 0.1 and m_j = 2.0, the former being in tension while the latter is under extensive levels of compressive stresses.

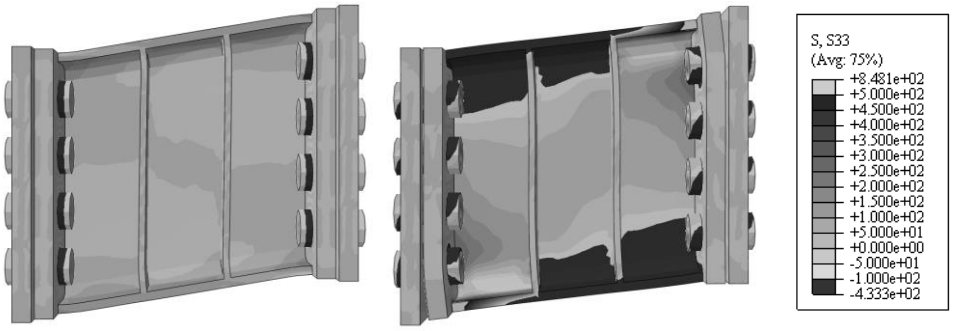

a) m_j = 0.10 b) m_j = 2.00

Figure 84 The normal stress for IPE400 0.50e_s considering varying m_j values

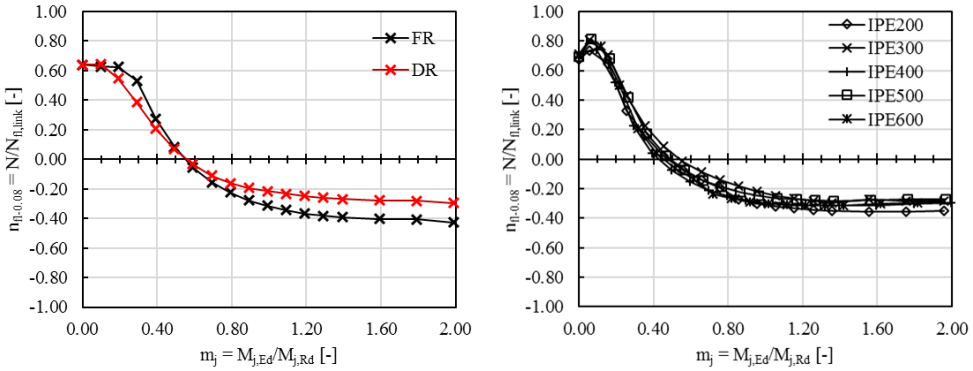

a) BC influence for IPE400 0.75e_s b) Depth influence for IPE 0.50e_s

Figure 85 Comparison of the plots for varying boundary conditions (a) and varying section depth (b)

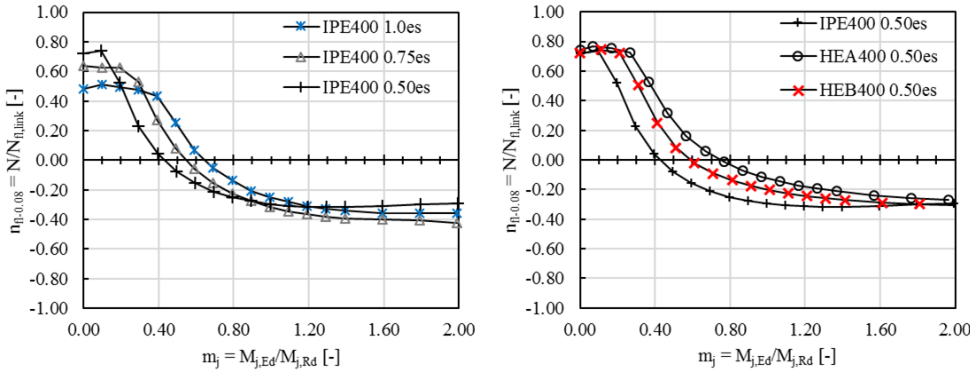

a) b)

Figure 86 Comparison of the plots for varying link length (a) and varying section tyoe (b)

In the case of axial force as well, the boundary conditions have an impact. Figure 85*a* shows the clear distinction between the case of IPE400 $0.75e_s$ assembly analyzed considering FR and DR. The less conservative deformable BCs lead to values roughly 25% smaller for the entire range of m_j.

Comparing the trends of the curves separately, first function of length (Figure 86*a*) and then function of the section type (Figure 86*b*), the conclusions of the parametric study on links presented in the previous chapter are confirmed. Namely, for conditions close to the fully restrained one i.e. very strong connections, the axial force for same depth link, with varying length will be highest for the very short link and lowest for the longer. At the same time, the section type is not relevant (same relative level of tension is reached for IPE, HEA and HEB profile). Based on these plots it can be noticed that the trends for varying lengths of the same link are shifted both parallel to the abscise and the ordinate axis. For varying section type, the curve shifts only relative to the vertical axis.

3.6.2 The extended end-plate connections (EEP)

3.6.2.1 Parametric study results

In terms of shear overstrength, the observations made for the FEP link assemblies are still valid for links with extended end-plate (EEP) connections – the seismic links have identical response in the elastic regions and there are small differences in the shear overstrength at 0.08 rad of link rotation (see Figure 87 and Figure 88).

The shear overstrength developed in the link models with EEPs is also independent from the boundary conditions as shown by the comparative graphs in Figure 87 and Figure 88, for the IPE profiles. Figure 89 *a* shows the sample comparative response of the IPE200 for fully-rigid and deformable boundary conditions, the curves being overlapped.

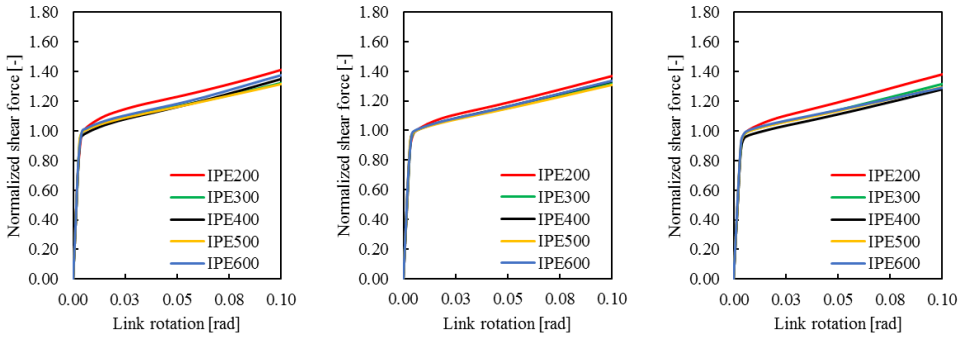

a) 0.5 e_s b) 0.75 e_s c) 1.0 e_s

Figure 87 Normalized shear force curves for IPE link assemblies with FR boundary conditions

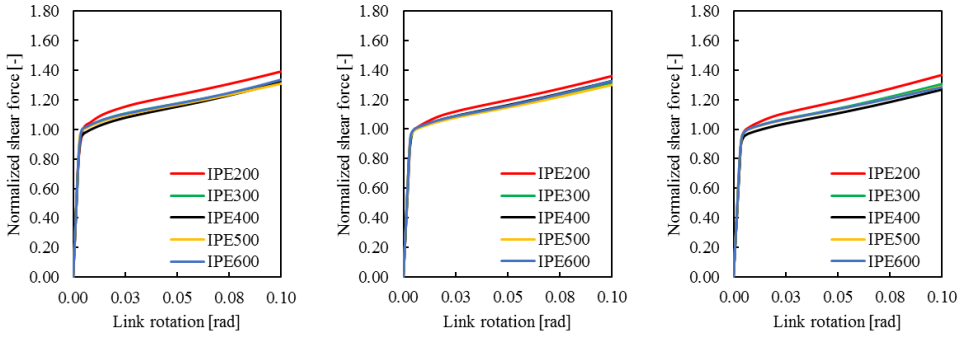

a) 0.5 e_s b) 0.75 e_s c)1.0 e_s

Figure 88 Normalized shear force curves for IPE link assemblies with DR boundary conditions

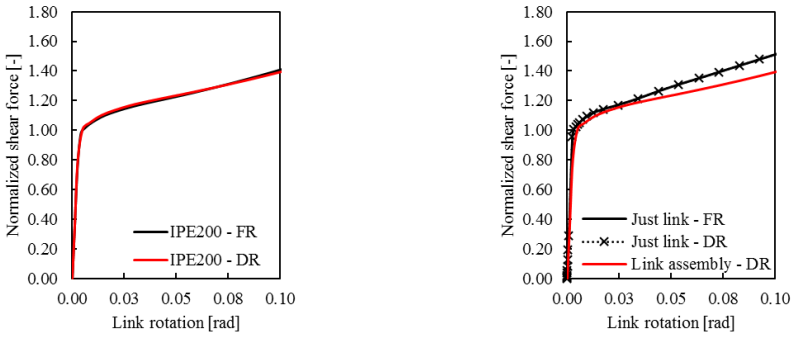

a) Link assembly FR vs DR *b) Just link vs Link assembly*

Figure 89. Shear response considering different boundary conditions

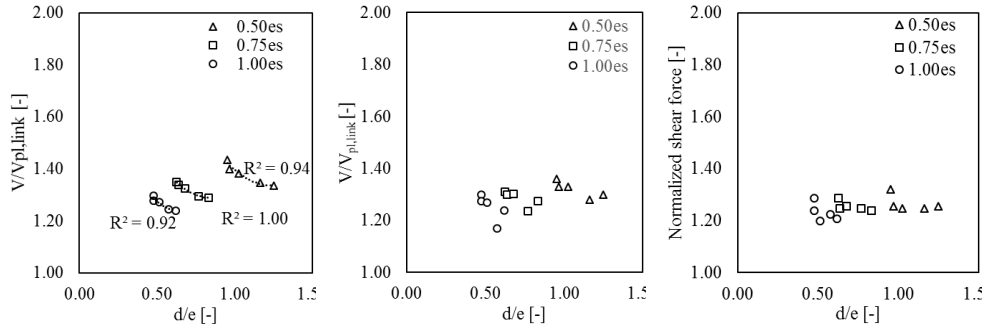

a) Link only (FR) *b) Link only (DR)* *c) EEP Link assemblies (DR)*

Figure 90 Shear overstrength at 8% link rotation vs. depth-link length ratio for the IPE links

Comparing the curve with the previous analyses of only the link having FR and DR (modelling frame and connection deformability) boundary conditions the shear overstrength is lower (Figure 89 *b*), meaning that the DR cannot accurately depict the effect the connection has on the shear hardening.

Plotting the shear overstrength at 0.08*rad* link rotation with respect to the ratio of profile depth *d* to link length *e*, Figure 90 shows that the decreasing trends (individual for each link length and section type) observed for full-rigid link-only models become less evident and in Figure 90*c*, an almost constant trend can be observed for IPE links with varying length ratios.

The impact the connection strength and stiffness have on the shear overstrength will be discussed in detail in subsequent sections, as it influences also the axial force developed.

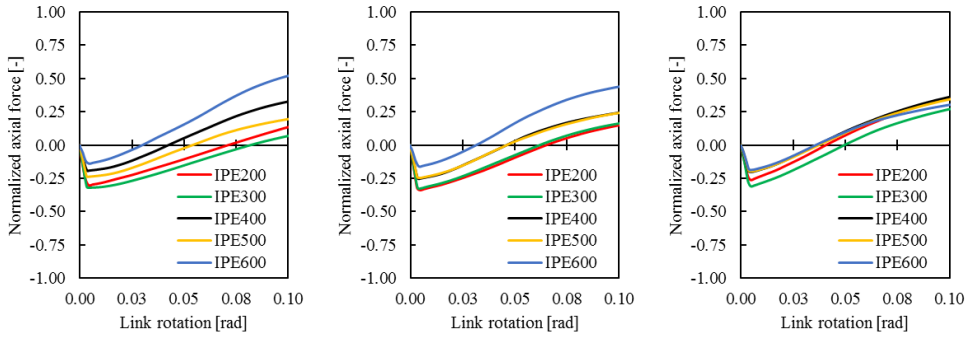

a) 0.5 e_s b) 0.75 e_s c) 1.0 e_s

Figure 91 Normalized axial force curves for IPE link assemblies with FR boundary conditions

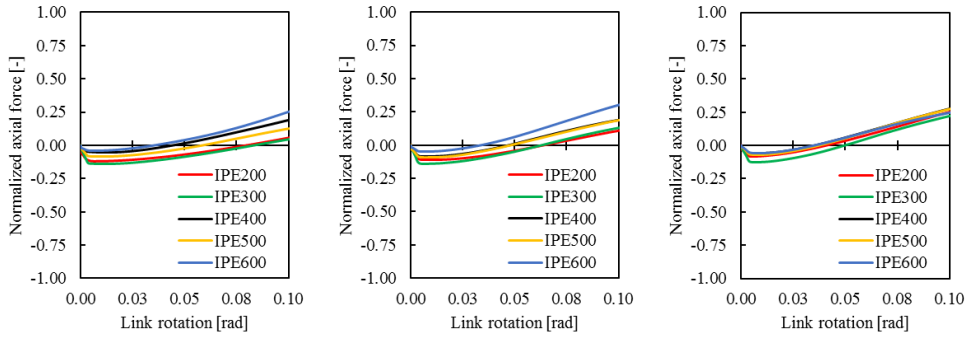

a) 0.5 e_s b) 0.75 e_s c)1.0 e_s

Figure 92 Normalized axial force curves for IPE link assemblies with DR boundary conditions

The level of axial force developed in the links detailed with EEP is different compared to the assemblies previously discussed (FEP) Unlike FEP connection assemblies that mostly remain in compression up to large plastic rotation levels, most EEP assemblies, especially those with longer links, reached tension before 0.08 *rad.* All assemblies showed significant increase in axial forces in both the compression and tension sides of the curve when fully rigid boundary conditions are imposed instead of deformable springs (Figure 91 and Figure 92).

The values presented in Figure 93 are the axial forces at 0.08 rad, which in most cases are in significant tension. There is an average decrease of 37% in tensile forces when the same model with initially fully rigid restraints is analyzed considering deformable springs. The decrease is more significant for shorter links with an average of 50% for $0.5e_s$, 33% for $0.75e_s$ and 30% for e_s.

Therefore, it remains valid for EEP that considering the deformability of the frame to which the link is connected reduces the axial demand on links.

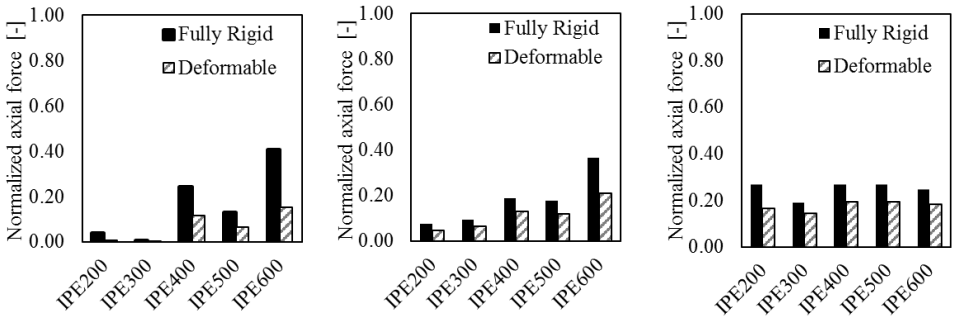

a) 0.5 e_s b) 0.75 e_s c)1.0 e_s

Figure 93 Normalized axial force for IPE link assemblies

3.6.2.2 Influence of the connection on the link response

Analyzing the link assemblies with EEP connections considering a variation of the connection strength ratio m_j, similar observations can be drawn (compared to the case of FEP).

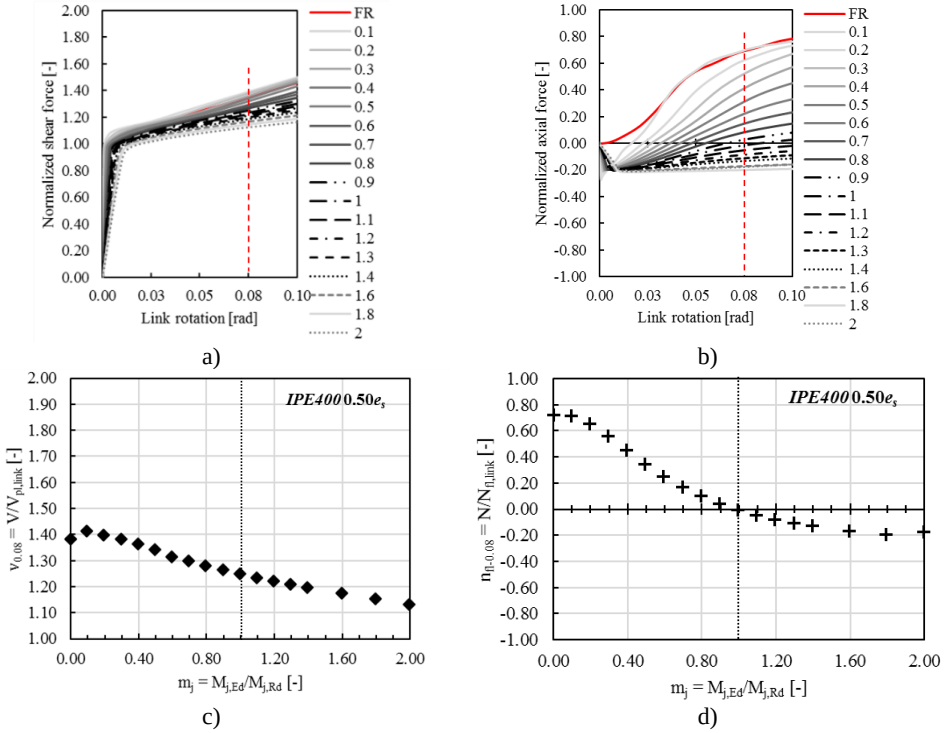

a) b) c) d)

Figure 94 Results of analyses considering the variation of m_j for IPE400 0.50e_s EEP assembly

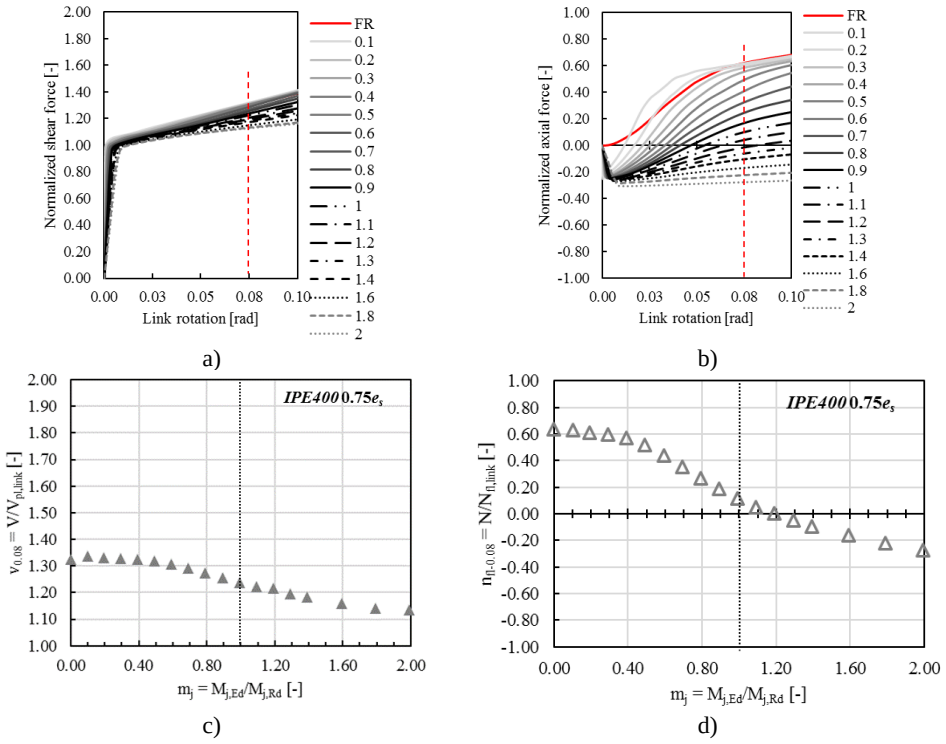

Figure 95 Results of analyses considering the variation of m_j for IPE400 0.75e_s EEP assembly

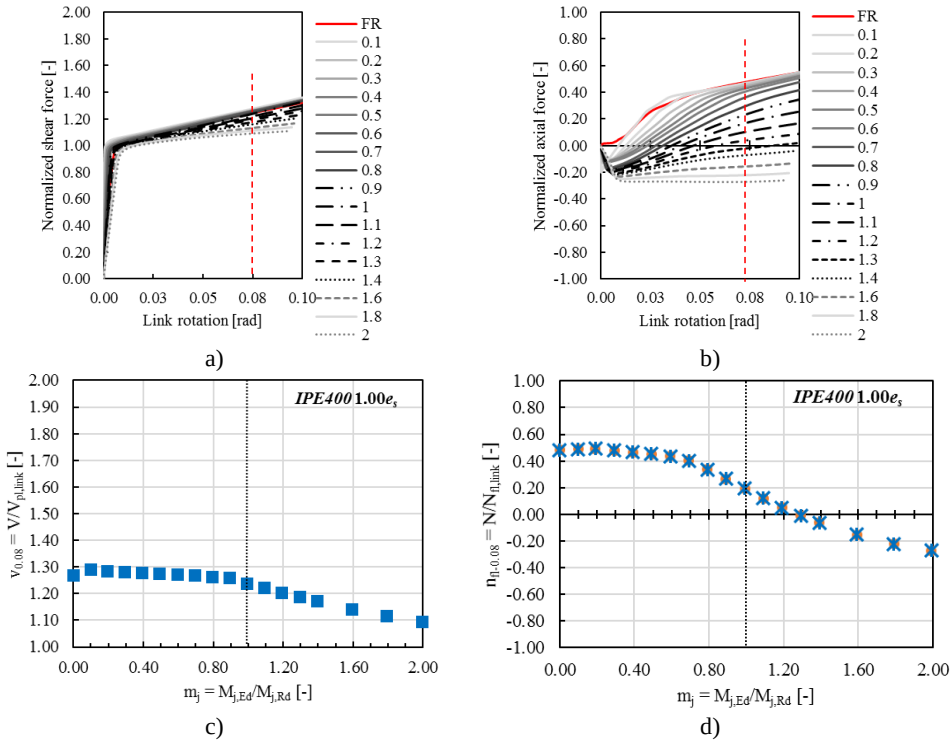

Figure 96 Results of analyses considering the variation of m_j for IPE400 1.00e_s EEP assembly

Figure 94, Figure 95 and Figure 96 *a* and *b* show the same trend of the normalized shear force and axial force curves in relation to the variation of the connection strength i.e. a decrease in the stiffness with the increase of the m_j ratio, a reduction of the shear overstrength and of the tensile forces, arriving at compression for very significant values of m_j (basically when the connection becomes a partial strength one).

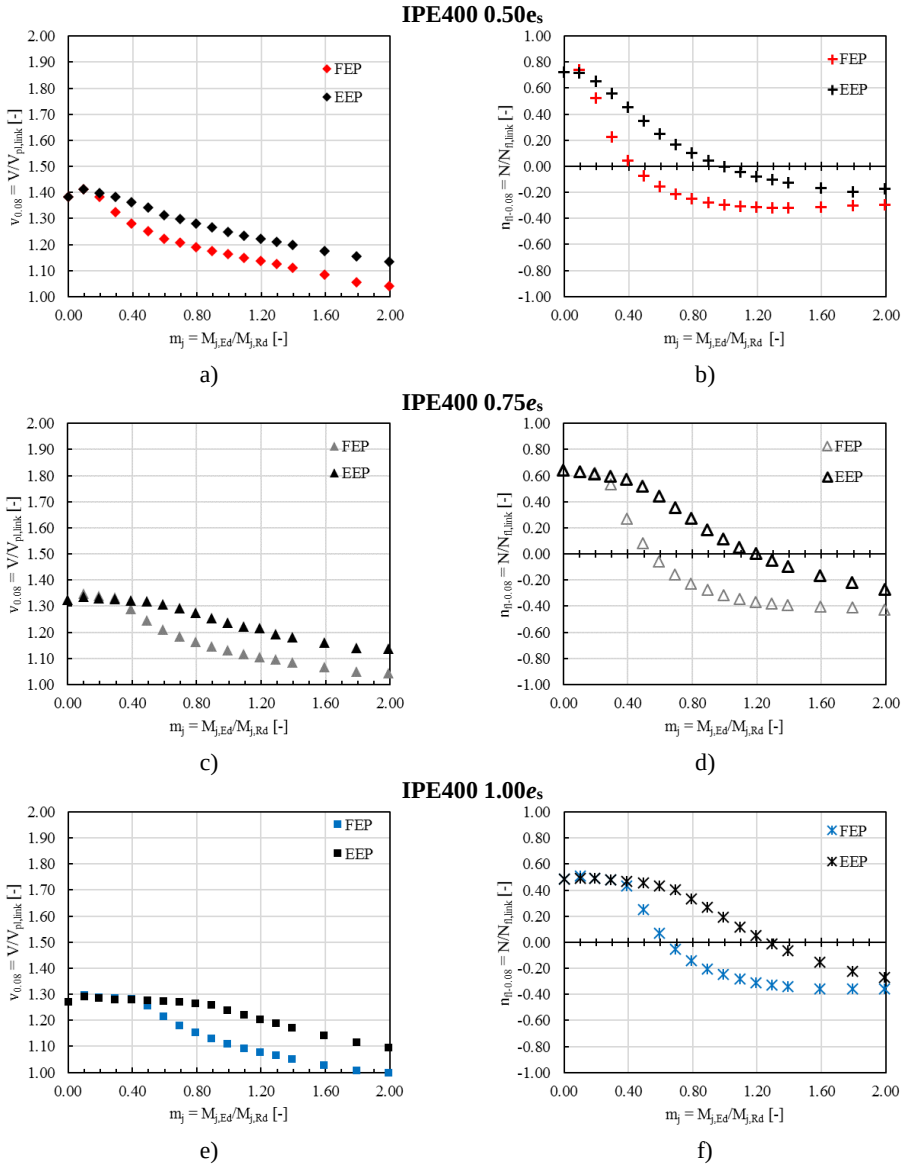

Figure 97 Comparative results of FEP and EEP assemblies considering the variation of m_j

Plotting the values of the shear overstrength at 0.08*rad* link rotation (Figure 94*c*, Figure 95*c* and Figure 96*c*) it can be noticed that the reduction of the shear overstrength is less severe compared to the equivalent FEP connection. In Figure 94*d*, Figure 95*d* and Figure 96*d*, a similar trend is observed, namely the reduction in terms of tensile forces, with the consequent achievement of compression is not so abrupt.

Indeed, comparing the results for the EEP with the corresponding flush end-plate connection (Figure 97) it is clear that the connection type, in terms of stiffness, and not only strength, influences both the shear overstrength and axial force developed. This indicates the importance of the connection stiffness in the determination of the two parameters. As a matter of fact, Figure 98 shows an almost double connection rotation of FEP for the same link assembly.

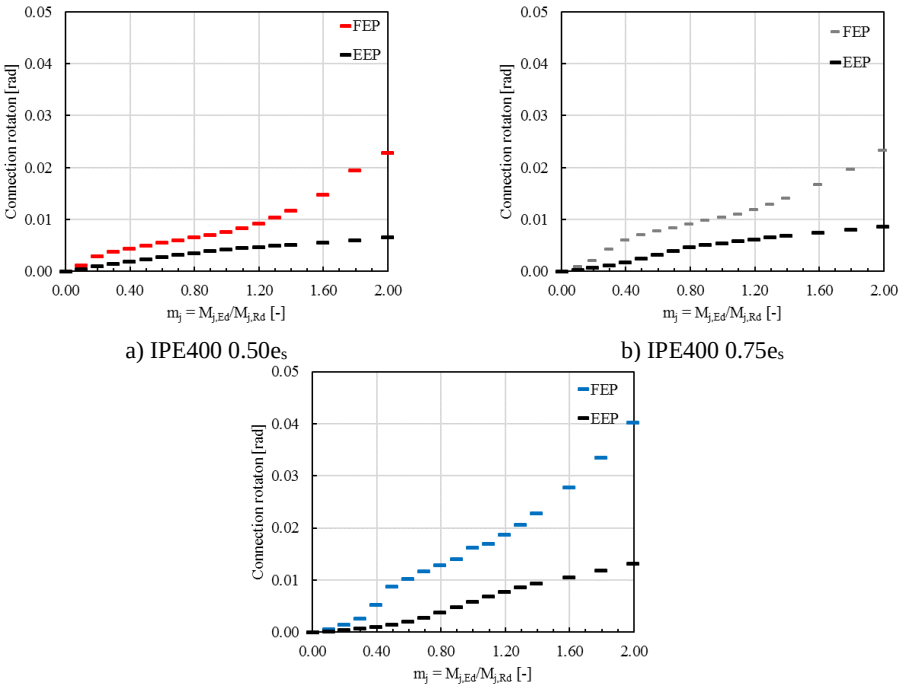

a) IPE400 0.50e_s

b) IPE400 0.75e_s

b) IPE400 1.00e_s

Figure 98 Connection rotation at 0.08rad link rotation

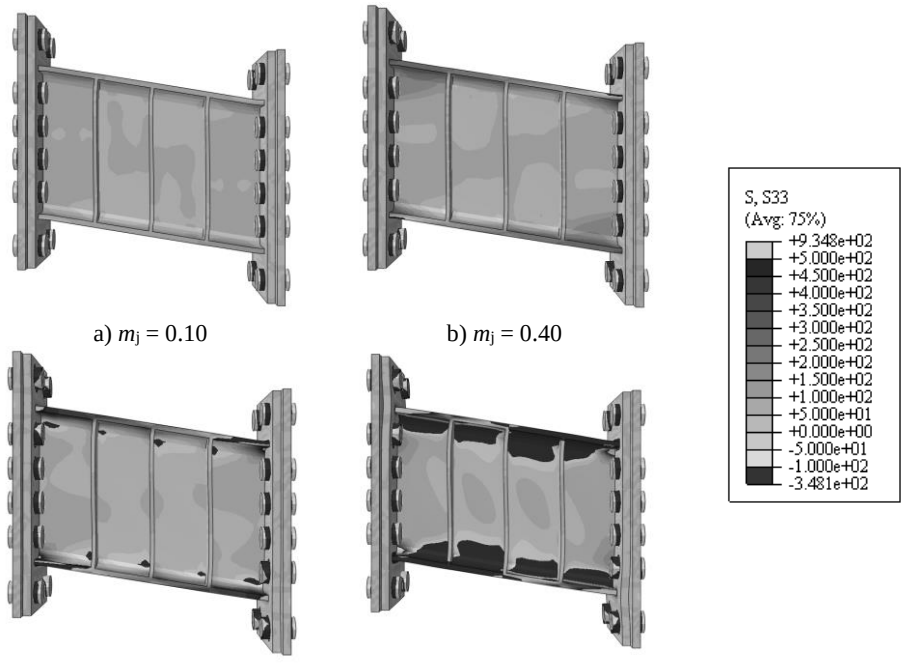

a) $m_j = 0.10$ b) $m_j = 0.40$

c) $m_j = 0.80$ d) $m_j = 2.0$ e) Legend

Figure 99 The normal stress for IPE400 0.75e_s considering varying m_j values

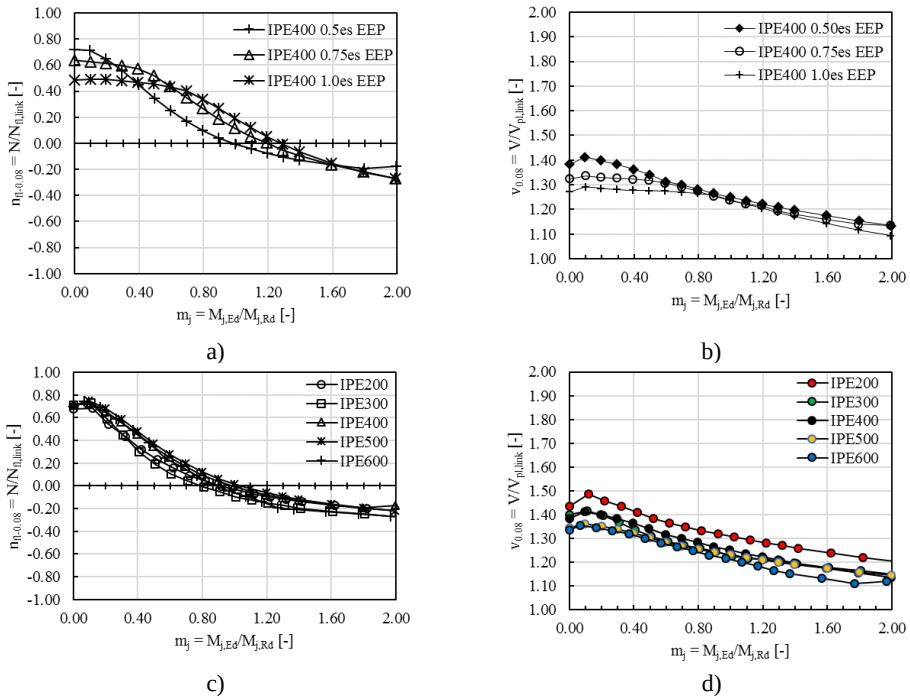

a) b)

c) d)

Figure 100 Overlapped curves for varying length (a and b) and varying depth (c and d)

The images of the axial force distribution in the link assuming varying levels of m_j are presented in Figure 99. Like in the comparison between the link and the link-connection assembly, it can be observed that for small values of m_j the link is in tension while for increasingly weaker connections, the compressive stresses become predominant.

The summary of the overlapped curves in terms of shear overstrength and axial force presented in Figure 100, reveals that the curves depend little on the sectiondepth and much more on the link assembly length.

3.6.3 Proposal for the evaluation of design forces and Design recommendations

The proper design of detachable links is largely dependent on the design of the connections and the way the capacity design rules are applied. The results presented in the previous paragraphs lead to the conclusion that important considerations are to be made with regards to the link shear overstrength at global level (i.e. for the capacity design of the structure) and local level (i.e. both shear overstrength and axial force to be considered to design the connections).

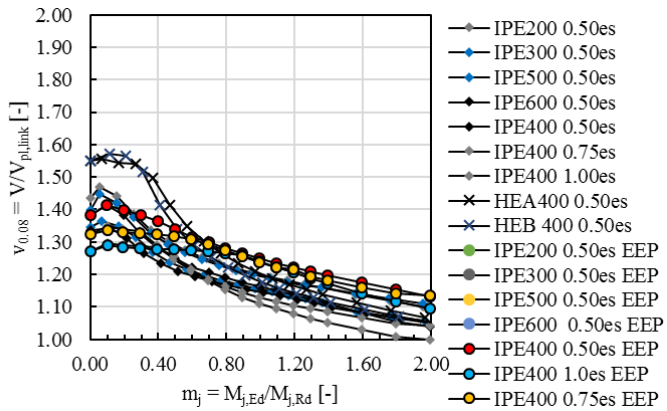

Figure 101 Shear overstrength vs. m_j curves

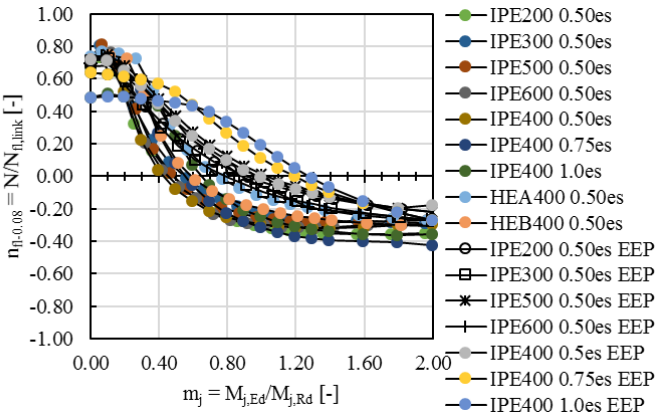

Figure 102 Normalized axial force vs. m_j curves

3.6.3.1 Proposed evaluation for the Design Shear force

The dependency of shear overstrength ($v_{0.08}$) with geometrical and mechanical parameters has been already demonstrated, even by the simple link models analyzed with rotational and axial springs. Looking at the overstrength $v_{0.08} - m_j$ curves in Figure 101 it can observed that for small m_j values, the shear overstrength is constant and close to the one of the link-only assuming FR boundary conditions (see Figure 103*a*). However, the $m_{j,limit}$ value changes function of the connection type and link length. Table 29 presents the $m_{j,limit}$ values observed for the cases investigated.

Table 29 The m_j limit of the constant shear overstrength range

	Flush EP connection			***Extended EP connection***		
	0.50e_s	**0.75e_s**	**1.0e_s**	**0.50e_s**	**0.75e_s**	**1.0e_s**
IPE	0.2	0.3	0.4	0.3	0.5	0.8
HE	0.3					

The trend of the data beyond $m_{j,limit}$ has been fitted with various functions (linear, polynomial, logarithmic) and the best fit of the $v_{0.08} - m_j$ data was obtained with the following function:

$$y(x) = \alpha \ln(x) + \beta \tag{3.45}$$

$$v_{0.08}(m_j) = \alpha \ln(m_j) + \beta \tag{3.46}$$

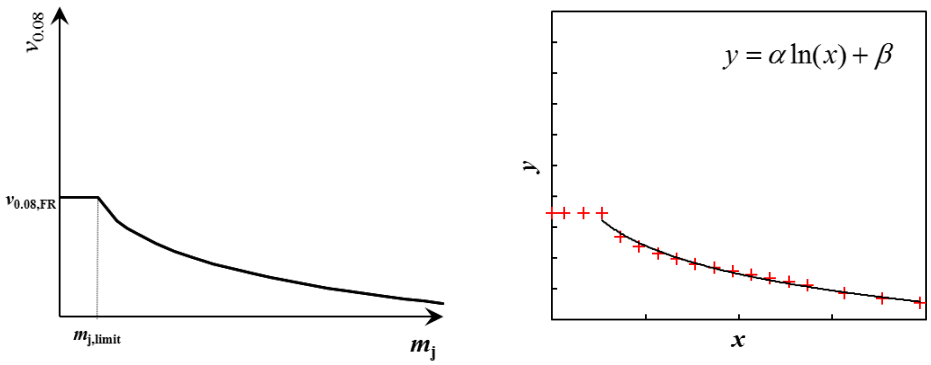

a) b)

Figure 103 Shape of the function used to fit the $v_{0.08} - m_j$ data

Table 30 Values for α

	HE	IPE		
	$0.50e_s$	$0.50e_s$	$0.75e_s$	$1.0e_s$
AVG	-0.25	-0.13	-0.15	-0.16
ST.dev	0.0781	0.011	0.0001	0.0052

Comparing the α values for the investigated cases, it was observed that it has constant values function of the link length and section type (IPE or HE). The average values and standard deviation are presented in Table 30. For the evaluation of β a linear regression function of the connection/link stiffness ratio ($k_{j,fl}$) is needed, separately for IPE and HE profiles and for Flush EP and Extended EP connections.

1. IPE links with Flush EP connections:

$$\beta = -0.017\frac{S_{j,ini}}{EI_{y,link}} \cdot e + 1.205 \tag{3.47}$$

2. IPE links with Extended EP connections:

$$\beta = -0.012\frac{S_{j,ini}}{EI_{y,link}} \cdot e + 1.25 \tag{3.48}$$

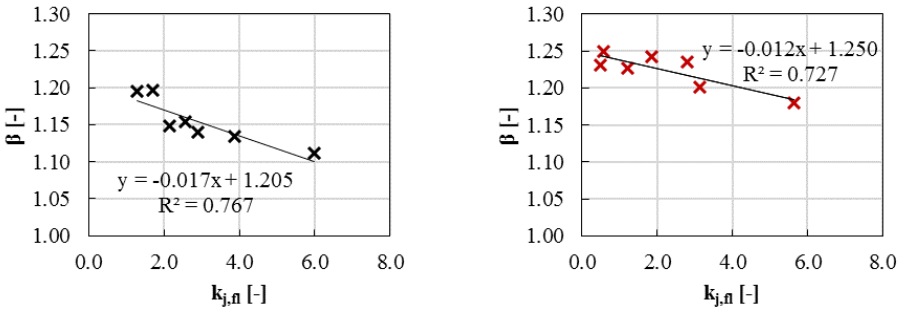

a) Flush EP connections b) Extended end-plate connections

Figure 104 Values of β for IPE profiles

3.6.3.2 The evaluation of the axial force in the link

The data in terms of normalized axial force ($n_{fl,0.08}$) and connection relative strength (m_j) is very nonlinear but the trend is evident (see Figure 102). The function below offers the best fit of the $n_{fl,0.08} - m_j$ data considering the parameters *a*, *b*, *c* and *k* dependent on the link and connection geometrical and mechanical parameters.

$$y(x) = e^{-a \cdot x^k + b} + c \tag{3.49}$$

$$n_{fl,0.08}(m_j) = e^{-a \cdot m_j^{\,k} + b} + c \tag{3.50}$$

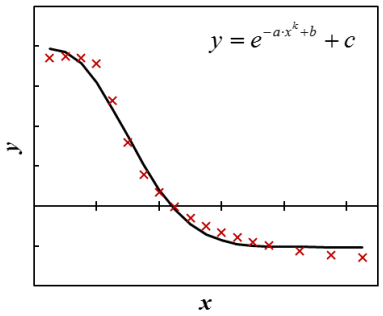

Figure 105 Shape of the function used to fit the $n_{fl,0.08} - m_j$ data

The parameters *a*, *k*, *b* and *c* were evaluated based on linear regressions as function of the link assemblies' properties, as depicted in Figure 106. The relative regression equations are given in Eq. [REF]. The respective R^2 values are given together with the plots and have values in the range of 0.75 – 0.85, considered good, given their proximity to 1.0.

Table 31 Tensile force in the links considering the link profile and FR boundary conditions ($n_{fl,T\,max}$)

Section	Value	**0.5e_s** [-]	**0.75e_s** [-]	**e_s** [-]
IPE	Mean:	0.70	0.62	0.46
	St. Dev:	0.017	0.010	0.012
HE	Mean:	0.73	0.61	0.45
	St. Dev:	0.023	0.024	0.023
All	Mean:	0.72	0.61	0.45
	St. Dev:	0.024	0.022	0.022

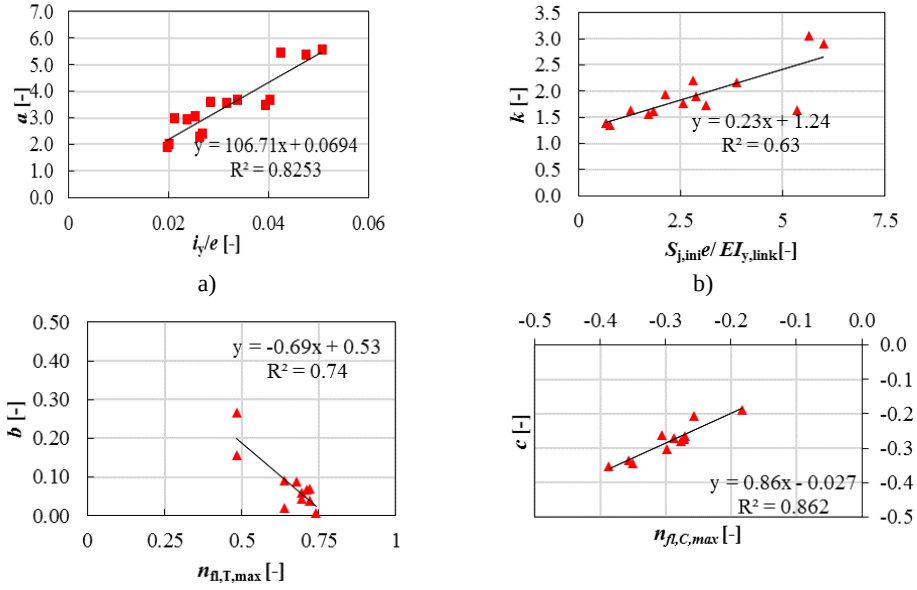

Figure 106 Regressions for the $n_{fl}(m_j)$ equation parameters a, k, b and c

The equations for the four parameters are as follows:

$$a = 106.7\frac{i_{y,link}}{e} - 0.07 \tag{3.51}$$

$$k = 0.23\frac{S_{j,ini}}{EI_{y,link}} \cdot e + 1.24 \tag{3.52}$$

$$b = 0.69 n_{fl,T,\max} + 0.53 \tag{3.53}$$

$$c = 0.86 n_{fl,C,\max} - 0.027 \tag{3.54}$$

Where: $i_{y,link}$ is the radius of gyration of the link section about *y-y* axis, e is the link length, $S_{j,ini}$ is the initial stiffness of the joint evaluated based on EC3 1-8. E is the Elastic modulus of steel (assumed equal to 210GPa), $I_{y,link}$ is the moment of inertia of the link section about *y-y* axis, $n_{fl,T,max}$ is the maximum tensile force developed by the link flanges at $0.08rad$ link rotation evaluated based on the link profile, assuming fully-restrained boundary conditions, $n_{fl,C,max}$ is the maximum compression force developed by one link flange at $0.08rad$ link rotation.

3.6.3.3 Recommendations for the design of detachable links

The current version of EC8 gives no recommendations regarding the design of detachable links. Matters such as the effect of the connection strength and stiffness on the assembly response has not been addressed. Even the design of links in regular EBFs is based on the use of a universal value for the shear overstrength for short links (1.5), although it has been proved in the literature that, function of the link length, section compactness and boundary conditions, the value varies widely (Della Corte *et al.*, 2013). Furthermore, the issues related to the catenary action and its impact is ignored. The need for improvements in the design process is evident.

In the light of the previous remarks, the following algorithm can be used for a more accurate design:

1. Based on the link length and section type, evaluate the design forces assuming fully-restrained (FR) boundary conditions i.e. use $v_{0.08,FR}$.
2. Design the connection according to EN1993 Part 1-8 (ignoring the axial force) and determine the connection mechanical characteristics ($M_{j,Rd}$, $V_{j,Rd}$, $S_{j,ini}$).
3. Using the m_j* obtained as the ratio of the previously determined values, the actual $v_{0.08}$ can be obtained.
4. The actual design forces ($V_{j,Ed}$, $M_{j,Ed}$) can be evaluated.
5. Based on the actualized value of m_j the magnitude of the axial force developed in the connection can be determined.
6. Further checks of the connection can be performed, if needed (in the case when significant tensile forces develop).

3.7 SUMMARY

In the last decades, the use of eccentrically braced frames in seismic areas has continually increased, supported by the continual effort of the research community in the direction of rendering the solution safer and more economical. In this context, EBFs with detachable links come as a natural step forward towards the improvement of the existing system by rendering it easily repairable in the earthquake aftermath.

However, newly revealed issues related to the connection and older observations related to short links, make the solution not quite ready for implementation in day to day constructional practice. The end-plate connections designed for replaceable links are critical because they need to remain elastic in order to ensure the link removal and replacement and the end-plate on the beam side needs to be undamaged as it cannot be replaced.

An issue previously brought up in literature, which has a direct impact on the link connection design, is the unsatisfactory evaluation of the link shear overstrength. It was hereby shown that the shorter and the more compact the link, the larger the shear overstrength. This goes both ways, in the way that slenderer links have lower shear overstrength. Therefore, the unique value currently provided by the Eurocode 8 can lead to either unsafe or uneconomical results. A more accurate way for determining the shear overstrength at 0.08*rad* link rotation was proposed, as a function of the link depth, length and flange/web area ratio.

The values thus determined do not consider the connection in the case of detachable links and are useful only for links in traditional EBFs. Indeed, it was demonstrated that the shear overstrength decreases with the decrease of the connection strength and stiffness. Equations which allow the consideration of the connection mechanical parameters are proposed.

Although typically assumed as too low to require accounting for, axial forces can develop in short links under large deformation demands. The current work showed that indeed, links which are fully restrained develop significant tensile force at 0.08*rad* link rotation, values almost constant for varying depth or profile compactness, but varying with link length.

In the case of detachable links, the axial force is dependent also with the connection strength and stiffness. Large tensile forces are being developed only when very strong connections are used, while if the connection is closer to a partial strength one, compressive forces will be predominant. The level of axial force for a link-connection assembly could be determined based on the proposed empirical equations.

Although further work is needed in order to render the equations more accurate, by using more data obtained numerically and experimentally, the results hereby presented shed light on some of the critical aspects related to the link and connection design for easily repairable EBFs.

4 BOLTED FRICTION CONNECTIONS

Introduction

In the framework of FREDAM (RFSR-CT-2015-00022) "*Free from damage connections*" research project, the innovative friction connection is a typical solution of Symmetric Friction Connection which is able to replace the plastic dissipation mechanism consecrated for MRFs with the "low-damage" alternative of friction based dissipation (Buttermore &McRae, 2000, Latour et al., 2011).

The connection which can be considered also a device, was proposed in two configurations, one with horizontal and another with vertical sliding plates added below the bottom flange of the beam in the form of a haunch and a rib, respectively. The dissipation occurs by the relative movement of these plates with respect to the friction pads clamped by means of high-strength bolts. The friction pad-steel plate interface is characterized by a certain friction coefficient and function of the level of preload applied by the bolts, the slip resistance can be easily evaluated. The bending resistance of the connection described is given by the product of the slip resistance and the lever arm. Therefore, in this case, the dissipative element is the friction device and, the beam, column and connection need to be designed as non-ductile elements with an overstrength given by the characteristics of the friction connection (static and dynamic friction coefficient, level of preload).

However, many aspects related to this structural solution need to be investigated, starting from the friction materials used to the response of structures equipped with such devices.

The current chapter presents the results of experimental and numerical investigations performed in the framework of the FREEDAM project. The main goal is to fully characterize the solution by introducing the fundamental concepts related to friction joints, their design and design of structures equipped with friction connections. It is desired that this will make the concept readily available in the constructional practice by offering fully qualified solutions which are easy to implement.

Objectives

The work carried out ranged over all levels, starting from sub-component to structural hence, the objectives are related to each of the investigation stages:

1. Characterization of the parameters influencing the friction response by means of sub-component experimental tests and FEAs performed with calibrated models
2. Assessment of the beam-to column joint response under cyclic loading for the selected friction parameters (material and clamping force level).
3. Evaluation of the influence of the variation of key parameters on the response of the joint
4. To propose design procedure and evaluate the seismic performance of structures equipped with friction devices
5. Based on the tests on joints and the investigated structures, propose a catalogue of friction devices to cover the practice requirements

4.1 BASIC CONCEPTS OF FRICTION

Latour *et al.* (2014) summarize in their work some basic concepts related to tribology. The authors describe two types of friction interactions occurring at the level of surfaces in contact: adhesion and ploughing. The adhesion component occurs due to the pressure applied to keep the surfaces in contact, all the rough asperities yield and practically the ‘‘cold-weld’’ is developed. Because of the intimate contact of these junctions, the shearing of the adhesive ties requires a certain sliding load. The ploughing is related to the relative out of plane displacement of the surfaces in contact for one of the elements to lift over the other.

The mathematical theory states that the adhesion must be proportional to the real contact area which, for metals with ideal elastic–plastic behavior can be assumed equal to $A = N/\sigma_0$, where A is the real area of contact, σ_0 is the material penetration hardness and N is the normal force. The adhesion friction force is given by:

$$F_A = A \cdot s = \frac{N}{\sigma_0} \cdot s \tag{4.1}$$

Where s is the force per unit area

The ploughing contribution, as defined by Bowden and Tabor (1950) is

$$F_P = n \cdot r \cdot h \cdot \sigma_0 \tag{4.2}$$

Where n is the number of asperities, r is the half width of the asperity, h is the height of the asperity.

The total friction force is:

$$F = F_A + F_P = \frac{N}{\sigma_0} \cdot s + n \cdot r \cdot h \cdot \sigma_0 \tag{4.3}$$

The ploughing is negligible compared to adhesion, in the case of metals. Hence, it can be observed based on the previous equation that the relationship between the friction force and the normal force is a constant that is independent on the contact area. Indeed, Bowden and Tabor (1950 and 1953) theory explains two of the three postulates of the classical theory of dry friction, which states:

1. "The total frictional force is independent of the apparent surface area of contact.
2. The total frictional force that can be developed is proportional to the normal applied action.
3. In case of slow sliding velocities, the total frictional force is independent on the sliding velocity." (Latou *et al.*, 2014)

The first two are called Amonton's laws while the third one, is due to Coulomb (Halling, 1978 and Person, 2000). The tangential force acting opposite to the motion direction can be evaluated based on the well-known Coulomb friction equation:

$$F = \mu \cdot N \tag{4.4}$$

Where F is the sliding force, N is the normal action and μ is the friction coefficient.

Friction connections, like those proposed in the framework of FREEDAM, have a dissipation mechanism characterized by the sliding of the inferior haunch flange or rib, which has slotted holes, with respect to the friction pads. The sliding occurs when the couple of forces given by the bending moment applied on the joint, reaches the design slip force F_{slip}. This slip force is evaluated, based on the Coulomb friction equation previously described.

$$F_{slip} = \mu \cdot n_s \cdot n_b \cdot N_b \tag{4.5}$$

Where μ is the friction coefficient of the slipping surface, n_s is the number of slipping surfaces, n_b is the number of bolts and N_b is the pretension force in the bolts clamping the plates together.

The friction coefficient μ is the parameter that singlehandedly influences the most the friction behavior of the joint. Indeed, μ is a material coefficient that depends on the material properties and surface mechanical preparation, which has a static and kinematic value Latour *et al.*, (2014). On the other hand, the tightening of the bolts is a sensitive process that introduces uncertainties, both in the construction phase and during the life time of the structure (due to relaxation). The difference between the static and the dynamic friction coefficient and the randomness of the two variables must be accounted for, especially for the hierarchy of the elements. The simplest way to do this is to consider the overstrength coefficient Ω_μ.

$$\Omega_\mu = \frac{\mu_{st.95\%}}{\mu_{dyn.5\%}} \cdot \frac{N_{b.95\%}}{N_{b.5\%}} \tag{4.6}$$

Where:

- $\mu_{dyn.5\%}, N_{b.5\%}$ lower-bound values of dynamic friction coefficient and tightening force
- $\mu_{st.95\%}, N_{b.95\%}$ upper-bound values of static friction coefficient and tightening force

The overstrength coefficient Ω_μ is essential for the implementation of the capacity design rules, because in the case of friction connections, the dissipative element is the friction damper hence, the sources of overstrength are related to the parameters controlling the sliding force.

4.2 DEFINITION OF FRICTION PROPERTIES

The first part of the FREEDAM experimental campaign was dedicated to the investigation of the frictional characteristics of selected materials by isolating the damper component out of the joint configuration and performing uniaxial lap-shear tests. The component tests are devoted to the selection of the fittest material for the friction interface and to understand other key factors that impact the overall response (clamping level, loss of preload, preloading strategy, effectiveness of the disc spring washers, creep effect, response under impact, etc.).

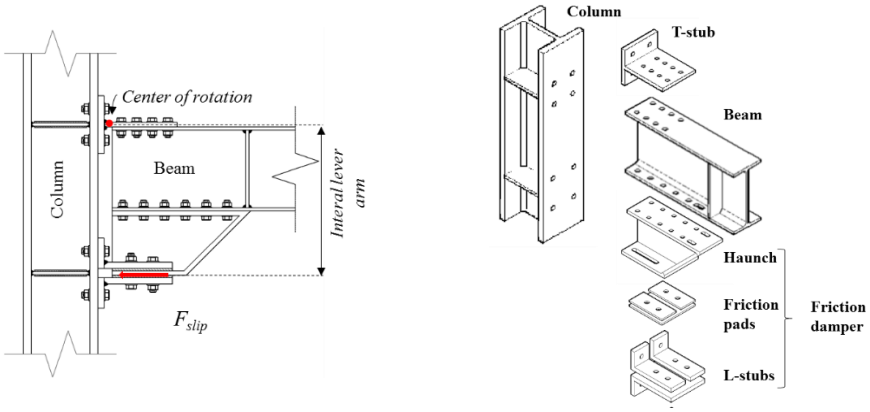

a) Mechanism b) Main components

Figure 107 Friction joint layout

The large bunk of the experimental campaign on lap-shear tests for the assessment of the friction materials, preload levels as well as the preloading strategy, took place at the STRENGTH laboratory of University of Salerno: Experimental tests on the same type of sub-components, concerning other issues like creep, impact loading, high velocity tests were performed in the laboratories of the FREEDAM project partners; however, these are not referred in the current work. The task of the University of Naples' involved researchers was to calibrate a numerical model based on the experimental results and perform additional investigations and measurements which could not be performed in the laboratory.

4.2.1 Preliminary FEAs on friction sub-assemblies

Prior to the commencement of the experimental campaign on lap-shear tests within FREEDAM, a numerical investigation was performed based on models with the geometry of the specimens tested in the past by Latour *et al.* (2014).

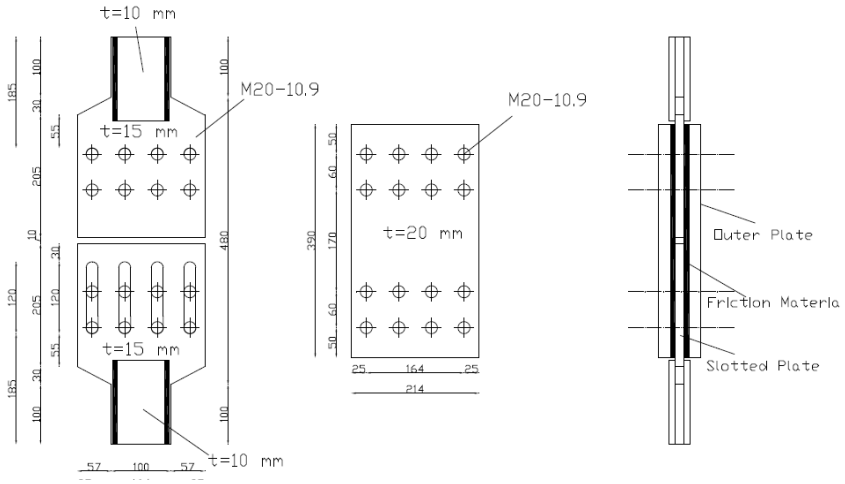

Figure 108 The experimental set-up of preliminary investigations by Latour et al. *(2014)*

Latour et al. (2014) carried out an experimental campaign to investigate effects of six different friction materials on supplemental damping devices. Six interfaces have been tested: steel–steel, brass–steel, sprayed aluminum–steel and three different rubber-based friction materials used in automotive applications, electrical machines and applications requiring low wearing, respectively. In the conclusions the authors of Latour et al. (2014) highlighted that the sprayed aluminum exhibits the most stable and predictable hysteretic response.

Based on this, the preliminary analyses presented hereinafter are carried out for sprayed aluminum–steel interfaces. The following paragraphs present the numerical assumptions (which were partially applied also for the lap-shear tests presented afterwards) and the obtained results.

4.2.1.1 FE modelling assumptions

The Finite element models were developed in ABAQUS v.6.14. The geometries of the numerical models were nominally identical with those of the tested specimens (Latour *et al.*, 2014) and reported in Figure 108 and Figure 109. The coating layer was modelled as an individual element. The model used solid finite element type C3D8I (an 8-node linear brick, incompatible mode) for all steel plates and high strength bolts. The element choice was based on its capacity to avoid the shear-locking, which can significantly affect the initial stiffness of connection.

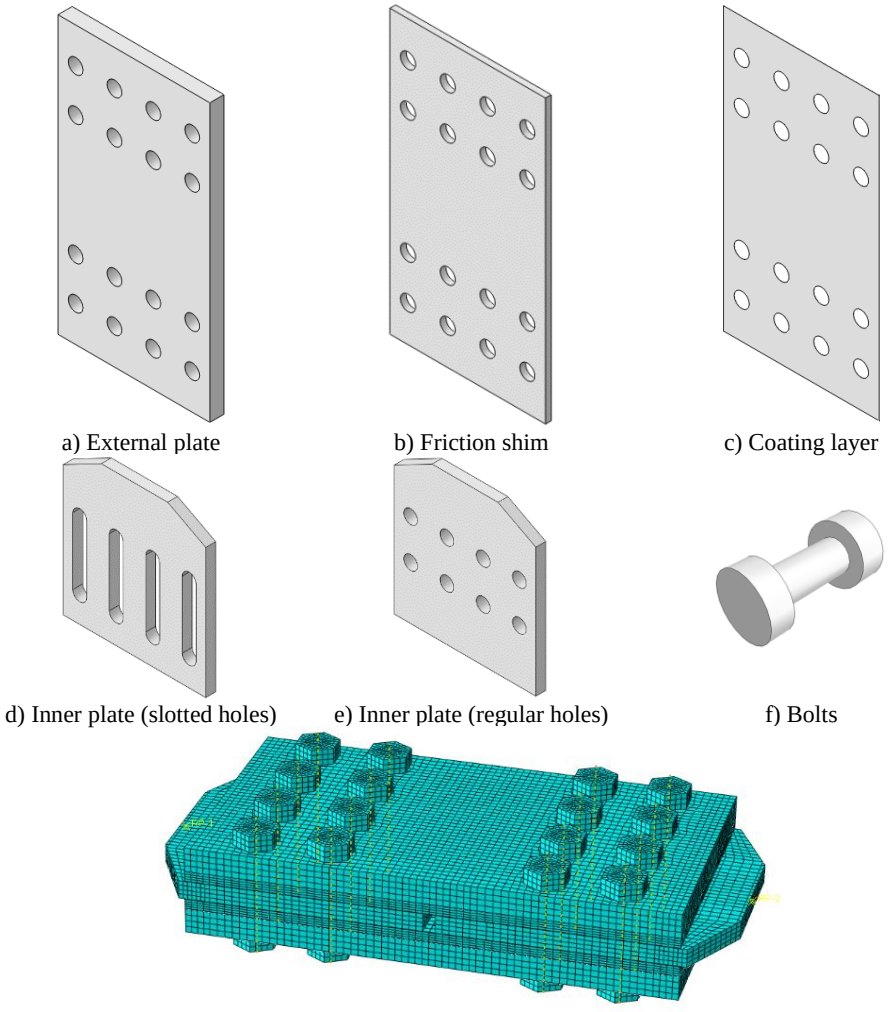

a) External plate b) Friction shim c) Coating layer

d) Inner plate (slotted holes) e) Inner plate (regular holes) f) Bolts

g) Meshed assembly

Figure 109 Meshed FE model

The steel properties for plates were modelled considering the nominal elastic properties, while the non-linear behavior was modelled by means of the von Mises yield criteria. Plastic hardening was represented using a nonlinear kinematic and isotropic hardening. Metal plasticity was considered for the coating layer as well. The true stress-true strain curves adopted for plates are given in Figure 110

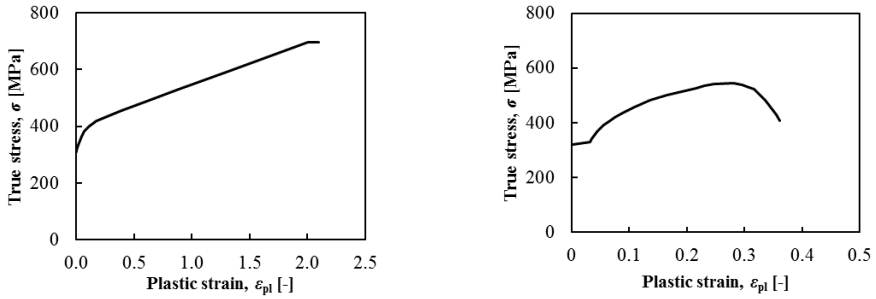

a) Coating material b) Steel

Figure 110 Plastic true-stress – true strain curves

The bolts were modelled by meshing a solid cylinder having the nominal circular gross area of the bolt and the true stress – true strain curves were derived from D'Aniello et al. (2016 and 2017).

All possible interactions (bolt head to outer plate, bolt shank to corresponding bolt hole, plates in contact) are modelled by means of "Surface to Surface contact" with finite sliding formulation. Both tangential and normal behavior are considered, the former using a "Penalty" friction formulation together with "slip-rate-dependent data", while the latter using the "Hard-Contact" formulation. "Tie" constraints were used to model the bond between the M4 coating layer and the steel shim.

The bolt clamping was modelled using the "Bolt load" feature available in the FE software and the design preload value was imposed. The clamping was applied in an individual step prior to the application of the loading protocol.

The external restraints were simulated by attaching to reference points (RP) the nodes belonging to the end portion of the internal plate of the device. The displacement history was imposed on the RP located at one end of the device.

In order to reproduce the temperature variation and propagation due to heating induced by friction, the thermal properties were also taken into account. The Specific Heat c was set equal to 4.52E+8 mJ/ton/^{o}C, the Thermal Expansion α_L was assumed equal to 1.26E-5 mm/mm/ ^{o}C and the Thermal Conductivity k equal to 48 mW/mm/ ^{o}C..

To investigate the computational efficiency and accuracy of the types of analysis, both dynamic implicit and explicit analyses have been carried out. The results show that both FE solvers are effective to simulate the overall behavior of the friction connections. Generally, implicit analyses provide more steady results than explicit ones. On the other hand, explicit analyses show more accurate force-displacement curves (Figure 111) which may be perceived as more evocative of the experiment as "slip-rate-dependent data" was used. Another advantage of explicit analyses is the significantly lower computational time (up to four times lower compared to the equivalent Implicit analyses in this investigation). However, this comes at the cost of uncertainty with regards to the correctness of the results, the explicit analyses being very sensitive to inertial effects.

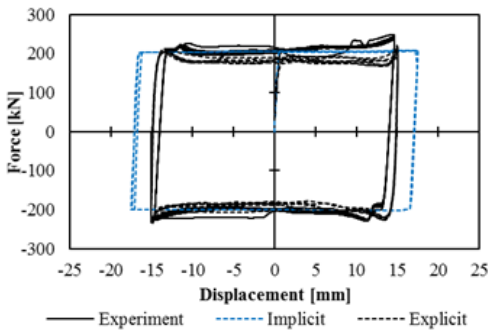

Figure 111 Comparison of Implicit and Explicit analyses for same experimental test

4.2.1.2 Results of preliminary analyses

The calibrated numerical model was used to investigate several parameters:

- The effect of reverse loading,
- Preload magnitudes,
- Number and arrangements of preloaded bolts
- Slip-rate and pressure dependency of friction coefficient

Figure 113 explains the meaning of the labelling used for the finite element analyses. Additional symbols added at the name end represent: R-reversed loading, SRF – strain rate dependent friction coefficient. Table 32 summarizes the features of the investigated models, while. Figure 113 depicts the difference between a square (SQ) and a straight (ST) distribution of the preloaded bolts.

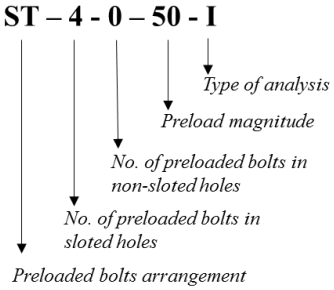

Figure 112 Labelling for the analyses performed

Table 32 The set values of the parameters

FEA	***Number of Bolts preloaded***		***Preload Magnitude***	***Total Magnitude***
	Slotted	***Non-Slotted***		
Implicit	4	0	50 kN	200 kN
	4	4	50 kN	200 kN
	4	0	75 kN	300 kN
	4	4	75 kN	300 kN
	4	0	100 kN	400 kN
	4	4	100 kN	400 kN
Explicit	4	0	50 kN	200 kN
	4	4	50 kN	200 kN
	4	0	75 kN	300 kN
	4	4	75 kN	300 kN
	4	0	100 kN	400 kN
	4	4	100 kN	400 kN

It is important to highlight that, for this parametric study, the bolts were assumed elastic and their diameter was kept constant while increasing the preloading magnitude.

The results obtained from the parametric study are discussed hereinafter in terms of

i) sliding force – displacement;
ii) total bolt preload – displacement;
iii) friction coefficient – displacement;
iv) pressure dependency of friction coefficients.

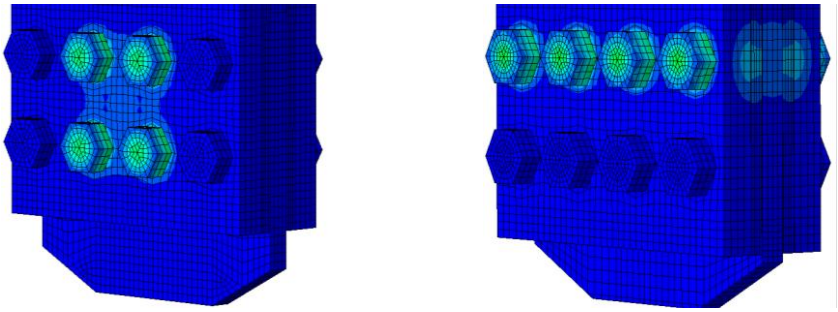

a) Square (SQ) distribution of preloaded bolts b) Straight (ST) distribution of preloaded bolts

Figure 113 Preloaded bolts distribution in assembly

4.2.1.2.1 Sliding force vs. displacement

Figure 114*a* shows the numerical response curve of model ST-4-0-50-I. In this model only one row of bolts at the level of the slotted inner plate are preloaded with 50 kN each and the rest are preloaded with 1 kN in order to increase the model stability.

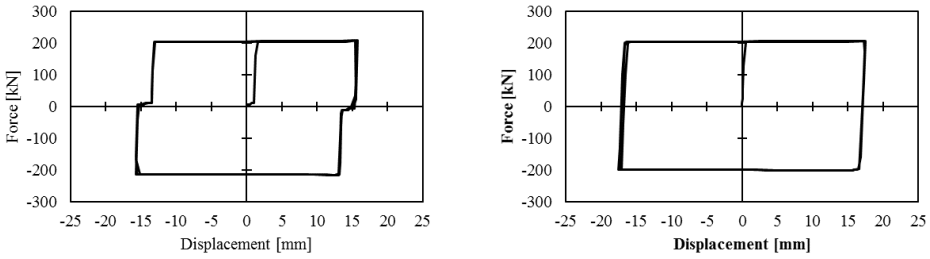

a) ST-4-0-5-I (one bolt row pretensioned) b) ST-4-4-5-I (two bolt row pretensioned)

Figure 114: sliding force vs displacement from implicit analysis

This kind of arrangement leads to "elbows" in the force-displacement plot. This effect indicates that when the uniaxial loading changes direction, there is a rigid body motion until the bolt shanks in non-slotted holes reach the facing hole surface. This rigid body motion gives a hint about the structures post-earthquake re-entering. Namely, the bolts in the normal holes of the friction connections, preloaded with smaller clamping forces, lead to smaller sliding forces. In this way the stiffness of the adjacent elastic frames can counterbalance the residual deformation, and therefore the re-cantering of the structure is facilitated. When both bolt rows (slotted inner plate and normal inner plate) are preloaded (see Figure 114*b*), there is no rigid body movement which is as expected.

Implicit analyses were proved not suitable for this set of analyses, as the degradation of the strength with the cycles was not captured (Figure 114).

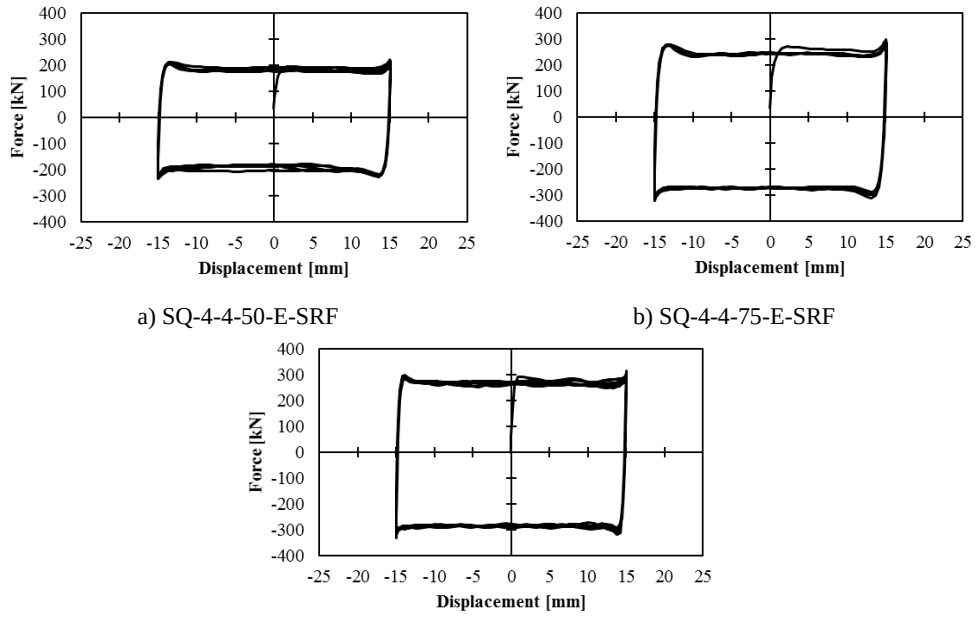

a) SQ-4-4-50-E-SRF

b) SQ-4-4-75-E-SRF

c) SQ-4-4-100-E-SRF

Figure 115: Sliding force vs displacement from explicit analysis.

The response from explicit analyses is shown in Figure 115. The plots have been obtained using slip-rate dependent friction coefficients. These curves show the stick-slip friction phenomenon in the upper right and lower

left corners of the hysteretic curves. During the first sliding, the shear force is higher due to the static friction. Subsequently, the dynamic friction mechanism is activated, and the sliding force decreases with the cumulative displacement. Moreover, during direction changes, the friction coefficient turns back to static for a moment, and this mechanism is repeated for each cyclic loop.

4.2.1.2.2 Total bolt preload vs. displacement

The bolts clamping force vs. the imposed slip of two distinctive models (i.e. SQ-4-4-50-E-SRF and SQ-4-4-75-E-SRF) are reported in Figure 116, where a ±2~3% fluctuation can be observed together with slight decrease of total preload force for each cycle. However, again this was not very noticeable in sliding force-displacement and friction coefficient-displacement plots.

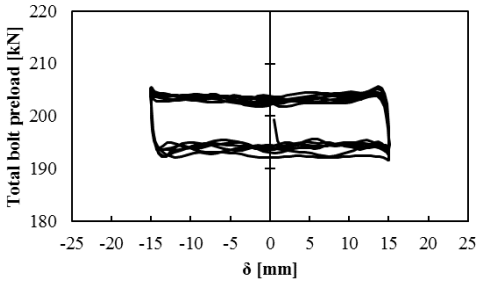

a) SQ-4-4-50-E-SRF

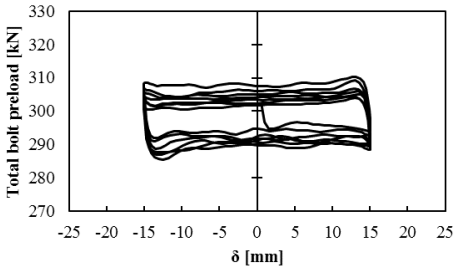

b) SQ-4-4-75-E-SRF

Figure 116: bolt preload vs. displacement *from explicit analysis.*

4.2.1.2.3 Friction coefficient vs. displacement

The small fluctuations of preloading forces don't reflect in the displacement plots vs. friction coefficients and sliding forces. Apart from small differences at direction changes due to modelling with and without slip-rate friction coefficient in explicit analyses, cyclic shape of the friction coefficient-displacement plots of the analyses are almost the same. The friction coefficient μ is determined as follows. The obtained results are summarized in Table 33 and Table 34.

$$\mu = \frac{F_{slip}}{n_s \cdot n_b \cdot N_b} \tag{4.7}$$

Where n_s is the number of surfaces in contact, n_b is the number of bolts, F_{slip} is the sliding force and N_b is the bolt preloading force from the output history of analyses.

Table 33 Given and obtained friction coefficients

	ST-4-0-50-I	***ST-4-4-50-I***	***ST-4-0-75-I***	***ST-4-4-75-I***	***ST-4-0-100-I***	***ST-4-4-100-I***	***ST-4-4-125-I***	***ST-4-4-200-I***	***ST-4-0-375-I***
Given	0,51	0,51	0,45	0,45	0,35	0,35	0,35	0,3	0,3
Max Avg.	0,519	0,508	0,454	0,448	0,353	0,354	0,357	0,297	0,292
Min Avg.	-0,517	-0,507	-0,452	-0,447	-0,347	-0,348	-0,347	-0,296	-0,299

	ST-4-4-375-I	***ST-4-0-500-I***	***ST-4-4-500-I***	***ST-8-8-200-I***	***ST-4-4-50-E***	***ST-4-4-50-E-K***	***ST-4-4-75-E***	***ST-4-4-100-E***
Given	0,3	0,3	0,3	0,3	0,51	0,51	0,45	0,35
Max Avg.	0,298	0,299	0,305	0,298	0,508	0,484	0,447	0,349
Min Avg.	-0,292	-0,296	-0,299	-0,288	-0,503	-0,481	-0,445	-0,347

Table 34 Given and obtained friction coefficients and slip rate data

	ST-4-4-75-E-SRF		***SQ-4-4-50-E-SRF***		***SQ-4-4-75-E-SRF***		***SQ-4-4-100-E-SRF***		***SQ-4-4-50-E-SRF-R***	
Given friction & Slip rates	0,5	0 mm/s	0,54	0 mm/s	0,5	0 mm/s	0,4	0 mm/s	0,54	0 mm/s
	0,44	1100 mm/s	0,5	1100 mm/s	0,44	1100 mm/s	0,35	1100 mm/s	0,5	1100 mm/s
Max Avg.	0,447		0,484		0,431		0,353		0,493	
Min Avg.	-0,445		-0,49		-0,457		0,363		0,5	

4.2.1.2.4 Pressure Dependency of Friction Coefficients

In order to investigate the pressure dependency of friction coefficients, contact area information and normal forces due to contacts for each interaction are recovered from the FEAs. It is possible thus to establish a relation between the measured frictional force from experiments, the contact pressure and its associated area of contact by means the following expression:

$$F_f = \mu\left(F_{pre}\right)\cdot F_{pre} \approx \int_A \mu(P)\cdot P\cdot dA \approx \sum_i \mu\left(P_i\right)\cdot P_i\cdot A_i \approx \mu\left(F_N\right)\cdot F \quad (4.8)$$

Where F_f is the friction force measured during experimental tests, F_{pre} is the normal force measured during experimental test (pretension), F_N is the normal force obtained from FE simulation, P is the contact pressure obtained from FE simulation, A is the contact area obtained from FE simulation, $\mu(F_{pre})$ is the friction coefficient calculated from experimental results and $\mu(F_N)$ is the friction coefficient generated from relationship between experimental results and FE simulation

As it can be seen in Figure 117 regardless of the load application direction (pulling or pushing), the contact area is slightly decreasing while contact pressure is increasing.

In addition to this, no matter the preloading magnitude (and therefore contact pressure), the measured contact areas are always following the same trend in the simulations of uniaxial experiments of friction devices, as it can be seen in Figure 118. This situation also shows that materials are rigid enough not to be affected by contact pressure. The slight decreasing of contact area might be a consequence of elastic/plastic strain of the surfaces or bending of plates in a small extent.

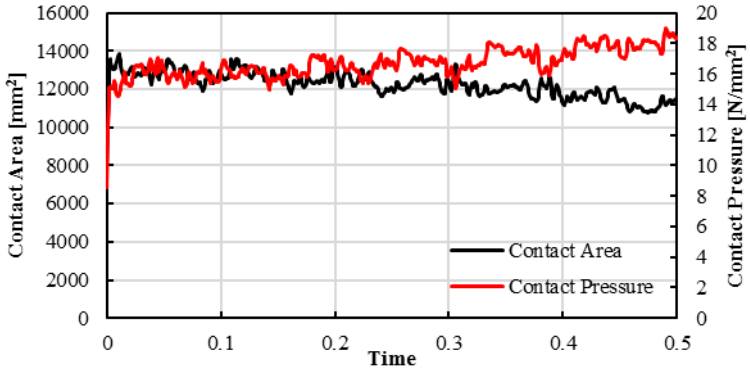

Figure 117: Contact area vs. Pressure.

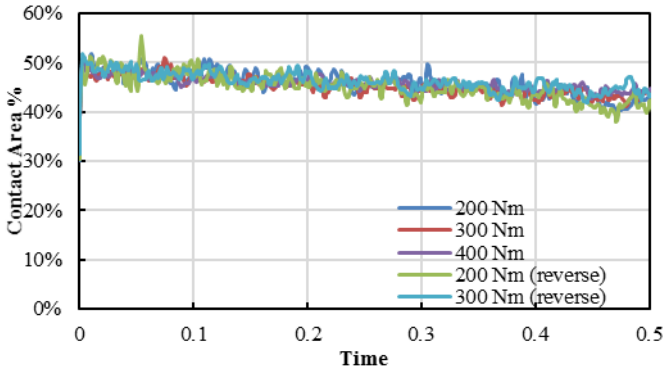

Figure 118: Contact Area Percentages of Slotted Inner Plate for Different Preload Torques.

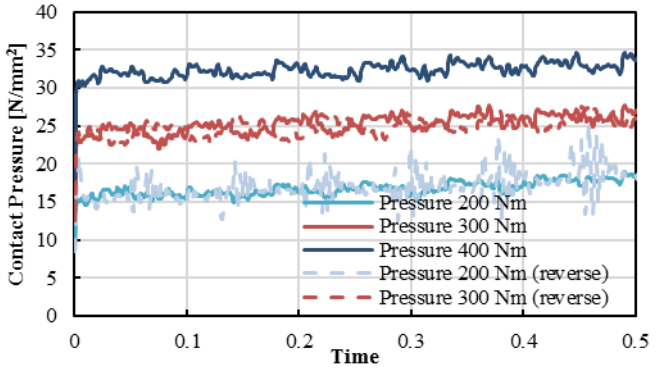

Figure 119: Contact Pressures of Slotted Inner Plate for Different Preload Torques.

However, the experiments indicated that higher preload magnitudes result in lower friction coefficients due to the tribological characteristic of the coating layer. In addition, with the continuous motion, very slight degradation of friction was observable, which might be due to the loss of contact area and the increase of pressure, which is also seen during analyses.

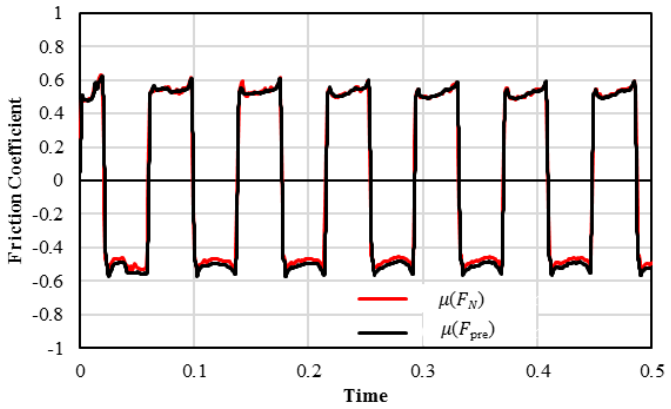

Figure 120: Friction coefficients generated from relation between experiment of 200 Nm and FE simulation $\mu(F_N)$ vs $\mu(F_{pre})$

As it can be seen in Figure 120, the branches of positive friction coefficients, namely, during pulling phase, are perfectly matching each other. However, during pushing phase, $\mu(F_N) < \mu(F_{pre})$ this slight difference might be due to lack of real-time measuring of preload magnitude during the experiment. There was a ±2~3% alteration of total preload force in the simulations, which made $\mu(F_N)$ smaller. The situation on the reverse analysis, where the inner plate is initially pushed instead of pulled, compared with the normal experiment, supports the explanation made i.e. $\mu(F_N)$ becomes smaller than $\mu(F_{pre})$ while pushing, and larger while pulling.

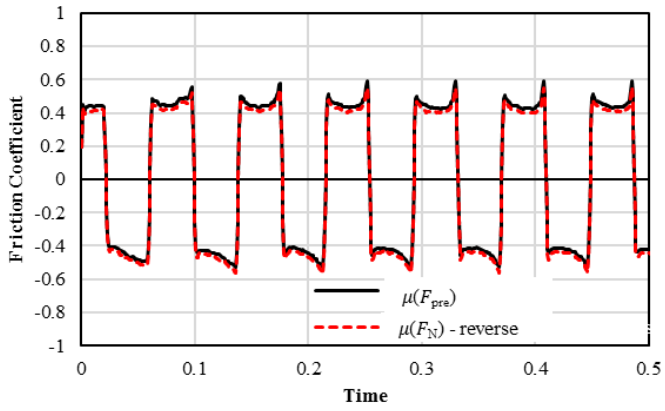

Figure 121: Friction coefficients generated from relation between experiment of 300 Nm and FE simulation $\mu(F_N)$ $\mu(F_N)$ vs that calculated from experiment $\mu(F_{pre})$

Overall, the friction coefficients $\mu(F_{pre})$ calculated from only experimental outputs and $\mu(F_N)$, the ones generated from the relation between experiment and FE simulation are in good agreement. This situation supports the reliability of the obtained contact area and contact pressure values from simulations.

In addition, it is found that contact pressure ratios of different preloaded analyses and contact pressure ratios at the beginning and ending of the analyses, fit with the decrease of friction coefficients observed from experiments. Therefore, the pressure information obtained from simulations can be considered reliable enough to corelate contact pressure and friction coefficients. In this way, the effect of preload magnitude together with slight degradation of friction with motion can be modelled by implementing pressure-dependent friction coefficients along with rate-dependent ones.

4.2.2 The lap-shear testing program

Based on the preliminary experimental investigations performed in the past (Latour et al., 2014) and on the numerical simulations previously presented, some conclusions could be drawn on the response of lap-shear sub-assemblies and some materials (the importance of the relative material hardness, the contact pressure/area dependency, preload distribution, etc.).

However, for the purpose of selecting the optimal friction material, the preload application technique and assessment of the influence of several parameters (preload magnitude, washer type, etc.,) a new set of experimental and numerical investigations were due within the framework of the FREEDAM research project. Only a summary of the relevant parts of the experimental campaign will be presented hereinafter, as this work was carried out with only a small contribution from the part of the author. These results

were published, together with the numerical investigation presented in the following chapter, in Zimbru *et al*. (2018).

4.2.2.1 Tested friction interfaces

The tested sub-assemblies regard, as explained in higher detail in the next section, elementary lap-shear friction connections with two bolts which, similarly to the dampers of a Symmetrical Friction Connection (SFC), are realized combining a slotted steel plate with friction shims made of mild steel coated with one of the materials subsequently described. The materials employed to coat the shims are selected in order to provide to the interface high values of the friction coefficient, with minimum deterioration, guaranteeing contemporarily the durability.

Pursuing this objective, the selected materials must be corrosion resistant and, based on previous experience (Ramhormozian *et al.* 2014, Latour *et al*., 2014, EN1090), they should be characterized by a superficial hardness strongly different from that of the internal steel plate. Indeed, a difference of superficial hardness of the plates in contact, as already demonstrated in technical literature by many authors, is for metals, a fundamental feature.

In fact, the friction coefficient, from a theoretical point of view, due to reasons of superficial interaction, tends to be governed by the ratio between the shear resistance of the weakest material (s_0) and the superficial hardness of the softest material (σ_0) (Latour *et al.*, 2014, Bowden & Tabor 1950) namely $\mu = s_0/\sigma_0$. Consequently, in order to obtain a high value of the sliding force, a high value of the shear resistance of the weakest material and/or a very low value of the superficial hardness of the softest material are needed.

If the internal plate of the friction damper is made of stainless steel AISI 304, which is characterized by a superficial hardness of about 130 HV, then the coating of the friction shims must be characterized by a much lower or

much higher value of the superficial hardness. In order to achieve this scope, the selection of the material for the friction shims has been carried out considering alternative possibilities, in which stainless steel has been combined with five "soft" materials labelled as M1 to M5 and three "hard" materials labelled as M6 to M8.

The "soft" materials are non-ferrous metals with hardness ranging from about 5 to 30 HV, while the "hard" materials in two cases (M6 and M7) are carbide alloys produced as powder blends and in the other case is nickel and diamond. The three hard coatings have a superficial hardness ranging from about 550 to 1200 HV. All the materials are applied on the steel plates by means of Thermal spray techniques, except for material M8 which was applied using chemical bonding.

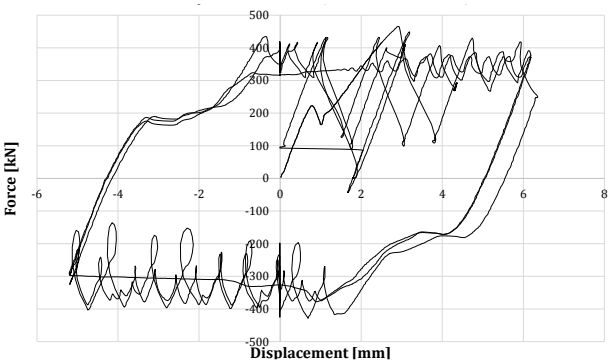

a) Stick-slip phenomena (material M7)

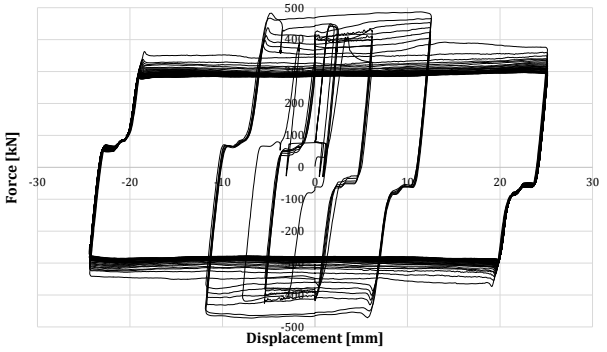

b) Strain hardening (material M8)

Figure 122 Undesired response of friction materials

It is useful to note that when stainless steel is combined with harder materials, the consumption of the steel plate is promoted and, therefore, the friction coefficient obtained is mainly governed by the ratio between the shear resistance and superficial hardness of the steel plate. Conversely, when steel is combined with a softer material, the wearing of the interface is due essentially to the consumption of the friction shims and the friction coefficient mainly depends on the ratio between the shear resistance and the superficial hardness of the material employed to coat the friction shim.

A number of 13 tests have been performed to preliminary assess the performance of the materials. Based on these tests five materials have been excluded due to their poor response. The materials M2, M3, M5 and M7 exhibited significant stick-slip phenomena, characterized by the sea-saw teeth hysteretic response (like depicted in Figure 122 *a* for M7) and the results of the test on the M8 showed severe strength degradation due to strain hardening in the initial cycles (Figure 122 *b*). For the subsequent tests only the three remaining materials (M1, M4 and M6) were considered, given their stable hysteretic response.

4.2.2.2 Adopted coating techniques

In the present experimental program seven out of eight materials have been applied on friction shims by means of thermal spray, while the remaining material, as above said, has been applied through electroless nickel plating. In general, thermal spraying is an industrial procedure to apply coatings by means of special devices/systems through which molten metals are propelled at high speed on cleaned and prepared surfaces.

In this procedure the coating material is melted by a heat source and then it is propelled by means of gases on a base material, where it solidifies forming a solid layer. For this experimental program, all the specimens coated with thermal spray have been realized following one of the following techniques:

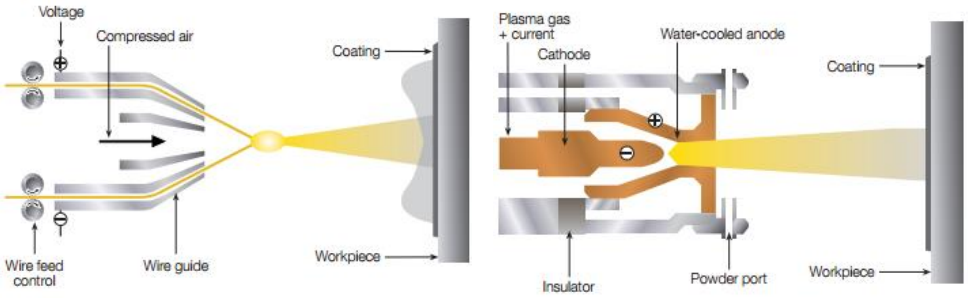

a) . Schematic drawing of the AWS process; b) Schematic diagram of the APS process

Figure 123 Different spray processes (Zimbru et al., 2018)

- ***Arc wire spray (AWS) used for 'soft' materials***. The electric arc wire process is based on the development of heat used to melt the coating feedstock (Figure 123*a*). The two wires are electrically charged with opposed polarities and are fed into the arc gun at a controlled speed. When the wires are at the contact point, the opposing charges on the wires create an arc that melts the tips of the wires. Compressed air is used to atomize the molten material in order to shoot it on a properly prepared workpiece surface. Prior to the coating application, the surfaces need to go through mechanical treatments of blasting and grinding and an adhesion layer is applied.

- ***Atmospheric plasma spray (APS) used for hard materials.*** This process can melt most powder coating materials. The plasma gun uses a chamber with one or more cathodes and an anode (Figure 123*b*). With this process gases flowing through the chamber are ionized such that a plasma plume develops. Afterwards, the feedstock material is injected into the hot gas plume, where it is melted and propelled towards the target substrate to form the coating. This is a more precise process as many of the parameters of application can be controlled (the gas flows, the applied current, the shape and bare size of the nozzle, the point and angle that the material is injected into the plume, the distance of the gun to the target surface.

- ***Electroless nickel plating (3M Gmbh).*** Electroless nickel plating is a process for depositing a nickel alloy from aqueous solutions onto a substrate without the use of electric current. It differs, therefore, from electroplating which depends on an external source of direct current to reduce nickel ions in the electrolyte to nickel metal on the substrate. In the case of the coating produced by 3M Gmbh, diamond powder is added to the bath obtaining a high hardness friction material.

4.2.2.3 Test layout

The typical specimen tested within the current experimental activity is composed by a group of steel plates assembled in order to test the uniaxial behavior of friction interfaces resulting from the coupling of a stainless-steel plate with friction shims coated with one of the eight materials previously mentioned. The tested subassembly is inspired from the specimen layout recommended by EN1090-2 for slip tests. In particular, it is constituted by a slotted steel plate realized in 1.4301 Stainless Steel (EN10088-1, 2005) equivalent to AISI 304 steel, a steel plate with normal holes used to connect the specimen to the testing machine and external steel plates and friction shims pre-stressed with M20 class 10.9 HV bolts (Figure 124*a*).

The tested specimen aims to simulate the same conditions that are expected in the friction damper of a symmetrical friction beam-to-column connection, like the one proposed in the FREEDAM project. The stainless-steel plate with slotted holes simulates the haunch flange or rib, while the external steel plates simulate the webs of the L-stubs used to fasten the friction damper to the face of the column.

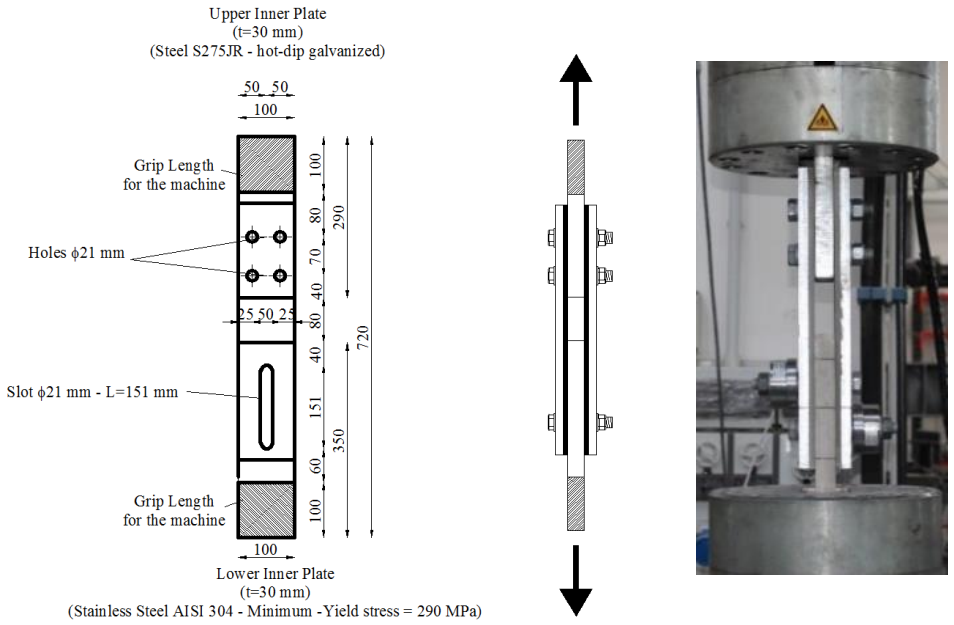

a) General geometry b) Specimen in the set-up

Figure 124 Lap shear specimen (Zimbru et al., 2018)

The loading protocol is that suggested by EN 15129, with variable displacement amplitudes ranging from a minimum of 6.25 mm to a maximum of 25 mm. The maximum amplitude has been defined providing a realistic estimate of the displacement demand arising at the friction damper level in current applications. The cycles were executed at increasing values of the speed, defined in order to remain in a quasi-static range and within the capabilities of the equipment. The cycles' velocity varied from 1 mm/s for the first 10 cycles to 5 mm/s for the cycles at the maximum amplitude.

In each test, both the upper and lower M20 high strength bolts have been tightened by means of a torque wrench, in order to reach the proof load equal to 171.5 kN (calculated in accordance with EC3 1-8).

All the tests have been carried out employing a universal testing machine Schenck Hydropuls S56 (Figure 124*b*). Different sensors have been used before and during the test to control continuously the bolt force, the slippage load, the tightening torque and the displacement. The axial displacements of

the device have been read directly from the transducer of the testing machine and, in the same way, the slippage force has been controlled directly exploiting the load cell of the machine. Before the test, the tightening torque has been applied through a hand torque wrench and monitored by means of a torque sensor and the pretension applied to the bolts has been monitored before and during the test by means of donut load cells installed in the connection under the nuts of the bolts used to pre-stress the friction interface.

4.2.2.4 Experimental results

4.2.2.4.1 Behavior of "hard" materials

A synthesis of the results of the tests on the interfaces coupling stainless steel with friction shims coated with the "hard" coatings M6, M7 and M8 are delivered in Figure 125, where the hysteretic curves of one of the two identical tests performed on each material are reported. In case of M6 carbide coating, the cyclic response has been characterized by the development of an initial value of the slip force equal to about 350 kN, followed by a progressive degradation that, at the end of the test amounted about 20%.

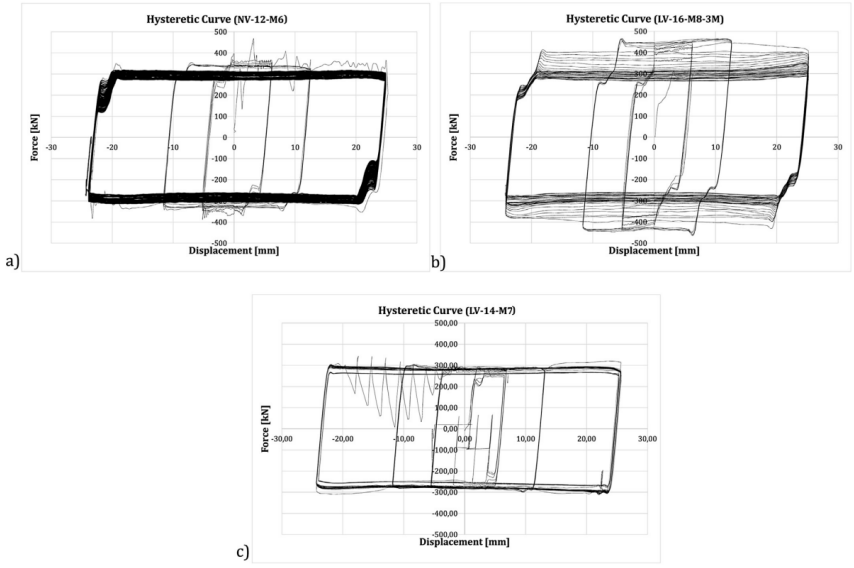

Figure 125 Hysteretic behavior of hard materials: a) M6 b) M8 c) M7

The hysteretic curve was affected by an initial stick-slip phase with the development of a first unstable cycle characterized by jumps of the force and sudden releases of energy. Nevertheless, after this first cycle, that probably allows to break the initial interatomic attraction between the surfaces in contact (adhesion component of friction), the slippage occurred regularly leading to a very stable response up to the end of the test.

In case of M7 carbide coating, globally, a similar response was observed. The behaviour, in this case, was characterized by an initial slip force equal to about 250 kN, that after few cycles increased slightly, stabilizing at a value of about 300 kN. Nevertheless, in this case a stronger stick and slip behavior was observed and it was necessary to reduce the velocity to perform the test. Material M8, was characterized by a response that, as already observed in past tests performed in the laboratory, with other materials such as brass or some types of phenolic rubbers (Tokoyama & Oki, 2010), with two different phases. A first phase where the interface provided a strain hardening behavior characterized by an increase of the slippage resistance of about 60% and a second phase characterized by a reduction of the slippage force which, at the end of the degradation returned to the initial value. In addition, in this case no stick and slip response was observed and all the cycles were characterized by a stable value of the slippage force. The initial value of the slippage force has been of about 400 kN. After the tests, the specimens have been opened in order to evaluate the damage of the interfaces, observing that, as expected, due to the higher hardness of the coating layer with respect to stainless steel, the greatest part of the damage was concentrated on the internal plate which at the end of the test had many scratches in the zone located underneath the bolt head. In Figure 126 is reported, for the specimen with friction pads coated with M6 carbide, a diagram of the bolt forces and of the friction coefficient, obtained dividing the slip force by the bolt forces read continuously during the test through the annular load cells, versus the cumulative travel done by the

damper. From such a figure it is possible to observe that both bolts, which are initially tightened in order to reach the proof load equal to 171.5 kN, after the first cycle of the loading history lose about the 7% of the initial pre-load and afterwards they uniformly loosen during the test reaching at the end a total loss of about 20%.

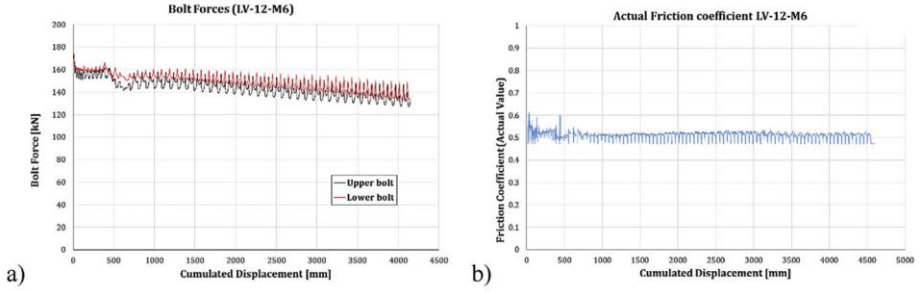

Figure 126 Bolt forces and friction coefficient vs cumulative travel Zimbru et al (2018)

Clearly, this initial loss, that seems to occur just after the first sliding of the connection, should be properly accounted for in the design of the damper. From the comparison between Figure 125 and Figure 126 it is possible to note also that the degradation of the sliding force observed during the test is essentially due to the degradation of the bolts' forces. In fact, they both degrade of about 20% while the friction coefficient remains constant. Even though, for the sake of simplicity, detailed graphs representing the behavior of the bolts and the degradation of the friction coefficient for the other materials are not reported, analogous results have been obtained for all the other "hard" interfaces. Therefore, also for the other interfaces a correspondence between the bolts' loosening and degradation of the sliding force has been observed.

4.2.2.4.2 Behavior of "soft" materials

Similar to M7, also some of the soft materials exhibited a behavior characterized by the stick-slip phenomenon. This is the case of three of the selected non-ferrous metals, namely M2, M3 and M5, whose response was characterized by alternate stops and starts of the motion with strong and

sudden releases of energy (Figure 127*a* and Figure 127*b*). Therefore, in all these cases the tests have been stopped prematurely in order to prevent damage to the testing equipment. For these materials, as reported in Figure 127*a* and *b*, the initial slippage force was equal to about 200 kN and was followed by an increase of the slippage resistance up to about 400 kN which corresponds to a value of the friction coefficient equal to about 0.58. Obviously, their cyclic behavior is not appropriate for seismic applications.

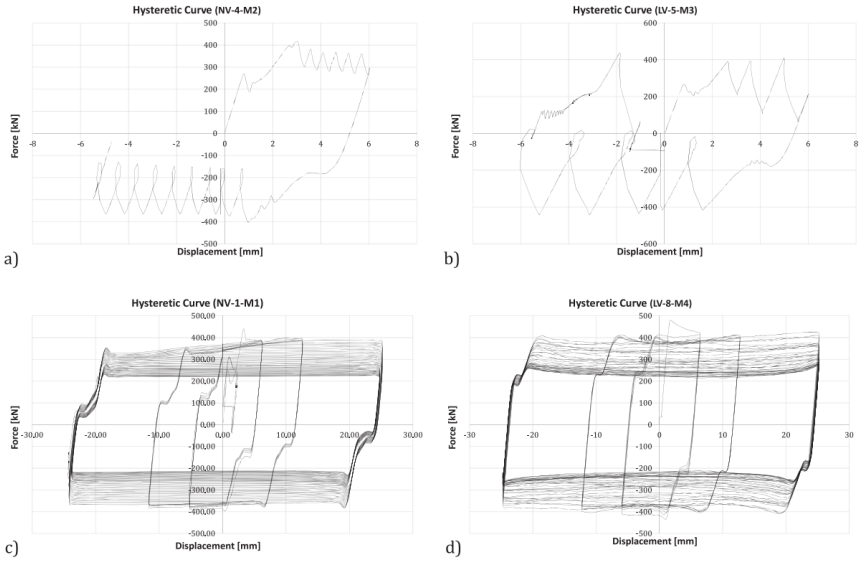

Figure 127 Hysteretic behavior of soft materials. a) M2, b) M3, c) M1, d) M4

Conversely, M1 and M4 metals have exhibited a very similar behavior (Figure 127c and d). Their hysteretic response has been characterized by a value of the slippage force higher than the corresponding obtained with the "hard" materials but, on the other hand, they have also provided a more significant degradation due to both bolt loosening and damage occurring in the friction pads.

In Figure 128 are represented the results expressed in terms of friction coefficient and bolt forces versus the cumulative sliding, for the two tests on the specimens with M4 friction pads. From these graphs, even though the

actual value of the friction coefficient does not vary in the two tests, the bolts provide a significantly different behavior leading, consequently, to a different hysteretic response.

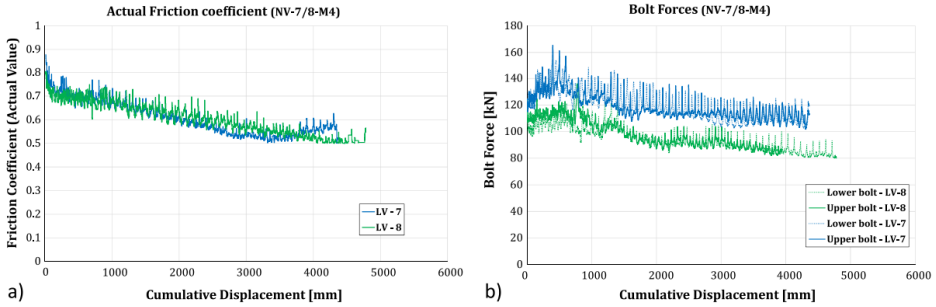

Figure 128 a) Actual friction coefficient- M4; b) Bolt forces – M4

In one of the two tests, after the first sliding, a sudden loss of bolt pretension of about 15% led to a proportional loss of the sliding force. Such a different response of the specimens can be probably due to the imperfections of the coating applied on the friction shims, which for soft coatings is completely manual and leads to a non-uniform spreading of the coating metal. Material M1 has a degradation of the slippage force at the end of the tests of 45%, while for M4 it was of about 50%. Nevertheless, both materials provided very high values of the friction coefficient and, the initial friction coefficient of materials M1 and M4 were equal to about 0.55/0.65 and 0.7/0.9, respectively.

As in the previous cases, also the specimens realized with soft materials were opened after the test, in order to evaluate the damage of the interfaces. As expected, in these cases the damage was mainly concentrated on the friction shims, while the stainless-steel plates were practically undamaged after the test.

4.2.3 Numerical analyses on the tested specimens

Very conclusive results were achieved from the extended testing campaign, of which only a small part was previously presented, and most of the questions regarding issues like the friction coefficient, preload level, preloading technique etc., were addressed. Therefore, there was no point in addressing them using also numerical methods.

However, aspects which were not clarified by means of experiments were investigated using FE software. The main points investigated are the contribution of the disc springs function of their number and the effect of temperature observed during the experimental tests. These further FE analyses were performed considering only two of the most performant materials: M4 (‘soft material’) and M6 (‘hard material’)

The FE models created have the geometry of the experimentally tested specimen (Figure 124*a*) and use the numerical assumptions presented in the previous section. The geometry of the fixed part was disregarded in order to decrease computational demand, as it has no influence on the results (see Figure 129).Table 35 reports the name of the experimental specimens with the corresponding number of disc springs (DS).

The numerical results are discussed based on the following outputs:

- Sliding Force [kN] - Displacement [mm] / Time [s]
- Total Preload Magnitude [kN] - Displacement [mm]
- Temperature [kN] - Displacement [mm] / Time [s].

Table 35 ID of specimens with disk springs

No. of DS	M4	M6
9 DS	NV 17	NV 21
6 DS	NV 18	NV 22
3 DS	NV 19	NV 23
0 DS	NV 20	NV 24

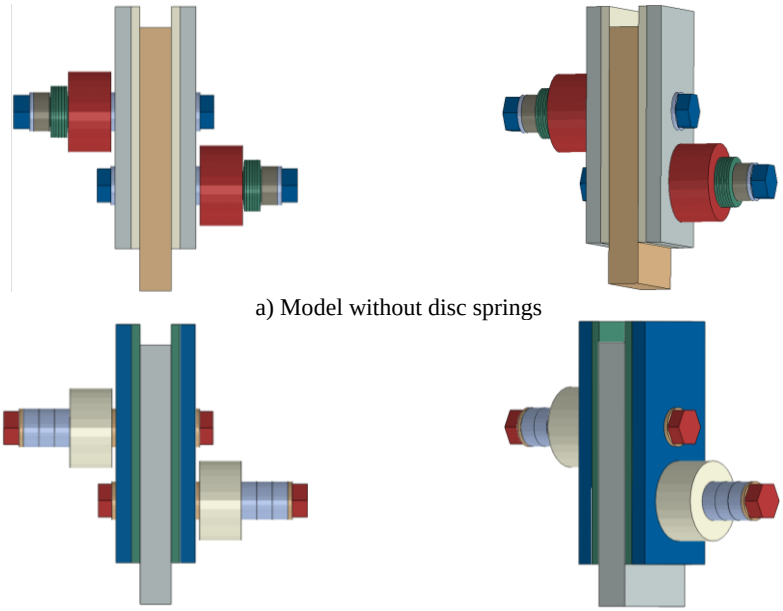

a) Model without disc springs

b) Model with disc springs

Figure 129. Geometry of Uniaxial FREEDAM sub-assembly with different number of disc springs

4.2.3.1 The influence of DS in lap shear joints with M4

Calibrating the models for each experiment with different number of springs is done in the way of manipulating preloading magnitude and friction coefficient to match the sliding force-displacement curves of experiments.

As observed during the experimental tests, material M4 exhibits significant degradation during the slip, resulting in a more difficult modelling. No significant differences in terms of loss of preload or degradation of friction coefficient was observed between the models with varying number of DS (see Figure 130b). However, as temperature increases because of continuous sliding of plates, friction coefficient decreases according to given temperature-dependent input data (see Figure 130a). The sliding force – displacement curves are depicted in Figure 131), where it can be recognized the distinct degradation of the slip capacity cycle by cycle.

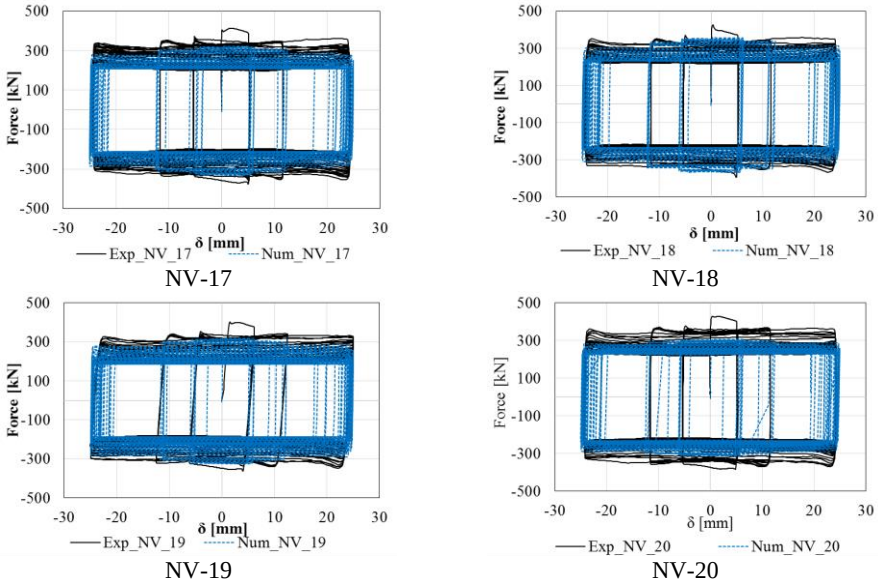

Figure 130 Lap shear joints with material M4: Sliding Force [kN] - Displacement [mm]

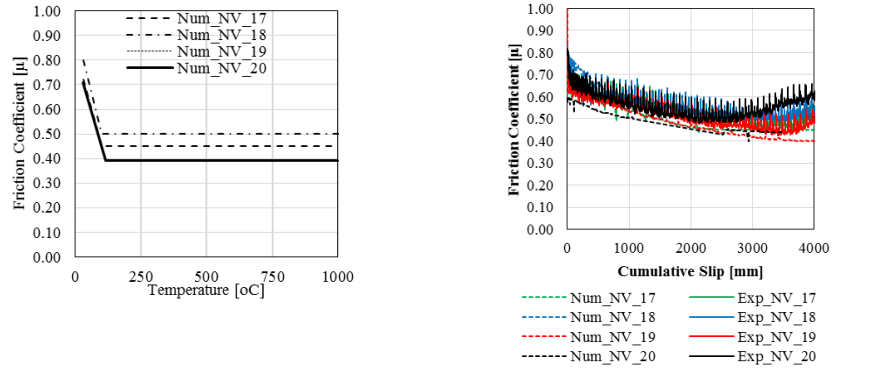

a) Temperature dependent friction coefficient b) Friction coefficient – displacement curves

Figure 131 The friction coefficient curves for lap shear joints with material M4

4.2.3.2 The influence of DS in lap shear joints with M6

Figure 132*a* shows for model NV-21 that the temperature in the assembly elements (bolts and plates) increases with cumulative sliding. As expected, the energy dissipated by friction is converted to thermal energy. It was observed that after 3000mm of cumulative slip, the average temperature difference between plate surface and bolt is about 15 to 20°C for all models. Even though thermal properties are modelled as mentioned before, it seems that the preload

forces have not been affected significantly and they remain constant in the models (see Figure 132b), mostly because the thermal expansion occurs in both the plates and bolts.

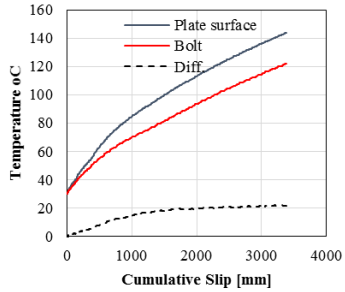

a) Temperature in the model elements

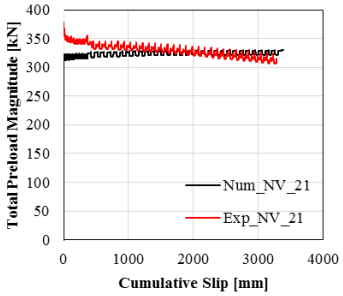

b) Total preload variation

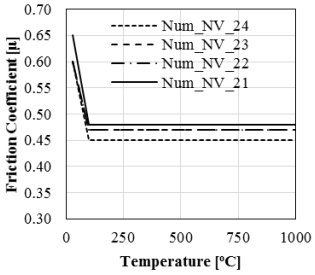

c) Temperature dependent friction coefficient

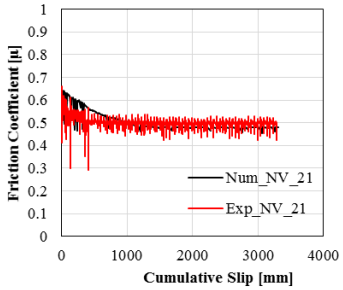

d) Friction coefficient variation

Figure 132. Model NV-21: Sliding Force [kN] - Displacement [mm]

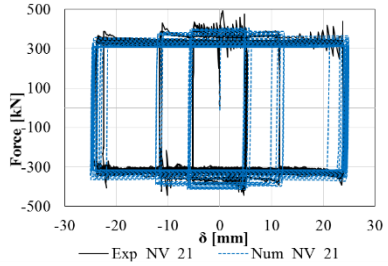

NV-21

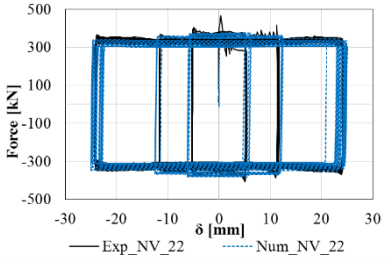

NV-22

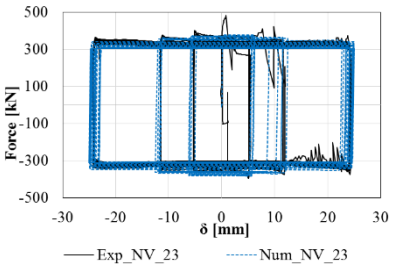

NV-23

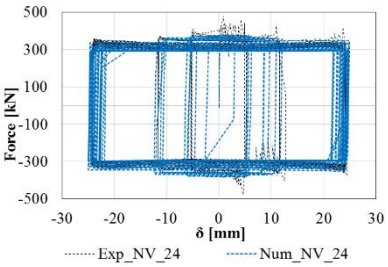

NV-24

Figure 133 Lap shear joints with material M6: Sliding Force [kN] – Displacement [mm]

The partial loss of friction coefficient was modelled in the FE models using temperature-dependent friction laws calibrated based on experimental results (see Figure 132c). As temperature increases because of continuous sliding of plates, friction coefficient decreases accordingly, and as possible to observe in Figure 132d, the model can predict this phenomenon. Figure 133 shows the comparison between the experimental and numerical curves in terms of sliding force and displacement. As it can be observed, the FE model can provide accurate results.

4.3 THE FREEDAM FRICTION CONNECTION

The central part of the FREEDAM project are the friction connections (devices) which will be presented in this chapter. The general configuration as well as the design of the two friction connections tested was established at University of Salerno. The experimental tests were carried out as a collaborative work between the Department of Structures for Architecture and Engineering of University of Naples "Federico II" and the Department of Civil Engineering at University of Salerno. The numerical simulations presented were performed at the former institution.

The proposed moment resisting friction connections are conceived to develop the dissipation mechanism by means of the relative slip into devices located between the lower beam flange and the L-stubs connecting it to the column flange, while the upper flange of the beam is connected to a T-stub bolted to the column. The friction damper is basically composed of a stack of steel plates that are clamped together by means of tightened high strength bolts, which are inserted in the slotted holes of the plates to allow the relative sliding. The web of the T-stub connecting the upper beam flange may be subjected to some moderate plastic bending deformations to accommodate the joint rotation following the sliding of the device, thus enforcing the formation of an ideal center of rotation that prevents the damage of the slab. All other details relative to the investigated connections will be presented hereinafter.

In the aftermath of the numerical and experimental campaigns on the lap-shear sub-assemblies, the following remarks are relevant to the investigation on friction connections:

1. The materials that passed the adequacy criteria by exhibiting a stable behavior, appropriate value of μ, degradation, stick-slip phenomena, etc., are M4 and M6. However, due to the impossibility to

find a reliable provider for friction pads made of M6, the solution deemed as optimal remained M4. This solution was agreed to be also the best in terms of costs and ease of application.

2. The level of preloading applied at the level of the friction damper should be within the limits of 30 – 60% of $F_{p,C}$. Larger values lead to potential damage in undesired areas while lower values are unfeasible due to limited slip resistance.

3. It is possible to model numerically the friction material as a contact interaction which accounts for slip-rate, temperature or pressure dependent data. instead of the actual layer. This allows for faster analyses with the preservation of the accuracy.

This chapter will present the results of the experimental campaign, the numerical validation of advanced FE models as well as the parametric study on the friction configurations designed. The results hereby presented are published in two articles: D'Aniello *et al.*, 2017 and Latour *et al.*, 2018.

4.3.1 Features of joints with removable friction dampers

The examined joints are similar to double split-T connections, where the bottom tee element is replaced by detachable friction dampers, as depicted in Figure 134. The main mechanical difference of the two investigated types of devices is the direction of the friction plane that is horizontal in the case of bolted haunch (hereinafter also identified as '*Configuration 1'*) in Figure 134*a*, and vertical in the case of the bolted rib plate (hereinafter also identified as *'Configuration 2'*) in Figure 134*b*. In both cases the friction pads are made of stainless steel covered by the coating material M4 selected based on the studies on lap-shear tests.

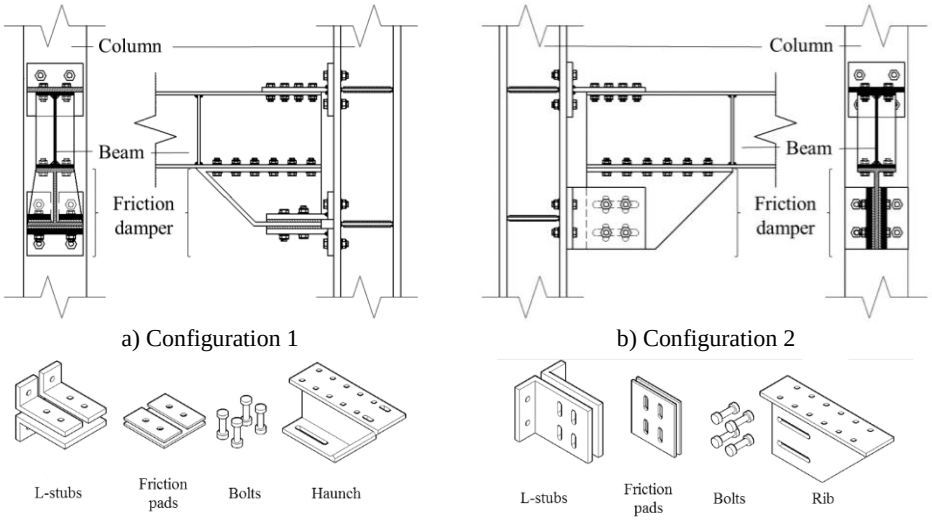

a) Configuration 1

b) Configuration 2

c) Components of the friction damper for configuration 1

c) Components of the friction damper for configuration 2

Figure 134: Geometric configurations of the two friction devices

The friction device of the configuration 1 is made of four main components (see Figure 134*c*), namely the L-stubs, the friction pads, the pre-loadable grade 10.9 HV bolts and the removable haunch, which is detailed with slotted holes on the lower side to facilitate the sliding at the interface with the friction pad, while clearance fit bolts are considered for the upper part of the haunch to prevent its relative sliding as respect to the lower beam flange. The L-stubs are welded built-up and have the role of (i) transferring the bolt forces, (ii) clamping together the friction pads and the haunch, and (iii) connecting the assembly to the column flange.

The friction damper of configuration 2 (see Figure 134*d*) has vertical sliding surfaces. Hence, to allow the relative slip both the mobile part (the rib plate) and the fixed parts i.e. L-stubs and friction pads are detailed with slotted holes.

4.3.1.1 The principle of the friction connections design

The moment resistance of the friction connections ($M_{slip,Rd}$) is assumed equal to the design moment (M_{Ed}), which can be set equal to either the value

obtained from the structural analysis under seismic condition ($M_{Ed,E}$) or the factored resistance of the beam cross section ($M_{pl,b,Rd}$).

In the first case the beam-to-column assembly should have moment resistance larger than the moment induced by non-seismic loads at ultimate limit state of non-seismic conditions and behave as a full rigid and partial strength joint, while full-rigid, full strength in the second case. In this study the experimental specimens were designed according to the second approach in order to exploit the maximum resistance of the assembly. Imposing $M_{pl,b,Rd}$ as the starting value for the joint design bending moment M_{Ed} leads to an iterative design process. Indeed, a reduction of M_{Ed} is needed because when the local hierarchy is imposed using Ω_{μ}, the bending moment at the haunch/rib tip has to be limited to $M_{pl,b,Rd}$.

Whichever design option is chosen to set M_{Ed} i.e. the design bending moment of the connection, the required slip resistance of the device is:

$$F_{slip,req} = \frac{M_{Ed}}{h_t} \tag{4.9}$$

Where h_t is the lever arm of the connection, namely the distance between the center of rotation and the axis of sliding.

In the present study, to exploit the larger flexural strength of the connection keeping elastic the spanning beam, the design moment demand of the connection was set equal to the factored plastic resistance of the beam, namely as following:

$$M_{Ed} = M_{pl,b,Rd} + s_h V_h \tag{4.10}$$

$$V_h = \frac{2M_{pl,b,Rd}}{L_h} + V_{Ed,G} \tag{4.11}$$

Where s_h is the distance from the tip of the haunch/rib plate to the column face and, being L_h the free span length of the beam from tip to tip of the haunches and $V_{Ed,G}$ is the shear force due to gravity loads. In the cases of the experimental specimens of this study $V_{Ed,G}$ was set equal to zero.

The number of friction interfaces (n_s), the mechanical characteristics of the friction material ($\mu_{dyn,5\%}$), the number (n_b) of bolts and their diameter (d) are fixed a-priori. Subsequently, by imposing that the effective slip force $F_{slip,eff}$ has to be larger or equal to the required value (see equation below), the necessary level of bolt preloading (N_b) can be easily determine as follows:

$$F_{slip,Rd} = \mu_{dyn,5\%} \cdot n_s \cdot n_b \cdot N_b \geq F_{slip,req} \rightarrow N_b \geq \frac{F_{slip,req}}{\mu_{dyn,5\%} \cdot n_s \cdot n_b} \tag{4.12}$$

In order to limit the relaxation of pre-loading due to creep phenomena and to prevent the yielding of the bolt shank under bending, on the basis of previous experimental studies (results presented in detail in Ferrante Cavallaro *et al.*, 2017 and 2018b) the optimal values of the clamping force should range within 30% to 60% of preloading force $F_{p,Cd}$ recommended by EN1993:1-8. The design values for N_b are given inTable 41 while the friction material properties are given in Table 42

The non-yielding components of the joints are designed according to EN1993:1-8 to resist the slip force and the associated moment magnified by the overstrength factor Ω_μ , which is defined as follows:

$$\Omega_\mu = \frac{\mu_{st.95\%}}{\mu_{dyn.5\%}} \cdot \frac{N_{b.95\%}}{N_{b.5\%}} = 1.97 \simeq 2.0 \tag{4.13}$$

Where $\mu_{dyn,5\%}$, $N_{b,5\%}$ are the lower-bound values of the dynamic friction coefficient and tightening force, respectively; $\mu_{st,95\%}$, $N_{b,95\%}$ are the upper-bound values of the static friction coefficient and tightening force, respectively.

The values of both static and dynamic friction coefficients as well as the tightening forces were derived based on previous experimental studies (lap shear tests).

4.3.1.2 Check for Shear Force

The shear check of the column face connection and column web panel was made based on the EN1993 1-8 and assuming the design shear force V_{Ed} evaluated based on the equation below i.e. the ratio between twice the capacity design bending moment (M_{CD}) and the distance between the column face connections (L). Both the T-stub and the L-stubs' webs were checked for the full value of the V_{Ed}, although it was assumed that the L-stubs will carry most of the vertical force, as the shear capacity of the T-stub is very much reduced by the tensile component.

$$V_{Ed} = \frac{2 \cdot M_{CD}}{L} \tag{4.14}$$

$$M_{CD} = \Omega_{\mu} M_{Ed} \tag{4.15}$$

4.3.2 Experimental campaign

4.3.2.1 Test Setup

The experimental campaign consisted of 4 tests on friction joints that were performed in the laboratory of the Department of Civil Engineering at University of Salerno in collaboration with researchers from University of Naples "Federico II".

The test setup is shown in Figure 135 The columns were pinned in the bending plane of the joint with a cylindrical hinge at one end and a roller at the opposite tip. The beam was laterally restrained by means of a braced frame to prevent its lateral-torsional buckling. Two MTS 243 actuators were used for

the tests. The top actuator (load capacity of ±250 kN and stroke range equal to ±500 mm) was used to apply the displacement history at the beam tip that was set according to the loading protocol recommended by AISC341. The second actuator (load capacity of ±1000 kN and stroke range equal to ±125 mm) was used to apply a constant compression force equal to 30% of the column squash load that was kept constant throughout the duration of each test.

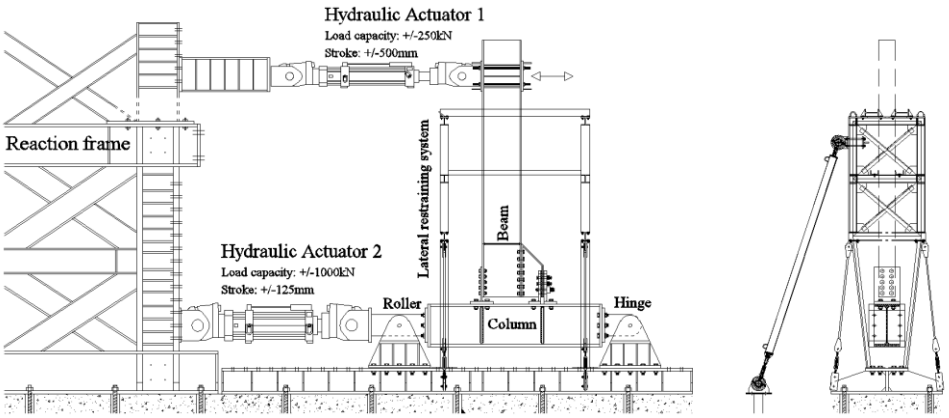

Figure 135 Experimental setup

4.3.2.2 Investigated joints and monitored parameters

As previously discussed, two types of friction dampers were investigated, and their main geometrical features are depicted in Figure 136 *a* to *g*. In addition, two beam-column assemblies per joint type were tested to cover the cases of both small- and large-scale structures (IPE270 – HE 220M and IPE450 - HE 500B, respectively). In all tested joints the bolts of the friction devices were equipped with disc spring (DS) washers which are believed to limit the loss of preloading under cumulated slip. These non-flat washers (Figure 136*h*) with a slight conical shape are commonly used to solve vibration, thermal expansion, relaxation and bolt creep problems.

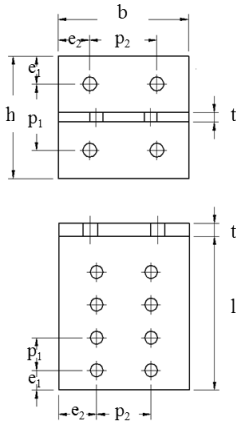

a) T-stub

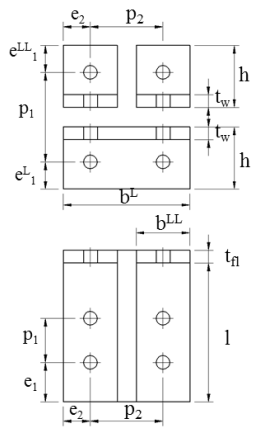

b) L-stub (Confiuration 1)

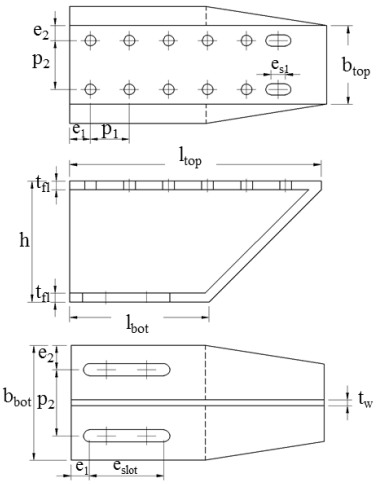

c) Haunch (Confiuration 1)

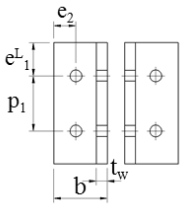

d) L-stub (Confiuration 2)

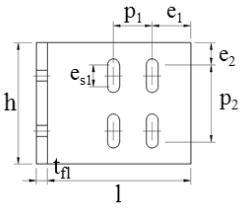

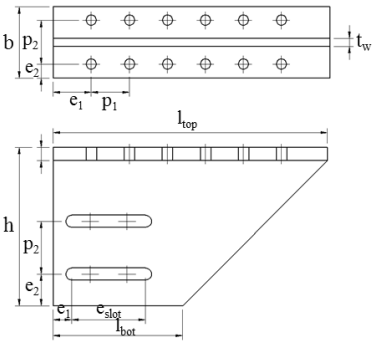

e) Rib (Confiuration 2)

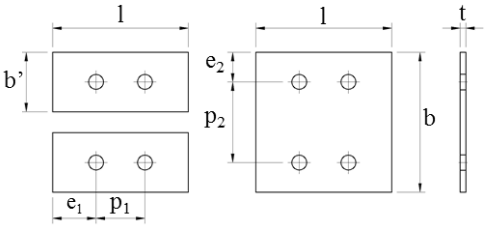

f) Friction pads (Configuration 1)

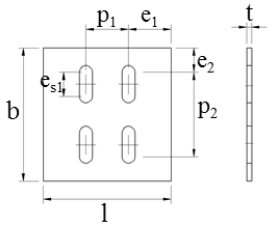

g) Friction pads (Configuration 2)

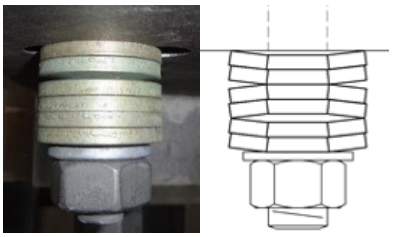

h) Adopted stacking of Disk Springs

Figure 136 Geometrical details of the tested friction devices

Table 36 Specimen geometrical configuration

Specimen	Connection type	Beam	Column	Length of the Beam "L"	Length of the column "H"	Internal level arm of the connection "z"	Thickness of beam web stiffener "$t_{stiff,\ beam}$"	Thickness of column continutiy plate "$t_{stiff,\ column}$"
				mm	*mm*	*mm*	*mm*	*mm*
FD-1-1	1	IPE270	HE 220M	1556	2700	478	10	10
FD -1-2	1	IPE450	HE 500B	2906	2700	710	15	20
FD -2-1	2	IPE270	HE 220M	1556	2700	458	10	10
FD -2-2	2	IPE450	HE 500B	2906	2700	710	15	20

Table 37 T-stub geometry details

	Flange								Web						
Specimen	**h**	**b**	**t_{fl}**	**Bolts**	**e_1**	**p_1**	**e_2**	**p_2**	l	**t_w**	**Bolts**	**e_1**	**p_1**	**e_2**	**p_2**
	mm	*mm*	*mm*		*mm*	*mm*	*mm*	*mm*	*mm*	*mm*		*mm*	*mm*	*mm*	*mm*
FD-1-1	187	200	20	M20	43	101	48.3	103.4	235	15	M18	30	50	58.3	83.4
FD-1-2	270	300	30	M30	70	130	75	150	410	20	M24	55	65	95.6	108.8
FD-2-1	195	200	20	M20	45	105	38.3	123.4	260	15	M18	30	50	58.3	83.4
FD-2-2	270	300	30	M30	70	130	75	150	485	20	M24	50	65	95.5	109

Table 38 L-stub geometry details

	Flange									Web						
Specimen	**h**	**b^L**	**b^{LL}**	**t_{fl}**	**Bolts**	**e_1^L**	**e_1^{LL}**	**e_2**	**p_2**	l	**t_w**	**Bolts**	**e_1**	**p_1**	**e_2**	**p_2**
	mm	*mm*	*mm*	*mm*		*mm*	*mm*	*mm*	*mm*	*mm*	*mm*		*mm*	*mm*	*mm*	*mm*
FD-1-1	98	200	85	20	M20	40	43	42.5	115	219	20	M20	62	70	42.5	115
FD-1-2	145	300	135	30	M30	60	60	67.5	165	360	30	M20	85	70	67.5	165
FD-2-1	220	97.5		20	M20	60	100	40.5		260	20	M20	70	70	40	160
FD-2-2	330	132		30	M30	90	150	57		366	30	M20	83	70	65	200

Table 39 Friction pads geometry details

Specimen	l	b	b	t	**Bolts**	**Disc spring**		**N_b**	**e_1**	**p_1**	**e_2**	**p_2**
	mm	*mm*	*mm*	*mm*				*kN*	*mm*	*mm*	*mm*	*mm*
FD-1-1	194	200	85	8	M20	w/	w/o	72	62	70	42.5	115
FD-1-2	310	300	135	8	M20	w/	w/o	87	85	70	67.5	165
FD-2-1	210	220		8	M20	w/	w/o	78	70	70	40	160
FD-2-2	306	330		8	M20	w/	w/o	96	83	70	65	200

Table 40 Haunch geometry details

Specimen	L_{top}	L_{bot}	t_{fl}	t_w	Bolts	e_1	p_1	e_2	p_2
	mm	*mm*	*mm*	*mm*		*mm*	*mm*	*mm*	*mm*
FD-1-1	419	234	15	10	M18	35.5	67	25.8	83.4
FD-1-2	590	365	20	15	M24	40.4	81	40.5	109
FD-2-1	520	245	15	15	M20	72.1	72.1	25.8	83.4
FD-2-2	756	356	20	20	M24	91.7	91.7	40.5	109

Table 41 Pretension levels in the bolts of the tested specimens

Model	N_b	$N_b/F_{p,c}$
	[kN]	*[%]*
FD-1-1	58	34%
FD-1-2	98	57%
FD-2-1	64	37%
FD-2-2	105	61%

The DS were stacked both in parallel and in series to increase the strength and the deformability, respectively as shown in Figure 136*g*. This arrangement was established based on the findings of the former experimental campaign on lap-shear connections. In addition, preloadable HV bolts were adopted to clamp the friction surfaces.

The overall geometrical features of the tested beam-to-column assemblies are depicted in Figure 136 and the corresponding values are also reported in Table 36 to Table 40. A label code is used to identify each assembly as follows: 'FD' stands for Friction Device; the first number is related to the joint configuration (1 or 2) and the second number refers to the size of the assembly (1 for small and 2 for large). The additional term "DS" identifies the use of disc springs. As example, FD-1-1-DS corresponds to the small assembly equipped with the device configuration 1 (i.e. horizontal friction surface) and disc springs.

Both global and local response parameters were monitored during the tests. At global level, the displacements at the tip of the beam and the relevant reaction forces of both actuators were measured (see Figure 137*a*). Namely, the bending moment in column axis was evaluated based on the reaction force in the actuator (F) and the corresponding lever arm (L – the distance between the actuator and the column axis). The displacement (u) at level of the actuator applying the displacement history is used to obtain the chord rotation (θ_{chord}) by dividing it with L.

Regarding the local response parameters, the relative displacements among the components of the connections were monitored by means of LVDTs and the forces into the bolts were measured throughout the experiments by means of torsional loading cells. The relative sliding of the friction damper with respect to the fixed parts (L-stubs) were measured by means of the LVDT-07 (for the configuration 1) and LVDT-02 and LVDT-07 (for the configuration 2), as depicted in Figure 138.

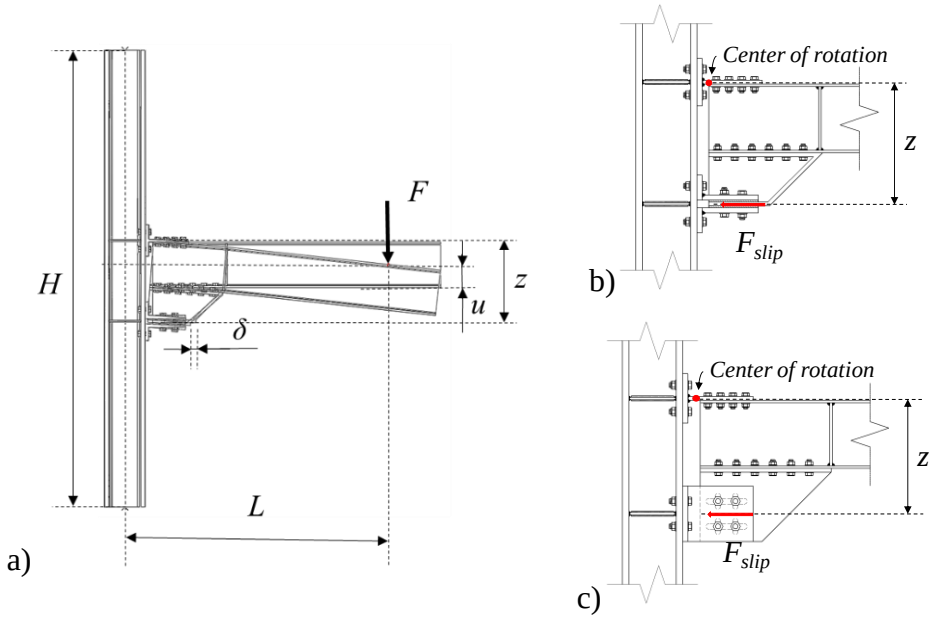

Figure 137 Monitored parameters: global (a) and local response (b, c)

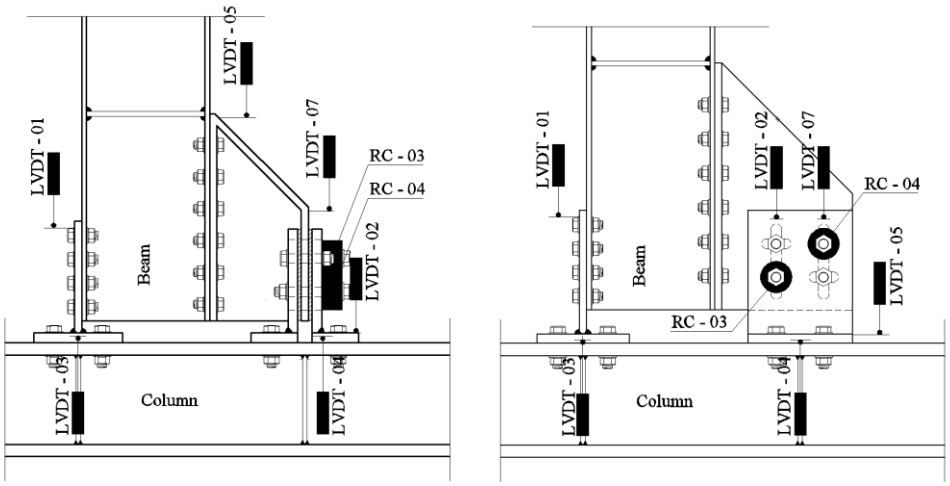

a) Joint FD-1-1 *b) Joint FD-2-1*

Figure 138 Layout of displacement transducers to measure the local response of joints

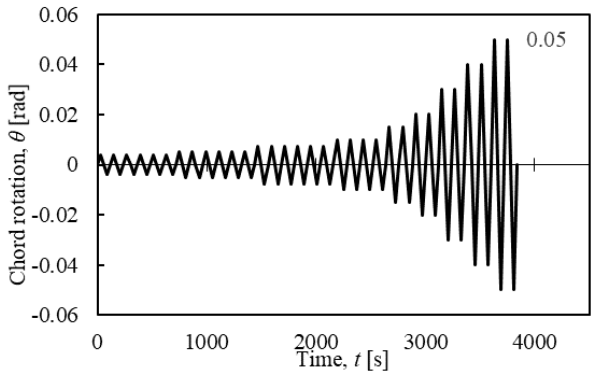

Figure 139 AISC 341-10 loading protocol up to 5% sorey drift

The obtained values were used to evaluate the friction damper rotation (θ_{device}), which is obtained by dividing the displacement δ with the connection lever arm z measured from the mid-thickness of the T-stub web to the geometrical center of the friction device as detailed in Figure 137 *b* and *c*. In addition, LVDT-03 was used to evaluate the opening of the cap T-stub connection, while LVDT-04 (for the configuration 1) and LVDT-05 (for the configuration 2) were used to monitor the gap opening of the lower L-stub connections.

4.3.2.3 Results

All performed tests showed an overall satisfactory response with stable hysteretic behavior and similar features, as depicted in Figure 140. Indeed, both types of connections performed as rigid up to the static friction resistance of the devices. Following the activation of the sliding, a loss of strength was observed but negligible stick-slip phenomena were observed under load reversal. Both friction assemblies lead to an asymmetric response of the joint, however the difference between the sagging and hogging resistance is larger in the case of the configuration 1 (i.e. horizontal friction surface), which also experienced the more pronounced degradation of the cyclic resistance, especially for the large assembly FD-1-2-DS.

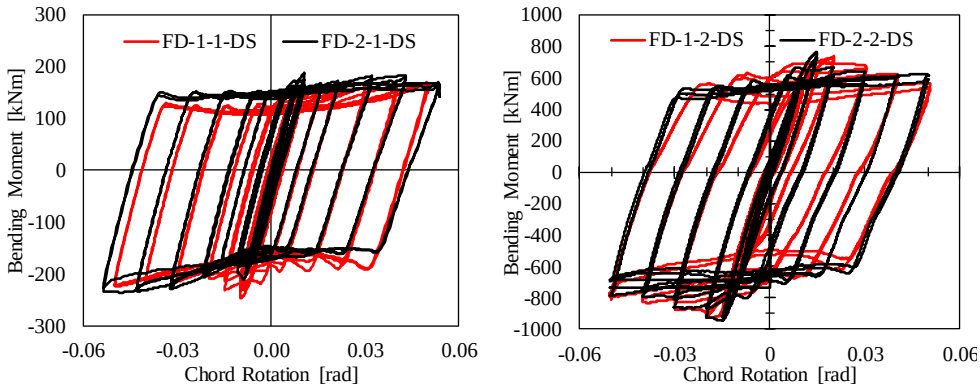

a) Small assemblies *b) Large assemblies*

Figure 140 Comparison between the response of the 2 device configurations

The different flexural resistance experienced under sagging and hogging can be explained by analyzing the local deformation demand in the upper T-Stub (which connects the top flange of the beam to the column) and the lower L-Stubs (which connect the device to the column). The upper Tee was the same for the same beam-column assembly of both joint types, thus the differences can be explained by considering the different deformability of the L-Stub arrangements that differ with the friction connection configurations.

As depicted in Figure 141, the deformation of the Tee has values in the same ranges for the 2 pairs of tested joint assemblies i.e. the small assemblies (i.e. FD-1-1-DS and FD-2-1-DS) and the large assemblies (i.e. FD-1-2-DS and FD-2-2-DS) present T-stub flange opening of maximum 0.5mm and 1.0mm, respectively. On the other hand, Figure 142 shows that the L-stub flange opening is substantially larger in the joint assemblies detailed with the horizontal friction damper configuration (i.e. FD-1-1-DS and FD-1-2-DS) than the values measured for the joints with the vertical damper (i.e. FD-2-1-DS and FD-2-2-DS). It is worth noting that the difference in terms of gap opening corresponds to the difference in terms of flexural strength under sagging loading.

In line with the findings of the numerical study carried out, the difference between sagging and hogging bending resistance for the first configuration can vary up to 25%, while the second configuration has a lower difference (about 15%). As shown in Figure 140, the larger beam-column assemblies exhibited the larger degradation of the strength for increasing levels of rotation.

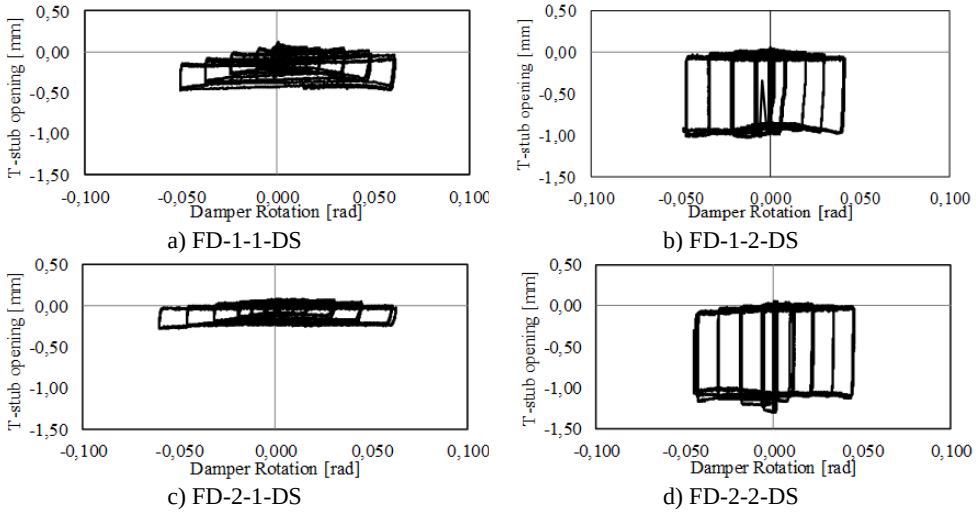

a) FD-1-1-DS b) FD-1-2-DS

c) FD-2-1-DS d) FD-2-2-DS

Figure 141 T-stub opening versus damper rotation

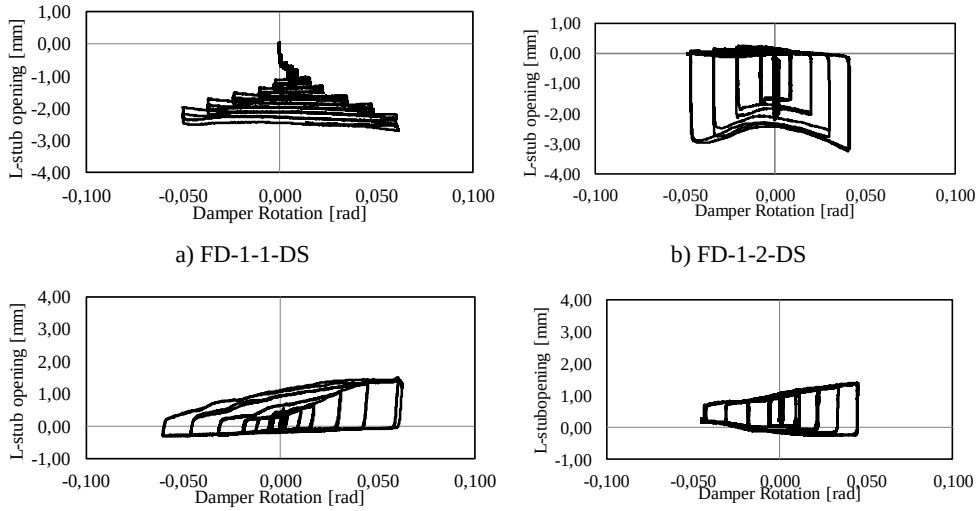

Figure 142 L-stub opening versus damper rotation

This was caused by two effects: first, the use of longer bolts (with the same diameter of those used for smaller specimens) and secondly, the bolt clamping was larger as seen in Table 41 that reports the average tightening forces for the tested specimens.

The larger flexibility of the bolts corresponds to larger bending demand in the shank as well as rotation of head and nut. This in turn leads to a consequential reduction in clamping force that translates into a reduction of the connection bending capacity. The larger preload directly affected the threshold and the evolution of the connection flexural strength, because larger clamping levels (e.g. closer to the EC3 1-8 recommended value) correspond to a reduced strength margin of the bolt shank relative to plastic damage, which can occur at lower slip displacements of the device.

Furthermore, the horizontal and vertical damper configurations induce different bearing forces on the bolts' shank, which leads to different patterns of local plastic strain (detailed in the numerical calibration section) and strength degradation when the rotation demand increases.

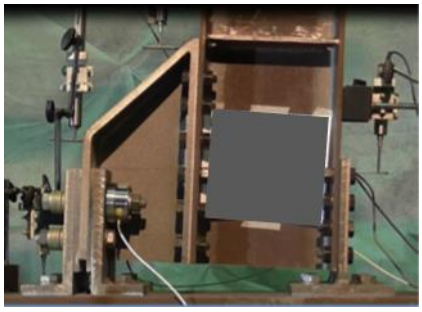

a) FD-1-1-DS

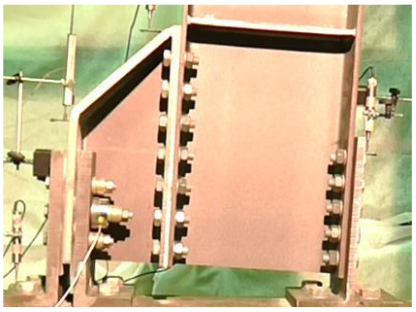

b) FD-1-2-DS

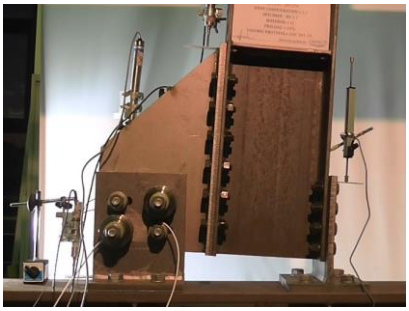

c) FD-2-1-DS

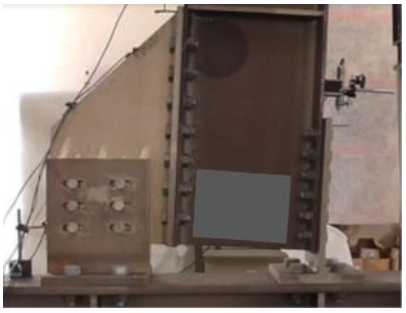

d) FD-2-2-DS

Figure 143 Deformed shape of the tested specimens at chord rotation equal to 0.05 rad

The experimental tests showed negligible plastic deformation in the beam or the T and L-stubs up to 0.04*rad* of chord rotation. Increasing the imposed rotation up to 0.05*rad*, which was set as the limit of the allowable displacement capacity of the friction devices, the overall response of the joints was still satisfactory, as shown in Figure 143, without appreciable damage except for the unique case of FD-1-2-DS where the instability of the beam web occurred. This phenomenon occurred due to the activation of a strut mechanism between the theoretical center of rotation around the T-stub web connecting the upper beam flange and the device. However, it is worth noting that this phenomenon is relevant solely for deep beams and it can be easily prevented by using transverse web stiffeners at the tip of the beam.

After the tests, it was observed that the friction pads underwent significant erosion of the superficial friction coatings and signs of plastic deformation in the bolts were also spotted.

4.3.3 Finite Element Analysis of friction joints

4.3.3.1 Geometry and modelling assumptions

Many of the numerical assumptions are like the ones previously presented for the case of lap-shear models, but given the significant differences, it was deemed necessary to reiterate them.

The two external joint configurations tested in the experimental campaign are presented in Figure 134. For each of the two configurations, two assemblies were tested:

- Assembly 1: Beam IPE270 – Column HE 220 M
- Assembly 2: Beam IPE450 – Column HE 500 B

The models, as well as the specimens tested, can be identified based on the scheme below (see Figure 144) i.e. the first number gives the joint configuration while the second denotes the beam-column assembly.

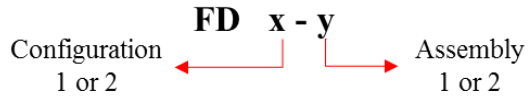

Figure 144: Definition of the model labeling

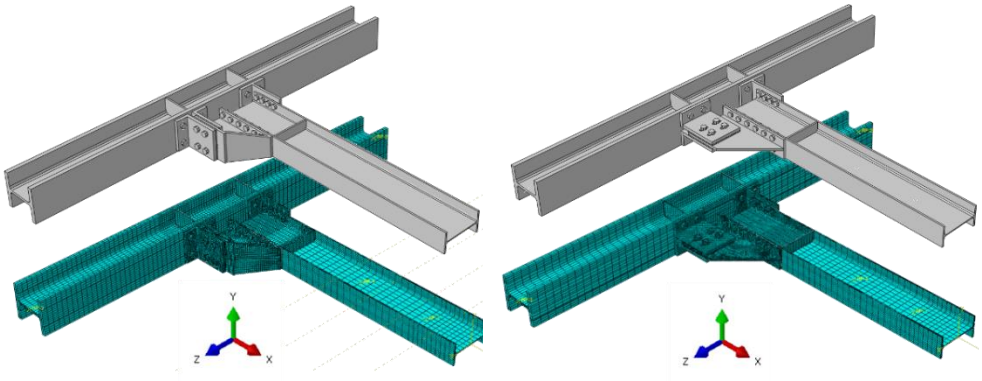

FD 1-1 FD 2-1

Figure 145: The FE model for Assembly 1

Abaqus v6.14.4 is used to carry out the finite element simulations. The geometrical features of the examined joints are reported in Figure 134. Structured mesh and the finite element type C3D8R (a 8-node linear brick with reduced integration) is adopted for steel beams, columns and high strength bolts. Figure 145 depicts as an example the FE models (basic and meshed view) for assembly 1.

For the larger beam-to column assembly 2, it was observed that the initial model, which neglected the connection of the column to the set-up, does not accurately describes the actual experimental response. To this end, a second set of more detailed models were created. The geometry of these joints is depicted in Figure 146.

In terms of material, the plastic true stress-true strain properties of S355 steel grade are assumed (Figure 147a). These materials were obtained by testing coupons cut from the investigated joints' elements, like the case of the beams and columns exemplified in Figure 147a. The yielding is modelled by means of the von Mises yield criteria. Plastic hardening is represented using a combined isotropic and kinematic hardening. HR 10.9 grade pre-loadable bolts are considered Figure 147b).

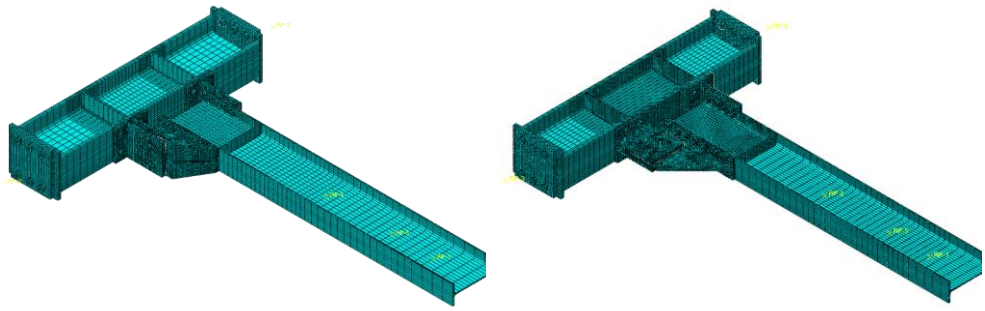

FD 1-2* FD 2-2*

Figure 146: Updated models for Assembly 2

Bolts were modelled by meshing a solid cylinder having the nominal circular gross area of the bolt. The true stress - true strain curve of the bolts was derived based on the tests carried out by D'Aniello et al (2016).

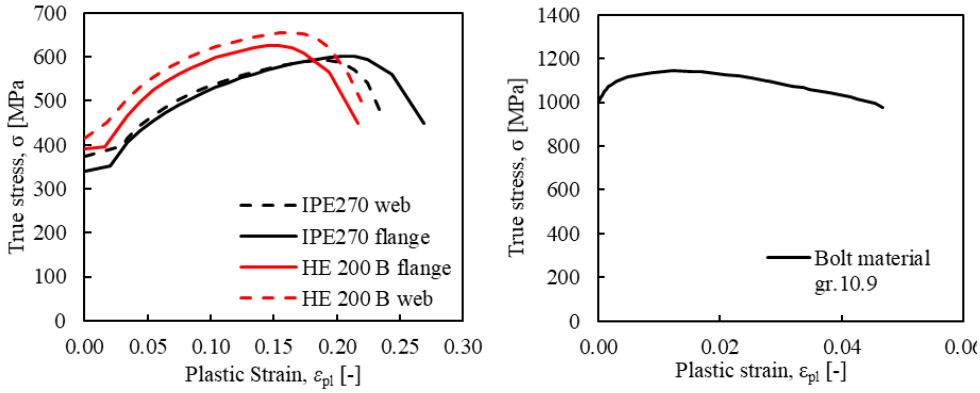

Figure 147 Materials used for the preliminary FEAs

In order to simulate the bolt strength using its nominal shank area, the material stress has been scaled as it follows:

$$f_{effective} = f_{actual} \frac{A_s}{A_{nom}} \tag{4.16}$$

Where $f_{\text{effective}}$ is the effective stress, f_{actual} is the actual stress, A_s is the tensile area of the bolt and A_{nom} is the nominal area of the shank.

This assumption is necessary because the bolt shank strength is governed by the threaded part of the shank, which has an effective bolt area that is smaller than the nominal gross area.

As the strength, the elastic stiffness of the shank is also affected by the threaded part. Therefore, the elastic model of the equivalent material constituting the shank was scaled in order to obtain the equivalent stiffness calculated according to Swanson and Leon (2001) as follows:

$$\frac{1}{k_b} = \frac{f \cdot d_b}{A_b \cdot E} + \frac{L_s}{A_b \cdot E} + \frac{L_{tg}}{A_{eb} \cdot E} + \frac{f \cdot d_b}{A_{be} \cdot E} \tag{4.17}$$

Where f is the stiffness correlation factor assumed equal to 0.55; d_b is the nominal diameter of the bolt; A_b is the nominal area of the bolt shank; A_{be} is the effective area of the threads; L_s is the shank length of the bolt; L_{tg} is the length of the threaded portion included in the bolt's grip; and E is the actual modulus of elasticity of steel.

The interactions between the surfaces in contact (e.g. bolt-to-plates, plate-to-plate) are modelled considering both "Normal" and "Tangential" behaviour. The former is implemented considering "Hard Contact", while the latter is modelled differently for the steel–to-steel interfaces and for the friction pad-to-steel interfaces. The main difference between the two types of contacts is the definition of the friction coefficient. For the steel-to-steel surfaces a constant value equal to 0.3 is considered, while the dynamic friction coefficients obtained from lap-shear tests with the friction material considered are used for the friction damper (see Table 42).

Table 42: Friction coefficients for material M-4

	$\mu_{dyn\ 5\%}$	μ_{avg}	$\mu_{dyn\ 95\%}$
Friction Material M-4	0.53	0.59	0.64

The clamping of the bolts is modelled by means of the "Bolt load" option available in the FE software. For the bolts belonging to the friction device, the values from Table 41 were used, in order to be consistent with the design and experimental assumptions. All other bolts were fully preloaded, as recommended by EN1993 1-8.

The boundary conditions are modelled to be representative of those adopted for the experimental set-up (see Figure 135*a*). Both column ends have translational and rotational degrees of freedom restrained, except for the in-plane rotation, and the beam is restrained to prevent lateral-torsional buckling. The loads are applied in the section corresponding to the actual position of the

actuator 1. Both monotonic and cyclic displacement histories are alternatively applied. The AISC 341-10 loading protocol (Figure 139) used for the experimental tests is applied also for the cyclic numerical analyses.

4.3.3.2 Validations and discussion of results

The adopted modelling assumptions effectively simulate both the global and the local response of the tested joints, as it can be observed Figure 148 and Figure 149 respectively. The response of the joint during the initial cycles are not accurately replicated by the numerical model due to the use of the dynamic 5% percentile of the friction coefficient. Disregarding the higher static friction coefficient, which is initially activated given the test typology (quasi-static), leads to this difference in response, negligible given the real seismic loading conditions

During the experimental campaign no damage was observed in the steel elements. However, the numerical analyses show some concentrations of plastic damage, depicted in terms of equivalent plastic strain (PEEQ) in Figure 149 at the base of the web of the upper T-stub (where the center of rotation is located), and either at the bases of the L-stubs, at the top web-flange area of the beam underneath the T-stub and in the shear bolts of the device. Furthermore, plastic deformations can be observed in the shanks of the bolts in the friction device.

The horizontal damper configuration induces shear type bending effects in the shanks with two bearing contacts in all bolts of the device. On the contrary, the bolts in the vertical damper have one bearing zone at mid-length of the clamped shank, which leads to larger local plastic strain (Figure 151) In addition, in this second case the bolts close to the column face do not exhibit plastic strains.

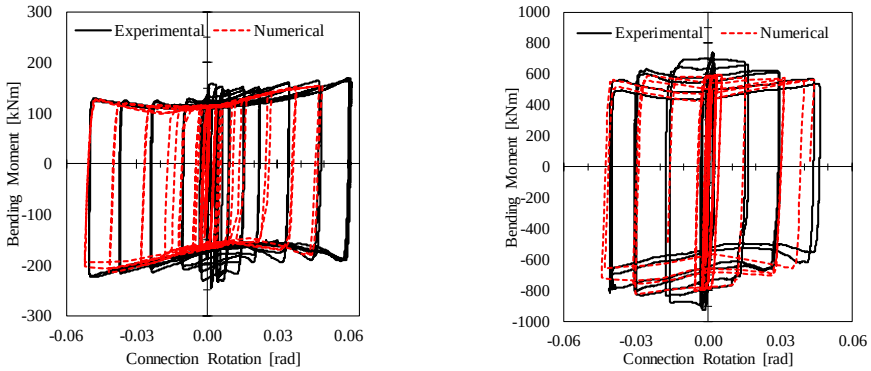

a) FD-1-1-DS b) FD-1-2-DS

c) FD-2-1-DS d) FD-2-2-DS

Figure 148 Experimental vs numerical results in terms of Bending Moment – Connection rotation

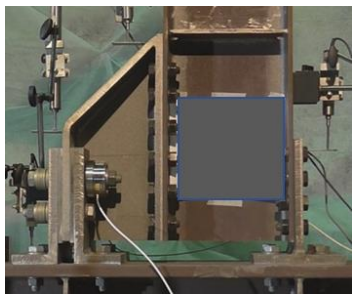

a) Experimental joint FD 1-1

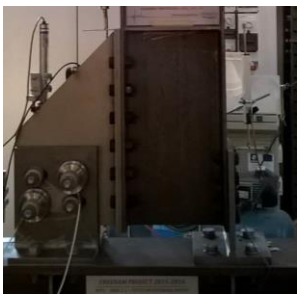

b) Experimental joint FD 2-1

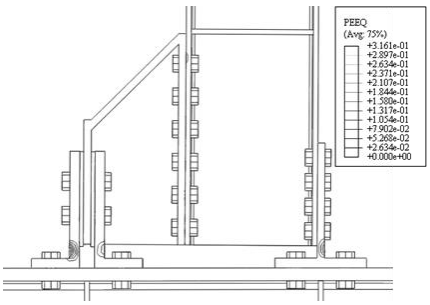

c) PEEQ distribution for model FD 1-1

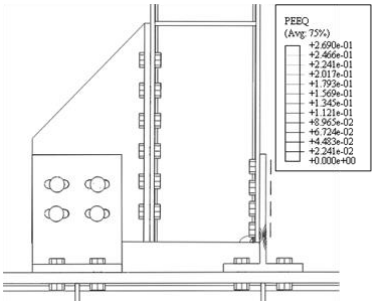

d) PEEQ distribution for model FD 2-1

Figure 149 Experimental vs. numerical models after cyclic test up to 5%

In the analyses performed on the models depicting the experimental tests it was observed that small concentration of damage is located in the base of the T-stub, the L-stubs (in the case of Configuration 1), the bolts of the friction damper and in a reduced extent in the beam (the web-flange junction at the beam end immediately below the T-stub and in the slotted holes at the end of the beam-haunch connection). These results are presented in Figure 152 in terms of PEEQ (equivalent plastic strain) distribution on the large beam to column assemblies. As it can be observed in the legend of PEEQ that are evaluated at the rotation equal to 0.05rad, the horizontal friction damper configuration leads to larger plastic deformations in the joint elements. As a matter of fact, this result can also be observed in terms of dissipated energy, presented in Figure 150.

Indeed, the friction energy normalized with respect to the total dissipated energy for the first configuration is smaller compared to the second configuration and the opposite is true in terms of normalized plastic energy. Although the second damper configuration leads to lower plastic damage, it is worth noting that the plastic damage is limited for both configuration, maximum plastic energy dissipation is less than 5% of the total energy dissipated at 0.05 rad.

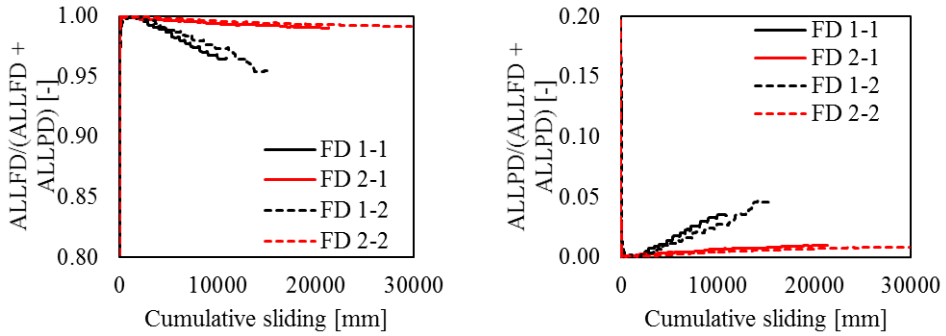

Figure 150 Normalised dissipated energy a) Friction energy and b) Plastic energy

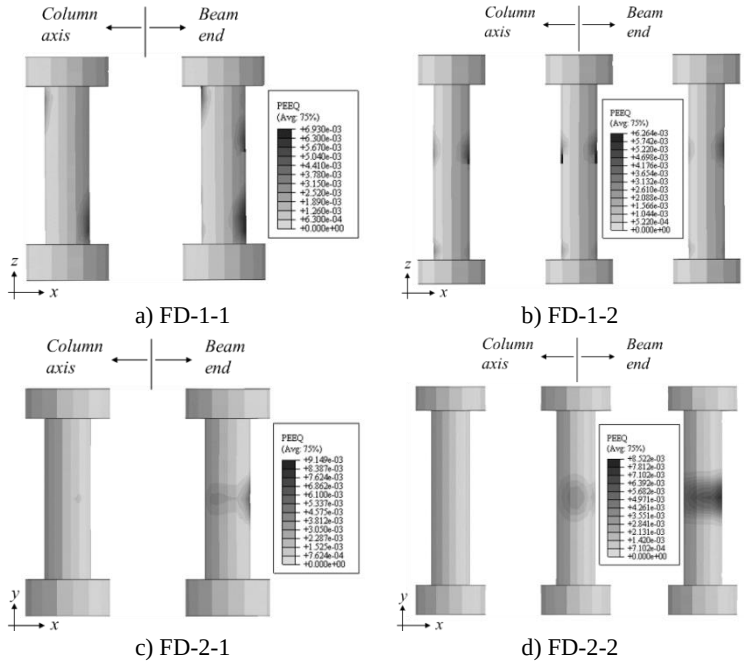

a) FD-1-1 b) FD-1-2

c) FD-2-1 d) FD-2-2

Figure 151 Equivalent plastic damage (PEEQ) in the damper bolts

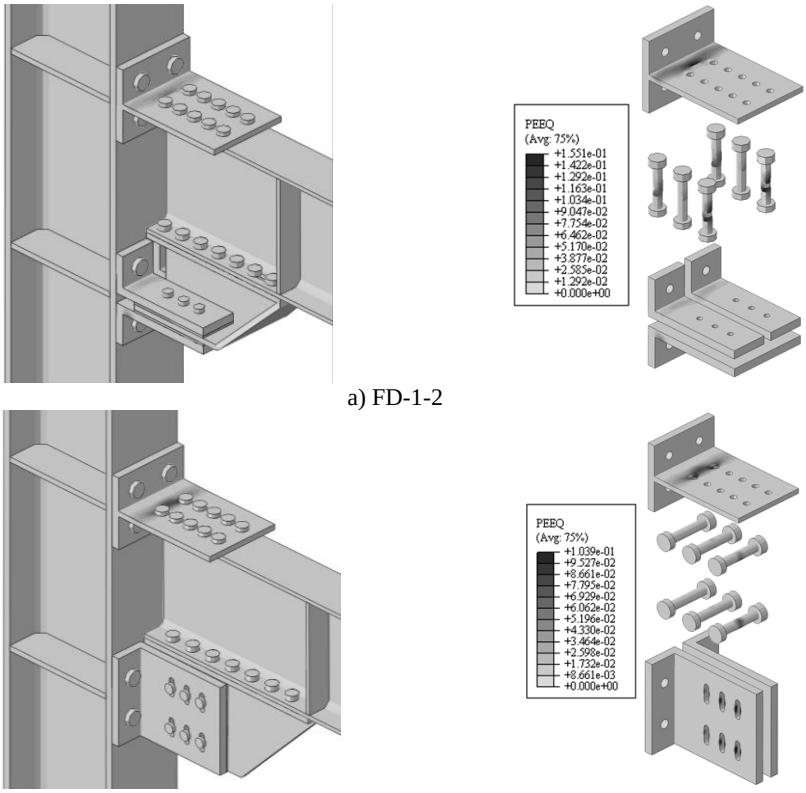

a) FD-1-2

b) FD-2-2

Figure 152 PEEQ Distribution at the end of the cyclic analysis for large joint assemblies

4.3.4 Parametric investigation: the clamping force and friction coefficient

The experimental tests confirmed the importance of the clamping force applied to the bolts into the device as well as the key role of the friction coefficient between the sliding surfaces. Therefore, the influence of the variation of these parameters on the response of the two tested joint configurations has been further investigated by means of finite element analyses based on the validated models previously described.

The range of variation for the parameters was based on the possibility that the parameter will reach that value. The preloading is a sensitive process, prone to errors due to the specific conditions required for a precise load application (straightness of plates to be tightened, number of plates tightened, bolt quality, wrench precision, etc.). The friction coefficient of the sliding interfaces has been statistically characterised and therefore it is assumed that the actual friction coefficient for a specific material will vary within the range of statistically representative values. Thus, the clamping force was varied by increasing and reducing the design value with 50%, assumed as a sufficiently large range because it goes beyond the limits recommended (30-60%$F_{\mathrm{p,Cd}}$), while the statistical values were assumed for the friction coefficient.

The examined parameters have been varied as follows:

- In addition to the pre-loading force adopted in the tests, namely N_b (Table 41) a value 50% smaller (0.5 N_{b}) and a value 50% larger (1.5 N_{b}) have been considered. It should be noted that in all cases 1.5 N_b is smaller than $F_{p,Cd}$ (which is equal to 172kN for M20 gr.10.9 bolts).
- Three values of the dynamic friction coefficient μ are considered, namely the 5% percentile ($\mu_{5\%}$), the average value (μ_{avg}) set equal to 0.59, and the 95% percentile ($\mu_{95\%}$) see Table 42

The equations below clarify the meaning of the mechanical parameter reported in the results summarising tables in the following paragraphs:

$$\Gamma^{(+)} = 1 + \frac{M_{0.5N_b}^{(+)} - M_{N_b}^{(+)}}{M_{N_b}^{(+)}} \tag{4.18}$$

$$\Gamma^{(-)} = 1 + \frac{M_{0.5N_b}^{(-)} - M_{N_b}^{(-)}}{M_{N_b}^{(-)}} \tag{4.19}$$

$$\Delta M^{(+/-)} / M^{(-)} = \frac{M^{(-)} - M^{(+)}}{M^{(-)}} \tag{4.20}$$

Where $\Gamma^{(+)}$ and $\Gamma^{(-)}$ represent the variation of the hogging and sagging bending moment capacity, respectively, considering alternatively the change in the clamping force from the design value N_b to 0.5 N_b and 1.5 N_b; $M^{(+)}$ and $M^{(-)}$ are the sagging and hogging bending moments. The subscripts depict the analysis from which the bending moment is taken, e.g. with clamping force equal to either 1.5 N_b or 0.5 N_b; $\Delta M^{(+/-)}/M^{(-)}$ represents the difference between the hogging and sagging bending moment for each respective analysis (considering the three values for N_b).

4.3.4.1 Influence of clamping force

Figure 153 shows the comparison of the response curves for the four joints (i.e. the two joint configurations and two assemblies) and Table 43 and Table 44 report the numerically measured mechanical properties of the joints. The bending moments reported, $M^{(+)}$ and $M^{(-)}$, represent the bending moment at the occurrence of the sliding under sagging and hogging, respectively.

As expected, the variation of the bending moment ($\Gamma^{(+)}$ and $\Gamma^{(-)}$) is proportional with the bolt pretension variation i.e. the increase/decrease under both sagging and hogging is of 50%.

$\Delta M^{(+/-)}/M^{(-)}$ reported in Table 43 and Table 44 shows the difference between sagging and hogging, which seems to be related to the joint configuration and constant with the beam depths, clamping force, or friction coefficient. The difference is about 24% for Configuration 1 and 14% for configuration 2.

Further observation that can be made based on Figure 153 is that the post-yield response of joint configuration 1 differs with the level of preloading which is relative to the maximum preloading force. In particular, the joints with lower relative preloading exhibits hardening (i.e. positive post-yield stiffness), while the joint with higher relative preloading shows softening (i.e. negative post-yield stiffness), the latter is evident for the larger beam These phenomena are more pronounced under hogging bending moment. The second configuration exhibits a more linear behaviour in both examined assemblies.

The stiffness of the joint is not affected by the variation of clamping force, since it is determined by the stiffness of the other components of the joint (the connection at column face, the column web panel, etc.).

4.3.4.2 Influence of Friction Coefficient

Figure 154 depicts the numerical curves, in terms of bending moment vs. chord rotation, of all the models analysed with larger values of friction coefficient (μ_{avg} and $\mu_{95\%}$) with respect to the design value ($\mu_{5\%}$) under hogging ($M^{(-)}$) and sagging ($M^{(+)}$) loading conditions. It is possible to observe that the higher percentile of the friction coefficient values, the larger is the joint capacity. This observation confirms the need to account for the variability of the friction properties of the friction pads to design the non-yielding structural members.

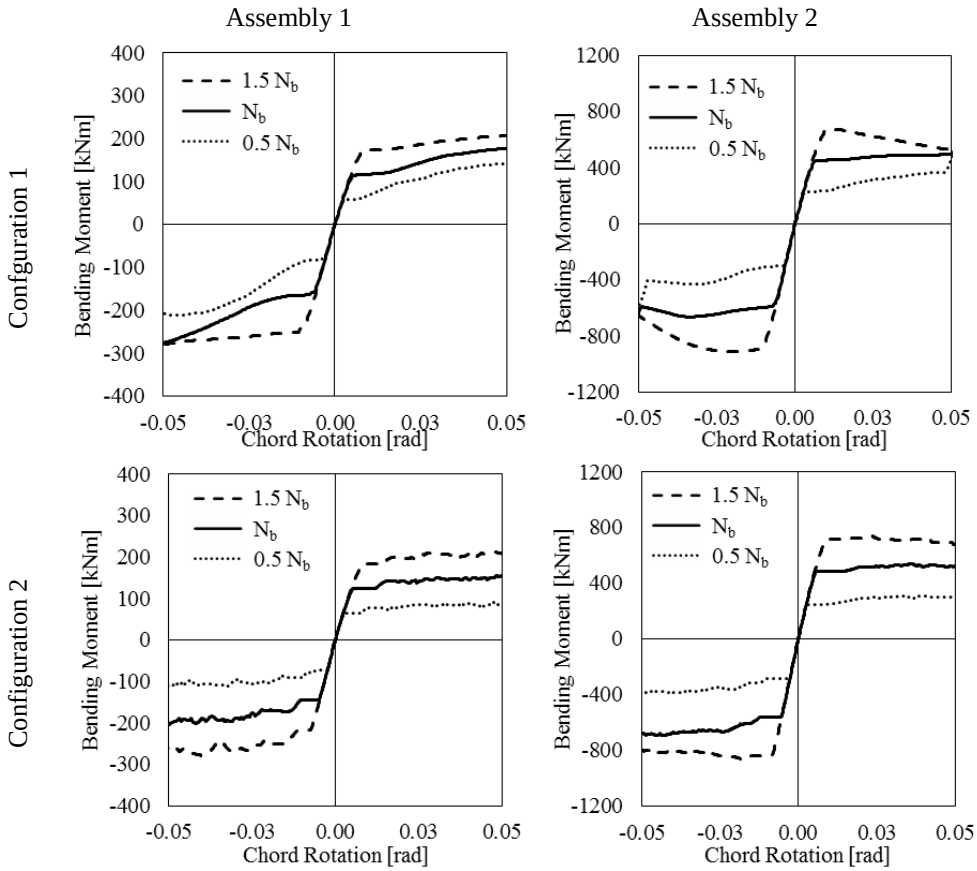

Figure 153 Influence of the clamping force on the bending moment capacity

Table 43 Bending moments for model FD 1-2-DS considering the variation of clamping force

Clamping force	$M^{(+)}$ *[kNm]*	$M^{(-)}$ *[kNm]*	$\Gamma^{(+)}$ *[-]*	$\Gamma^{(-)}$ *[-]*	$\Delta M^{(+/-)}/M^{(-)}$ *[-]*
N_b	453	602	-	-	25%
$0.5N_b$	230	298	51%	50%	23%
$1.5N_b$	690	902	152%	150%	24%

Table 44 Bending moments for model FD 2-2-DS considering the variation of clamping force

Clamping force	$M^{(+)}$ *[kNm]*	$M^{(-)}$ *[kNm]*	$\Gamma^{(+)}$ *[-]*	$\Gamma^{(-)}$ *[-]*	$\Delta M^{(+/-)}/M^{(-)}$ *[-]*
N_b	484	564	-	-	14%
$0.5N_b$	250	290	52%	51%	14%
$1.5N_b$	714	838	148%	149%	15%

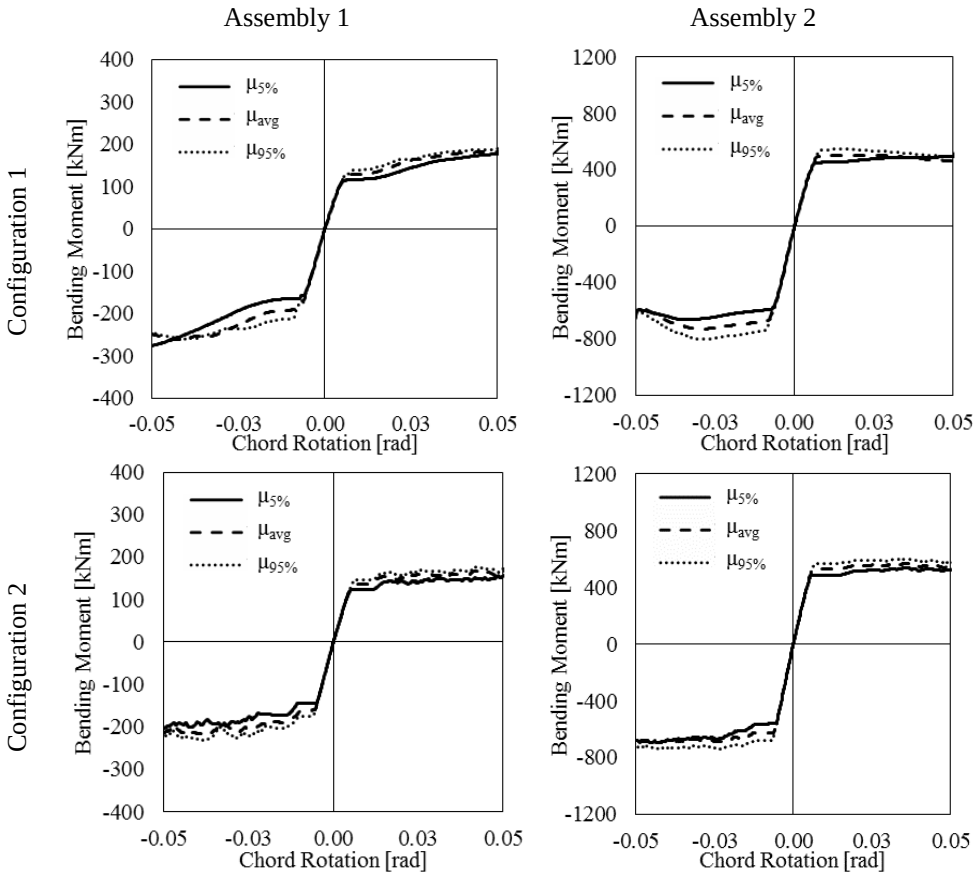

Figure 154 The influence of the friction coefficient on the bending moment resistance

Table 45 Bending moments for model FD 1-2 considering the friction coefficient variation

Friction coefficient	$\Delta\mu$	$M^{(+)}$	$M^{(-)}$	$\Gamma^{(+)}$	$\Gamma^{(-)}$	$\Delta M^{(+/-)}/M^{(-)}$
	[-]	*[kNm]*	*[kNm]*	*[-]*	*[-]*	*[-]*
$\mu_{5\%}$	-	446	593	-	-	25%
μ_{avg}	110%	521	670	117%	113%	22%
$\mu_{95\%}$	117%	535	733	120%	124%	27%

Table 46 Bending moments for model FD 2-2 considering the friction coefficient variation

Friction coefficient	$\Delta\mu$	$M^{(+)}$	$M^{(-)}$	$\Gamma^{(+)}$	$\Gamma^{(-)}$	$\Delta M^{(+/-)}/M^{(-)}$
	[-]	*[kNm]*	*[kNm]*	*[-]*	*[-]*	*[-]*
$\mu_{5\%}$	-	484	564	-	-	14%
μ_{avg}	110%	529	627	109%	111%	16%
$\mu_{95\%}$	117%	568	679	117%	120%	16%

Similar hardening/softening behaviour can be observed for both joint configurations, however, the models of Configuration 1 revealed the same response observed in the investigation of the clamping force i.e. a more significant hardening with the decrease of μ and a more pronounced softening when μ is increased. In the case of the second configuration, the response curves seem scaled proportionality with the friction coefficient.

Table 45 and Table 46 depict the variation of the bending capacity ($\Gamma^{(+)}$ and $\Gamma^{(-)}$) and the difference between sagging and hogging ($\Delta M^{(+/-)}/M^{(-)}$). The variation for configuration1 differs with respect to the variation of the friction coefficient, they are not proportional like in the case of the clamping force variation. A larger increase of bending moment can be observed for the same increase of friction coefficient. On the other side, the analyses of the second configuration show a closer dependency of the bending capacity with the friction property randomness.

The difference between sagging and hogging ($\Delta M^{(+/-)}/M^{(-)}$) is very similar to the cases investigated under clamping force variation (25% and 17% respectively). This result indicates that the sagging/hogging resistance difference is a parameter depending on the joint configuration, related to the column face connection dissymmetry shown also experimentally.

4.3.5 The friction connection shear transfer mechanism

A crucial aspect related to the design of the connections at column face is the shear check, because the T-stub and L-stubs should guarantee the resistance to combined tensile and shear forces to avoid premature failure.

Figure 155 shows the distribution of shear forces at the level of the T-stub and L-stubs as well as the total shear force in the section at the column face. In both tested friction device configurations, the cumulated shear in the two components (i.e. the sum of the relevant absolute values) is larger than the

overall shear force (see Figure 155*a* and *c* for configuration 1 and Figure 155*b* and *d* for configuration 2).In order to investigate the evolution of the shear force with the connection rotation, monotonic analyses under both hogging and sagging loading conditions were alternatively performed.

The results presented in Figure 156 confirm the previous observations and offer insight into the magnitude of the shear transferred by each component. Indeed, for the investigated cases, the L-stubs transfer larger shear force compared to the T-stub. Configuration 1 joints are characterized by levels of maximum shear force transferred by the Tee of about 50% of the total shear, while the L stubs reach values close to 100% of the total shear (Figure 156 *a* and *c*).

However, while Configuration 1 components transfer shear of up to maximum total shear, Configuration 2 assemblies (Figure 156 *b* and *d*) exhibit the same behavior observed cyclically i.e. the shear in the components reach values larger than the total shear, with the shear transferred by the L-stubs reaching values almost 2 times larger than the total shear for rotation values close to 0.06 rad.

The differences of shear force distributions between the 2 components is mainly due to the larger stiffness provided by the L-stubs in the vertical plane and the vertical sliding force component. Looking at the distribution of shear forces amongst the components of the connection (Figure 157) it can be remarked that the shear transfer mechanism is highly complex and configuration dependent. The type 1 joint (FD 1-1-DS) is characterized by same sign shear forces transferred by the L-stubs and in a smaller measure by the T-stub. On the contrary, the T-stub of FD 2-1-DS carries an opposite sign shear force, owing to the heightened level of shear force transferred by the L-stubs, in order to preserve the equilibrium at the column face. The hogging/sagging loading conditions lead to the same distribution of forces between the components for the same configuration, with a smoother transfer of the forces under positive bending.

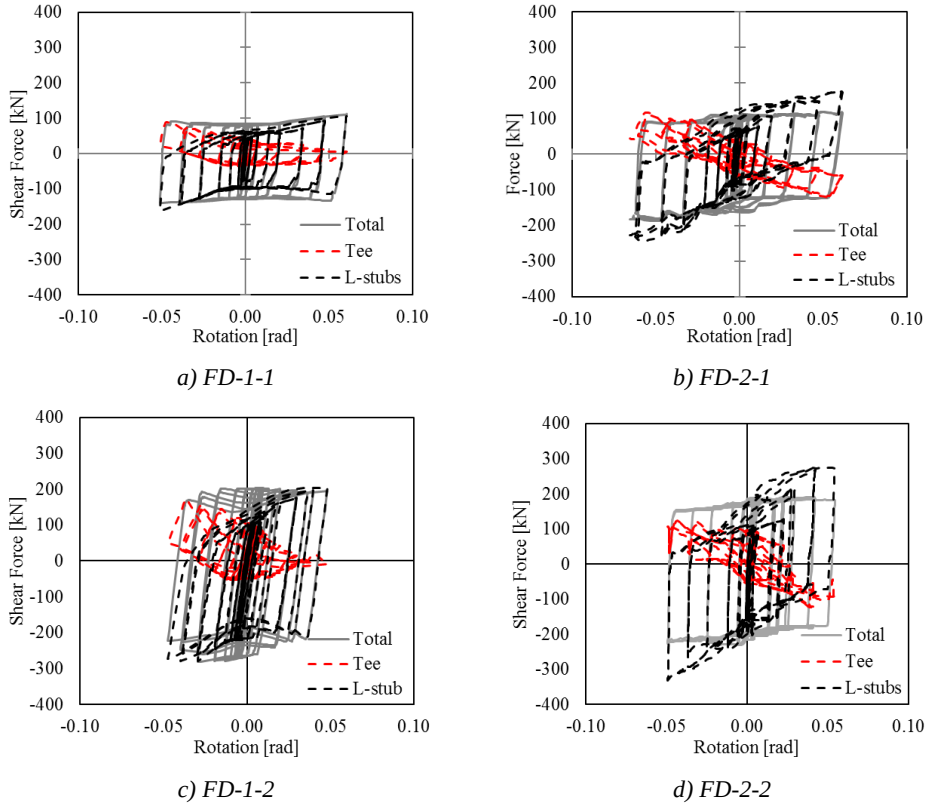

a) FD-1-1 b) FD-2-1

c) FD-1-2 d) FD-2-2

Figure 155 Shear force transferred by different components

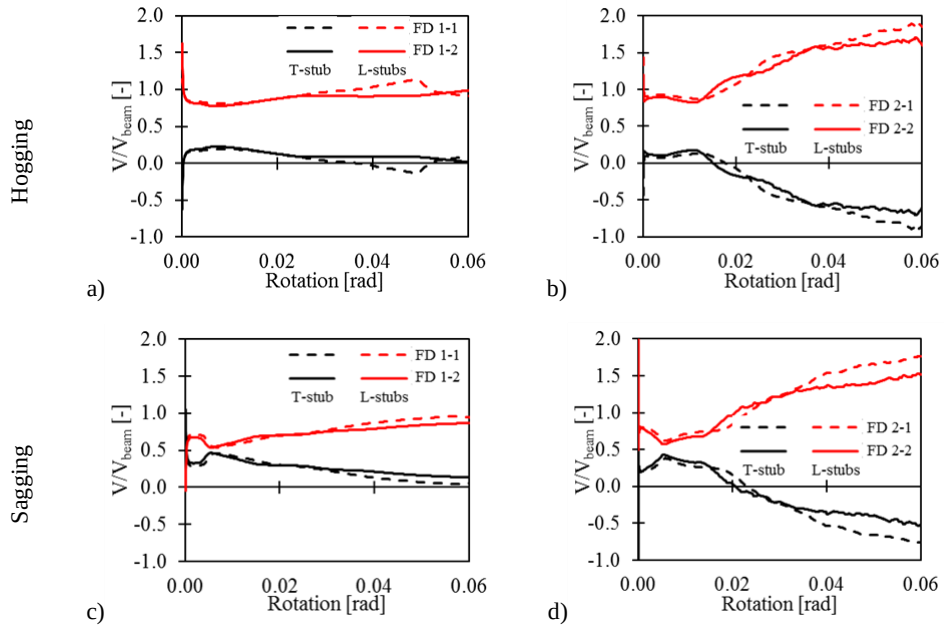

Figure 156 Shear force at the connection face

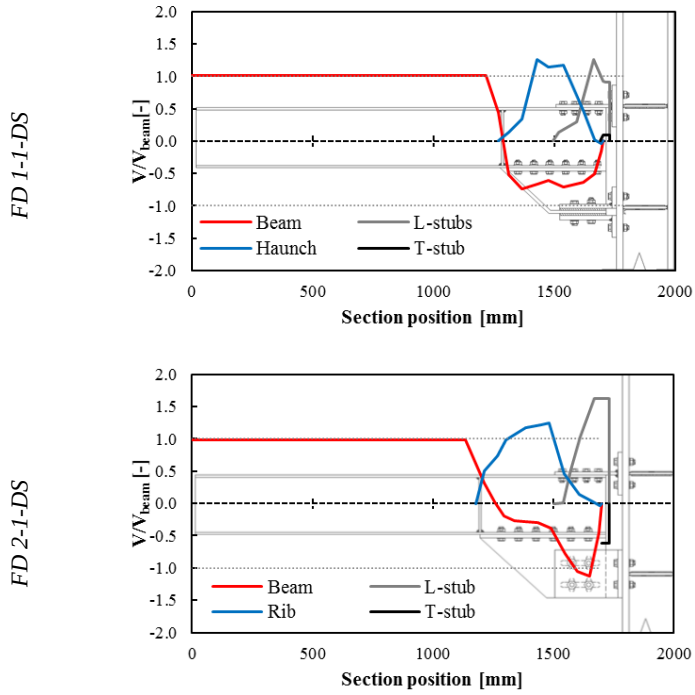

Figure 157 Distribution of shear in the connected elements at 0.04 rad damper rotation (Hogging)

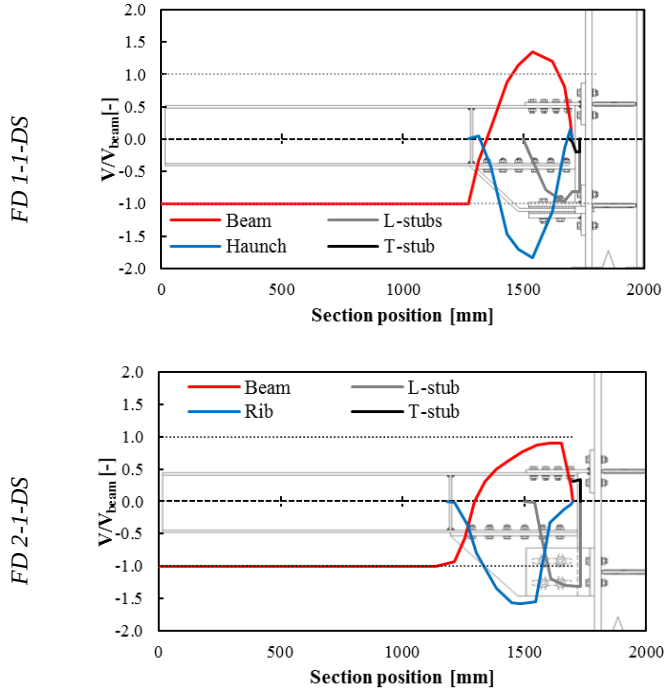

Figure 158 Distribution of shear in the connected elements at 0.04 rad damper rotation (Sagging)

4.4 FULL SCALE TESTS ON FRAME EQUIPPED WITH THE FREEDAM FRICTION DEVICE

4.4.1 Investigated structures

In order to assess the behavior of frames equipped with friction device a part of the FREEDAM Project experimental campaign will be dedicated to the investigation of a full-scale frame (Figure 159) equipped with friction devices. As a basis for comparison, initially a test on a frame with the same geometrical configuration but detailed with conventional reduced beam section (RBS) and extended end-plate connection will be performed (Figure 160*a*).

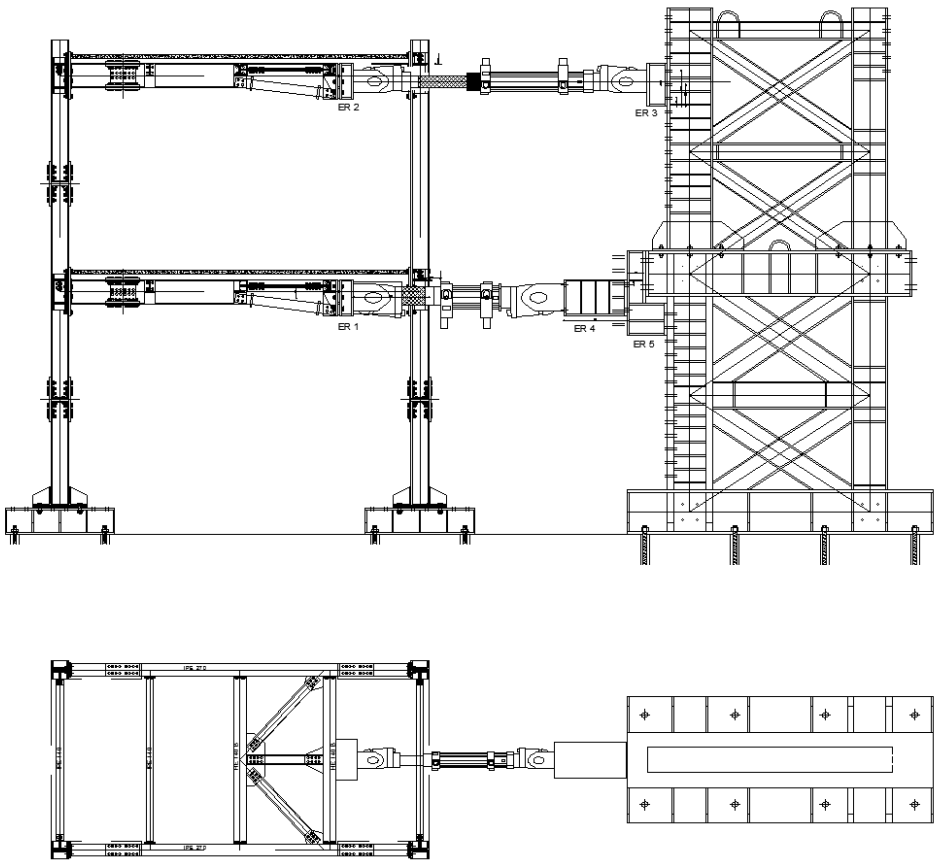

Figure 159 General mock-up test layout

The full-scale dynamic tests can provide significant insight on the real response of structures equipped with friction devices. However, due to the complexity of the task at hand, it is useful to perform numerical blind predictions of the mock-up frame in order to have an idea about the potential response of the structures to be tested.

The models were developed in advanced FE software Abaqus. The investigation was focused on planar frames depicting half the structure to be tested and account was made for the loads, masses and boundary conditions such that the experimental conditions were simulated correctly. Nonlinear static pushover, cyclic quasi-static and dynamic nonlinear (Timehistory) analyses were performed and the main parameters monitored were the base shear, interstorey drift and the floor reactions. Both the structure detailed with traditional steel joints (reduced beam section - RBS) and friction joints (FD) were investigated. As the subsequent step in the research was the investigation of a large number of structures, a simplified model of the mock-up structure was also developed in SAP2000 and the results were compared with the advanced FE model The comparison between the results provided by different software allowed to highlight the main parameters which govern the prediction of the structural response and the critical aspects of the numerical simulation.

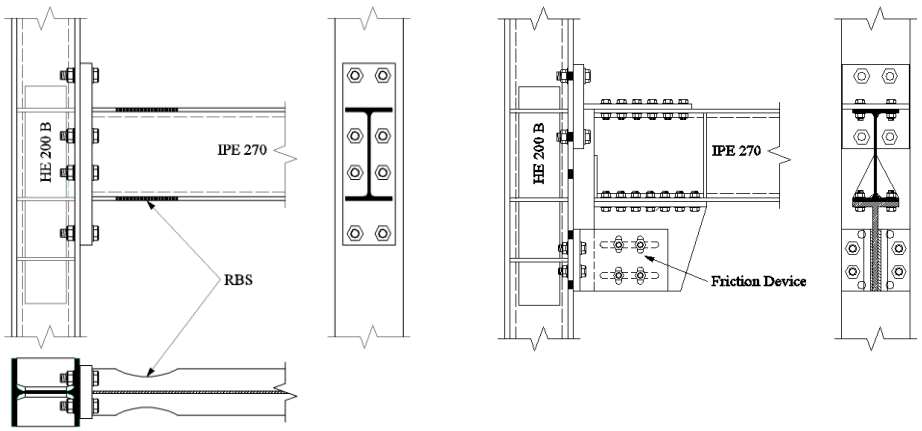

RBS joint detail FD joint detail

Figure 160 Joint details of the 2 tested frames

4.4.2 Assumptions for preliminary FE investigations

4.4.2.1 The advanced FE model

The full-scale tests consist in the testing of 2 frames:

1. Frame equipped with traditional joint – reduced beam section (RBS)
2. Frame equipped with innovative joints - friction devices (FD)

In both cases the structure consists of a one bay – one span – two floors structure. The numerical simulations were made on planar models consisting in one of the MRFs.

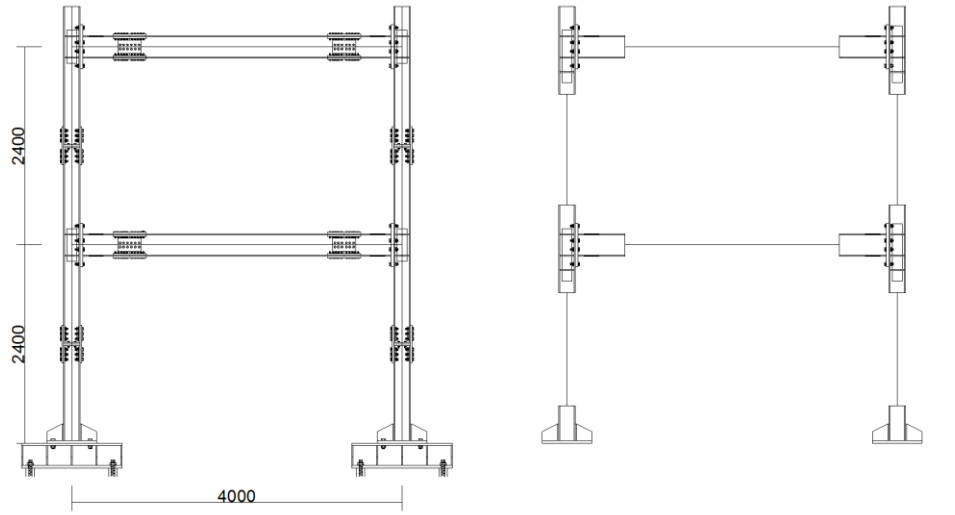

RBS model

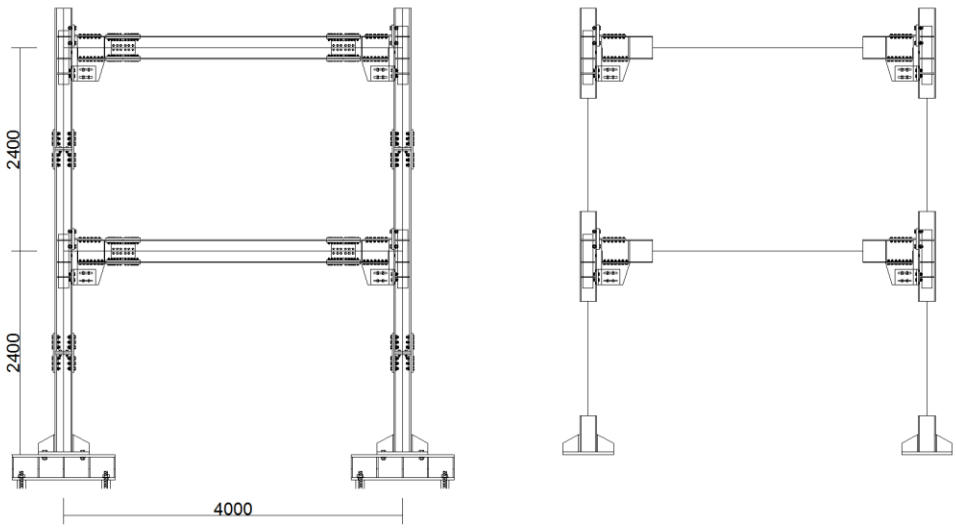

FD model

Figure 161 The frame models

Figure 160 depicts the geometry of the nodes for the 2 types of joints while Figure 161 depicts the experimental (left) and advanced numerical model (right) geometrical configuration of the frames. As it can be observed, the numerical model was detailed using solid C3D8R finite element (8 node linear brick reduced integration) in the node regions, and wire elements (B31 - a 2-node linear beam in space) for the beams and columns outside the areas of interest (joint).

4.4.2.1.1 Modelling assumptions

Abaqus v6.14.4 is used to carry out the finite element simulations. For the definition of the elastic domain of the material properties the nominal values were used (Young's modulus is 210 GPa and Poisson coefficient is 0.3). The nonlinear material properties used for the modelling of the steel parts were obtained by means of tensile tests performed at University of Salerno (see Figure 162a).

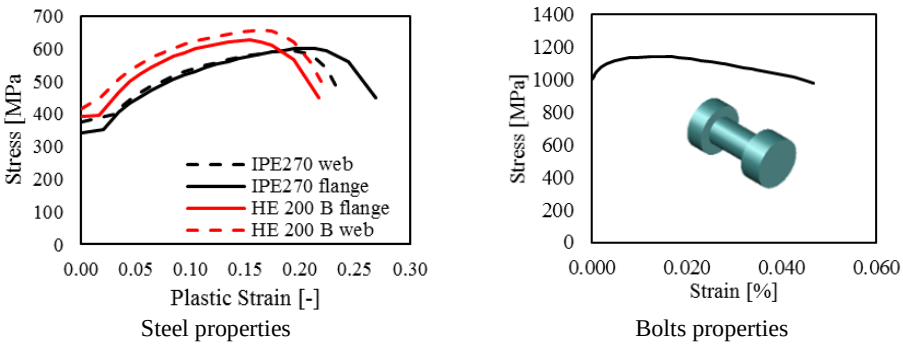

Figure 162 Material properties

This assumption for the modelling of bolts are the same as presented in Section 3.8.3 *Finite Element Analysis of friction joints* and therefore it's deemed unnecessary to repeat them.

To simulate the geometrical and mechanical imperfections, a buckling analysis was performed, and four buckling modes were selected as the most representative of the expected damage to occur during testing (see Figure 163).

Different scaling factors were used to magnify the deformed shapes and give the adequate value for the out of square imperfections. Figure 164 shows the effect of the imperfections on the bending moment capacity of the RBS. The buckling modes were scaled in order to achieve a level of degradation of 20%, at 0.05*rad* joint rotation, similarly to the results of experimental tests performed by Latour *et al.* (2011*a)* on similar joints.

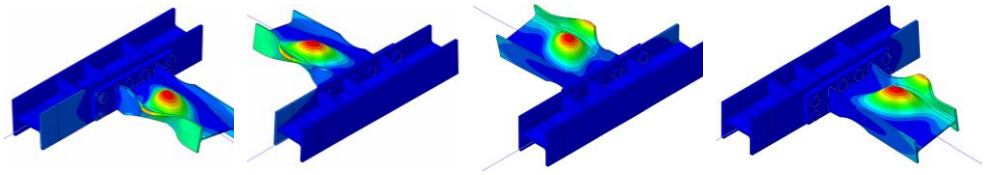

Mode 15 Mode 16 Mode 21 Mode 22

Figure 163 Buckling modes for modelling imperfections

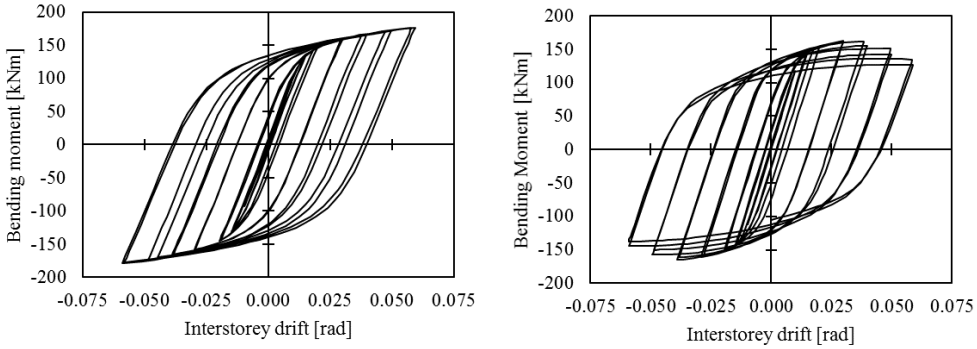

a) SF = 0.1 b) SF = 4

Figure 164 Imperfection effect on the bending capacity of the RBS

Interaction properties were defined for all the steel parts in contact (plates and bolts). The contact properties were defined both in terms of Normal Behavior (considering the "Hard contact" option) and Tangential Behavior (considering the "Penalty" option). The friction device interaction was defined considering the properties of the friction material in Section 3.8.3 *Finite element analysis of friction joints (*Table 42*)*

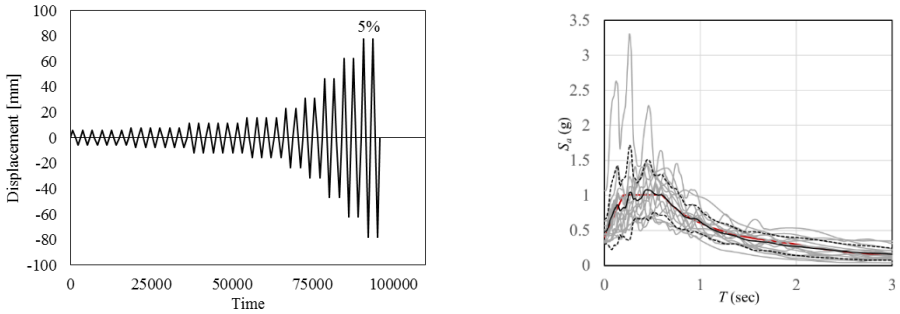

a) AISC 341(10) loading protocol

b) The 14 records for nonlinear dynamic analyses

Figure 165 Loading actions

The boundary conditions are modelled to be representative of those adopted for the experiments. The column bases were fully restrained, and the beams had lateral torsional restraints in the points of intersection with the secondary beams. The permanent loads were applied in the first step, together with the clamping of the bolts (applied using the "Bolt load" option in the software), while the lateral loads were applied in the last step, at the level of the beam to column joint, on the column external face, as a simplification with respect to the experimental setup. The Dynamic Implicit solver was used for all the analyses. Three types of analyses were performed:

- Static pushover analysis (considering a modal lateral force distribution)
- Quasi-static cyclic analysis (considering the AISC341-10 loading protocol in Figure 165a)
- Timehistory analysis (considering the 14 accelerograms in Figure 165*b*, which were used in the large investigation on MRFs)

4.4.2.1.2 Monitored parameters

Throughout the numerical investigations, the following parameters were monitored: Base shear, floor reaction, interstorey drift, the joint bending moment and the equivalent plastic strain (PEEQ).

4.4.2.2 The simplified FE model

The simplified planar models of the frames were created in SAP2000 considering identical geometrical configuration with the experimental frame. The mass was defined by setting the software to consider the lumped masses assigned for each floor (m_1 = 34.86t and m_2 = 25.68t) and the weight of the structural members. The gravity loads were applied as concentrated forces in the points of intersection of the secondary beams.

The material properties for the beams and columns were defined in accordance with the results of the coupon tests presented in Figure 162a. This was crucial for the RBS model, as the definition of the plastic hinge properties is highly correlated with the material definition. The hinges are assigned to the RBS section in the appropriate position (relative to the intersection of the beam and column axis see Figure 166*a*) and in a similar manner, automatic P-M plastic hinge properties were assumed for the columns.

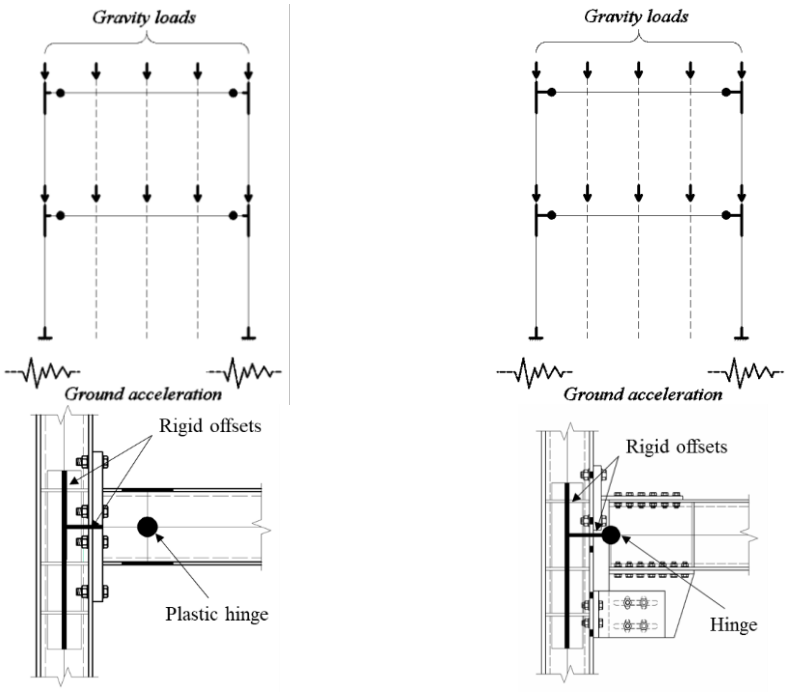

a) RBS model b) FD model

Figure 166 Schematic representation of SAP2000 models

For the definition of the FD model hinges corresponding to the friction joint, a similar hinge property was used (Figure 166*b*), but the yield bending moment was defined explicitly (evaluated based on the design slip force). The post-yield hardening was neglected, and an asymmetric response was assumed, with the hogging bending resistance 15% larger compared to the one under sagging loading (as observed experimentally and numerically).

Another important aspect of the modelling are the rigid offsets at both beam ends, at the column-beam intersection and column base. The members are modelled by means of "beam" finite elements and so, the actual size of the node area is not modelled explicitly. Therefore, these very rigid zones are simulated fictitiously by means of rigid offsets.

Two types of analyses were performed using this model: (i) Static Pushover Analysis (considering a modal lateral force distribution) and (ii) Timehistory Analysis (considering the same accelerograms as the advanced ABAQUS FE model).

4.4.3 Results of the preliminary numerical investigation

4.4.3.1 Advanced FE model (ABAQUS)

The results presented in Figure 167 and Figure 168 are relative to the model of the RBS frame. The frame response depicted in Figure 167 shows that the maximum base shear for the planar frame is approximately 390kN, while the floor reactions are 224kN for the first and 183kN for the second. This result is consistent between the static pushover and cyclic quasi-static analyses.

As observable from Figure 168, the RBS exhibits the expected cyclic and monotonic response, when compared with the analytically evaluated bending capacity. A more significant cyclic strength degradation in the beam on the

first floor is observable, like observable also from the PEEQ distribution in Figure 170.

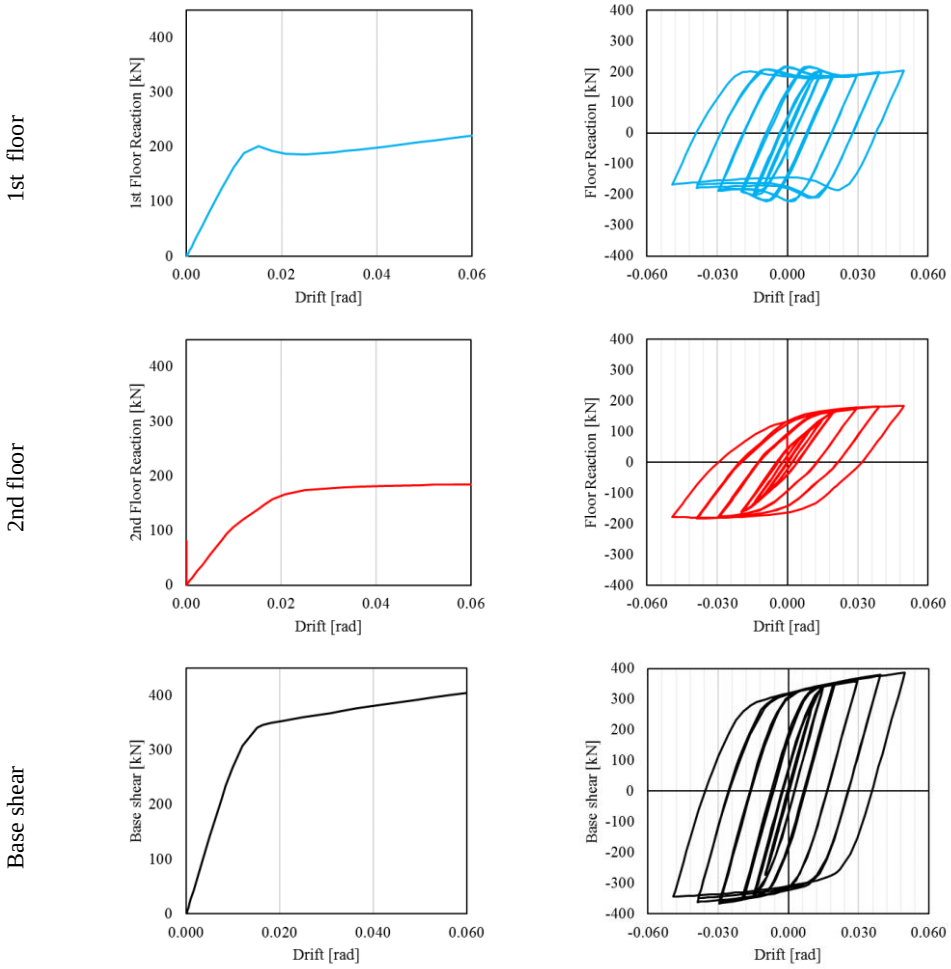

Figure 167 Abaqus results of SPO Analysis and cyclic quasi static analysis for the RBS model

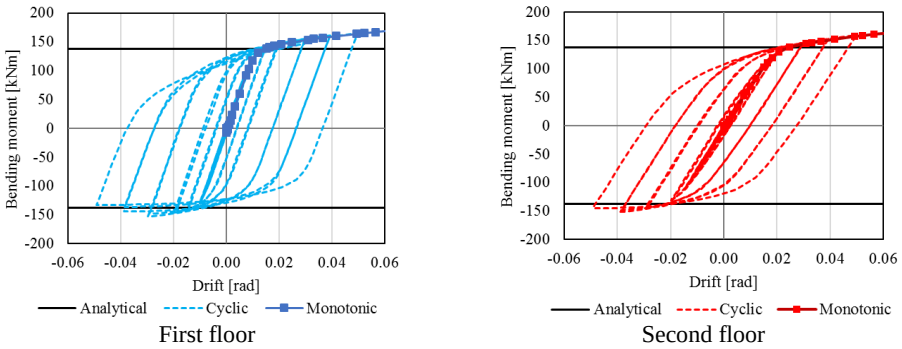

Figure 168 Bending moment in the RBS

Figure 169 shows the results of the static pushover and cyclic quasi-static analysis on the FD frame model. In this case the first floor has a lower contribution (150kN) while the contribution of the second floor is increased (239kN).

Figure 171 depicts the PEEQ in the FD frame, and as visible from the images, the damage is concentrated only at the base of the columns, with a similar value to the RBS frame. The plastic strain concentration at the column level are due to the local effects caused by the application of the loads and therefore can be overlooked.

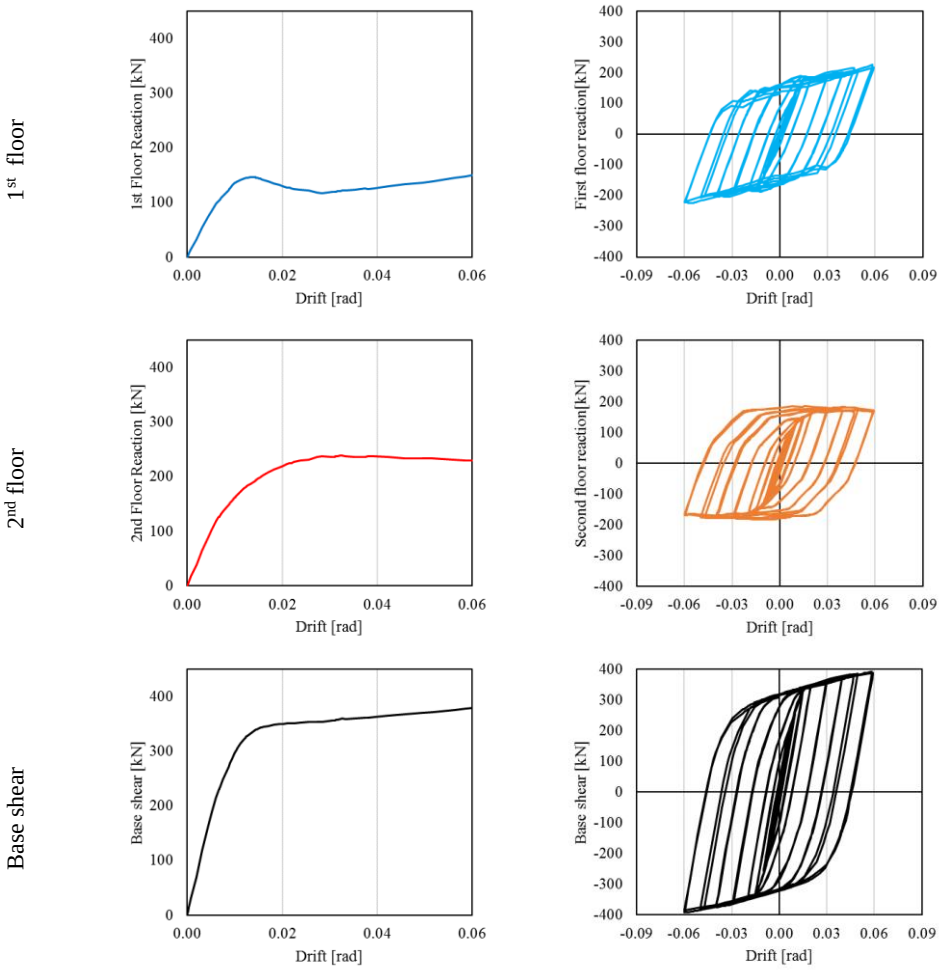

Figure 169 Abaqus results of SPO Analysis and cyclic quasi static analysis for the FD model

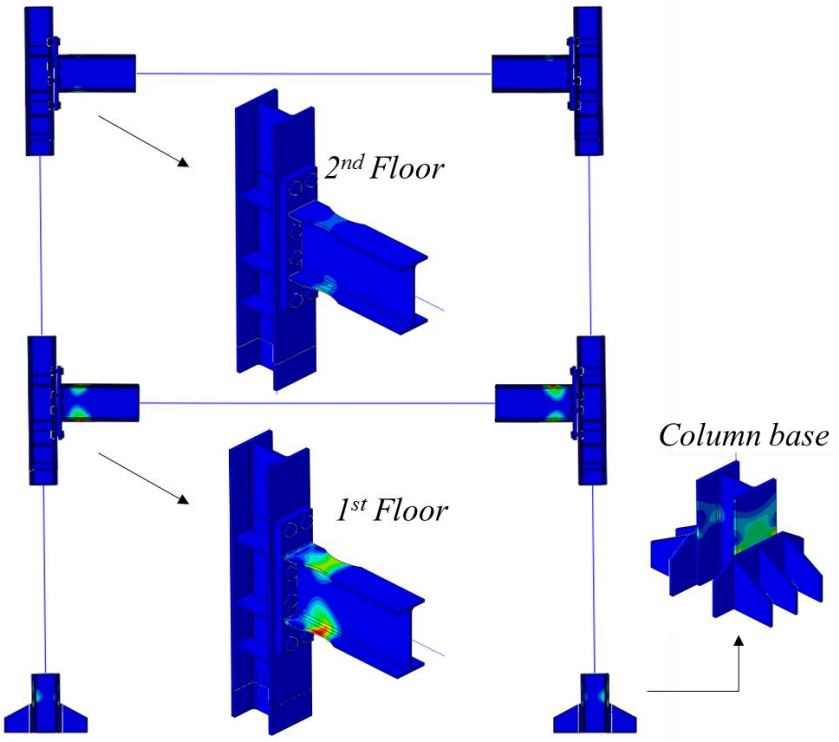

Figure 170 Plastic deformation in the RBS frame (cyclic analysis)

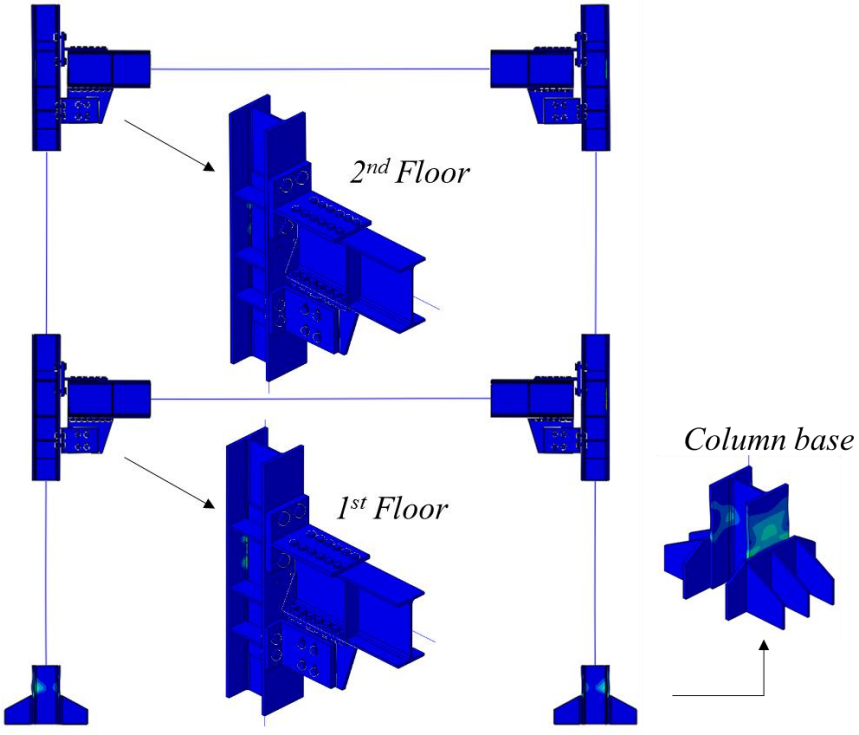

Figure 171 Plastic deformation in the FD frame (cyclic analysis)

4.4.3.2 Comparison between the RBS and FD frame model

As evident from Figure 172, the maximum base shear of the RBS and FD frame are very close, the capacity curves being almost overlapped. The FD frame however exhibits a slightly more rigid response, which is easily explained by the more rigid joint, and lower strength.

In terms of the joint response, the results show similarities although the general shape of the cycles is different i.e. a smooth shape for the RBS and a jerkier one (after the initiation of the sliding) for the FD. Nevertheless, both configurations reach the design bending resistance and exhibit similar energy dissipation capacities with minimal degradation in strength up to 5% interstorey drift.

The most significant difference in the response is the plastic damage distribution. As it was expected, the RBS, as the dissipative zone, suffered large plastic deformations, while the FD joint dissipated the energy by mans of relative sliding of the vertical rib with respect to the friction pads. This is detailed in Figure 170 and Figure 171 which show the PEEQ distribution for the two structures.

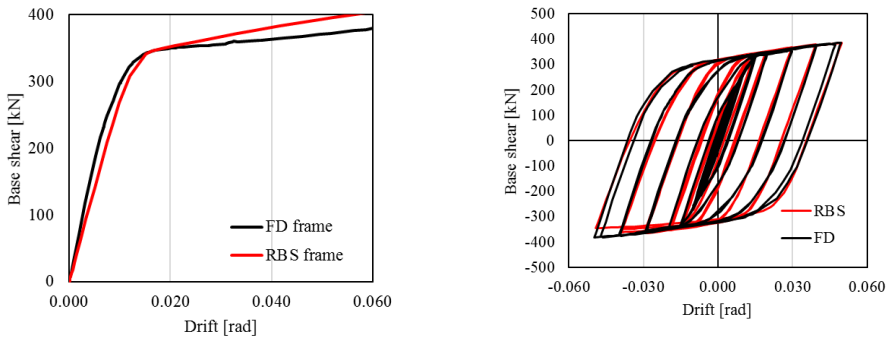

SPO analysis Cyclic quasi-static analysis

Figure 172 Comparison of RBS and FD frame response

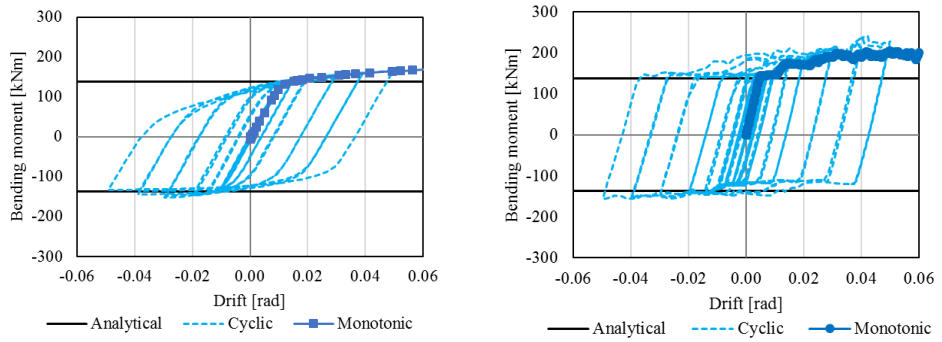

a) RBS b) FD

Figure 173 Comparison of RBS and FD joint response

4.4.3.3 *Comparison of Simplified (SAP2000) and Advanced (ABAQUS) model*

As presented in Figure 174, the simplified model gives a very good approximation of the response of the more detailed ABAQUS model in terms of static nonlinear analyses. Reasonable results are reached also in the case of the nonlinear dynamic analysis, considering the significant simplifications made. However, it is clear that in terms of peak base shear force and residual drift, the SAP2000 model is lacking, leading to underestimations of both measurements.

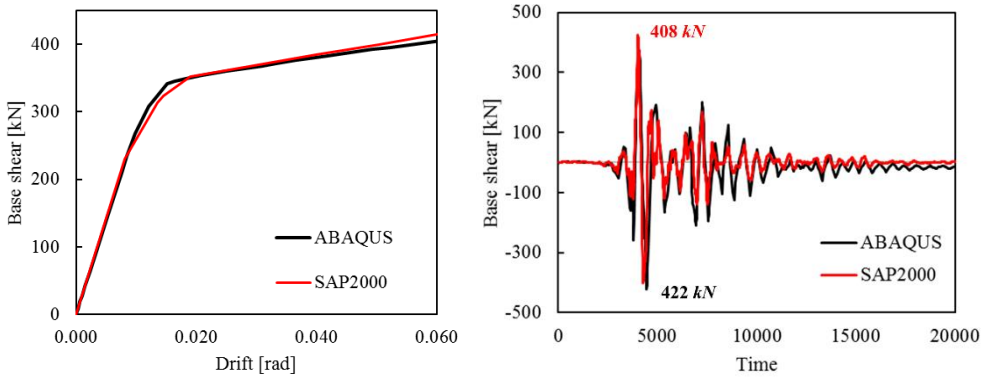

Static pushover analysis Time history analysis

Figure 174 Comparison between advanced and simplified RBS frame model

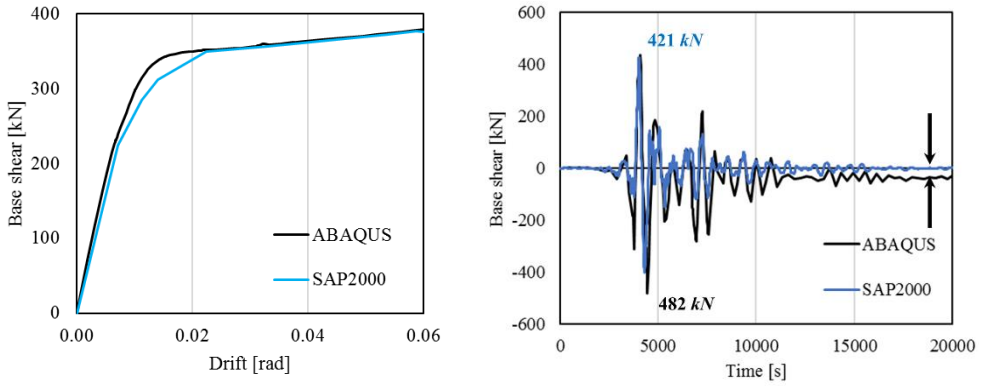

Static pushover analysis Time history analysis

Figure 175 Comparison between advanced and simplified FD frame model

Therefore, with regards to both models (RBS and FD) it can be concluded that the simplified model can be used to perform more computationally demanding analyses, or for large number of structures, when the desired result is a general idea of the global response. The advanced FE model is more adapted for the detailed investigation of the local effects within the framework of the entire structure (distribution of plastic damage, structures tested in laboratories, etc.).

4.4.3.4 Nonlinear dynamic response of RBS frame under natural records

Prior to the full-scale experimental test on the RBS structure, it was necessary to select a ground motion which would be a balanced solution between sufficient demand on the structure and the safety considerations of the setup and laboratory.

Table 47 Ground motions details

Epicenter	*Date*	*Details*
Coalinga, USA	02 May 1983	6.5 ML 16:43:00 PDT 36.25N 120.30W Depth 9.0 km
Spitak, Armenia	07 December 1988	6.8 ML 10:41:25 GMT 40.94N 44.29E Depth 10 km
Imperial Valley, USA	15 October 1979	6.6 ML 16:16:00 PDT 32.67N 115.36W Depth 15.0 km

From the large number of preliminary selected ground motions (GM), three of them were considered appropriate: Coalinga, Spitak and Imperial Valley. Table 47 and Figure 176 show details of the three selected ground motions. The accelerograms were scaled based on the design seismic action. The advanced numerical RBS model was used for the assessment of the structure's response. The most relevant results are the maximum horizontal floor reactions and base shear, the maximum storey drift and the residual drift. The forces are of particular importance for the check of the actuator capacity.

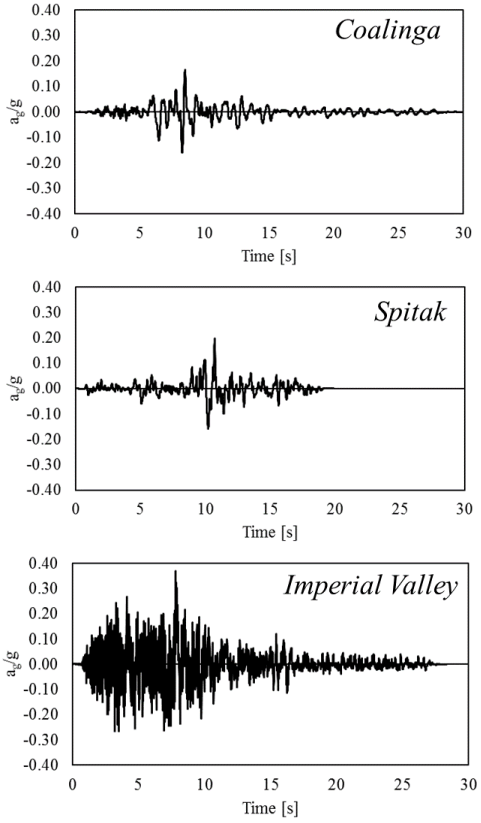

Figure 176 Ground motions accelerograms

Table 48 Summary of the FEAs results

GM	$F_{1st,max}$	$F_{2nd,max}$	$V_{b,max}$	$\theta_{1st,max}$	$\theta_{2nd,max}$	θ_{res}
	[kN]	*[kN]*	*[kN]*	*[-]*	*[-]*	*[-]*
Coalinga	283	215	393	3.61%	3.54%	1.73
Spitak	332	224	415	3.95%	3.43%	0.66%
Imperial Valley	314	200	403	3.57%	3.40%	0.81%

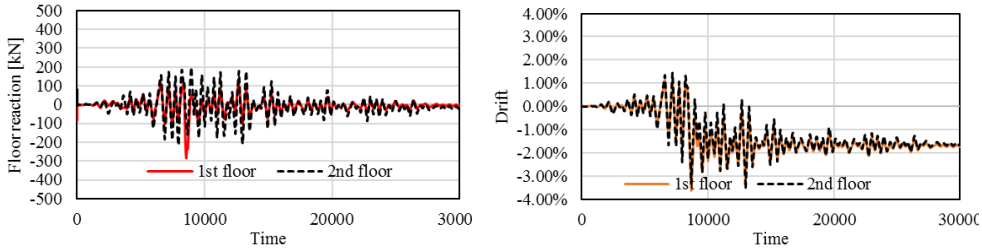

a) Coalinga GM

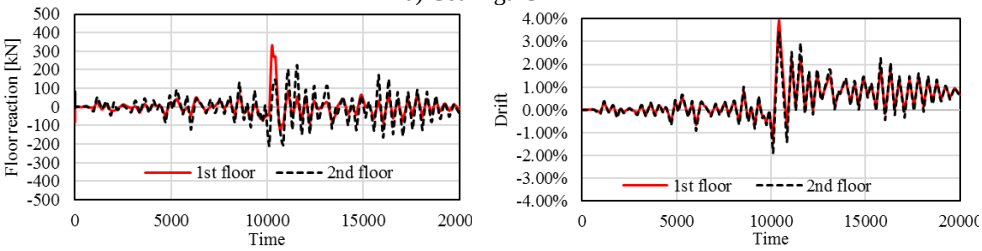

b) Spitak GM

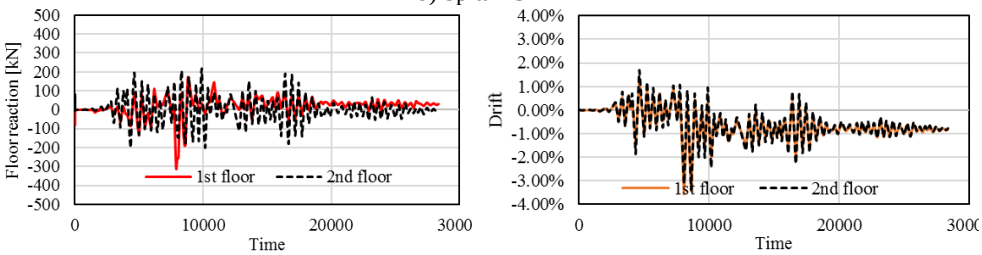

c) Imperial Valley GM

Figure 177 Floor reactions and drift histories for the considered ground motions

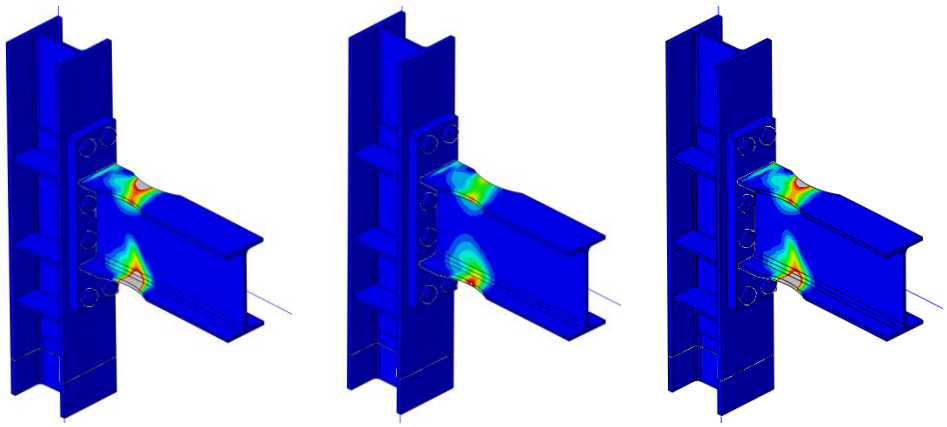

a) Coalinga b) Spitak c) Imperial Valley

Figure 178 PEEQ in the RBS on the 1st floor

The largest values in terms of horizontal forces and transient storey drifts were obtained for the Spitak GM, with the lowest residual drift, as depicted in Table 48 and Figure 177. The largest residual drift (θ_{res} = 1.73%) was obtained for Coalinga GM and this is reflected also in the equivalent plastic strain distribution (PEEQ) in Figure 178.

For all the ground motions the reaction resulting forces were within the limits set due to the actuators capacity and the lateral relative displacements were below te 4% limit agreed upon for safety reasons.

The Imperial Valley GM gives intermediate results in terms of forces and transient storey drifts, as well as residual drift. The balanced damage distribution (Figure 178c) and the large number of cycles which are expected to be particularly demanding on the structure, confirm that the Imperial Valley GM is a good option for the pseudo-dynamic tests.

4.5 DESIGN AND ANALYSIS OF FRAMES EQUIPPED WITH FRICTION DEVICES

4.5.1 General description of the EC8 compliant design methodologies

The fundamental difference between the traditional MRFs and the FD-MRFs (moment resisting frames equipped with friction devices) is the dissipative element i.e. the beam for the former, while the friction connection (or damper) for the latter.

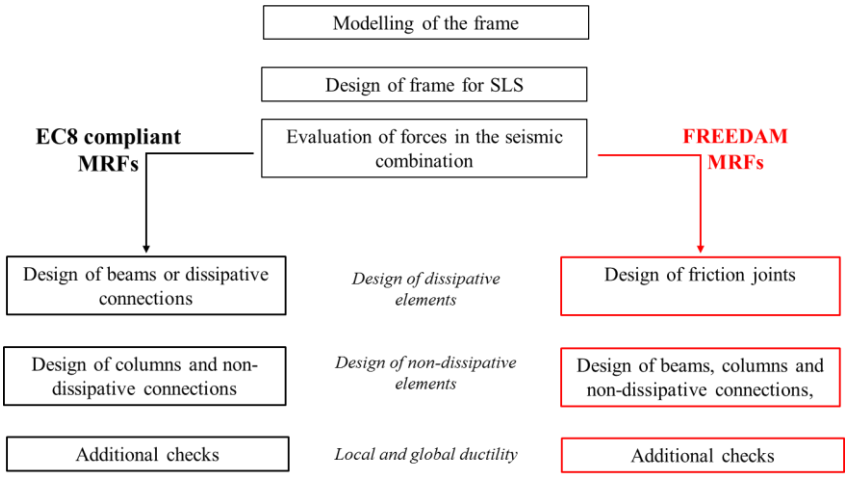

Figure 179 Design algorithm

As depicted in Figure 179, the initial steps are naturally identical with the design of traditional moment resisting frames, as the friction devices do not bring substantial alterations of the MRFs. However, the design requirements differ consistently, due to the special application of the capacity design rules. Within the current work, two possible approaches were initially assumed for the design of the MRFs equipped with friction devices. The main difference between the proposed approaches is the establishment of the friction device design bending moment (M_{FD}). Detailed explanations are hereinafter presented for both methodologies.

4.5.1.1 FD-A

The first design approach (proposed by the partners of University of Salerno) defines the design forces for the dissipative element (friction damper) function of the capacity of the connected beam ($M_{\mathrm{pl,bRd}}$). Initially, it is assumed that the forces to be carried by the damper correspond to the formation of the plastic hinge at the beam end, out of the protruding part of the connection. Figure 180*a* depicts the schematic distribution of bending moment at the beam end, in the joint area for the FD-A design methodology. The reference points A, B and C are detailed in Figure 181 together with the explanation of the distances.

The procedure starts by assuming the bending moment at point C as equal to $M_{\mathrm{pl,b,Rd}}$ and the subsequent evaluation of $F^{*}_{slip,req}$, the initial required slip resistance (see equation below) and the effective slip resistance ($F^{*}_{slip,Rd}$) which is detailed in Section 4.3.1.1 "*The principle of the friction connections design".*

$$F^{*}_{slip,req} = \frac{M_{pl,b,Rd}}{h_t} \tag{4.21}$$

Where $M_{pl,b,Rd}$ is the beam plastic bending resistance and h_t is the connection lever arm (distance from the middle of the Tee web to the middle of the haunch bottom flange).

In the next step, the capacity design bending moment (M^{*}_{CD}) for the non-dissipative elements is evaluated based on the design slip force ($F^{*}_{slip,Rd}$ previously defined) and considering the overstrength coefficient Ω_{μ} as defined in equation (4.22).

$$M^{*}_{CD} = \Omega_{\mu} F^{*}_{slip,Rd} h_t \tag{4.22}$$

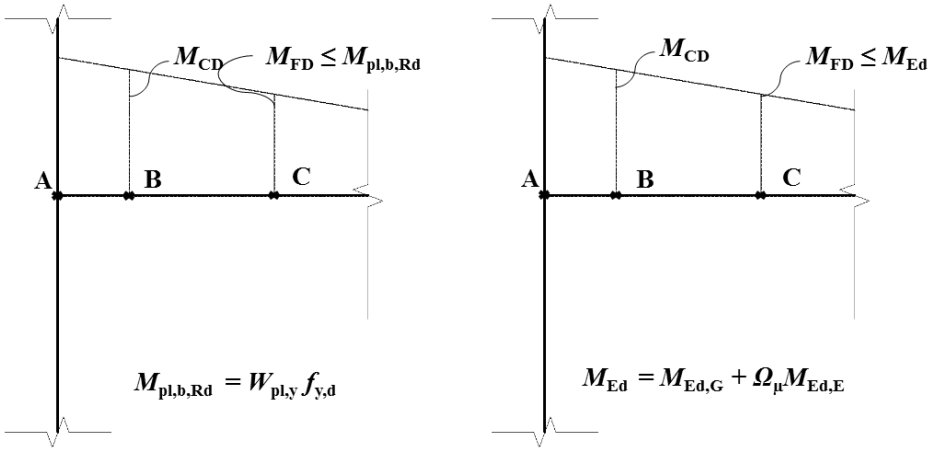

a) Scheme for FD-A b) Scheme for FD-B

Figure 180 Details for the joint design force

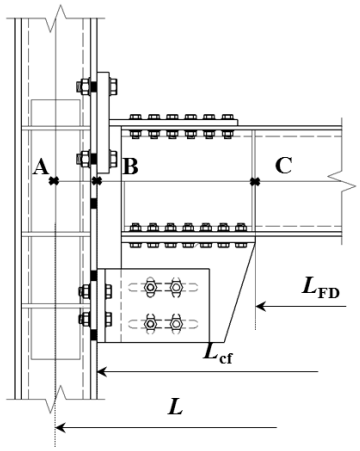

A – the ideal node

B - the column face

C – the end of the protruding part of the connection

L – *span length measured as distance between column axes*

L_{cf} – *span length measured in-between column faces*

L_{FD} – *span length measured in-between friction device ends*

Figure 181 Points of reference for the design forces

The forces obtained have to satisfy the initial assumption i.e. that the maximum bending moment in point C is not larger than $M_{pl,b,Rd}$.

$$M_{FD} = \frac{L-a}{L} M_{CD}^{*} \le M_{pl,b,Rd} \tag{4.23}$$

$$a = \frac{L_{cf} - L_{FD}}{2} \tag{4.24}$$

This implies a reduction of both the damper slip resistance (and bending resistance M_{FD}) and the forces for the capacity design (M_{CD}).

$$M_{CD} = \Omega_{\mu} F_{slip,Rd} h_{tot} \leq \frac{L}{L-a} \cdot M_{pl,b,Rd} \tag{4.25}$$

$$F_{slip,Rd} \leq \frac{L}{L-a} \cdot \frac{M_{pl,b,Rd}}{h_{tot} \Omega_{\mu}} \tag{4.26}$$

$$M_{FD} = F_{slip,Rd} h_{tot} \tag{4.27}$$

The resistance of the friction device is thus set based on the beam capacity and, given the current Eurocode 8 rules, this in turn will lead to large member section and friction connections with corresponding significant capacities.

4.5.1.2 FD-B

In this design approach, the dissipative element (friction damper) is designed for the forces from the seismic combination (considering the seismic forces reduced by *q*) obtained from the elastic analysis. Figure 180*b* details the distribution of the bending moment in the joint zone for the current design methodology. The values are obtained as follows:

$$F_{slip,req} = \frac{M_{FD}}{h_t} \tag{4.28}$$

$$M_{FD} \leq M_{Ed} = M_{Ed,G} + M_{Ed,E} \tag{4.29}$$

Where M_{FD} is the design bending moment for the dissipative element, M_{Ed} is the design bending moment from the seismic combination, $M_{Ed,G}$ is the contribution of the gravitational loads to the design bending moment and $M_{Ed,E}$ represents the contribution of the exceptional loads (reduced by *q*) to the design bending moment.

The non-dissipative elements (column-face connections, beams, columns) are designed considering the overstrength factor Ω_{μ}

$$M_{cf} = M_{Ed,G} + \Omega_{\mu} \cdot M_{Ed,E} \tag{4.30}$$

Where $M_{Ed,G}$ and $M_{Ed,E}$ represent the same as above, but in the column face section and Ω_{μ} is the overstrength coefficient defined in the following Section.

4.5.1.3 *The overstrength coefficient Ω_{μ}*

In both proposed methodologies, the Ω_{μ} is of crucial importance, and it is defined as:

$$\Omega_{\mu} = \frac{\mu_{st.95\%}}{\mu_{dyn.5\%}} \cdot \frac{N_{b.95\%}}{N_{b.5\%}} \tag{4.31}$$

Where:

- $\mu_{dyn.5\%}, N_{b.5\%}$ (lower-bound values) for the design of the dissipative connection
- $\mu_{st.95\%}, N_{b.95\%}$ (upper-bound values) for the design of the other non-dissipative elements

Considering the friction coefficient values obtained from lap shear test ($\mu_{dyn.5\%} = 0.53$ and $\mu_{st.95\%} = 0.84$) and the ratio $N_{b.95\%} / \ N_{b.5\%} = 1.20$, it results that $\Omega_{\mu} \cong 1.9$.

4.5.2 Design Assumptions for the Case Study

In order to assess the performance of the new structural system, a set of traditional MRFs were designed according to EC8. Starting from these frames, identical sets were designed following the new proposed strategies for the design of free from damage moment resisting frames (FD-MRFs).

The geometrical features of the examined frames selected are shown in Figure 182, where the parameters chosen for variation i.e. number of storeys

(3 or 6), number of spans (3 or 5) and the span length (6 or 8m) are also depicted. The structures had a square in-plane configuration and the MRFs to be designed were considered the 2 outer-most frames (assuming all bays as lateral resisting bays). The secondary beams were assumed parallel with the MRF and at a constant space of 2 *m*, allowing the 6 and 8 *m* span frames to have the same distributed load on the MRF beam.

The combination for the evaluation of the design vertical forces is defined by the following equation:

$$\sum G_k \text{ "+" } \sum \psi_{2,i} Q_{k,i} \tag{4.32}$$

Where $G_{k,i}$ represent the characteristic permanent loads, $Q_{k,i}$ represent the characteristic variable loads and $\psi_{2,i}$ is the combination coefficient for the quasi-permanent value of the variable action *i*, which is a function of the destination of use of the building.

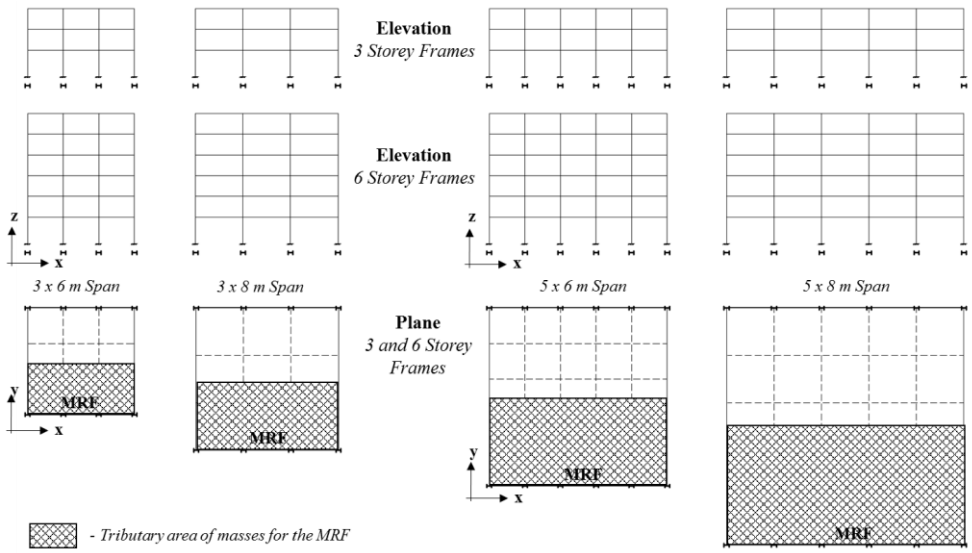

Figure 182 Frame configuration

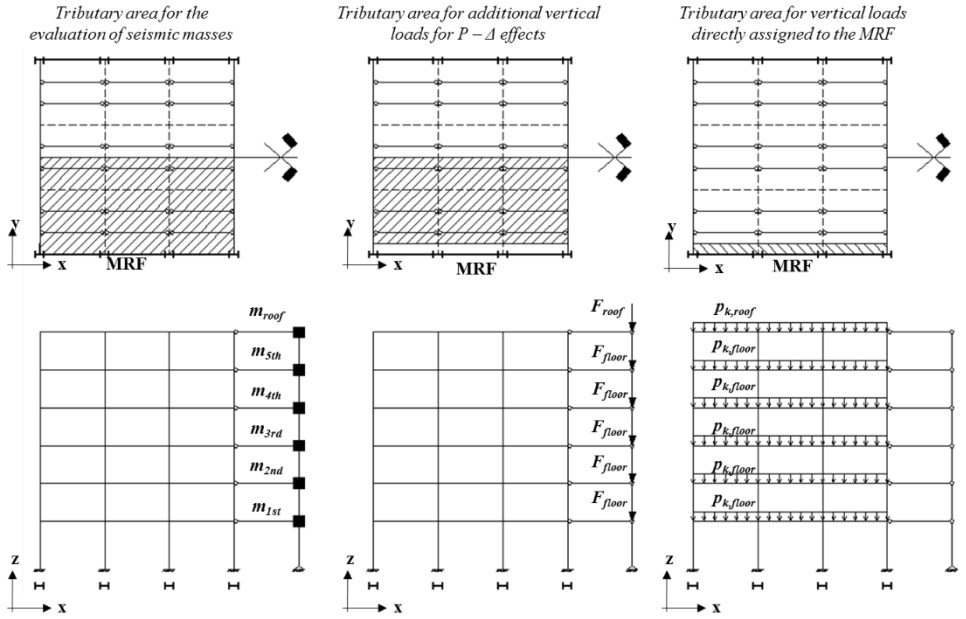

Figure 183 The tributary area for masses, additional gravity loads for P-Δ effects and the vertical loads directly assigned to the MRF

The seismic masses were evaluated considering the gravitational loads from the combination in equation below and the self-weight of the frame members. The tributary area for the gravity loads is considered as in Figure 183.

$$\sum G_k \text{ "+" } \sum \psi_{E,i} Q_{k,i} \tag{4.33}$$

Where $\psi_{E,i} = \varphi \cdot \psi_{2,i}$ is the combination coefficient for variable action *i*, which takes into account the likelihood of the loads $Q_{k,i}$ to be not present over the entire structure during the earthquake, as well as a reduced participation in the motion of the structure due to a non-rigid connection with the structure. The combination coefficients are defined in Table 49.

Table 49 The combination coefficients

	$\cdot\psi_{2,i}$	φ	$\psi_{E,i}$
Intermediate floor	0.30	0.50	0.15
Roof	0.30	0.80	0.24

The permanent and live loads considered for design were chosen within a practical range (4.5 kN/m^2 and 2 kN/m^2 respectively). As for the combinations, there will be two of significance, namely:

The seismic combination for dissipative elements (i.e. damper):

$$ULS - S_{dissip} = \sum G_k "+" \sum \psi_{2,i} Q_{k,i} "+" A_{Ed} \tag{4.34}$$

And the seismic combination for non-dissipative elements:

$$ULS - S_{non-dissip} = \sum G_k "+" \sum \psi_{2,i} Q_{k,i} "+" \Omega_\mu A_{Ed} \tag{4.35}$$

The seismic action was modelled assuming a response spectrum Type 1 and soil Type C. As depicted in Figure 184, three seismicity levels were considered for the design of the structures: Medium (MH), High Hazard (HH) and Very High Hazard, with PGAs equal to 0.25*g* 0.35*g* and 0.45*g*, respectively, The maximum behavior factor q = 6.5 was adopted for the design spectrum.

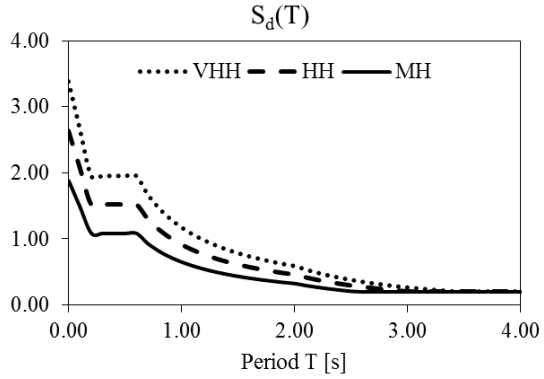

Figure 184 Design spectra

4.5.2.1 Imperfections

The unfavourable effects of construction errors (within the allowable tolerances) are considered as an equivalent imperfection in the form of an initial sway imperfection.

The procedure given in EN1993 1-1 allows modelling the global sway imperfections as equivaent horizontal forces evaluated based on:

$$H_{i,d} = \phi p_d \tag{4.36}$$

Where ϕ is the global initial deformastion assumed*)* and p_d represents the total design vertical loads defined by the following equations:

$$\phi = \phi_0 \alpha_m \alpha_h \tag{4.37}$$

$$p_d = 1.35 g_k + 1.50 q_k \tag{4.38}$$

Where ϕ_0 has the basic value 1/200 and α_m is the reduction factor for the number of columns in a row *m* and α_h is a reduction factor for height *h* applicable to columns. The two coefficeints are defined in the equations:

$$\alpha_m = \sqrt{0.5\left(1 + \frac{1}{m}\right)} \tag{4.39}$$

$$\alpha_h = \frac{2}{\sqrt{h}} \tag{4.40}$$

The forces above are applied at each storey and considered in all combinations.

4.5.2.2 Torsional effects

Accidental torsional effects must be accounted for in accordance with the Eurocode design rules. However, in case of the planar design of frames the value is reduced to 1.3 (from 1.6) in order to avoid an over conservative design.

4.5.2.3 The P-Δ effects

In order to avoid overdesigning the structures due to the very restrictive code limitations for the $P-\Delta$ effects, it was assumed that the interstorey drift sensitivity coefficient (θ) should be in between 0.1 and 0.2, and the lateral force to be

amplified accordingly with $\alpha = 1/(1-\theta)$. According to EC8 Part 1 the interstorey drift sensitivity coefficient is evaluated as:

$$\theta = \frac{P_{tot} d_t}{V_{tot} h_{storey}} \tag{4.41}$$

Where P_{tot} is the total gravity load at and above the storey considered in the seismic design situation, d_t is the design interstorey drift, evaluated as the difference of the average lateral displacements ds at the top and bottom of the storey under consideration, V_{tot} is the total seismic storey shear and h_{storey} is the interstorey height.

4.5.2.4 Material Properties and Member sections

The steel members were assumed with typical I European profiles. The beams were modelled considering IPE profiles, while for the columns HE B, HE M and HD sections were used. All members in the investigated structures were considered made of a S355 steel.

4.5.2.5 SLS check

The verification for drift considerations was made according to EC8, considering:

$$\delta_r \nu \leq 0.010 h_{storey} \tag{4.42}$$

Where δ_r is the design inter-storey drift, ν is the reduction factor which takes into account the lower return period of the seismic action associated with the damage limitation requirement (considered 0.5) and h_{storey} is the storey height.

4.5.2.6 ULS checks

Since the dissipative element of this structural configuration is the friction damper and not the beam ends, both the beam and column will be treated as non-dissipative elements.

The strength and stability checks according to EC3 Part 1-1 need to be performed for both beam and column. The internal forces for the named checks (M_{Ed} , V_{Ed} , and N_{Ed}) are evaluated based on the seismic combination for non-dissipative elements $ULS - S_{non-dissip}$, as depicted in:

$$M_{Ed} = M_{Ed,G} + \Omega_{\mu} M_{Ed,E} \tag{4.43}$$

$$V_{Ed} = V_{Ed,G} + \Omega_{\mu} V_{Ed,E} \tag{4.44}$$

$$N_{Ed} = N_{Ed,G} + \Omega_{\mu} N_{Ed,E} \tag{4.45}$$

In the case of columns, it is required that the shear force to be limited at 50% of the shear plastic capacity of the column, as defined:

$$\frac{V_{Ed}}{V_{pl,Rd}} \leq 0.50 \tag{4.46}$$

EC8 regulations do not allow the formation of soft storey plastic mechanisms, as this kind of mechanism calls for high local ductility demands in the columns of the soft storey. In order to prevent the development of such mechanism, the local check must be satisfied at all nodes, except for the last floor.

$$\sum M_{Rc} \geq 1.3 \sum M_{Rb} \tag{4.47}$$

Where: $\sum M_{Rc}$ is the sum of the moment of resistance of the columns framing the node and $\sum M_{Rb}$ - is the sum of the moments at the face of the column and is evaluated as:

$$\sum M_{Rb} = \Omega_{\mu} \sum M_{j,Rd} + s_h \cdot V_{Ed,G} \tag{4.48}$$

Where s_h is the distance from the tip of the haunch/rib plate to the column face and $V_{Ed,G}$ is the shear force due to gravity loads.

4.6 ANALYSIS ASSUMPTIONS FOR THE CASE STUDY

4.6.1 Material, elements and general modelling assumptions

The nonlinear static (Pushover) and dynamic (Timehistory) analyses were performed in SeismoStruct 2016.

The S355 steel was modelled considering a Menegotto-Pinto material model. The mean yield strength is determined as shown in the equation below and the modulus of elasticity was assumed with a value of 210GPa.

$$\gamma_{ov} \cdot f_{y,k} = 1.25 \cdot 355 = 443 MPa \tag{4.49}$$

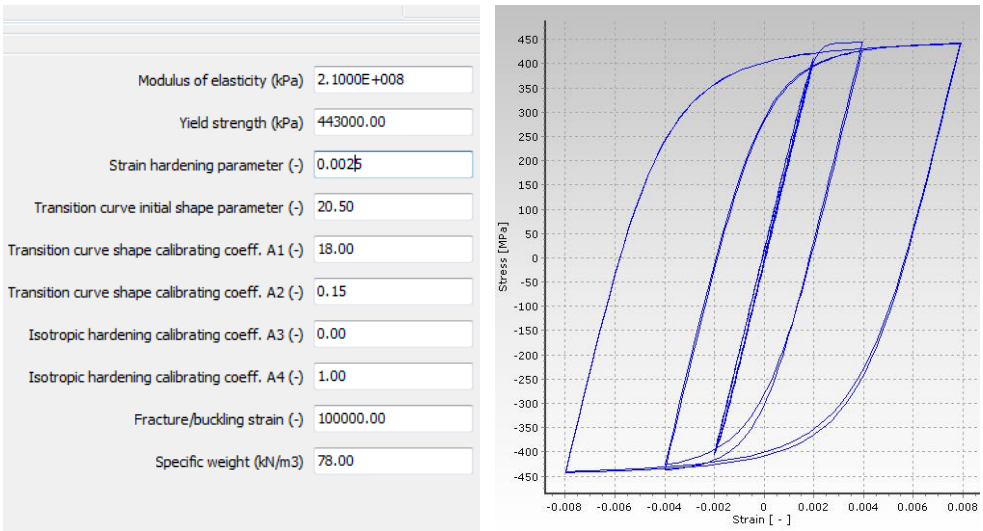

a) Material properties b) Sample curve

Figure 185 Menegotto-Pinto material model implemented in SeismoStruct

For all steel members an inelastic force-based frame element was used (*infrmFB*), considering 5 integration sections and 150 section fibers.

In the beam to column nodes, rigid links were modeled in order to simulate the higher stiffness of the joint (column web panel, haunched connection). These members were modelled considering a material with a very high Young's modulus and resistance, allowing thus no elastic or plastic deformation. The elements of the leaning column have been defined as Truss elements i.e. elements that have no rotational DOF.

The nodes of the structure have been defined in accordance with the actual geometry of the member sections, allowing the physical dimensions of the connection to be defined (see Figure 186).

Both Eurocode 8 compliant (EC8-MRFs) and the models of the frames with friction devices (FD-MRFs) were detailed with rotational springs at the column face. These elements were used in order to model the bending capacity of the full-strength haunch joint and the friction device, respectively.

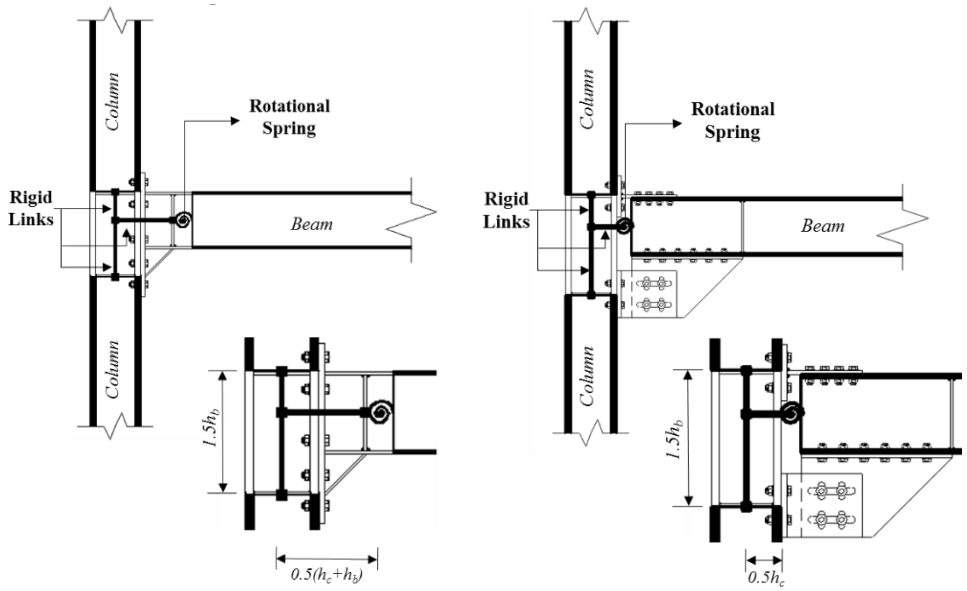

a) Node modelling for EC8-MRFs b) Node modelling for FD-MRFs

Figure 186 Node modelling

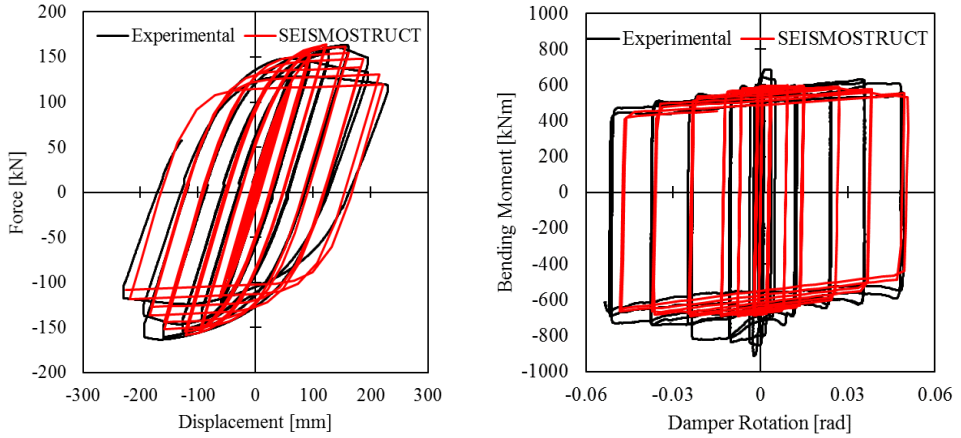

a) Calibration of smooth model b) Calibration of multilinear model

Figure 187 Spring calibration for FREEDAM Frames

The response of the traditional full-strength joint was modelled based on the experimental tests performed within the EQUALJoints RFCS Research Project (RFSR-CT-2013-00021) using a smooth model (Figure 187*a*).

Given that the two design approaches (FD-A and FD-B) define differently the joint resistance, the bending resistance of the rotational spring was also defined differently, as given by:

$$M_{j,Rd|FD-A} = 0.80 M_{pl,b} \tag{4.50}$$

$$M_{j,Rd|FD-B} = m \cdot M_{pl,b} \tag{4.51}$$

Where m is the utilization factor of the FREEDAM devices necessary for the obtained frame members. Practically, m is a rounded value of the $M_{Ed}/M_{pl,b,Rd}$ ratio obtained from the analysis, being M_{Ed} the bending moment from the seismic combination considering an elastic analysis.

From the stiffness point of view, the joints were assumed as full rigid, as the experimental and numerical tests on both small and large joint subassemblies showed that the stiffness of the column face connection exceeds 25 times the beam stiffness (see Figure 188). The characteristics of the springs

were modelled considering a multilinear model that was calibrated based on the experimental results on joints (Figure 187*b*).

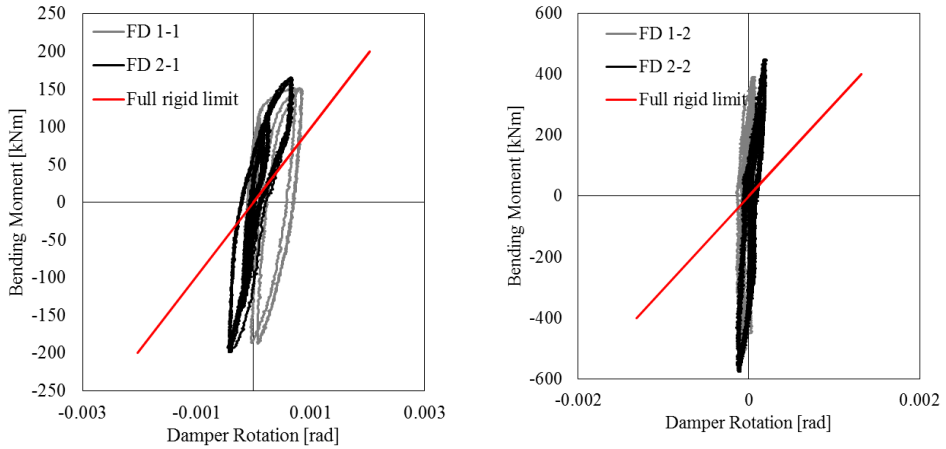

a) IPE270 - HE 220M b) IPE450 – HE 500B

Figure 188 The stiffness of the experimentally tested connections

4.6.2 Boundary conditions and Loads

The column bases have been fully restrained, in accordance with the design assumptions. All nodes, for each level have been constrained by horizontal rigid diaphragms and the out of plane displacement and rotation have been restrained (*rx+y+rz*).

The seismic masses evaluated considering the tributary area detailed in Figure 183, have been modelled as lumped masses in the leaning column nodes. Therefore, the settings were set for the software to define the masses from the element self-weight and the lumped masses.

The vertical loads corresponding to the tributary area of the beams (half of a secondary beam span) have been modelled as distributed forces. The additional vertical forces corresponding to the MRF tributary area (the remaining gravity forces for half the structure, necessary for the P-Δ effects) have been modelled as concentrated forces on the leaning column (see Figure

183). In consequence, the loads were entirely defined, and the settings of the software were set to not evaluate loads from masses.

4.6.3 Analyses performed

4.6.3.1 Static Pushover Analysis

Nonlinear static analyses have been performed considering triangular and uniform lateral force distribution based on the distribution on the frame height of the design base shear function of the floor mass and height.

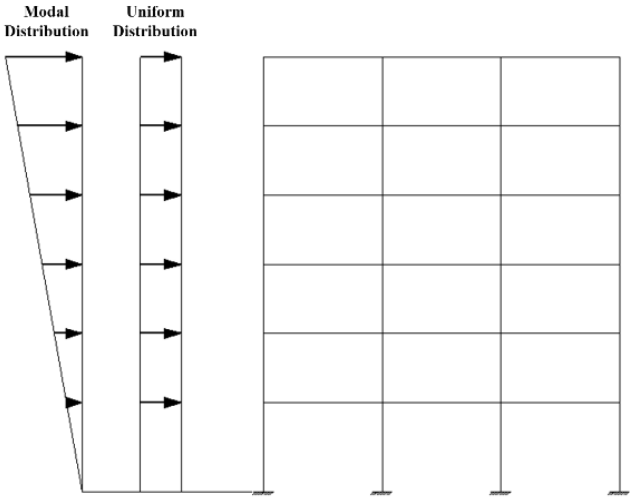

Figure 189 Lateral force distribution

In terms of monitored output the following results have been deemed of importance:

- The frame overdesign: V_1 / V_d - α_1 according to EC8 i.e. design base shear multiplier in order to attain first plastic hinge
- The frame redundancy: V_y / V_1 - α_u / α_1 according to EC8
- The frame overall overstrength: V_y / V_d - α_u according to EC8 i.e. design base shear multiplier in order to attain the collapse mechanism

The values of V_1, V_d and V_y are as defined in Figure 190. The design base shear V_d was evaluated based on the fundamental period T_1 obtainedby means of Eigenvalue analysis in Seismostruct.

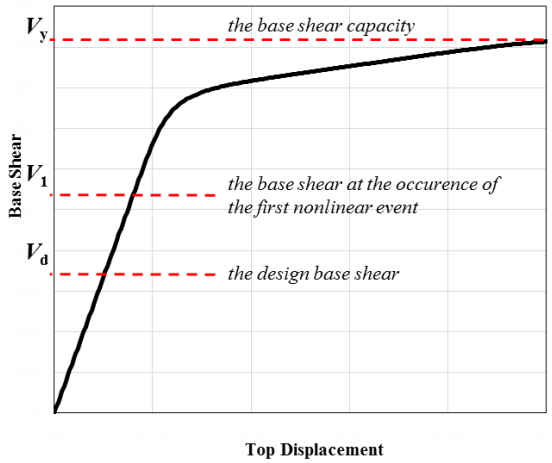

Figure 190 The base shear – top displacement curve

4.6.3.2 Nonlinear Dynamic Analyses

The Timehistory analyses have been performed considering a set of 14 natural earthquake acceleration records (Table 50). The signals were obtained from the RESORCE ground motion database in order to match 1.3 (due to torsional effects) times the elastic acceleration spectrum provided by EN 1998-1 (see Figure 191). The Timehistory analyses were performed considering the 0.59, 1.00 and 1.73 multipliers corresponding to the three limit states defined by EN1998-1, i.e. damage limitation (DL), significant damage (SD) and near collapse (NC), respectively.

The following parameters have been monitored:

- Peak Transient inter-storey drift – also referred to as PTID
- Residual interstorey drift (PRID) - for the Timehistory analyses, the records have been extended in order to allow the assessment of this result

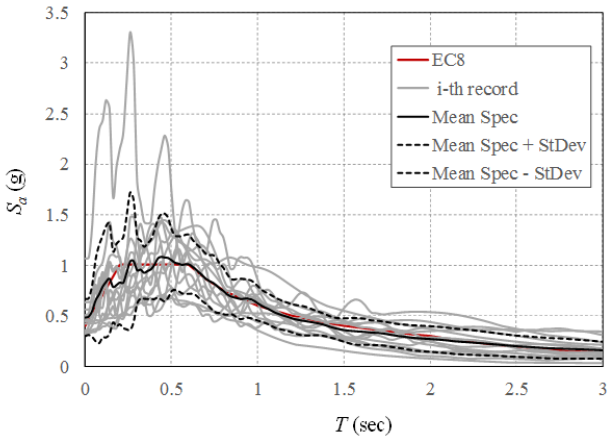

Figure 191 Comparison between natural signals and EC8 design spectrum

Table 50 Basic data of the selected ground motions

Earthquake name	Date	Station Name	Station Country	Magnitude Mw	Fault mechanism
Alkion	24.02.1981	Xylokastro-O.T.E.	Greece	6.6	Normal
Montenegro	24.05.1979	Bar-Skupstina Opstine	Montenegro	6.2	Reverse
Izmit	13.09.1999	Yarimca (Eri)	Turkey	5.8	Strike-Slip
Izmit	13.09.1999	Usgs Golden Station Kor	Turkey	5.8	Strike-Slip
Faial	09.07.1998	Horta	Portugal	6.1	Strike-Slip
L'Aquila	06.04.2009	L'Aquila - V. Aterno - Aquila Park In	Italy	6.3	Normal
Aigion	15.06.1995	Aigio-OTE	Greece	6.5	Normal
Alkion	24.02.1981	Korinthos-OTE Building	Greece	6.6	Normal
Umbria-Marche	26.09.1997	Castelnuovo-Assisi	Italy	6.0	Normal
Izmit	17.08.1999	Heybeliada-Senatoryum	Turkey	7.4	Strike-Slip
Izmit	17.08.1999	Istanbul-Zeytinburnu	Turkey	7.4	Strike-Slip
Ishakli	03.02.2002	Afyon-Bayindirlik ve Iskan	Turkey	5.8	Normal
Olfus	29.05.2008	Ljosafoss-Hydroelectric Power	Iceland	6.3	Strike-Slip
Olfus	29.05.2008	Selfoss-City Hall	Iceland	6.3	Strike-Slip

4.7 RESULTS OF THE NUMERICAL ANALYSES

The steel frame weight quantified and compared in Figure 192 shows that frames designed with the FD-A approach require a higher material consumption than those designed with EC8 and FD-B. This result is ascribable to the need to provide adequate lateral stiffness and fulfil the stronger requirements for local and global hierarchy criteria. The comparison between the three methodologies shows that the lowest material consumption obtained for all frames is for FD-B frames and that from an economical point of view, the latter solution turns out to be more effective.

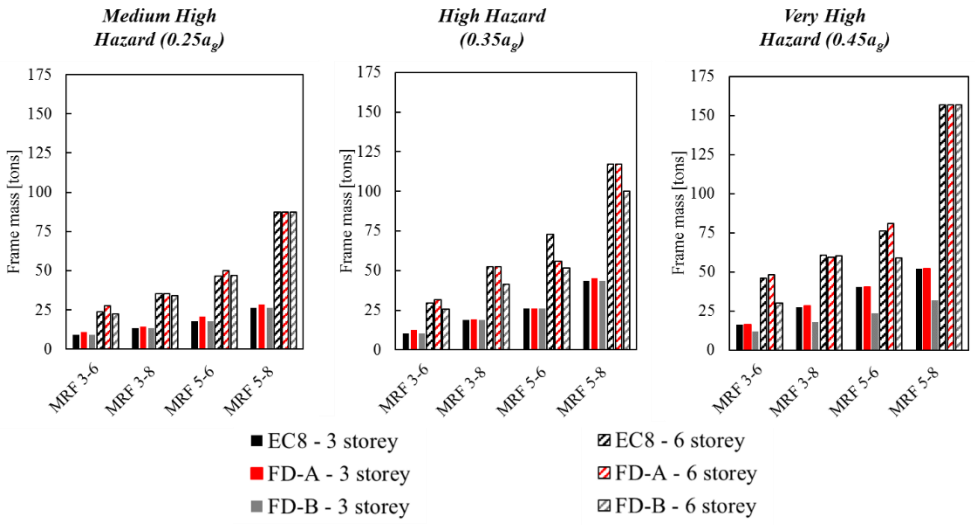

Figure 192 The designed MRF weight

4.7.1 Static nonlinear (Pushover) analyses

The static nonlinear analyses were performed considering both a modal and uniform force distribution (to consider higher vibration modes) and the results of the two are presented.

The pushover curves presented in Figure 193 for a sample structure (MRF 6-3-6) for all three design criteria (EC8, FD-A and FD-B) offer a first

understanding of the level of overstrength that EC8 compliant frames have, especially the frames designed considering medium high seismic hazard level (0.25*g*).

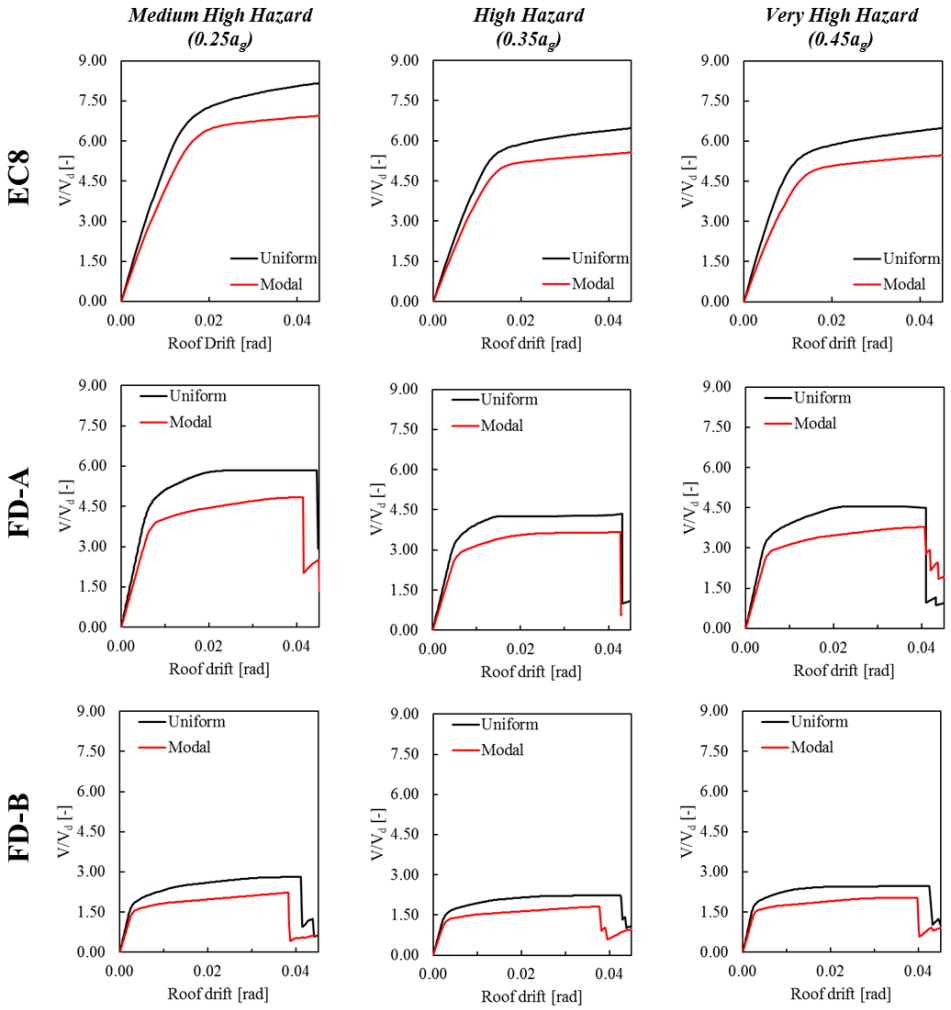

Figure 193 Normalized Pushover curves for MRF 6-3-6

Basically, the EC8 structures exhibit values of the collapse multiplier α (V/V_d) comparable to the reduction factor q, meaning in fact that the structures remain elastic under design level seismic events. This was expected, as during the design process, the effect of the seismic action had to be severely amplified due to the $P-\Delta$ effects and the interstorey drift limitations were governing in most of the cases (even for FD-MRFs). The EC8 compliant frames designed

for larger seismic hazards have lower α, however still not very far of the value of *q* adopted for the design (i.e. 6.5).

In the case of FD-A approach, the strength and the stiffness of the frames are not effectively decoupled, since the bending strength of the friction joints are set equal to the strength of the connected beams ($M_{j,Rd} \approx M_{pl,b,Rd}$). This leads to large column cross sections needed in order to satisfy the local resistance hierarchy and, in combination with the structural overdesigned caused by the deformability limitations, to large values of overdesign.

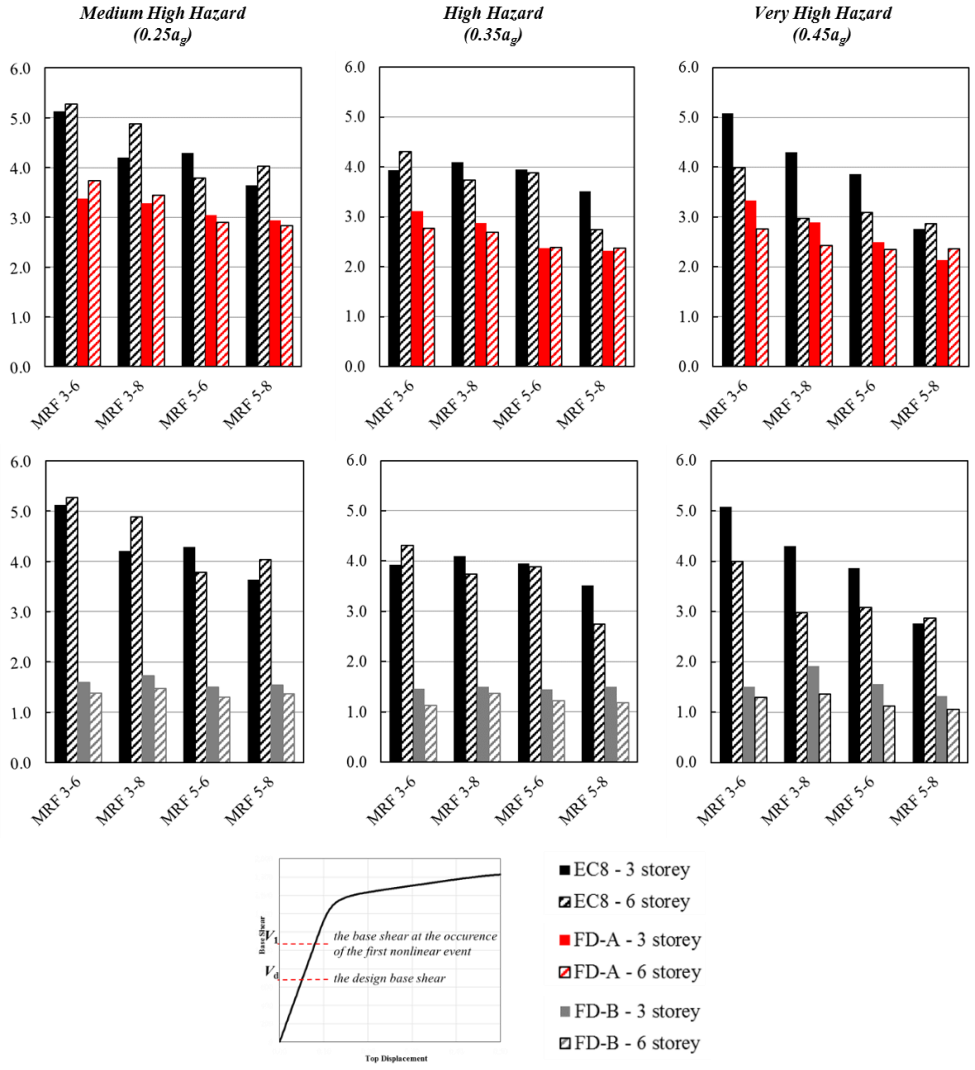

Figure 194 Average overdesign between modal and uniform lateral loading case

On the contrary, for the FD-B set of frames, the friction joints are designed to match the seismically induced forces ($M_{j,Rd} \approx M_{Ed}$), while the required lateral stiffness is guaranteed by the inertia of the girders, thus allowing to decouple the strength and the stiffness of the frames. This in turn leads to smaller overstrength and lower consumption of steel compared to the FD-A set of frames.

A more interesting way to look at the results is in terms of the different ratios between V_y, V_1 and V_d. The average of the modal and uniform lateral force distribution analyses is plotted in the following diagrams. In order to assess the efficiency of the new design methodologies (FD-A and FD-B) it is interesting to look at the comparative diagrams in Figure 194 which show the V_1/V_d ratio (a measure of the overdesign of the frame).

As expected, the EC8 compliant frames are heavily overdesigned due to the large overstrength factor that results from the need to satisfy the design drift limits imposed for the serviceability limit state (SLS). The frames designed with the FD-A approach exhibit overdesign coefficients not so far away from the EC8 ones i.e. the average is 2.80 with respect to 3.93. Although the new methodology introduced has lower overstrength coefficients and reduces the demand in terms of design interstorey drift, the local ductility requirement i.e. the hierarchy criterion at the level of the beam to column node, leads to further increase of sections.

Applying the FD-B design approach leads to very reasonable overdesign values averaging about 1.3. The low values are easily explained by the way the design and the critical requirements for the verifications proceeded. Similar with the EC8, the FD-B models are mostly designed for SLS, but different from the code compliant frames, the non-dissipative members are checked for lower forces obtained using a smaller overstrength factor Ω_μ. This is a significant advantage because in this way it is possible to calibrate the

design resistance of the connection to the design bending and shear demand, also allowing a more effective application of hierarchy rules without the need of overdesigning excessively the columns compared to the traditional EC8 and FD-A approaches.

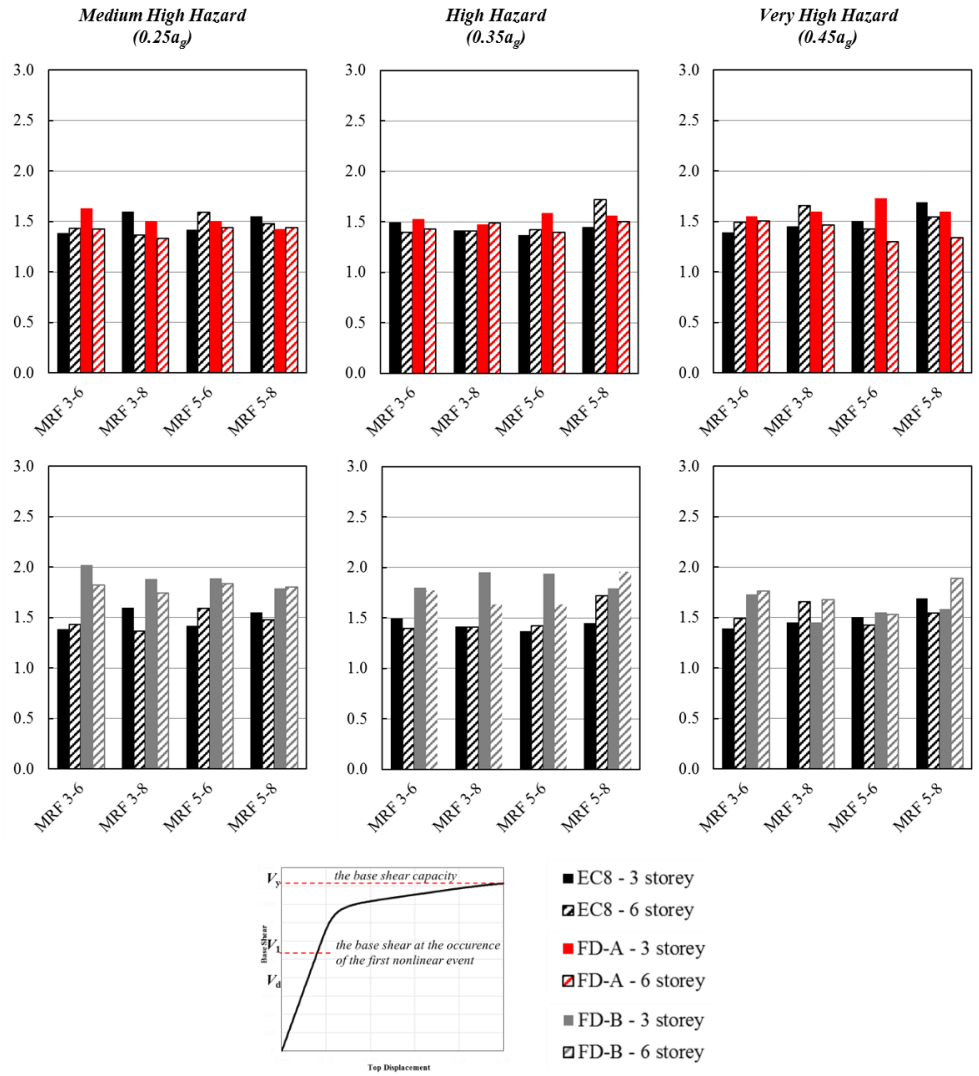

Figure 195 Average redundancy between modal and uniform lateral loading case

Figure 195 shows the comparison of the V_y/V_1 ratio that is a representative factor for the redundancy of the structures and can be found in the EN 1998-1 as the α_u/α_1 ratio. For the design of multi-storey multi-bay frames a value of 1.3 is recommended but allowance is made for values up to 1.6, provided that

they are justified by means of pushover analyses. As it can be seen from the plot, the EC8 and FD-A structures reach the same average values of 1.49, respectively but with frames having ratios larger than 1.6. However, for the FD-B set, all the frames exceed the maximum factor of 1.6, averaging around 1.7. This means that the MRF typology allows activating a large number of friction connections but not simultaneously, thus resulting a large redundancy. Such a result suggests the necessity to provide large slip capacity to the FD connections in order to guarantee adequate rotation capacity.

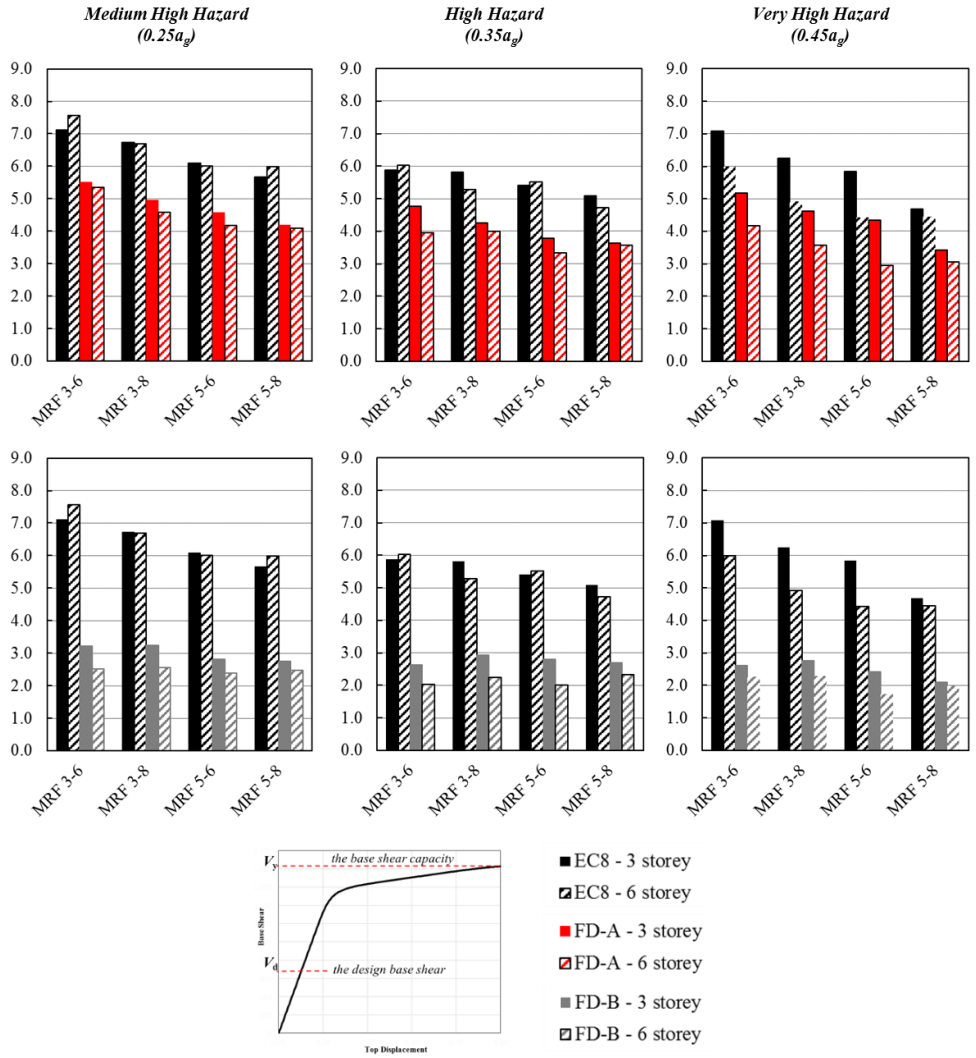

Figure 196 Average overall overstrength between modal and uniform lateral loading case

The overall overstrength of the three sets of frames presented in Figure 196 summarizes the aspects already discussed and reveals that the EC8 and FD-A set of frames have a great amount of inherent overstrength i.e. on average 5.8 and 4.2 of the design capacity, respectively. On the other side, the FD-B frames present more reasonable levels, averaging at 2.2.

Due to the un-desirable response of the frames designed according to the design methodology FD-A, the nonlinear dynamic analyses have not been performed for these structures. Therefore, from this point on only the results of EC8 compliant frames and the FD-B methodology frames will be discussed. To simplify matters, the FD-B set of frames will be addresses simply as FD.

4.7.2 The dynamic performance at the code-set levels (DL, SD and CP)

The assessment of the structural response at the three limit states imposed by EC8 is made based on the peak transient interstorey drift (PTID) and peak residual interstorey drift (PRID). The three limit states have the failure criteria defined in Table 51.

Table 51 Failure criteria for the EC8 limit states

Limit state	Return period [years]	Scaling factor	Failure criteria
Damage limitation (DL)	*225*	*0.59*	*0.75% TID ratio*
Significant damage (SD)	*475*	*1.0*	*2.5% TID ratio* *1% RID ratio*
Near collapse (NC)	*2475*	*1.73*	*5% TID ratio* *5& RID ratio*

For the sample frame MRF 6-3-6 (66 storey, 3 bays of 6m) the PTID at the Dl limit state (Figure 197) shows that both the EC8 compliant and the FD frames cross the limit of 0.75%, with values closer to 0.8% and 0.9% respectively as expected, owing to the deformability guided design for which the admissible value used was 1.0%.

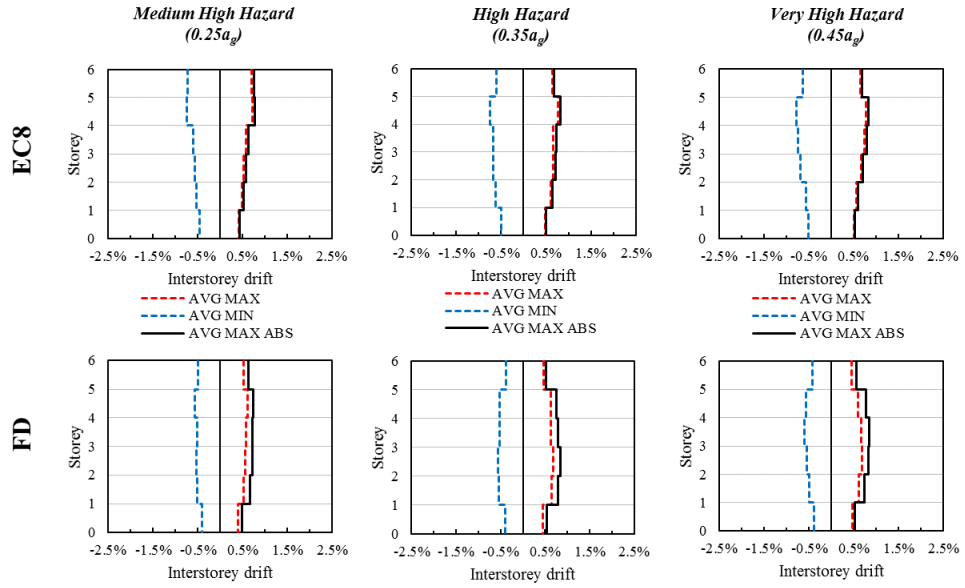

Figure 197 Transient interstorey drift for MRF 6-3-6 at DL (SF = 0.59)

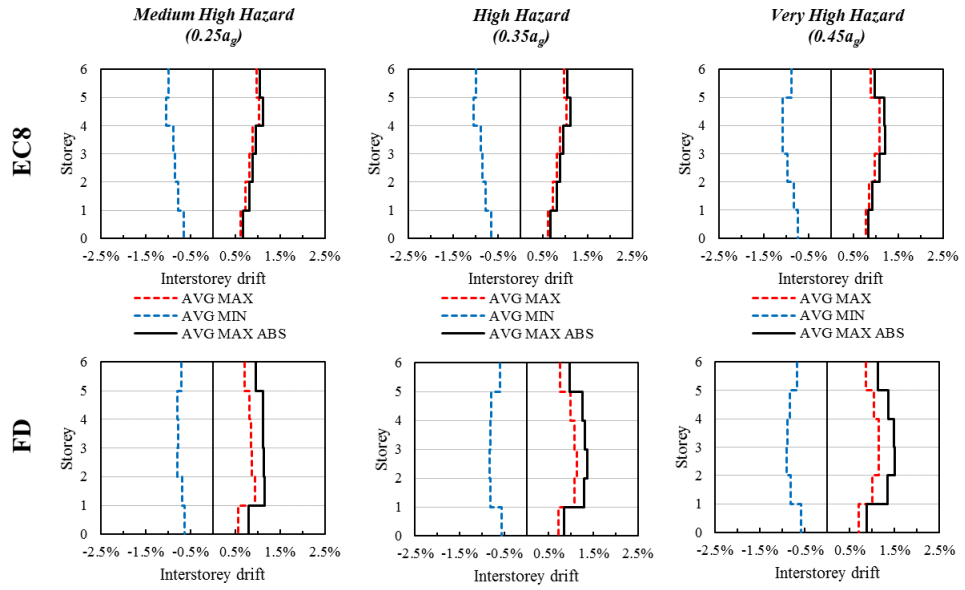

Figure 198 Peak transient interstorey drift for MRF 6-3-6 at SD (SF = 1.00)

At the significant damage limit state (SF - 1) the maximum PTID were within the limit (for example maximum 1.2 and 1.4, 8 respectively for the two design methodologies, considering the MRF 6-3-6 HH). An interesting observation drawn from the shape of the PTID in Figure 197 and Figure 198

is that the EC8 set of frames exhibit more of a cantilever deformation type, while the FD frames develop a drift distribution typical of a shear type mechanism.

The shape is lost for the CP limit state due to the plastic incursions. Figure 199 shows that the proportions between the PTID of the EC8 compliant frames and the FD frames continue in the same direction. Maximum values of 1.8% and 2.2% (well within the limit) are attained respectively for the MRF 6-3-6 HH, the values being proportional also for the frames designed in the other seismic hazard levels

The residual drifts (PRID) diagrams in Figure 200 show first of all, very low values for all frames (both design sets have the maximum residual drift below 0.5% for SD and below 1% for CP). Secondly, it can be observed that the FD set of frames has larger levels of residual drifts, almost double the one of EC8 compliant frames. This difference is caused by the severely overdesigned solutions, especially for the EC8 compliant frames.

As a matter of fact, for the frames designed for very high hazard (PGA 0.45*g* – VHH), as the ULS strength and stability requirements became more important, both solutions provide closer values for CP limit state. The same cantilever (for EC8) and shear type (for FD) deformed shape can be recognized.

The consideration which can be drawn from these analyses is that the FD frames exhibit an adequate seismic response at the code limit levels, not very far from the one of the EC8 compliant frames, but slightly more flexible. However, the severe deformability design code requirements limited the solutions for the frames which were very similar in terms of members, with the difference in terms of the dissipation mechanism and the force level at which the nonlinear events occur (being them plastic deformation or sliding).

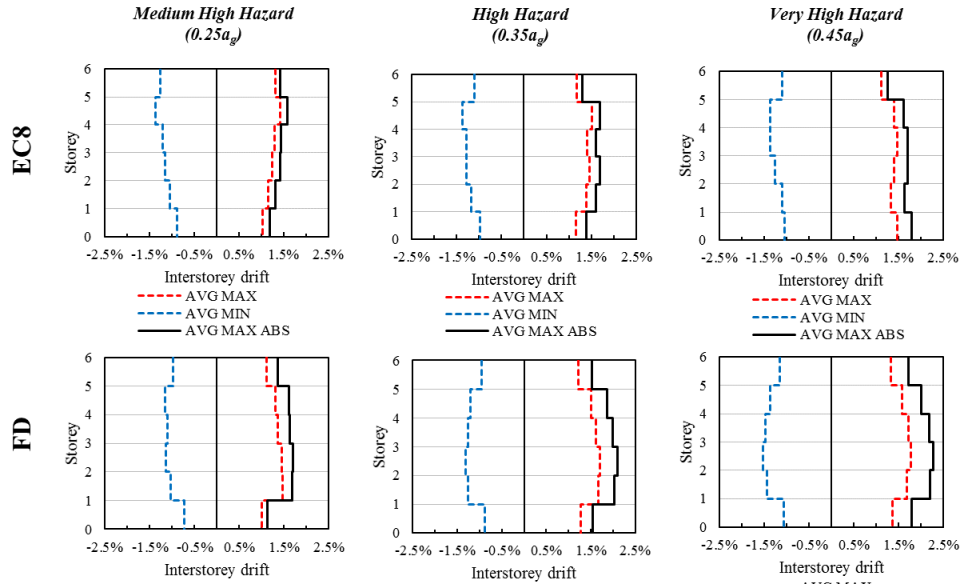

Figure 199 Transient interstorey drift for MRF 6-3-6 at CP (SF = 1.73)

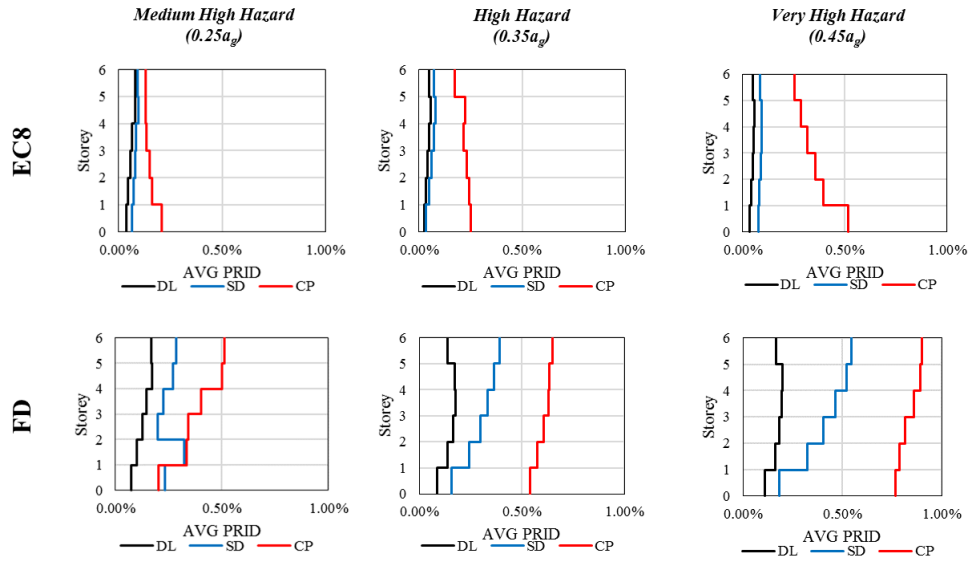

Figure 200 Peak transient interstorey drift for MRF 6-3-6

4.8 SUMMARY

The part of the thesis presenting the friction connections investigated in the framework of the FREEDAM project was structured in accordance with the three levels at which both experimental and numerical investigations were performed i.e. (i) sub-component level, (ii) beam-to-column assembly level and (iii) structural level. Each level led to a set of conclusive remarks which influenced the subsequent stages of the investigation and in the end a set of friction devices which can be used for MRFs with IPE beam profiles was defined. In this way the goal of fully characterizing the solution was achieved and the concept is readily available, being a fully qualified solution, which is easy to implement into practical applications.

The preliminary FE analyses carried out on very detailed models of friction dampers tested in the past by Latour *et al.* (2014) were useful in determining the influence of parameters such as the preload sequence, slip-rate influence, pressure and contact area influence. It was highlighted that the explicit modelling of the coating (friction material) is not mandatory if the interaction at the sliding interface level is properly implemented. The second set of numerical models, calibrated based on experimental tests carried out at University of Salerno within the framework of the project, confirmed the lack of effectiveness of disc spring washers in preventing preload loss.

The experimental campaign on the beam-to-column assemblies proved the stable and predictable response of friction connections under cyclic loading. Both investigated configurations (with horizontal and vertical sliding interfaces) had a rigid elastic response and reached the design level bending resistance. The connections did not exhibit significant degradation of strength and negligble plastic deformations were observed in the beam and the column. The FE models were able to accurately replicate the experimental results and provide further insight into the friction connection behavior. The numerical

investigations focused on the influence of friction coefficient and clamping force variability and the shear force transfer mechanism. The first parametric study highlighted the correlation between the two parameters and the bending resistance, but also strengthened the observation coming from the lap-shear tests that the clamping force must be kept in an optimal range (30 to 60% of $F_{p,Cd}$ – the clamping force according to EN1993 1-8) in order to avoid unwanted softening or hardening behavior.

The larger asymmetry of the horizontal friction damper (about 25%) as well as the undesired hardening/softening behavior (observed in the parametric study results) and the degradation in strength for the large assembly (observed during the experimental tests) rendered the second solution preferable for subsequent development. The friction connection with vertical damper has a lower asymmetry (about 15%) and exhibits less pronounced hardening/softening behavior hence, this was the configuration considered for the analysis of frames and the development of the final friction devices.

Preliminary analyses on advanced and simplified numerical models of full-scale structures equipped with traditional partial strength connections (reduced beam section - RBS) and the investigated friction devices, show that the two have similar nonlinear behavior with the difference that the latter is a low-damage easily repairable solution.

Starting from the current design procedure of MRFs in the European framework, two strategies were proposed for the design of frames equipped with friction devices. The investigated frames showed that in order to efficiently implement the solution, the device needs to have a capacity based on the design seismic forces (FD-B methodology) and not based on the beam capacity (FD-A methodology). This aspect is particularly important as MRFs need to meet very restrictive deformability limitations hence, disconnecting

the strength and stiffness of the frame (FD-B) is the only way to allow the activation of sliding under design level earthquake.

Among the aims of the FREEDAM research project there was the definition of design catalogue for easy-to-use selection of the friction connections. The catalogue was set with reference to 5 devices, which were designed in such a manner that most of the IPE profile depths were covered. Indeed, by setting the beam section type and the utilization factor m from the structural analysis ($m = M_{Ed}/M_{Rd}$) it is possible to select the required friction device and no additional column-face connection checks are required as the device is prequalified.

This activity was carried out in collaboration with the industrial partners of the project (FIP Industriale) with the aim at offering the device on the constructional steel market as a readily available low-damage and easily repairable solution. Figure 201 shows a draft of the brochure presented by the company at the final workshop of the project.

Figure 201 Catalogue developed by FIP Industriale

5 CONCLUSIONS

5.1 GENERAL REMARKS

The thesis presents the investigation on bolted connections for resilient steel structural systems characterized by ease of repairability in the earthquake aftermath. The international experiences of recent earthquakes highlight the need to implement structural solutions which mitigate the post-earthquake repair costs. Among the large number of potential solutions (e.g. viscous dampers, hysteretic dampers, base isolation, BRBs, replaceable links, shear panels, friction connections, etc.) the most suitable solutions are the friction connections for moment resisting frames (MRFs) and concentrically braced frames (CBFs) and the replaceable links for eccentrically braced frames (EBFs) as they minimally change the design and construction processes while bringing life-cycle cost mitigation.

In this study the focus was on EBFs and MRFs. In the framework of these two structures, the most effective innovative solution were investigated: replaceable links for EBFs and friction connections for MRFs.

Although conceptually similar, the two solutions address the problem differently:

1. The solutions concern different lateral resisting system i.e. detachable links for eccentrically braced frames and the friction connections for moment resisting frames. In the first case the solution

is easily repairable because the dissipative ductile element (the link) can be replaced owing to the end-plate connections, while in the case of the moment resisting frames, the plastic energy dissipation mechanism provided by the plastic hinges at the beam ends is replaced by the friction dissipation provided by the connection

2. The connections for the detachable links represent traditional end-plate solutions while the connections for the MRFs are novel friction connections which have a different dissipation mechanism.

3. In the case of detachable links, the connections must be designed to remain elastic, in order to facilitate the link replacement, while the friction connection is a special type of partial strength connection, therefore it is expected that the damage (even if minimal) would be localized in its components.

Considering the conceptual differences and the level at which the state of the art is for the two solutions, it is evident that in investigating the two structural typologies, different issues need to be addressed. Therefore, the main conclusions drawn from the hereby presented work will be presented separately for the two parts and in the end common remarks for the easy-repairable innovative structural systems will be highlighted.

5.2 BOLTED CONNECTIONS FOR DETACHABLE LINKS

The most important issues regarding the detachable links are as follows:

(i) the actual level of shear overstrength at 0.08*rad* link rotation;

(ii) the development of axial force in the link;

(iii) the design of end-plate connections;

Using experimentally validated numerical models two parametric studies were performed: one considering the link profiles only (Figure 202*a* and *b*) and a second one considering link-connection assemblies (Figure 202*c* and *d*).

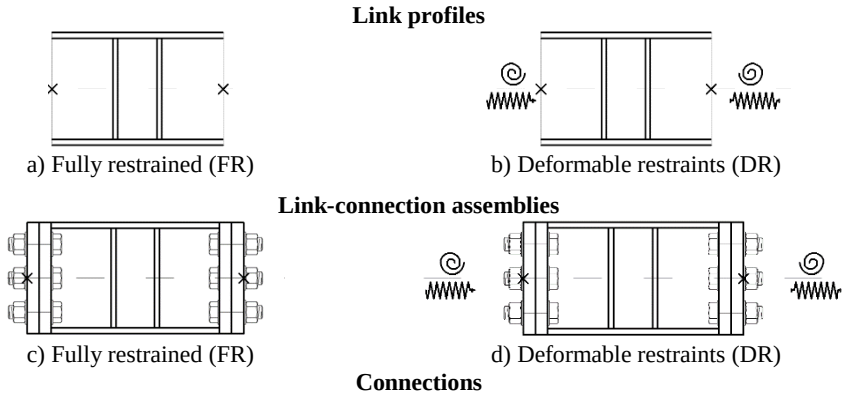

Figure 202 Analyzed models geometrical features

5.2.1 Numerical investigation on the links

The first parametric study investigated both the shear overstrength and the axial force in links assuming fully restrained boundary conditions (practically the case of links in traditional EBFs) and deformable restraints (the frame and connection deformability were modelled). The main conclusions drawn are:

- The shear overstrength in the case of fully restrained boundary conditions is dependent on the link profile type (narrow or wide flange), on the link depth (d) and length (e). Namely, the universal value proposed in the EC8 is leading to either unconservative or overconservative approximations of the design force.
- Using a multi-linear regression, it is possible to derive an equation function of d/e and A_{fl}/A_w, that can be used in determining a more accurate value of the shear overstrength.
- The analyses considering deformable restraints lead to a reduction of the shear overstrength and a loss of correlation with the link

geometrical features. This gives a hint into the dependency between the shear overstrength and the connection mechanical characteristics (stiffness, strength).

- When the link models were investigated with fully-restrained BCs and axial release at one end (no acial force can develop) the shear iverstrength was significantly reduced, the result hinting at the effect the axial force has in inducing second-order shear in the link.
- The analyses performed considering only the link revealed in fact that significant tensile forces develop when fully restrained boundary conditions are assumed. As mentioned before, this is the case for links in traditional EBFs and the axial force may affect the design, its presence leading to an increase in the shear overstrength due to the induced second order shear.
- No correlation between the level of axial strength and any geometrical properties of the links can be observed and the tensile force at $0.08rad$ is constant for same length links ($1.0e_s$, $0.75e_{s,}$ and $0.50e_s$).

5.2.2 Numerical investigation on the detachable links (link-connection assemblies)

The second parametric study was aimed at assessing the link-connection assemblies considering the flush and extended end-plate connections designed according to the code compliant methodology and verified considering two alternative methods. The results led to the following conclusions:

- Coherent with the analyses on the links and the simplified connection modelled as nonlinear spring, the correlation between the shear overstrength and the link geometrical characteristics is lost for the link-connection assemblies. It was demonstrated that this is directly dependent

on the connection utilization ratio m_j (the ratio between the connection design bending moment, $M_{j,Ed}$, and the connection bending resistance $M_{j,Rd}$). Indeed, as the connection gets weaker, the shear overstrength gets smaller. The stiffness of the connection plays a significant role as well, as it was shown that the stiffer extended end-plate connections develop larger shear overstrength compared to flush end-plate connections, for the same m_j.

- The significant values of tensile force observed in the case of fully restrained links was either severely reduced or changed sign, becoming compression, as a result of the significant compressive arch developing in the links. It became clear that the stronger connections were prone to develop tensile forces, while the connections with an m_j closer to the limit of 1.0 were likely to remain in compression. This is explained by the fact that the closer to the fully restrained boundary conditions, the closer the tensile force is to the value obtained from the analyses on the link only. Similar to the shear overstrength, the axial force in the links of the link-connection assemblies is function of the connection strength and stiffness and an exponential function can be used to fit the obtained data.

*

The conclusions resulting from the parametric studies are useful to propose recommendations for the design of the link connections and EBFs equipped with detachable short links. A step-by-step methodology was proposed at the end of Chapter 3. By following the recommendations, it is possible to accurately account for the shear overstrength and axial force both in the connection design and at a global level.

5.3 BOLTED FRICTION CONNECTIONS

Moment resisting friction connections are a relatively recent concept. In Europe there are no existing applications on actual constructions. However, the concept has been studied, tested and successfully implemented in New Zealand (Clifton *et al.*, 2011 and 2012).

"Free from damage connections" (FREEDAM) Research project was born as a research partnership between 4 universities (University of Salerno, University of Naples in Italy, University of Liege in Belgium and University of Coimbra in Portugal) and 2 private companies (OFELIZ and FIP Industriale) aiming at investigating friction connections and make the solution of MRFs equipped with such devices ready for practical applications in Europe.

Within the framework of this project, the solution was investigated at all levels (sub-component, beam-to column assembly, frames with friction connections) and considering most of the issues affecting the friction connection i.e. friction material, bolt, clamping, durability, impact loading, high slip rate, post-slippage behavior, etc.

The thesis presents some experimental results obtained from the tests performed at the laboratory of the Department of Civil Engineering of University of Salerno in partnership with the researchers of University of Naples 'Federico II' and the numerical investigations performed at the latter institution. The following paragraphs summarize the main conclusions of each research stage.

5.3.1 Investigation on the friction damper sub-component

The lap-shear tests performed at University of Salerno have been conducted in order to give insight on the friction behavior of various materials considered as potential solutions for the friction damper. The results of the experimental campaign have been further used to calibrate FE models.

- Preliminary numerical investigation on friction subassemblies tested in the past by Latour *et al.* (2014) show that the roughness of the clamped surfaces does not have to be micro-modelled. Indeed, it is sufficient to properly set the gross average frictional properties (pressure dependency, slip-rate dependency)
- The experimental campaign showed that both hard and soft friction materials can be used in combination with stainless steel obtaining satisfactory performance under cyclic loads.
- FEA results confirm the significant variability of the bolt forces during sliding which needs to be accounted for in design. The analyses also confirm that the presence and the number of disc springs does not significantly influence the response in terms of bolt preload loss.
- At high slip velocities, large temperatures are developed within the specimen. When modelling temperature-dependent friction coefficients calibrated on experimental results, good agreement can be obtained by the FE models. Modelling this effect is crucial as it causes reduction in the slip force capacity. This is due to the transverse dilatation that initially increase the pressure, while bolt tightening reduces due to elongation of the shank. However, in the case of beam-to-column experimental tests, the temperatures stayed low, therefore they were neglected in the subsequent analyses.

5.3.2 Investigation on friction connections

The seismic response of steel beam-to-column assemblies equipped with two types of friction dampers has been investigated by means of both experimental tests and finite element simulations. Based on the obtained outcomes, the following remarks can be drawn:

- Both types of friction joints provided satisfactory overall performance with stable and predictable hysteretic response, as well as preventing from damage the non-yielding members. However, asymmetric response under sagging and hogging was observed.
- The joint configuration dictates the level of the response symmetry under sagging and hogging bending. The configuration with vertical friction surface exhibited slightly better response, showing lower degradation under cumulated rotation demand with smaller difference between hogging and sagging bending. Indeed, the different resistance under sagging and hogging conditions ranges about 25% for the configuration with horizontal friction surface and 15% for that with vertical friction surface.
- The FE models accurately predict the response of experimental tests. The models allowed characterizing the local response of the joints, which exhibit some plastic deformations in the bolts and in the connecting L-stubs and T-Stubs. The FE analyses also showed that the joints equipped with the vertical friction damper exhibit plastic deformations lower than the corresponding device with horizontal friction surface.
- The variation of the bending capacity of both joint configurations is directly proportional with the bolt pretension force. Therefore, the bolt tightening process needs to be very well controlled because either larger or smaller tightening forces can impair the proper dissipative mechanisms. Indeed, the upper bound values lead to the

development of larger forces in the damper, situation that hinders the hierarchy in the joint, while lower clamping forces can lead to sliding in the damper under serviceability conditions.

- The randomness of the friction properties must be accounted for in the design phase, because this variability can inflict in the joint response and, consequently, the global behavior of the structure.
- The shear capacity of the column face connection needs to be properly designed. The FEA show that the L-stub of thevertical friction connection transfers shear force almost double the design shear force.

5.3.3 Investigation of full-scale mock-up

The investigation was focused on numerical analysis of the full-scale frame models equipped with traditional (RBS) and innovative (friction devices) connections which were tested within the framework of the project. The investigations include the static and dynamic analyses using the advanced (Abaqus) and commercial software (SAP2000). Based on the obtained results, the following considerations can be drawn:

- When comparing the RBS and FD frames, similar response was observed, with small difference in terms of initial stiffness (larger for the FD frame owing to the more rigid connections).
- The simplified model in SAP2000 offers results sufficiently close to the more realistic ones obtained from the ABAQUS model hence, it can be used to perform more demanding nonlinear dynamic analyses, while the advanced model is useful for the understanding of the local effects.
- The preliminary FEAs allowed to estimate the values of the horizontal seismic forces and displacement demand in order to verify the capacity of the actuators.

5.3.4 Investigation of MRFs equipped with friction connections

A parametric study based on both nonlinear static and dynamic analyses was carried out with the aim of investigating the seismic performance of moment-resisting frames (MRFs) equipped with friction beam-to-column connections. These frames have been designed according to two modified Eurocode compliant approaches (FD-A and FD-B) and the results were compared with a set of traditional EC8 compliant MRFs. Based on the obtained results the following remarks can be made:

- The FD-A set of frames has significantly larger column sections (for the same beam profiles as the FD-B) resulting from the local ductility check at the node level. Indeed, the FD-A approach leads to structures heavier even than the EC8 set. Conversely, although the beam and column sections are mostly set based on the serviceability and global stability limitations, the designed structures are lighter owing to the lower demands at the node level. These results confirm the need for improvements on the way to account for the P-Δ effects in the design based on the EC8.
- The FD-B led to frames that possess the lowest overstrength for all seismic hazard levels, due to the way the connection was designed for the forces coming from the seismic combination. On the other hand, the FD-A approach had frames with much larger overstrength closer to the traditional EC8-MRFs. Therefore, frames equipped with friction dampers exhibit enough overstrength and redundancy when appropriately designed, while being cost effective due to the reduction in member size.
- Based on the nonlinear dynamic analyses, it is clear that the FD frames exhibit an adequate seismic response at the code limit levels, similar to the EC8 compliant frames, but slightly more flexible. However,

the severe deformability design code requirements limited the solutions for the frames which were very similar in terms of members, with the difference in terms of the dissipation mechanism and the force level at which the nonlinear events occur (being them plastic deformation or sliding).

- The residual interstorey drifts are very small (bellow the limit states allowable limits) for both FD frames and traditional ones, with particularly low values for the latter. The results are easily explained, as the traditional frames are severely overdesigned and therefore remain elastic even under destructive seismic events. On the other hand, MRFs equipped with friction devices are slightly more flexible and in addition, the sliding mechanism gets activated when the design seismic intensity is reached.

*

The friction connections represent a solution with great potential for the replacement of the plastic hinge dissipation mechanism characteristic of moment resisting frames. This thesis, within the framework of the FREEDAM European research project, presented conclusive results confirming the effectiveness of such connections.

5.4 FUTURE RESEARCH

The Author believes that the current work is a contribution to the advancement of knowledge with regards to the two solutions presented. The research ventures (DUAREM, INNOSEIS and FREEDAM) and the partners involved making their most to solve doubts, develop design rules and promote the application in practice.

Nevertheless, several aspects require further investigation, especially the less traditional friction devices. The main future research points are:

- Codification of actual shear overstrength and accounting for axial force effect on link connection
- Assessment of the 5 friction devices proposed for use with IPE beam profiles
- Influence of the column face connection on the asymmetry under hogging and sagging loading conditions
- Shear design of column face connection
- More rational code methodology to account for the second order effects
- Performing full scale tests on structures equipped with friction connections (the full scale tests on the FREEDAM mock-uo)
- Development of low-damage column base solutions

6 REFERENCES

Abdi, H., Hejazi F., Saifulnaz R., Karim I. A., and Jaafar M. S., (2015) ‘‘Response Modification Factor for Steel Structure Equipped with Viscous Damper Device” International Journal of Steel Structures 15(3): 605-622

Abidelah, A., Bouchaïr, A. and Kerdal, D.E. (2012) “Experimental and analytical behavior of bolted end-plate connections with or without stiffeners”, J. Constr. Steel Res., 76, 13-27.

Aceti, R., Ballio G., Capsoni A., Corradi L. (2004) “A limit analysis study to interpret the ultimate behavior of bolted joints” *Journal of Constructional Steel Research* 60 pp. 1333–1351

Aiken I.D, Clark P.W., Kelly J.M., (1993) “Design and Ultimate-Level Earthquake Tests of a 1/2.5 Scale Base-Isolated Reinforced-Concrete Building” Proceedings of ATC-17-1 Seminar on seismic Isolation, Passive Energy Dissipation and Active Control. San Francisco. California.

Akkar S, Sandıkkaya MA, Senyurt M, Azari Sisi A, Ay BÖ, Traversa P, et al. Reference database for seismic ground-motion in Europe (RESORCE). Bull Earthq Eng 2014;12(1):311–39. http://dx.doi.org/10.1007/s10518-013-9506-8.

ANSI/AISC 341-16 (2016), Seismic Provisions for Structural Steel Buildings; American Institute of Steel Construction, Chicago, IL, USA.

ANSI/AISC 358-16 (2016), Prequalified Connections for Special and Intermediate Steel Moment Frames for Seismic Applications; Chicago, IL, USA.

Aribert, J-M., Braham, M., Lachal A., (2004) “Testing of ‘‘simple’’ joints and their characterisation for structural analysis” *Journal of Constructional Steel Research* 60, pp. 659–681

Atael, A., Bradford, M.A., Valipour H.R., (2014) “Moment-Rotation Model for Blind-Bolted Flush End-Plate Connections in Composite Frame Structures” *J. Struct. Eng*. 04014211-1

Azad, K.S.. & Topkaya, C., (2017). “A review of research on steel eccentrically braced frames” *Journal of Constructional Steel Research*, 128, 53-71

Bakır Bozkurt, M., and Topkaya, C. (2017) "Replaceable links with direct brace attachments for eccentrically braced frames" Earthquake Engineering and Structural Dynamics. DOI: 10.1002/eqe.2896

Barecchia, E., D'Aniello M., Della Corte G., and Mazzolani F.M., (2006) "Eccentric bracing in seismic retrofitting: from full scale tests to numerical FEM analysis". In: Proceedings of International Conference On Metal Structures 2006 "Steel - A New And Traditional Material For Building" Poiana Brasov September 20-22, 2006.

Beattie, G.J., Megget L.M. and Andrews A.L., (2008) "The historic development of earthquake engineering in New Zealand", *The 14th World Conference on Earthquake Engineering*, October 12-17, 2008, Beijing, China

Blume JA, Newmark NM, Corning LH.Design of Multistory Reinforced Concrete Buildings for Earthquake Motions. Skokie, ILL: Portland Cement Association; 1961 318p

Borzouie, J., Macrae, G., Chase J., et al.. (2015*a*) "Cyclic performance of asymmetric friction connections with grade 10.9 bolts" Bridg. Struct. Eng. 45 (1).

Borzouie J., MacRae G.A, Chase J.G., Rodgers G.W., Clifton G.C., (2015*b*) "Experimental studies on cyclic performance of column base weak axis aligned asymmetric friction connection" *Journal of Constructional Steel Research* 112, pp. 252-262.

Bosco, M., and Marino E.M., (2013) "Design method and behavior factor for steel frames with buckling restrained braces", Earthquake Engineering & Structural Dynamics, vol. 42, pp. 1243-63.

Bosco, M., Marino E:M:, Rossi P.P., (2014) "Proposal of modifications to the design provisions of Eurocode 8 for buildings with split K eccentric braces" *Engineering Structures* 61, pp. 209-223,.

Bosco, M., Marino E:M:, Rossi P.P., (2015) "Critical review of the EC8 design provisions for buildings with eccentric braces" Earthquake and Structures, 8(6), 1407-1433

Bowden F, Tabor D. The friction and lubrication of solids: Part I. Oxford: Oxford University Press; 1950.

Bowers R, Clinton W, Zisman W. Frictional behavior of polyethilene, polytetrafluorethylene and halogenated derivatives. Lubr Eng 1953;9:204–9.

Braham, M., Jaspart J.P. (2004) "Is it safe to design a building structure with simple joints, when they are known to exhibit a semi-rigid behaviour?". JCSR 60 713–723

Broderick, B.M., Thomson A.W., (2002) "The response of flush end-plate joints under earthquake loading" *Journal of Constructional Steel Research* 58, pp. 1161–1175

Bruneau, M. and McRae, G. (2017) "Reconstructing Christchurch: A Seismic Shift in Building Structural Systems" The Quake Centre, University of Canterbury; 2017.

BSLJ Japanese seismic design code

Bursi O.S., Jaspart J.P. (1997*a*) "Benchmarks for finite element modelling of bolted steel connections". JCSR 43 17–42

Bursi O.S., Jaspart J.P. (1997*b*) "Calibration of a finite element model for isolated bolted end-plate steel connections". JCSR 44 225–262

Butterworth J.W., Clifton G.C. (2000) "Performance of hierarchical friction dissipating joints in moment resisting steel frames" 12th World Conference on Earthquake Engineering, Paper N. 718,

Calado L., De Matteis G., Landolfo R.. (2000) "Experimental response of top and seat angle semi-rigid steel frame connections". Material and Structures, Vol.33, , pp.499-510.

Cancellara D., De Angelis F., (2017) "Assessment and dynamic nonlinear analysis of different base isolation systems for a multi-storey RC building irregular in plan" *Computers and Structures* 180, pp. 74–88

Cassiano D., D'Aniello M., Rebelo C., (2017) "Parametric finite element analyses on flush end-plate joints under column removal" Journal of Constructional Steel Research, Volume 137, October 2017, Pages 77–92

Cassiano D., D'Aniello M., Rebelo C., (2018). "Seismic behaviour of gravity load designed flush end-plate joints" Steel and Composite Structures, Vol. 26, No. 5, March10 2018, pages 621-634

Chenaghlou M. R., Nooshin H., (2015*a*) "Axial force–bending moment interaction in a jointing system part I: (Experimental study)" *Journal of Constructional Steel Research* 113, pp. 261–276

Chenaghlou M. R., Nooshin H., (2015*b*) "Axial force–bending moment interaction in a jointing system Part II: Analytical study" *Journal of Constructional Steel Research* 113, pp. 277–285

Christopoulos C. Filiatrault A., (2000) Principles of Passive Supplemental Damping and Seismic Isolation. IUSS PRESS. Pavia. Italy

Ciutina, A., Dubina, D. and Danku, G. (2013) "Influence of steel-concrete interaction in dissipative zones of frames: I – Experimental study" *Steel and Composite Structures.* 15(3), 281-000.

Clifton, G.C., Butterworth, J.W. and Weber, J., "Moment-resisting steel framed seismic-resisting systems with semi-rigid connections", SESOC Journal, Vol. 11, No. 2, September 1998.

Clifton C., MacRae G.A, Mackinven H., Pampanin S., (2007) "Sliding Hinge Joints Subassemblies for Steel Moment Frames" NZSEE Conference, 2007

Clifton, C., Bruneau, M., MacRae, G. L. R. & Fussell, A., (2011) "Steel structures damage from the Christchurch earthquake series of 2010 and 2011" Bulletin of the New Zealand Society for Earthquake Engineering, 44(4), pp. 297-318.

Clifton G.C., Nashid H., Ferguson G, Hodgson M., Seal C., Bruneau M., MacRae G.A. and Gardiner S. (2012) "Performance of Eccentrically Braced Framed Buildings In The Christchurch Earthquake Series of 2010/2011" *Proceedings. of 15th WCEE,* Lisbon, Portugal, September 24-28.

Climent, A.B. (2006) "Influence of hysteretic dampers on the seismic response of reinforced concrete wide beam–column connections", Engineering Structures, vol. 28, pp. 580-92

Constantinou, M.C., Soong, T.T., Dargush, G.F., (1998) "Passive Energy Dissipation Systems for Structural Design and Retrofit" Multidisciplinary Center for Earthquake Engineering Research, University at Buffalo, State of New York.

D'Aniello, M., Della Corte, G., and Mazzolani, F.M., (2006) "Seismic Upgrading of RC Buildings by Eccentric Braces: Experimental Results vs. Numerical Modeling", In: Proceedings of STESSA Conference 2006, Japan, 14-17 August 2006.

D'Aniello, M., Tartaglia, R., Costanzo, S., Campanella, G., Landolfo R., De Martino A. (2018). Experimental Tests on Extended Stiffened End-Plate Joints within Equal Joints Project. Key Engineering Materials. ISSN: 1662-9795, Vol. 763, pp 406-413.

D'Aniello, M., Della Corte, G., and Mazzolani, F.M. (2008) "Experimental tests of a real building seismically retrofitted by special buckling restrained braces", In: Proceedings of 2008 Seismic Engineering Conference Commemorating the 1908 Messina and Reggio Calabria Earthquake. Book Series: AIP Conference Proceedings, vol. 1020, pp. 1513-20, 2008.

D'Aniello M., Cassiano D., Landolfo R. "Monotonic and cyclic inelastic tensile response of European preloadable GR10.9 bolt assemblies". *Journal of Constructional Steel Research*, **124:** 77–90, 2016.

D'Aniello, M., Cassiano D., Landolfo R., (2017a)"Simplified criteria for finite element modelling of European preloadable bolts", Steel and Composite Structures, vol. 24(6), pp. 643-658, 2017.

D'Aniello, M., Tartaglia R., Costanzo S., Landolfo R.(2017b) "Seismic design of extended stiffened end-plate joints in the framework of Eurocodes". Journal of Constructional Steel Research, 128, 512–527

D'Aniello, M., Zimbru M., Landolfo R. Latour M., Rizzano G., Piluso V., (2017c) "Finite element analyses on free from damage seismic resisting beam-to-column joints" Eccomas Proceedia COMPDYN (2017) 802-814

Da Silva L.S., de Lima L. R. O., da S. Vellasco P. C. G., de Andrade S.A.L. (2004) "Behaviour of flush end-plate beam-to-column joints under bending and axial force" *Steel and Composite Structures*, Vol. 4, No. 2, pp. 77-94,

Da Silva, L. & Coelho, A., (2001) "An analytical evaluation of the response of steel joints under bending and axial force" *Computers and Structures*, 79(8), pp. 873-881.

Da Silva, L., de Lima, L. & da S. Vellasco, P., (2004) "Behavior of flush end-plate beam-to-column joints under bending and axial force" *Steel and Composite Structures*, 4(2), pp. 77-97.

Danku, G., Dubina, D., and Ciutina, A. (2013). "Influence of steel-concrete interaction in dissipative zones of frames: II - Numerical study". *Steel and Composite Structures.* 15(3), 305-000.

De Matteis G., Mazzolani F.M., Landolfo R., Milev J. (1999) "Q-factor evaluation of moment resisting steel frames with semi-rigid connections by applying different approaches" Acta Polytechnica, Journal of Czech Technical University, Vol.39, No. 5, pp.183-194.

De Matteis G., Formisano A., Mazzolani F.M., and Panico S, (2005) "Design of low-yield metal shear panels for energy dissipation". In: Proceedings of the Final Conference of COST Action C12, Innsbruck (Austria), pp. 665-675, 20-22 January 2005,

De Matteis G., Landolfo R., Calado L. (2000) "Cyclic Behaviour of Semi-Rigid Angle Connections: a Comparative Study of Tests and Modelling". Proc. of Third International

Conference "Behaviour of Steel Structures in Seismic Areas", Montreal (Canada), August, 2000, Balkema pp.165-174.

Del Savio, L. et al., (2009). "Generalized component-based model for beam-to-column connections including axial versus moment interaction" *Journal of Constructional Steel Research,* 65(8), pp. 1876-1895.

Della Corte G., De Matteis G., Landolfo R. (2000) "The influence of connection modelling on the seismic response of MR steel frames" (in "Moment Resistant Connections of Steel Frames in Seismic Areas: Design and Reliability", Mazzolani ed., E & FN SPON, pp. 485-512).

Della Corte, G., De Matteis, G., Landolfo, R., Mazzolani, F.M. (2002) "Seismic analysis of MR steel frames based on refined hysteretic models of connections". JCSR 58 1331–1345.

Della Corte, G., D'Aniello, M. and Mazzolani, F.M. (2007) "Inelastic response of shear links with axial restraints: Numerical vs. analytical results". In: Proceedings of 5th International Conference on Advances in Steel Structures, ICASS2007.

Della Corte, G., D'Aniello, M. and Landolfo, R. (2013) "Analytical and numerical study of plastic overstrength of shear links", Journal of Constructional Steel Research, vol. 82, pp. 19-32.

Della Corte, G. D'Aniello, M. and Landolfo, R. (2014) "Field testing of all-steel buckling restrained braces applied to a damaged reinforced concrete building", Journal of Structural Engineering, ASCE DOI: 10.1061/(ASCE)ST.1943-541X.0001080, 2014.

Díaz C., Martí P., Victoria M., Querin, O. M. (2011) "Review on the modelling of joint behaviour in steel frames" *Journal of Constructional Steel Research* 67 741–758

Dong B., Ricles J.M., Sause R., (2016) "Seismic Response of steel MRF Building with Nonlinear viscous dampers" Front. Struct. Civ. Eng. 10(3), pp. 254–271

Dong B., Sause R., Ricles J. M., (2010) "Seismic Response of a steel MRF Building with Nonlinear viscous dampers under DBE and MCE" J Struct Eng, 142(0) 1-1

DUAREM Project Final Report "Full-scale experimental validation of dual eccentrically braced frame with removable links", SERIES Project No. 227887, Revision 6 March 2014

Dubina D., Ciutina A., Stratan A. (2001) "Cyclic tests of double-sided beam-to-column joints" Journal of Structural Engineering (ASCE) 127(2):129–36.

Dubina, D., Stratan, A., Dinu, F. (2007). "High Strength Steel EB frames with low strength bolted links" *Proceedings of the 5th International Conference on Advances in Steel Structures,* ICASS 2007, 249-254, Singapore, December 5-7.

Dubina, R., Stratan, A. & Dinu, F., (2008) "Dual high-strength steel eccentrically braced frames with removable links" *Earthquake Engineering and Structural Dynamics,* Volume 37, pp. 1703-1720.

Dubina, D., Stratan, A., Dinu F., (2011) "Re-centring capacity of dual-steel frames", Steel Constr. 4 (2) (2011) 73–84.

Dusicka, P., Itani, A. & Buckle, I., (2010) ”Cyclic behavior of shear links of various grades of plate steel”. *Journal of Structural Engineering,* 136(4).

Elnashai, A. S. and Elghazouli, A. Y. (1994) “Seismic Behaviour of Semi-Rigid Steel Frames: Experimental and Analytical Investigations”, JCSR, 29 149-174.

Elnashai, A., S., Elghazouli, A. Y. and Danish-Ashtiani, F. A. (1998). “Response of Semi-Rigid Steel Frames to Cyclic and Earthquake Loads”, JSTRENG, ASCE, 124(8), 857-867.

EN 1090-2, Execution of steel structure and aluminium structure: Technical requirements for steel structures. Annex G: Test to determine slip factor, CEN 2008.

EN 10088-1, 2005. Part 1: List of stainless steels

EN 1993 1-8 (2005), Eurocode 3: Design of Steel Structures. Part 1-8: Design of Joints; European Committee for Standardization, Brussels, Belgium.

EN 1993-1-1 (2005), Eurocode 3: Design of steel structures. Part 1-1: General rules and rules for buildings; European Committee for Standardization, Brussels, Belgium.

EN 1998-1 (2005), Design of Structures for Earthquake Resistance. Part 1: General Rules, Seismic Actions and Rules for Buildings; European Committee for Standardization, Brussels, Belgium.

Faella C., Piluso V., Rizzano G. (2000) “Structural steel semirigid connections: theory design and software”, CRC Press LLC,.

Faella, C., Piluso, V. & Rizzano, G., (1998) “Cyclic Behaviour of Bolted Joint Components” Journal of Constructional Steel Research, 46.

Fardis M.N. (2018) Capacity design: Early history, Earthquake Engng Struct Dyn. 2018;47:2887–2896

FEMA 350, “Recommended Seismic Design Provisions for New Moment Frame Buildings Report,” Federal Emergency Management Agency, Washington DC, 2000

Ferrante Cavallaro G., Francavilla A.B., Latour M., Piluso V., Rizzano G. (2017) “Experimental behaviour of innovative thermal spray coating materials for FREEDAM joints” Composites Part B: Engineering, 115: 289-299.

Ferrante Cavallaro G, Francavilla A, Latour M, Piluso V, Rizzano G. (2018a) Cyclic responseof friction materials for low yielding connections. Submitt Soil Dyn Earthq Eng2018.

Ferrante Cavallaro G, Latour M, Francavilla AB, Piluso V, Rizzano G. (2018b) Standardised friction damper bolt assemblies time-related relaxation and installed tension variability. J Constr Steel Res 2018;141:145–55.

Formisano, A., De Matteis G. and Mazzolani F.M., (2010) “Numerical and experimental behaviour of a full-scale RC structure upgraded with steel and aluminum shear panels”, Computers and Structures, vol. 88, Issue 23-24, pp. 1348-60, 2010.

Fussell A.J., Cowie K.A., Clifton G.C., Mago N., (2014) “Development and research of eccentrically braced frames with replaceable active links” NZSEE Conference 2014

Goudarzi A., Ghassemieh M., Baei M., (2012) "The Effect of Axial Force on the Behavior of Flush End-plate moment connections" World conference on Earthquake engineering, Lisbon Portugal

Güneyisi, E. M. and Altay, G. (2008) "Seismic fragility assessment of effectiveness of viscous dampers in R/C buildings under scenario earthquakes", Structural Safety, vol. 30, pp. 461-80

Güneyisi E. M. (2012) "Seismic reliability of steel moment resisting framed buildings retrofitted with buckling restrained braces", Earthquake Engineering and Structural Dynamics, vol. 41, pp. 853-74

Guneyisi E. M., D'aniello M, Raffaele Landolfo, (2014) "Seismic upgrading of steel Moment-Resisting Frames by means of friction devices" The Open Construction and Building Technology Journal, 8, (Suppl 1: M9) 289-299

Guo L., Gao S., Fu F., (2015) "Structural performance of semi-rigid composite frame under column loss" *Engineering Structures* 95, pp. 112-126.

Guo, B., Gu, Q. and Liu, F. (2006) "Experimental Behavior of Stiffened and Unstiffened End-Plate Connections under Cyclic Loading", J. Struct. Eng., 132(9), 1352-1357

Han, X., (2008) "Eccentrically braced frame design for moderate seismic egions" Beijing, China, 14th World Conference on Earthquake Engineering.

Halling J. Principles of tribology. London: Macmilln Education LTD.; 1978.

Haremza C., Santiago A., Demonceau J-f., Jaspart J-P., Simoes da Silva L., (2016) "Composite joints under M-N at elevated temperatures" *Journal of Constructional Steel Research* 124, pp. 173-186

Hjelmstad, K. & Popov, E., (1983) "Cyclic behavior an design of link beams" *Journal on Structural Engineering*, 109(10), pp. 2387-2403.

Hollings, J.P. (1969*a*) "Reinforced Concrete Seismic Design" Bulletin of the New Zealand Society for Earthquake Engineering, 2(3), 217-250.

Hollings, J.P. (1969*b*) "A reinforced concrete building in Wellington" Bulletin of the New Zealand Society for Earthquake Engineering, 2(4), 420-442.

Iannone, F., Latour, M., Piluso, V. & Rizzano, G., (2011) "Experimental Analysis of Bolted Steel Beam-to-Column Connections: Component Identification" Journal of Earthquake Engineering, 15(2), pp.214-44

Ioan, A., Stratan, A. & Dubina, D., (2013) "Numerical simulation of bolted links removal in eccentrically braced frames" *Pollack Periodica* 2013;8(1):15–26..

Ioan A., Stratan A., Dubina A., Poljanšek M., Molina F.J., Taucer F., Pegon P., Sabau G., (2016) "Experimental validation of re-centring capability of eccentrically braced frames with removable links" *Engineering Structures* 113, 335-346

Ishiyama Y., (2011) "Introduction to Earthquake Enginering and seismic codes in the world" February 2011

Jaspart, J.P. (1991) "Etude de la semi-rigidite des noeuds poutre-colonne et son influence sur la resistance et la stabilite des ossature en acier" PhD Thesis, University of Liege, Liege Belgium

Jaspart, J. & Cerfontaine, F., (2002) "Analytical study of the interaction between bending and axial force in bolted joints" Proceedings of the Third European Conference on Steel Structures, (EUROSTEEL).

Jaspart J.P., Demonceau J.F.. (2008) "European design recommendations for simple joints in steel structures". Journal of Constructional Steel Research, 64/7-8 822-832.

Jaspart J.P., Demonceau J.F. (2009) "Simple connections", Publ. 126, ECCS Press, Brussels, 2009.

Ji X., Wang Y., Ma Q., and Okazaki T., (2016*a*) "Cyclic Behavior of Very Short Steel Shear Links" *J. Struct. Eng*., 142(2): 04015114

Ji X., Wang Y., Ma Q., and Okazaki T., (2016*b*) "Cyclic Behavior of Replaceable Steel Coupling Beams" *J. Struct Eng* 04016169.

Jiang Z., Guo Y., Zhang B., Zhang X., (2015) "Influence of design parameters of buckling-restrained brace on its performance" *Journal of Constructional Steel Research* 105 139-150

Kam W. Y., Pampanin St, (2011) The seismic performance of RC buildings in the 22 February 2011 Christchurch earthquak, Structural Concrete 12 (2011), No. 4

Karavasilis T. L., (2016) "Assessment of capacity design of columns in steel moment resisting frames with viscous dampers" Soil Dynamics and Earthquake Engineering 88, 215–222

Kasai, K. and Popov E., (1984) "On the seismic design of eccentrically braced steel frames" Proceedings of the 8th World conference on Earthquake engineering, San Francisco (CA), USA 387-394

Kasai, K. and Popov E., (1986) "General behavior of WF steel shear link beams" J. Struct. Eng., 112(2): 362-38

Ke K., Chen Y., (2016) "Seismic performance of MRFs with high strength steel main frames and EDBs" Journal of Constructional Steel Research 126 214–228

Kelly, J., Skinner, R. & Heine, A., (1972) "Mechanisms of Energy Absorption in Special Devices for Use in Earthquake Resistant Structures" Bullettin of the New Zealand Society for Earthquake Engineering, 5(3), pp.63-88.

Kelly J.M., (1979) "A seismic Base Isolation: A review" Proceedings, 2nd U.S. National Conference on Earthquake Engineering, Stanford, CA, 823-837

Khademi, Y. & Rezaie, M., (2017) "Comparison study of CBFs and EBFs bracing in steel structures with nonlinear time history analysis". *Civil Engineering Journal*, 3(11), pp. 1157-1165.

Khoo H-H., Clifton C., Butterworth J., MacRae G., Fergurson G., (2012*a*) "Influence of steel shim hardness on the sliding hinge joint performance" *Journal of Constructional Steel Research* 72 pp. 119-129,.

Khoo H-H., Clifton C., Butterworth J., MacRae G., Gledhill S., Sidwell G. (2012*b*) "Development of the self-centering Sliding Hinge Joint with friction ring springs" *Journal of Constructional Steel Research* 78 pp. 201-211,

Khoo H-H., Clifton C., Butterworth J., MacRae G., (2013) "Experimental Study of Full-Scale Self-Centering Sliding Hinge Joint Connections with Friction Ring Springs" *Journal of Earthquake Engineering* 17:7, pp. 972-997,

Khoo H-H., Clifton C., MacRae G., Zhou H., Rambormozian S., (2014) "Proposed design models for the asymmetric friction connection" *Earthquake Engineering & Structural Dynamics*,

Latour, M., Piluso, V. & Rizzano , G., (2011*a*) "Cyclic Modeling of Bolted Beam-to-Column Connections: Component Approach" *Journal of Earthquake Engineering*, 15(4), pp.537-63.

Latour, M., Piluso, V. & Rizzano , G., (2011b). "Experimental Behaviour of innovative dissipative bolted double split tee beam-to-column connections" Steel Construction, 4(2). pp. 53-64.

Latour, M. & Rizzano, G., (2012) "Experimental Behavior and Mechanical Modeling of Dissipative T-Stub Connections*" Journal of Structural Engineering*, 138(2), pp.170-82.

Latour, M.,Piluso, V. & Rizzano , G., (2013). "Experimental Behaviour of friction T-stub beam-to-column joints under cyclic loads" Steel Construction, 6(1). pp. 11-18.

Latour, M., Piluso, V. & Rizzano , G., (2014*a*) "Friction Joints Equipped with Sprayed Aluminium Dampers: Experimental Analysis and Design" 7th European Conference on Steel and Composite Structures. EUROSTEEL 2014, Napoli, September 10-12.

Latour, M., Piluso, V. & Rizzano , G., (2014*b*) "Experimental Analysis on Friction Materials for Supplemental Damping Devices". Construction and Building Materials, 65. pp. 159-176.

Latour, M., Piluso, V., Rizzano, G., (2015) "Free from damage beam-to-column joints: Testing and design of DST connections with friction pads", *Engineering Structures* 85, 219–233

Latour, M., D'Aniello, M., Zimbru, M., Rizzano, G., Piluso, V., Landolfo, R., (2018*a*) "Removable friction dampers for low-damage steel beam-to-column joints", *Soil Dynamics and Earthquake Engineering* 115, 66–81

Latour M., Piluso V., Rizzano G. (2018*b*) "Experimental analysis of beam-to-column joints equipped with sprayed aluminum friction dampers" *Journal of Constructional Steel Research*, 146:33–48.

Latour M, Rizzano G, Santiago A, Simoes da Silva L. (2018*c*). "Experimental response of a low-yielding, re-centering, rocking base plate joint with friction dampers". Soil dynamics and Earthquake Engineering.

Lemaitre, J., (1992). A course on damage mechanics. Berlin/Heidelberg: Springer-Verlag

Lemaitre, J., (2001). Handbook of Materials Behaviour Models, Vol. I, Deformations of Materials, Academic Press

Malley, J. & Popov, E., (1984) "Shear links in eccentrically braced frames" *Journal of Structural Engineering*, 110(9), pp. 2275-2295.

Mansour N., Shen Y., Christopoulos C., and Tremblay R. (2008) "Experimental evaluation of nonlinear replaceable links in eccentrically braced frames and moment resisting frames" The 14th Conference on Earthquake engineering, October 12-17, 2008, Beijing, China

Marsh, C., Pall, A.S., (1981), "Friction Devices to Control Seismic Response", Proceedings Second ASCF,/EMD Specialty Conference on Dynamic Response of Structures, Atlanta, U.S.A., January, pp. 809-818.

Mazzolani F. M., Della Corte G., D'Aniello M., (2009) "Experimental analysis of steel dissipative bracing systems for seismic upgrading" J*ournal of civil engineering and management* 15(1), 7–19.

Mazzolani F.M. (Editor). (2000) "Moment Resistant Connections of Steel Frames in Seismic Areas, Design and Reliability", E&FN Spoon,.

McDaniel, C., Uang, C. & Seible, F., (2003) "Cyclic testing of built-up steel shear links for the new bay bridge" *Journal of Structural Engineering*, 129(6), pp. 801-809.

Mohamadi-shooreh M.R., Mofid M., (2013) "Prediction of the yielding moment of flush endplate splice connections using finite element modelling" Scientia Iranica A 20 (2), pp. 270–277

Montuori R., Nastri E., Piluso V., (2016) "Theory of Plastic Mechanism Control for MRF–EBF dual systems: Closed form solution" Engineering Structures 118, 287–306

Mualla I., Belev B. (2002) "Seismic response of steel frames equipped with a new friction damper device under earthquake excitation" Eng. Struct.; 24 (3):365–371.

Murray, T.M. (1990), AISC Design Guide 4, Extended End-Plate Moment Connections, AISC (American Institute of Steel Construction), Chicago, IL, USA.

Murray, T.M. and Sumner, E.A. (2004), AISC Design Guide 4, Extended End-Plate Moment Connections—Seismic and Wind Applications, (2nd Edition), AISC (American Institute of Steel Construction), Chicago, IL USA.

Nakashima M, Inoue K., and Tada M. (1998) "Classification of damage to steel buildings observed in the 1995 Hyogoken-Nanbu earthquake," Engineering Structures, vol. 20, pp. 271-81

Nastri E., Montuori R., Piluso V., (2015) "Seismic Design of MRF-EBF Dual Systems with Vertical Links: EC8 vs Plastic Design" *Journal of Earthquake Engineering*, 19, pp. 480–504

NEHRP. NEHRP Recommended provisions for new buildings and other structures (FEMA 450). Part 1: Provisions and Part 2: Commentary. Building seismic safety council. Washington, D.C.: National Institute of Building Sciences; 2003

Nogueiro P., Simões da Silva L., Bento R., Simões R., (2006) "Experimental behaviour of standardised European end-plate beam-to-column steel joints under arbitrary cyclic loading", Proc. of SDSS'06 –Int.l Colloquium on Stability and Ductility of Steel Structures, Portugal, 2006.

Nogueiro P., Simões da Silva L., Bento R., Simões R., (2007) "Numerical implementation and calibration of a hysteretic model with pinching for the cyclic response of steel joints", International Journal of Advanced Steel Construction 3(1), pp. 128-153

Nunes P. C., de Lima L. R. O., da Silva J. G. S., da S. Vellasco P. C. G., de Andrade S. A. L., (2007) "Parametrical Analysis of Extended Endplate Semi-Rigid Joints Subjected to Bending Moment and Axial Force" *Latin American Journal of Solids and Structures*, March 2007

NZS 1170.5:2004, Structural Design Actions, Part 5, Earthquake actions - New Zealand, 2004, Issued by Standards New Zealand

Ono S., Nakahira K., Tsujioka S., Uno N. (1996) "Energy absorption capacity of thermally sprayed aluminum friction dampers" J. Therm. Spray Technol. 5 (3).

Oosterhof S.A., Driver R.G., (2015) "Behavior of Steel Shear Connections under Column-Removal Demands" *J. Struct. Eng.*, 141(4): 04014126

Oviedo-Amezquita J. A., Midorikawa M., and Asari T.. (2010) "Earthquake response of ten-story story drift–controlled reinforced concrete frames with hysteretic dampers", Engineering Structures, vol. 32, pp. 1735-46.

P100-1/2013. Seismic design code – Part 1: Rules for buildings; 2013 [in Romanian].

Pall, A.S., Marsh, C., Fazio, P., (1979) "Limited Slip Bolted Joints for Large Panel Structures", Proceedings, Symposium on Behavior of Building Systems and Building Components, Nashville, U.S.A., March, pp. 385-494.

Pall, A.S. and Marsh, C., (1982) "Response of Friction Damped Braced Frames", Journal of Structural Division, ASCE, Vol. 108, No. ST6, June, pp. 1313-1323.

Park R. and Paulay T., "*Reinforced Concrete Structures"*, John Wiley & Sons, Inc 1975, ISBN 0471659177

Paulay T. and Priestley M. J. N. "*Seismic Design of Reinforced Concrete and Masonry Buildings"* John Wiley & Sons, Inc, 1992, ISBN 0471549150

Pavlović, M., Heistermann, C., Veljković, M., Pak, D., Feldmann, M., Rebelo, C., Simões da Silva, L. "Connections in towers for wind converters, part I: Evaluation of down-scaled experiments" *Journal of Constructional Steel Research* http://dx.doi.org/10.1016/j.jcsr.2015.09.002

Persson B. Sliding friction. Berlin: Springer; 2000.

Piluso, V., ., Faella C., Rizzano G (2001*a*) "Ultimate behavior of bolted T-stubs I Theoretical model" J. Struct. Eng. 127(6), 686-693

Piluso, V., ., Faella C., Rizzano G (2001*b*) "Ultimate behavior of bolted T-stubs II Model validation" J. Struct. Eng. 127(6), 694-704

Piluso V., Montuori R., Troisi M. (2014) "Innovative structural details in MR-frames for free from damage structures", Mechanics Research Communications; 58: 146-156.

Popov, E., Kasai, K. & Engelhardt, M., (1987) "Advances in design of eccentrically braced frames" *Bulletin of the New Zealand National Society for Earthquake Engineering*, 20(1).

Popov, E., Ricles, J. & Kasai, K., (1992) "Methodology for optimum EBF link design". Proceedings of the 10th World Conference. Earthquake Engineering, Balkema, Rotterdam,

Popov, E.G., Grigorian, C.E. and Yang, T-S., "Developments in seismic structural analysis and design", Engineering Structures, Vol. 17, No. 3, 1995.

Ramhormozian S., Clifton G.C, MacRae G.A., (2014) "The Asymmetric Friction Connection with Belleville springs in the Sliding Hinge Joint" In: Proceedings of the NZSEE Conference

Reyes-Salazar, A., Llanes-T M D.. Bojorquez J., Bojorquez E., Lopez-Barraza A., Haldar A., (2016) "Force reduction factors for steel buildings with welded and post-tensioned connections" Bull Earthquake Eng 14:2827–2858

Richards P.W., Uang C-M., (2005) "Effect of flange width-thickness ratio on eccentrically braced frames link cyclic rotation capacity" *J. Struct. Eng.*, 131(10) 1546-1552

Roeder, C. & Popov, E., (1978) "Eccentrically Braced Steel Frames for Earthquakes" *J. Structural Division, ASCE,* 104(ST3)

Roy B. K., Chakraborty S., (2015)"Robust optimum design of base isolation system in seismic vibration control of structures under random system parameters" *Structural Safety* 55, pp. 49–59

Saeedi F., Shabakhty N., Mousavi S. R. (2016) "Seismic assessment of steel frames with triangular-plate added damping and stiffness devices" Journal of Constructional Steel Research 12515-25

Sato A., Kimura K., Suita K., Inoue K. (2009) "Cyclic test of high strength steel beam-to-column connection composed with knee-brace damper and friction damper connected by high strength bolts" Proceedings of the SEEBUS 2009. Kyoto, Japan

SEAOC Recommended lateral force requirements and commentary1973. Seismology Committee, Structural Engineers Association ofCalifornia, San Francisco, Ca, 146 p

"SeismoStruct 2016 – A computer program for static and dynamic nonlinear analysis of framed structures," available from http://www.seismosoft.com

Seki M., Katsumata H., Uchida H., Takeda T., (1988) "Study on earthquake response of twostoried steel frame with y-shaped braces" Proceedings of the 9thWorld Conference on Earthquake Engineering, Tokyo-Kyoto, Japan 1988, pp. 65–70.

Shaker F.M.F., and Elrahman W.M. Abd., (2014) "Behavior of Flush and Extended End-Plate Beam-To-Column Joints under Bending and Axial Force" *World Applied Sciences Journal* 30 (6), pp. 685-695

Shi, Y., Shi, G. and Wang, Y. (2007*a*) "Behaviour of end-plate moment connections under earthquake loading", Eng. Struct., 29(5), 703-716.

Shi, Y., Shi, G. and Wang, Y. (2007*b*) "Experimental and theoretical analysis of the moment-rotation behaviour of stiffened extended end-plate connections", J. Constr. Steel Res., 63(9), 1279-1293.

Skinner, R:I:, Tyler R.G., Heine, A.J. and Robinson W.H., (1980) "Hysteretic dampers for the protection of structures from earthquake" Buletin of New Zealand National Society for Earthquake engineering Vol 13. No. 1

Soong T.T., Spencer B.F. (2002) "Supplemental energy dissipation: state-of-the-art and state-of-the-practice" Eng. Struct.; 24:243–259.

Stratan A., Dubina D., Dinu F., (2003) "Control of global performance of seismic resistant EBF with removable link" Proceedings of the 4th International Conference on Behaviour of Steel Structures in Seismic Areas (STESSA 2003), Naples, Italy 2003, pp. 175–180.

Stratan A, Dubina˘ D. Bolted links for eccentrically braced steel frames. In: Bijlaard FSK, Gres-nigt AM, van der Vegte GJ (Eds.), Proc. of the fifth AISC/ECCS international workshop ‘‘Connections in steel structures V. behaviour, strength & design”, June 3–5, Delft University of Technology, The Netherlands; 2004. p.223–32.

Stratan, A. & Dubina, D., (2004) ”Bolted links for eccentrically braced steel frames. *Connections in Steel Structures,* Volume V, pp. 223-332.

Stylianidis P.M., Nethercot D.A., (2015*b*) “Modelling of connection behaviour for progressive collapse analysis” *Journal of constructional steel research* 113, pp. 169-184

Stylianidis P.M., Nethercot D.A., Izzuddin B.A., Elghazouli A.Y., (2015*a*) “Modelling of beam response for progressive collapse analysis” *Structures*

Stylianidis P.M., Nethercot D.A., Izzuddin B.A., Elghazouli A.Y., (2016) “Robustness assessment of frame structures using simplified beam and grillage models” *Engineering Structures* 115, pp. 78-95

Sumner, E.A. and Murray, T.M. (2000) “Performance of Extended Moment End-Plate Connections Subject to Seismic Loading”, U.S.–Japan Workshop on Seismic Fracture Issues in Steel Structures, San Francisco, CA, USA, February-March.

Sumner, E.A. and Murray, T.M. (2002) “Behavior of extended end-plate moment connections subject to cyclic loading” J. Struct. Eng., 128(4), 501-508.

Swanson J. A., Leon R. “Stiffness modeling of bolted t-stub connection components”. *Journal of Structural Engineering*, **127**(5), 2001.

Symans M. D., Charney, F. A., Whittaker, S. Constantinou, C. (2008) “Energy Dissipation Systems for Seismic Applications: Current Practice and Recent Developments” Journal of structural engineering 184(1)

Taghi Nikoukalam M.; Mirghaderi S. R. and Dolatshahi K. M., (2015) “Analytical Study of Moment-Resisting Frames Retrofitted with Shear Slotted Bolted Connection” J. Struct. Eng. 141(11), 04015019

Tan K. G., and Christopoulos C., (2016) “Development of Replaceable Cast Steel Links for Eccentrically Braced Frames” *J. Struct. Eng.*, 04016079.

Tan, K. & Christopoulos, C., (2016) “Development of replaceable cast steel links for eccentrically braced frames” Journal of Structural Engineering.

Tartaglia R., D’Aniello M., Rassati G.A., Swanson J.A., Landolfo R. (2018*a*). Full strength extended stiffened end-plate joints: AISC vs recent European design criteria. Engineering Structures, Volume 159, 15 March 2018, Pages 155–171.

Tartaglia R., D’Aniello M., Zimbru M. and Landolfo R. (2018*b*) “Finite element simulations on the ultimate response of extended stiffened end-plate joints” *Steel and Composite Structures*, Vol. 27, No. 6 727-745

Tremblay R., Timler P., Bruneau M., and Filiatrault A., (1995) “Performance of steel structures during the 1994 Northridge earthquake,’’ Journal of Civil Engineering, vol. 22, pp. 338-60

Tzimas S., Kamaris G. S., Karavasilis T. L., Galasso C. (2016) “Collapse risk and residual drift performance of steel buildings using post-tensioned MRFs and viscous dampers in near-fault regions” Bull Earthquake Eng 14:1643–1662

Urbonas K., Daniunas A., (2006) "Behaviour of semi-rigid steel beam-to-beam joints under bending and axial forces" *Journal of Constructional Steel Research* 62, pp. 1244–1249

Vataman, A., Ciutina, A. & Grecea, D., (2016) "Numerical analysis of short link steel in eccentrically-braced frames under seismic actions" *Pollack Periodica*, 11(2), pp. 29-42.

Watanabe E., Sugiura K., Nagata K., and Kitane Y., (1998) "Performances and damages to steel structures during 1995 Hyogoken-Nanbu earthquake," Engineering Structures, vol. 20, pp. 282-90

Whittaker A.S., Constantinou M.C., Ramirez O.M., Johnson M.W., Chrysostomou C.Z. (2003) "Equivalent lateral force and modal analysis procedures of the 2000 NEHRP provisions for buildings with damping systems". Earthquake Spectra 19(4):959–980

Yang, M.S., (1982) "Seismic behavior of an eccentrically X-braced steel structure" Earthquake Engineering Research Center, University of California, Berkeley, CA, Report No. UCB/EERC-82/14, 1982.

Yang T-S., Popov E.P., (1995) "Experimental and Analytical Studies of Steel Connections and Energy Dissipators" Report No. UCB/EERC-95/13, University of California, Berkeley.

Yeung S., Zhou H., Khoo H-H., Clifton G.C., MacRae G.A. (2013) "Sliding shear capacities of the asymmetric friction connection", NZSEE Conference, April 26–28, Wellington, 2013 (Paper n. 27).

Yokoyama S., Oki T.. (2000) "Connecting Structure of beam and column and building having it structure" JP2000 3 28 650 (A) 11-28.

Youssef N., Bonowitz D., and Gross J., (1995) "A Survey of Steel Moment-Resisting Frame Buildings Affected by the 1994 Northridge Earthquake", Research report no. NISTIR 5625. Gaithersburg (MD, USA): National Institute of Science and Technology (NIST)

Yu H., Burgess I. W., Davison J. B., Plank R.J., (2011) "Experimental and Numerical Investigations of the Behavior of Flush End Plate Connections at Elevated Temperatures" *J. Struct. Eng*. 137 pp. 80-87.

Zarsav S., Zahrai S.M. and Oskouei A.V. (2016) "Effect of stiffener arrangement on hysteretic behavior of link-to-column connections" *Structural Engineering and Mechanics*, Vol. 57, No. 6, pp. 1051-1064,

Zimbru, M., D'Aniello, M., De Martino, A., Latour, M., Rizzano G., and Piluso V., (2018) "Investigation on Friction Features of Dissipative Lap Shear Connections by Means of Experimental and Numerical Tests" The Open Construction and Building Technology Journal, 2018, 12, (Suppl-1, M9) 154-169

Zoetemeijer, P. (1974) "A design method for the tension side of statically loaded, bolted beam-to-column connections", Heron, 20(1) 1-59